Three-dimensional Numerical Modeling of Cohesive Sediment Flocculation Processes in Turbulent Flows

Zur Erlangung des akademischen Grades eines

DOKTOR-INGENIEURS

von der Fakultät für
Bauingenieur-, Geo- und Umweltwissenschaften
des Karlsruher Instituts für Technologie (KIT)

genehmigte

DISSERTATION

von
Dipl.-Ing. Irina Klassen
aus Karlsruhe

Tag der mündlichen Prüfung
15.02.2017

Referent: Prof. Dr.-Ing. Dr. h.c. mult. Franz Nestmann
Korreferent: Prof. Dr.-Ing. Nils Reidar B. Olsen

Karlsruhe 2017

Kurzfassung

Kohäsive Sedimente spielen eine wichtige Rolle im Bereich der Morphodynamik. Ökologische Probleme resultieren aus der Adsorption von Schadstoffen, wirtschaftliche Probleme entstehen durch hohe Sedimentationsraten kohäsiver Sedimente in strömungsberuhigten Bereichen. Die Vorhersage des Schwebstofftransports erfordert numerische Modelle, welche die dominierenden physikalisch-chemischen Prozesse feiner Sedimente nachbilden können. Besonders im Hinblick auf die Modellierung mikro-skaliger Prozesse, spielen Flockungsprozesse kohäsiver Feinsedimente, d.h. die Aggregation und Disaggregation (Zerbrechen) der Feinstpartikel, eine besondere Rolle, da diese den Transport und das Absetzen der Feinstpartikel beeinflussen. Die numerische Modellierung kohäsiver Flockungsprozesse stellt gegenwärtig aufgrund der vielschichtigen Eigenschaften kohäsiver Sedimente, der verschiedenen physikalisch-chemischen Einflussfaktoren und nicht zuletzt aufgrund noch bestehender Wissenslücken im Prozessverständnis eine große Herausforderung für ingenieurpraktische Fragestellungen, sowie für das Forschungsumfeld des Sedimenttransports dar.

Das Ziel dieser Arbeit war es daher das Verständnis von Flockungsprozessen und ihrer verschiedenen Einflussfaktoren durch die Anwendung von hydrodynamischen, numerischen Sedimenttransportmodellen zu verbessern. Zu diesem Zweck wurde das dreidimensionale Sedimenttransportmodell SSIIM durch die Implementierung eines physikalisch basierten Flockungsmodells basierend auf dem Ansatz nach McAnally (2000) erweitert. Der Flockungsalgorithmus wurde auf ein physikalisches Modell im offenen Kreisgerinne, als auch auf eine Fallstudie an der Stauhaltung Iffezheim am Rhein angewandt.

Die Ergebnisse der Flockungsmodellierung zeigen eine erfolgreiche Umsetzung der Modellimplementierung in SSIIM für beide Fallstudien. Zur Untersuchung des Einflusses unbekannter Parametergrößen, Anfangs- und Randbedingungen auf die Modellergebnisse wurden im Kreisgerinne Sensitivitätsstudien durchgeführt. Die numerischen Analysen haben gezeigt, dass die berechneten Flockengrößen sensitiv gegenüber allen untersuchten Faktoren sind. Die höchste Sensitivität wurde gegenüber der fraktalen Dimension und dem Koeffizienten zur Berechnung der Partikelfestigkeit identifiziert. Des Weiteren wurde die Disaggregation der Flocken aufgrund turbulenzinduzierter Scherspannungen als ein signifikanter Mechanismus hinsichtlich der modellierten zeitlichen Flockengrößenentwicklung identifiziert. Die Berechnungen haben außerdem gezeigt, dass der implementierte Flockungsalgorithmus, im Gegensatz zu vereinfachten Modellen, die Flockungsprozesse explizit ausschließen, physikalisch plausiblere Flockengrößen und eine wesentlich bessere Übereinstimmung mit gemessenen Aggregatgrößen liefert.

Die Anwendung des Flockungsmodells auf die Stauhaltung Iffezheim hat gezeigt, dass die modellierten Flockengrößen in einem physikalisch belastbaren Rahmen liegen. Ebenso wurde eine räumliche Variabilität der simulierten Flockengrößen aufgrund unterschiedlicher Turbulenzintensitäten in der Stauhaltung realistisch berechnet. Die numerischen Analysen haben auch in dieser Fallstudie hervorgehoben, dass Unsicherheiten bezüglich der fraktalen Dimension und des Partikelfestigkeitskoeffizienten die modellierten Flockengrößen maßgeblich beeinflussen können. Darüber hinaus können unrealistische Annahmen hinsichtlich der Primärpartikelgrößen und der Partikelgrößen-Zuflussrandbedingung am Modellrand zu physikalisch ungenauen oder inkorrekt berechneten Flockengrößen führen.

Insgesamt verdeutlichen beide Fallstudien die Herausforderungen hinsichtlich einer physikalisch exakten und quantitativen Flockungsmodellierung aufgrund von Unsicherheiten in der Spezifikation der verschiedenen empirischen Parameter und der hohen Komplexität der Feinsedimentdynamik. Dies wiederum unterstreicht die Notwendigkeit von zuverlässigen Messdaten zu Flockeneigenschaften für zukünftige Anwendungen des

implementierten Flockungsalgorithmus. Die Ergebnisse dieser Arbeit dienen somit als Grundlage für ein besseres Verständnis und eine genauere Prognose von Flockungsprozessen und können zukünftig für die Optimierung und Weiterentwicklung des implementierten Flockungsalgorithmus herangezogen werden.

Abstract

Cohesive sediments play an important role in the field of river morphodynamics. Environmental risks are related to the adsorption of contaminants, economic problems arise from high deposition rates of cohesive sediments during low flow conditions. The prediction of cohesive sediment transport requires numerical models which include the dominant physico-chemical processes of fine sediments. Mainly in terms of simulating small-scale processes, flocculation of cohesive sediment, i. e. the aggregation and disaggregation (break-up) mechanisms of the fine sediment particles, play an important role since they affect the transport and settling of fine-grained particles. Due to the multilayered particle properties, the various physico-chemical influencing factors and not least because of the still existing knowledge gaps, the numerical modeling of flocculation processes is nowadays a crucial challenge in the science of cohesive sediments and civil engineering.

The objective of this work was therefore to gain a better understanding of the flocculation processes and its different involving mechanisms and impact factors by applying computational fluid dynamics (CFD) sediment transport models. For this purpose, the three-dimensional sediment transport software SSIIM was extended by implementing a physics-based flocculation model derived by McAnally (2000). The flocculation algorithm was applied on a physical model in the open annular flume and on a real case study in the Iffezheim reservoir, Germany.

The flocculation modeling results show a successful realization of the model implementation for both applications. Sensitivity studies in the annular flume were carried out to investigate the impact of unknown parameter values and initial/boundary conditions on the flocculation modeling results. It was found that the simulated floc sizes in the annular flume are sensitive towards all tested factors. However, the highest sensitivity of the model results was identified towards the fractal dimension and the particle yield strength coefficient. Furthermore, the floc break-up mechanism due to turbulence-induced shear stresses was evaluated as a significant process in terms of the temporal floc size evolution. The flocculation modeling results were compared with simplified models by excluding the flocculation algorithm. It was shown that the implemented flocculation model provides physically more realistic floc sizes and a much better correspondence with measured aggregate sizes than the simplified models which exclude flocculation processes.

The flocculation model application on the Iffezheim reservoir has shown that modeled floc sizes were reasonable predicted in terms of both their value range and spatial variability due to varying turbulences in the reservoir. The numerical studies again pointed out that uncertainties about the fractal dimension and the particle yield strength coefficient may imply a major impact on the modeled floc sizes. Furthermore, unrealistic assumptions in terms of the primary and the inflow particle sizes at the model boundary may lead to physically imprecise or incorrect modeled floc sizes.

In conclusion, both case studies demonstrated the difficulty of a physically precise and quantitative flocculation modeling due to uncertainties in the specification of the various empirical parameter values and the complexity of fine sediments. This in turn highlights the need for reliable measurement data of the floc characteristics for future applications of the implemented flocculation algorithm. The findings from this work provide a basis to better understand and predict the interactions of flocculation processes and can be used to improve and further develop the flocculation algorithm.

Acknowledgments

The present dissertation was developed during my work as a research associate at the Institute for Water and River Basin Management (IWG) at the Karlsruhe Institute of Technology (KIT) within a cooperation project with the Federal Institute of Hydrology (BfG), Koblenz. There are a number of people who made this thesis possible and to whom I would like to express my thanks.

First of all, I would like to express my gratitude to Prof. Dr.-Ing. Dr. h.c. mult. Franz Nestmann, head of the IWG, for giving me the opportunity to work at his institute and for the takeover of the main referee. His confidence and support in my work as well as the scientific freedoms during my research work have contributed considerably to the success of this work.

Special thanks also goes to Prof. Dr.-Ing. Nils Reidar B. Olsen from the Department of Hydraulic and Environmental Engineering at the Norwegian University of Science and Technology (NTNU) in Trondheim, as the co-supervisor of this thesis. Many thanks for supporting me during the numerical studies with SSIIM, the valuable technical encouragement and the discussions over the years.

I am also very grateful to Prof. Dr.-Ing. habil. Boris Lehmann from the Institute of Hydraulic Engineering at the Technical University of Darmstadt, and Dr.-Ing. Stefan Vollmer, head of unit M3 at the BfG. They both enabled the close and fruitful cooperation with the Federal Institute of Hydrology providing me the foundation to work on this thesis.

Special warm thanks goes to Dr.-Ing. Gudrun Hillebrand from the BfG, who supported me in so many ways. I had the pleasure to be her office mate at the BfG. During the years I have been working with Gudrun, she always found the time for discussions, giving the right advice or just making numerical algorithms about flocculation look easier. Her scientific experience and knowledge influenced this work in a major way.

I also want to thank Dr.-Ing. Frank Seidel from the IWG, who gave me the necessary space to focus on my work in the final stage. Furthermore, I am very grateful to all my colleagues from the IWG in Karlsruhe and the BfG in Koblenz for the collegial, friendly and open-minded working atmosphere. I thank you for listening and supporting me through this entire period.

I would also like to thank Dr.-Ing. Sina Wunder and Dr.-Ing. Gudrun Hillebrand, who carefully read the first drafts of this work, for their valuable suggestions and critical comments. For the linguistic improvements of this thesis I want to thank my brother-in-law Paul Janson. I am very grateful for their patience and invested time.

Finally, last but by no means least, I am very thankful to my friends and family, above all my parents and sister, for their never ending encouragement, the necessary distractions from my research and their acceptance of my frequent absence during the intensive writing period.

Contents

List of Figures

List of Tables

Symbol Directory

a, b	empirical coefficients to calculate the settling velocity	[–]
a_c	size of the cube	[m]
a_f	size of the aggregate	[m]
a_{ref}	distance from the bed to where C_{bed} is computed in SSIIM	[m]
B_D	constant to calculate the median floc size	[–]
B_j	coefficient characteristic of sediment and particle of size j	[1/s]
B_ρ	empirical sediment- and flow-dependent density function	[kg/m³]
B_τ	empirical sediment- and flow-dependent stress function	[N/m²]
C	suspended sediment concentration (SCC)	[kg/m³]
$\overline{C}$	depth-averaged concentration	[kg/m³]
$\dot{C}$	rate of mass concentration changes	[kg/m³s]
C_D	drag coefficient	[–]
C_b	near-bed concentration	[kg/m³]
C_{bed}	equilibrium sediment concentration close to the bed in SSIIM	[m³/m³]
C_0	initial concentration in SSIIM	[m³/m³]
C_μ	empirical constant to calculate the turbulent eddy-viscosity	[–]
CEC	sediment cation exchange capacity	[meq/100g]
CEC_0	reference sediment cation exchange capacity	[meq/100g]
D	particle diameter	[m]
D_{dep}	deposition rate	[kg/m²s]
D_{diff}	diffusion coefficient	[m²/s]
D_f	diameter of the aggregate/floc	[m]
D_{fc}	characteristic floc size	[m]
$D_{f,e}$	equilibrium floc size	[m]
$D_{f,max}$	maximum floc diameter	[m]
$D_{f,median}$	median floc size	[m]
D_g	diameter of the grain particle	[m]
D_m	arithmetic mean diameter	[m]
D_{turb}	turbulent diffusion coefficient	[m²/s]
F_I	inertial force	[kgm/s²]
F_V	viscous force	[kgm/s²]
$F_{R,i}$	sediment pick-up rate	[kg/m²s]
F_c	collision diameter function	[–]
F_d	drag force	[kgm/s²]
F_{dep}	deposition flux	[kg/m²s]
F_e	erosion flux	[kg/m²s]
$F_g{}'$	submerged gravity force	[kgm/s²]

F_p	relative (non-dimensional) depth of interparticle penetration during a collision	[–]
f_c	parameter as a function of sediment concentration and fluid flow	[–]
FF	form factor of a sediment particle	[–]
G	velocity gradient	$[1/s]$
G_l	velocity gradient in laminar flow	$[1/s]$
G_t	velocity gradient in turbulent flow	$[1/s]$
g	acceleration of gravity	$[m^2/s]$
h	water depth	[m]
J_{advec}	advective mass flux	$[kg/m^2s]$
$J_{diff,mol}$	molecular diffusion mass flux	$[kg/m^2s]$
$J_{diff,turb}$	turbulent diffusion mass flux	$[kg/m^2s]$
J_{disp}	dispersion mass flux	$[kg/m^2s]$
$J_{settling}$	vertical mass flux due to self-weight of particles	$[kg/m^2s]$
K	constant to calculate the maximum floc size	$[m/s]$
K_F	empirical sediment dependent coefficient to calculate the strength of a fractal floc	$[N/m^2]$
K_{disp}	dispersion coefficient	$[m^2/s]$
k	parameter depending on sediment composition to calculate the settling velocity	[–]
k_A	dimensional aggregation parameter	$[m^2/kg]$
k_B	dimensional floc break-up parameter	$[s^{1/2}/m^2]$
k_s	wall roughness	[m]
k_{st}	Strickler-coefficient	$[m^{1/3}/s]$
L	characteristic length	[m]
M	(average) sediment particle mass	$[kg/particle]$
M_e	erosion coefficient	$[kg/m^2s]$
$M(lower)$	class lower limit on particle mass	$[kg/particle]$
$M(upper)$	class upper limit on particle mass	$[kg/particle]$
m_D	constant to calculate the median floc size	[–]
m, n	empirical coefficients to calculate the settling velocity	[–]
N_f	number of particles in a fractal aggregate	[–]
N_{ik}	collision efficiency of particles of size i and k	$[1/m^3s]$
n_b	constant to calculate the maximum floc size	[–]
n_f	fractal dimension	[–]
n_{fc}	characteristic fractal dimension	[–]
n_j	number concentration of particles of size j per unit volume	$[1/m^3]$
P	pressure	$[N/m^2]$
P_{ik}	probability of disaggregation of particles of size i into size k	[–]
p	probability mass function	[–]
Q	discharge	$[m^3/s]$
q_{bed}	dimensionless bed load transport	[–]
Re	Reynolds number	[–]
Re_f	floc Reynolds number	[–]
Re_g	particle Reynolds number	[–]

r	conversion factor between volume of sediment particles and volume of deposits on the bed	[kg/m^3]
S	salinity	[ppt]
S_0	reference salinity	[ppt]
T	temperature	[K]
T_S	settling time	[sec]
T_f	flocculation time	[sec]
T_0	reference temperature	[K]
t	time	[sec]
TKE	turbulent kinetic energy	[m^2/s^2]
U	characteristic flow velocity	[m/s]
$U(y)$	flow velocity at a distance y from the wall	[m/s]
u_i	i class particle velocity relative to a k class particle	[m/s]
u_*	shear velocity	[m/s]
u, v, w	fluid velocity components in x-, y-, z-direction	[m/s]
$\overline{u}$, $\overline{v}$, $\overline{w}$	mean component of flow velocity in x-, y- and z-direction	[m/s]
$u^{'}$, $v^{'}$, $w^{'}$	velocity fluctuation component of flow velocity in x-, y- and z-direction	[m/s]
w_s	settling velocity	[m/s]
$w_{s,char}$	characteristic settling velocity	[m/s]
$w_{s,f}$	settling velocity of the floc	[m/s]
$w_{s,g}$	settling velocity of the grain particle	[m/s]
$w_{s,0}$	reference settling velocity	[m/s]
w_0	settling velocity of an individual floc or particle	[m/s]
x, y, z	coordinate system	[m]
$\alpha_{a,ik}$	aggregation factor between two particles of size i and k	[–]
$\beta_{B,ik}$	collision frequency function between two particles of size i and k due to Brownian motion	[m^3/s]
$\beta_{D,ik}$	collision frequency function between two particles of size i and k due to differential settling	[m^3/s]
β_{Re}	function of the particles Reynolds number	[–]
$\beta_{S,ik}$	collision frequency function between two particles of size i and k due to fluid shear	[m^3/s]
β_{ik}	collision frequency function between two particles of size i and k	[m^3/s]
$\beta_{sum,ik}$	total collision frequency function between two particles of size i and k	[m^3/s]
Δt	time step	[sec]
Δz	bed level changes	[m]
ϵ	turbulent dissipation rate	[m^2/s^3]
η	Kolmogorov micro-scale of turbulence	[m]
γ_{ml}	probability that a particle of size l will be formed after disaggregation of a particle of size m	[–]
κ	von Karman's constant	[–]
κ_B	Boltzmann constant	[J/K]
μ	dynamic viscosity of fluid	[kg/ms]

ν	kinematic viscosity of fluid	$[\mathrm{m^2/s}]$
ν_t	turbulent eddy-viscosity	$[\mathrm{m^2/s}]$
Π_c	non-dimensional term	$[-]$
ρ_f	density of the aggregate/floc	$[\mathrm{kg/m^3}]$
ρ_g	density of the grain particle	$[\mathrm{kg/m^3}]$
ρ_w	fluid density	$[\mathrm{kg/m^3}]$
τ_b	bed shear stress	$[\mathrm{N/m^2}]$
τ_c	critical bed shear stress for erosion	$[\mathrm{N/m^2}]$
τ_d	critical shear stress for deposition	$[\mathrm{N/m^2}]$
τ_f	strength of a fractal floc	$[\mathrm{N/m^2}]$
$\tau_{ik,k}$	shear stress experienced by the k aggregate during a collision with a particle from size class i	$[\mathrm{N/m^2}]$
τ_u	flow shear stress	$[\mathrm{N/m^2}]$
θ	angle between direction of the velocity vector of a colliding particle and the line connecting both colliding particle centers	$[^\circ]$

1 Introduction

1.1 Issue and Relevance

River systems represent a natural transport system for sediments. The processes of sediment erosion, transport and deposition are the key components of river morphodynamics. Depending on the size of the sediments and the flow conditions, sediment transport traditionally can be divided in bed load and suspended load transport. As bed load, the coarser portion of the sediment saltates, rolls and slides close to the river bed. As suspended load, the fine sediment particles are carried in suspension by the fluid turbulence. This work focuses on the suspended sediment dynamics.

Human intervention by engineering measures affects the sediment transport in natural river systems in different ways. River regulations concerning flood protection and land reclamation as well as the use of rivers as navigable waterways and for the production of electrical energy involve changes in the sediment regime. For example, the construction of dams and barrages interrupts the continuity of sediment transport through river systems causing suspended sediments to deposit upstream of the barrages where flow velocities and turbulence are low, while downstream sediment erosion takes place. Deposition of fine-grained sediment is one of the major problems with respect to the sustainable use of zero-emission hydropower worldwide, since it leads to a decrease of the reservoir volume and to a threatened dam stability over time. The World Bank estimates that around 1 % of the volume of the water reservoirs in the world are lost per year due to sedimentation (Mahmood, 1987). Walling and Fang (2003) identified reservoir construction as probably the most important influence on land-ocean sediment fluxes. The construction of groynes to ensure navigable waterways is accompanied by sediment deposition in the groyne fields as well. Furthermore, many ports suffer from sedimentation of their berthing and manoeuvring areas. To ensure flood protection and required water depths regular extensive maintenance dredging operations are necessary. In Germany, for example, approximately 46 million m^3 of sediment need to be dredged annually, which is very costly for the responsible authorities (Bundesministerium für Verkehr, Bau- und Wohnungswesen, 2004).

In addition to the economic problems, suspended sediments may also cause an environmental risk in terms of the ecological water quality of the rivers. Fine sediments consist of inorganic minerals (such as clay and silt) and organic matter (e. g. plants and animal parts, leafy matter, biopolymers, bacteria, etc.). High suspended sediment loads increase turbidity which can restrict the penetration of sunlight and decrease food availability, thus affecting aquatic life (e. g. Davies-Colley et al., 1992). High suspended sediment loads may also imply deleterious effects on riverine habitats (e. g. Carling and McCahon, 1987). Wood and Armitage (1997) summarize that in extreme cases fine sediments may change the river morphology, kill aquatic flora, clog the interstices between substrate clasts and reduce the available habitat for benthic organisms.

Fine sediments not only have an impact on flora and fauna, they are also able to adsorb other substances due to their high specific surface area. These substances can be anthropogenic contaminants such as heavy metals, which deposit with the fine sediments, becoming resuspended during flood events and thus are transported again downstream. For example, the deposited sediments in the barrages of the Upper Rhine river in Germany are highly contaminated with hexachlorobenzene (HCB) due to historic industrial emissions of particle-bound micropollutants into the Rhine (Pohlert et al., 2011). The mean HCB-concentration at the Iffezheim barrage in 2009 was 207 μg per kg suspended matter (Breitung, 2009), at the Marckolsheim barrage a mean HCB-concentrations of 609 μg per kg suspended matter was measured in 2001 (International Commission for the Protection of the River Rhine (ICPR), 2009). Since these HCB-concentrations exceed the values that allow a relocation of the dredged sediments, the contaminated material needs to be disposed.[1] It gets obvious that in case of contaminated sediments, cohesive sediments may pose even more serious ecological problems and greater maintenance costs.

Due to the environmental and economic problems associated with suspended sediments, the objective of the responsible authorities is to find solutions for a long-term ecologically and economically optimized, sustainable sediment management. To this end, knowledge about the relevant processes that influence the transport and deposition behavior of fine sediments and particle-bound contaminants is essential.

A key process in fine sediment dynamics is the flocculation process which arises from cohesion of fine-grained sediments due to electrochemical surface charge of fine particles. Flocculation implies both aggregation into larger, less dense aggregates or flocs and disaggregation (floc break-up) due to fluid shear stresses and particle-collision induced stresses. Flocculation induces changes in the properties of fine-grained sediments in terms of both the effective particle size and the particle density/floc structure of the growing flocs or aggregates. Therefore, flocculation processes of cohesive sediments have a major impact on the transport and settling of the suspended sediment flocs. Since flocculation processes change the particle size distribution of the suspended sediment, the distribution of particle-bound contaminants on the individual particle size fractions is also exposed to continuous change. Hence, flocculation alters the processes of particle-bound contaminants as well.

In natural river systems, flocculation is a complex phenomenon which is affected by numerous parameters: physico-chemical factors (e. g. particle properties, particle concentration, salt content, pH-value, temperature), biological (e. g. organic matter) and flow-dependent factors (e. g. turbulence intensity). Due to the various involving influencing factors and the complex processes interactions, flocculation processes are not fully understood yet. In order to improve the understanding of flocculation processes, experimental methods in laboratory and field campaigns are applied, which have been increasingly complemented by computational fluid dynamics (CFD) sediment transport models over the recent years due to improved numerical techniques and an increase in computing power capacity. CFD sediment transport models are used for both applications in cohesive sediment engineering and for research studies on sediment dynamics. The advantage of numerical models is that they close spatial and temporal gaps between experimental data. Additionally, they can be used for making long term predictions of cohesive sediment processes or for conducting sensitivity studies in order to better assess the impact of different influencing factors on cohesive sediment processes in general, and flocculation processes in particular.

In this work, the three-dimensional CFD sediment transport model SSIIM (Olsen, 2014) was used to gain insight into the flocculation processes and its process complexity. For this purpose, the SSIIM software

[1] The environmental objective for HCB, that was introduced by the International Commission for the Protection of the River Rhine (ICPR), is 40 μg per kg suspended matter.

was extended by a flocculation algorithm derived by McAnally (2000). The implemented flocculation algorithm was applied for two cases studies: in a physical model in the open annular flume and for a real case study in the Iffezheim reservoir, located at the Upper Rhine river in Germany. The objective of the numerical investigations was to improve the understanding of aggregation and disaggregation mechanisms and to better assess the impact of the influencing factors on flocculation processes. The findings from this work contribute to a better prediction of flocculation processes in future numerical cohesive sediment studies.

1.2 Structure of the Work

Figure 1.1 gives an overview of the structure of the work, which consists of two main parts: Based on the fundamental chapter on cohesive sediment processes, the first main part focuses on the mathematical formulations for modeling flocculation processes and the SSIIM model extension by the implementation of an existing flocculation algorithm. The second main part describes the application of the implemented algorithm for modeling flocculation in turbulent flows within two case studies, the open annular flume and the Iffezheim reservoir at the Upper Rhine river in Germany.

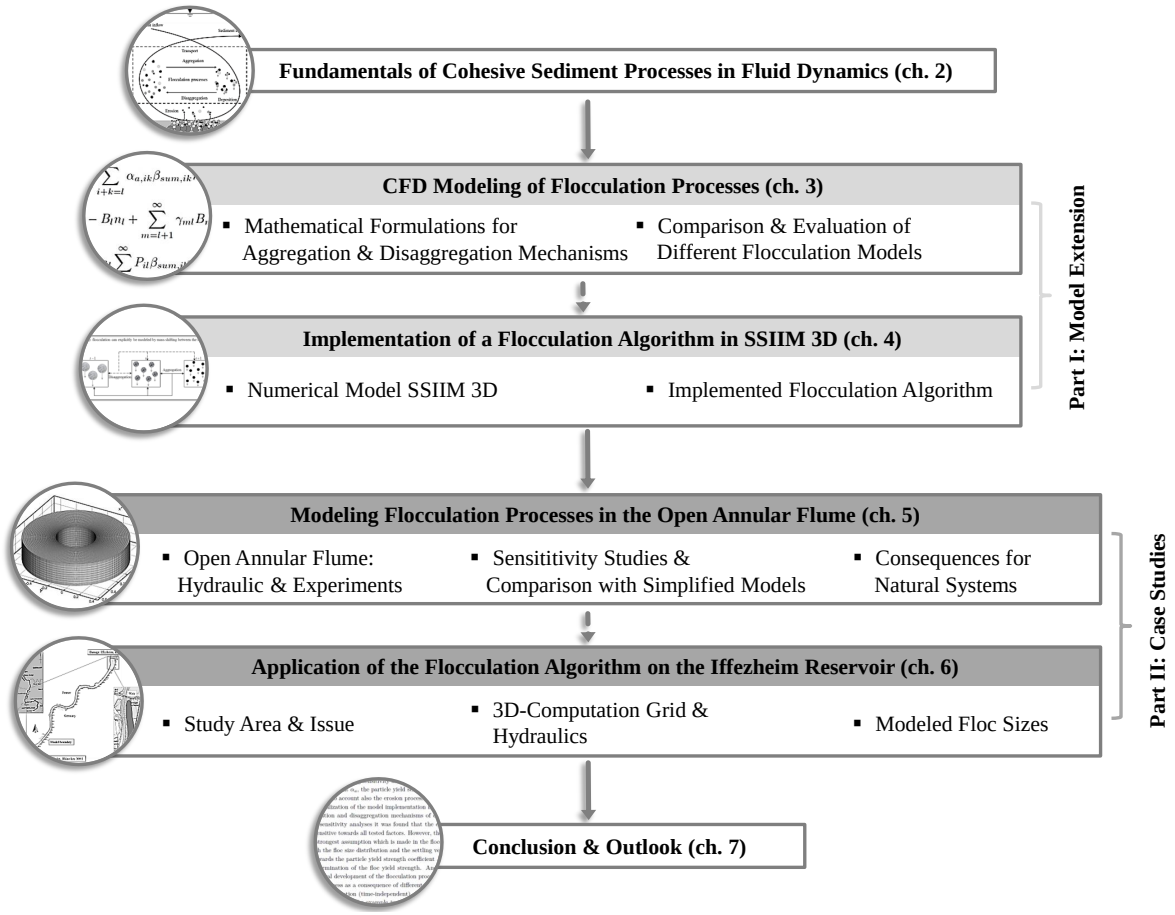

Figure 1.1: Overview of the structure of the work.

Chapter 2 describes the main physical characteristics of the transport and deposition behavior of cohesive sediments in fluid flows, whereby the focus in particular is placed on the description of the key micro-scale flocculation processes. After a brief overview of hydrodynamic processes in fluid dynamic and its relevance for cohesive sediment processes, fine sediments are described in the context of their chemical characteristics. Afterwards flocculation processes are presented in detail, with particular focus on the description of the floc structure and the impact of turbulence. The chapter closes with a description of the deposition behavior of fine sediments including formulations for calculating the floc settling velocity.

In chapter 3, a review on numerical modeling of flocculation from literature is illustrated. It contains the presentation of the mathematical formulations and model approaches for simulating aggregation and disaggregation mechanisms. Furthermore, a comparative study of several existing flocculation models is presented. The models are evaluated with regard to their ability for a physical close reproduction of flocculation processes and a suitable implementation in SSIIM. Based on the comparative study, the flocculation algorithm derived by McAnally (2000) was chosen for the implementation in SSIIM.

In the first part of chapter 4 a brief overview of the used CFD software SSIIM is given including its main theoretical principles for modeling hydraulics and sediment transport. In the second part, the implemented flocculation algorithm based on McAnally (2000) is described by its main mathematical terms and physical descriptions.

In chapter 5, the flocculation modeling results of the first case study in the open annular flume are presented. The implemented flocculation algorithm was used for simulating floc sizes and suspended sediment concentrations of kaolinite. The first aim of this application was the testing and validation of the implemented flocculation algorithm in SSIIM. The second aim was to evaluate uncertainties of different parameters and initial/boundary conditions on the flocculation modeling results. To this end, several numerical sensitivity studies in the annular flume were conducted. In this chapter, firstly the open annular flume is described, followed by a characterization of the flow field by comparing measurement data with numerical simulation. In the next part, experimental techniques and methods as well as the measurement results of the cohesive sediment studies in the annular flume are presented. The focus of this chapter lies on the presentation and discussion of the sensitivity analyses for the numerical modeling of flocculation and deposition in the annular flume. To investigate the issue to which degree the observed processes in the laboratory can be simulated physically correctly by excluding the implemented flocculation algorithm from the computation, the flocculation computations were compared with simplified models which exclude the flocculation algorithm. The chapter closes with an evaluation of the numerical sensitivity studies with respect to the consequences of the application of the implemented flocculation algorithm for natural river systems.

Chapter 6 contains the flocculation modeling results of the second case study in the Iffezheim reservoir. The objective of the flocculation algorithm application was firstly the validation of the implemented algorithm in terms of a physcially reasonable reproduction of flocculation processes for a natural system. Secondly, it was investigated which influencing factors and parameters are relevant and need to be considered when using the implemented algorithm for future flocculation computations in the Iffezheim reservoir. In the first part of the chapter, the Iffezheim reservoir and the problems which occur with sedimentation of contaminated sediments upstream of the reservoir are described. In the second part, the established 3D-computation grid in SSIIM is characterized and hydraulics in the reservoir are analyzed. The third part contains the presentation and discussion of the flocculation modeling results.

The work concludes in chapter 7 with a summary of the main findings and an outlook for future research investigations on flocculation.

2 Fundamentals of the Interaction of Cohesive Sediment Processes and Fluid Dynamics

In this chapter the main physical characteristics of the transport and deposition of cohesive sediments in fluid flows are illustrated. The focus lies in particular on flocculation processes, i. e. the aggregation and disaggregation of flocs and particles. The chapter first presents a brief overview of the relevant hydrodynamic processes which stand in complex interaction with the fine sediment processes. Based on the knowledge of the hydraulic forces, fundamentals in cohesive sediment transport and deposition processes are given. This implies first the definition of fine sediments and their chemical characteristics. Afterwards flocculation processes are described in detail, with respect to their major physical characteristics. The chapter closes with formulations for the settling velocity and a description of the deposition behavior of cohesive sediments.

The objective of this chapter is to give an understanding of the small-scale processes of cohesive sediment dynamics, i. e. the formation and break-up of flocs, with the overall objective to link these phenomena with the large-scale sediment processes in fluid dynamics such as sediment transport and sediment deposition.

2.1 Fluid Dynamics Background

Cohesive sediment transport and deposition are significantly affected by the properties of the fluid flow. In order to get an overall understanding of the interactions between cohesive sediments and water flow dynamics, knowledge about the hydraulic fluid forces is essential. In the following a brief overview of hydrodynamic processes in fluid dynamic and its relevance for cohesive sediment processes is given.

2.1.1 Navier-Stokes Equations

In fluid dynamics the three-dimensional Navier-Stokes equations are used to describe the water motion in fluid flows. They are solved in order to obtain the flow velocities and pressure field. The Navier-Stokes

equations are derived from two fundamental equations of fluid dynamics, the continuity and momentum equation. For non-compressible and constant density flow the Navier-Stokes equations are given as:

$$\frac{\partial u}{\partial x} + \frac{\partial v}{\partial y} + \frac{\partial w}{\partial z} = 0 \tag{2.1a}$$

$$\rho_w \frac{\partial u}{\partial t} + \rho_w u \frac{\partial u}{\partial x} + \rho_w v \frac{\partial u}{\partial y} + \rho_w w \frac{\partial u}{\partial z} = -\frac{\partial P}{\partial x} + \mu \left(\frac{\partial^2 u}{\partial x^2} + \frac{\partial^2 u}{\partial y^2} + \frac{\partial^2 u}{\partial z^2} \right) \tag{2.1b}$$

$$\rho_w \frac{\partial v}{\partial t} + \rho_w u \frac{\partial v}{\partial x} + \rho_w v \frac{\partial v}{\partial y} + \rho_w w \frac{\partial v}{\partial z} = -\frac{\partial P}{\partial y} + \mu \left(\frac{\partial^2 v}{\partial x^2} + \frac{\partial^2 v}{\partial y^2} + \frac{\partial^2 v}{\partial z^2} \right) \tag{2.1c}$$

$$\rho_w \frac{\partial w}{\partial t} + \rho_w u \frac{\partial w}{\partial x} + \rho_w v \frac{\partial w}{\partial y} + \rho_w w \frac{\partial w}{\partial z} = -\frac{\partial P}{\partial z} + \mu \left(\frac{\partial^2 w}{\partial x^2} + \frac{\partial^2 w}{\partial y^2} + \frac{\partial^2 w}{\partial z^2} \right) + \rho_w g_z \tag{2.1d}$$

where

x, y, z	coordinate system	[m]
u, v, w	fluid velocity components in x-, y-, z-direction	[m/s]
ρ_w	fluid density	[kg/m³]
t	time	[s]
P	pressure	[N/m²]
μ	dynamic viscosity of fluid	[kg/ms]
g	acceleration of gravity	[m/s²]

The first equation expresses the three-dimensional continuity equation representing the conservation of mass in a non-compressible fluid. It is derived by the balance of mass fluxes into and out of a physically infinitesimally, small control volume. Equations (2.1b) to (2.1d) represent the momentum equations for each flow direction x, y and z. The momentum equations are derived by balancing the sum of all applied forces on the control volume according to Newton's second law ($F = ma$). The law relates the sum of the forces acting on a fluid element to its rate of momentum change. There are five different types of forces acting on the fluid in a control volume:

- Transient forces due to the time rate of change following a moving fluid element (first term on the left side of the equations).
- Convective forces due to the movement of the fluid element from one location to another where the flow properties are spatially different (the remaining three terms on the left side of the equations).
- Pressure forces act directly on the surface of the fluid element caused by the fluid surrounding the control volume (first term on the right side of the equations).
- Stress (viscous) forces act on the surface of the fluid. They are imposed by the outside fluid by means of friction (second term on the right side of the equations).
- Gravity forces act directly on the volumetric mass of the fluid element (third term on the right side of the equations).

Using the non-dimensional form of the incompressible Navier-Stokes equations, different dimensionless fluid variables can be derived. The Reynolds number is an essential dimensionless number in fluid mechanics

which characterizes and quantifies the state of the flow, i. e. whether the flow is laminar (viscous) or turbulent. The Reynolds number Re (–) is defined as the ratio of inertial forces F_I to viscous forces F_V:

$$\frac{F_I}{F_V} \propto \frac{U \cdot L}{\nu} = Re \tag{2.2}$$

where

Re	Reynolds number	[–]
F_I	inertial forces	$[\mathrm{kg \cdot m/s^2}]$
F_V	viscous forces	$[\mathrm{kg \cdot m/s^2}]$
U	characteristic flow velocity	$[\mathrm{m/s}]$
L	characteristic length	[m]
ν	kinematic viscosity of fluid	$[\mathrm{m^2/s}]$

Reynolds numbers with $Re < 500$ refer to laminar flow, which is smooth and mostly stationary. Under conditions of laminar flow, the flow behavior is determined primarily by the fluid viscosity (or low flow velocities). Reynolds numbers greater than $Re > 2000$ usually characterize a fully turbulent flow, which is always transient with considerable mixing and high flow velocities.[1] An intermediate condition that is partly laminar and partly turbulent is referred to as transitional flow with Reynolds numbers of $500 < Re < 2000$. In most natural rivers the Reynolds number is usually large in the order of $Re = 10^5 - 10^6$ (Dingman, 1984). Thus, for many natural river systems and for practical purposes fluid flow can be assumed as highly turbulent. In terms of the interaction between cohesive sediment particles and fluid flow dynamics, turbulence represents an important phenomenon. Therefore, in the next chapter a brief description of turbulent flows is presented based on turbulence theory for high Reynolds numbers (e. g. Tennekes and Lumley, 1972, Pope, 2000).

2.1.2 Turbulence

Fluid flow which is unsteady, irregular, seemingly random, and chaotic is called turbulent. Turbulent flow is characterized by a temporally and spatially fluctuating velocity field which is described in statistical terms. The instantaneous values of the flow velocity components in x-, y- and z-direction can be divided in each location and time into a mean component of flow velocity ($\overline{u}$, $\overline{v}$, $\overline{w}$), plus a velocity fluctuation component ($u^{'}$, $v^{'}$, $w^{'}$). The velocity u in x-direction comprises the following equation (see figure 2.1):

$$u = \overline{u} + u^{'} \tag{2.3}$$

where

$\overline{u}$	mean component of flow velocity in x-direction	$[\mathrm{m/s}]$
$u^{'}$	velocity fluctuation component of flow velocity in x-direction	$[\mathrm{m/s}]$

[1] A turbulent flow can, however, be statistically stationary (Pope, 2000).

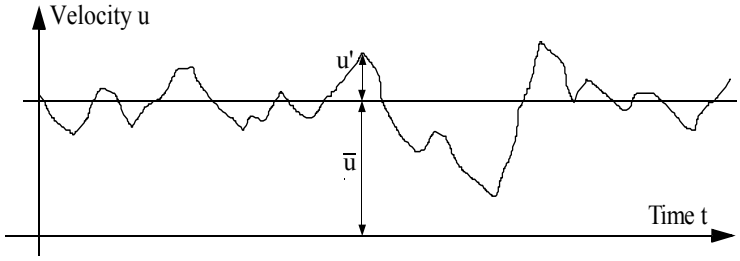

Figure 2.1: Time series of velocity u at a given location in a stationary, turbulent flow. The velocity u is divided into a mean component $\overline{u}$ plus a velocity fluctuation component $u^{'}$.

An important quantity when estimating the rate at which fine sediments are suspended by turbulent flow is the turbulent kinetic energy per unit mass of fluid. The turbulent kinetic energy TKE is obtained from the root-mean-square (rms) velocity fluctuations for each direction and is defined as (Tennekes and Lumley, 1972):

$$TKE = \frac{1}{2} \cdot \left(\overline{u'^2} + \overline{v'^2} + \overline{w'^2} \right) \tag{2.4}$$

where

TKE	turbulent kinetic energy	$[\mathrm{m}^2/\mathrm{s}^2]$
$\overline{u'^2}$, $\overline{v'^2}$, $\overline{w'^2}$	mean-square velocity fluctuations in x-, y-, z-direction	$[\mathrm{m}^2/\mathrm{s}^2]$

Turbulence causes the formation of eddies of various scales. Most of the kinetic energy of the turbulent motion is obtained from the mean flow field by the largest eddies. Via an energy cascade, the large macro-scale eddies are stretched by local velocity gradients into smaller, micro-scale eddies. This process creates a hierarchy of eddies and is continuing until the dimensions of the eddies are so small that molecular diffusion becomes important and the contained energy of the smallest eddies will be dissipated by the fluid viscosity into heat and sound. The fluid viscosity prevents the creation of infinitely small scale eddies. Thus, the smallest length scale of a turbulent flow will automatically adjust to the value of the viscosity. For a turbulent flow in natural rivers, the maximum size of the macro-scale eddies will be in the size of the flow field (water depth or river width). The smallest energy-dissipating eddies do not depend on the motion of the larger eddies and the flow field geometry. Their scale only depends on the energy dissipation rate and the fluid viscosity. Based on these two parameters, the size of the smallest eddies, which is defined as the Kolmogorov micro-scale η, can be calculated as follows:

$$\eta = \left(\frac{\nu^3}{\epsilon} \right)^{1/4} \tag{2.5}$$

where

η	Kolmogorov micro-scale of turbulence	[m]
ϵ	turbulent dissipation rate	$[\mathrm{m}^2/\mathrm{s}^3]$

Based on the dissipation rate and the kinematic fluid viscosity another turbulent parameter can be formulated. It is often used to describe the interaction between cohesive sediment particles and turbulence:

the absolute turbulent velocity gradient G_t. It is a shear parameter defined by Camp and Stein (1943) as the square root of the energy dissipation at a point divided by the kinematic fluid viscosity:

$$G_t = \sqrt{\frac{\epsilon}{\nu}} = \frac{\nu}{\eta^2} \tag{2.6}$$

where

G_t velocity gradient in turbulent flow $[1/s]$

In chapter 2.3.5 it is described how the various length scales of turbulence influence the interaction between cohesive sediment particles and turbulent flow. In particular, the smallest eddies of the Kolmogorov micro-scale play an important role, since they influence the size of the largest sediment aggregates/flocs.

2.2 Classification and Physico-Chemical Characteristics of Cohesive Sediments

2.2.1 Classification and Composition

In natural rivers a huge amount of solid particles is transported, eroded or deposited with the water flow. A commonly used classification of these sediment particles is based on the parameter term *grain size*. As illustrated in table 2.1 there is a distinction between clay and silt (fine grained particles) and between sand, gravel, stones and blocks (coarse grained particles).

Table 2.1: Grain size by DIN EN 14688-1 and DIN 4022-1 (Schmidt, 2006).

Description		Symbol (DIN EN 14688)	Diameter (mm)
Coarse grains	Blocks	Bo	> 200
	Stones	Co	> 63 - 200
	Gravel	Gr (Gravel)	> 2.0 - 63
	- Coarse gravel	CGr	> 20 - 63
	- Middle gravel	MGr	> 6.3 - 20
	- Fine gravel	FGr	> 2.0 - 6.3
	Sand	Sa (Sand)	> 0.063 - 2.0
	- Coarse sand	CSa	> 0.6 - 2.0
	- Middle sand	MSa	> 0.2 - 0.6
	- Fine sand	FSa	> 0.063 - 0.2
Fine grains	Silt	Si (Silt)	> 0.002 - 0.063
	- Coarse silt	CSi	> 0.02 - 0.063
	- Middle silt	MSi	> 0.006 - 0.02
	- Fine silt	FSi	> 0.002 - 0.006
	Clay	Cl (Clay)	< 0.002

Coarse grains are almost exclusively composed of mineral material, while fine grains consist of inorganic minerals (clay, silt, (fine) sand) and organic matter. Organic matter includes macro-organisms (plants and animal parts) as well as micro-organisms (leafy matter, spores, fecal pellets, worm tubes, biopolymers, bacteria, etc.).

According to the classification, particles smaller than 0.063 mm ($< 63\,\mu$m) are classified as fine grains, and particles greater than 0.063 mm as coarse grains. Clay has a grain size smaller than 0.002 mm ($< 2\,\mu$m). The finest sediment particles are characteristically taken to be $0.1\,\mu$m (Mehta, 2014). A suspension of particles smaller than $1\,\mu$m is called a sol or colloidal suspension. The particles of the colloidal fraction typically do not settle in water due to Brownian motion.[2] Therefore sol particles, particularly those smaller than $0.1\,\mu$m, are not classified as constituents of sediment, even though they are present in water as a solid phase (Mehta, 2014). They are often denoted as dissolved matter (Winterwerp and van Kesteren, 2004).

Organic Matter

Besides the mineral amount, also the organic matter plays a role in terms of its effect on the physical properties of sediment flocs in suspension and in the river bed. Organic matter in mud exists in two entities: particulate organic matter (POM) and dissolved matter (DOC). In literature, little quantitative information with regard to natural environment or engineering science is available on this topic (Mehta, 2014). Basically, organic matter consists primarily of organic polymers which occur as charged or as neutral particles (Winterwerp and van Kesteren, 2004). From an environmental point of view the neutral particles are important, since non-ionic polymers which are produced by bacteria, algae, etc. can be adsorbed by clay particles. These polymers in turn can reinforce the physico-chemical bonds holding particles together (Kranck, 1986, Spork, 1997, Luettich et al., 1993, Mehta, 2014). Several studies have shown that biological processes, in particular micro-organisms, lead to a strengthening and biogenic stabilization of the bed sediment particles, i. e. contribute to an increase in erosion resistance (e. g. Kranck and Milligan, 1980, Mehta, 1991, Tolhurst et al., 2006). Contrary, some studies also indicate that biota may also act as bio-destabilizers and cause an increase in erodibility (e. g. *Hydrobia ulvae*, *Corophium volutator*) (Andersen et al., 2002, Widdows et al., 2006). However, the majority of the studies have demonstrated that organic matter modify the erosion threshold in terms of an increased sediment stability. For a detailed description of the different biogenic stabilization mechanisms the reader is referred to Spork (1997).

It has to be noted that the organic/non-organic composition of natural sediments is also inherently linked to temperature. Therefore, fine-grained sediments can have a strong seasonal component as well as a spatially variation. Accounting for temporal and spatial variability is an additional challenge in fine sediment dynamics.

Particle Size and Cohesion

Separating fine sediments solely according to their grain size is insufficient. From soil mechanics, it is known that a sediment mixture will show a behavior strongly influenced by clay with only a clay fraction of 5 % to 10 % (Spork, 1997, Raudkivi, 1998). Hence, sediment mixtures of fine grained particles are not merely described according to their grain sizes, but also with respect to their soil characteristics (Möller, 2001). A crucial property in fine sediment dynamics which is related to the grain size is the degree of electrochemical cohesion. Intermolecular forces are the reason why fine grains, contrary to coarser sediment sizes, exist in aggregates of several single grains. Whereas the transport of non-cohesive sediments

[2] The process Brownian motion is explained further below in chapter 2.3.2.

is influenced mainly by flow, gravity forces and fluid viscosity, the transport of cohesive sediments is characterized additionally by several physico-chemical and biological factors. The possibility of primary, individual fine particles to form larger aggregates or flocs which are composed of many small individual particles, is called aggregation. Aggregation on the one hand depends on the collision probability of the sediment particles (discussed in detail in chapter 2.3.2) and on the other hand on the particles cohesion. The degree of cohesion of fine sediments is related to the sediment size due to their electro-chemical properties. Table 2.2 shows the relationship of sediment size to its degree of cohesion qualitatively.

Table 2.2: Relationship of sediment size to its cohesion (based on observations by Mehta and Lee (1994)).

Size range (μm)	Classification	Qualitative degree of cohesion
> 63	Coarse	Cohesionless
63 to 40	Coarse silt	Practically cohesionless
40 to 20	Coarse silt	Cohesion increasingly important
20 to 2	Medium and fine silts	Cohesion important
2 to 0.1	Coarse, medium and fine clays	Cohesion very important

According to table 2.2, Mehta and Lee (1994) propose the 20 μm size to be the transition size differentiating cohesive and cohesionless sediment transport behaviors. For particle sizes between $20\,\mu\text{m} - 40\,\mu\text{m}$ cohesion is not highly important. For sediment sizes between 20 μm and 2 μm the effect of cohesion increases with decreasing sediment size and plays a significant role especially for sediment sizes smaller than 2 μm. This effect is caused by an increasing specific surface area as the particles get smaller. This in turn means that electrochemical surface forces dominate over particle weight, and therefore cohesion increases governing the sediment transport behavior in water. Similar observations concerning a limit value between very cohesive and cohesionless particles were made by Stevens (1991). Stevens (1991) suggests from laboratory experiments with quartz and feldspar a 16 μm boundary to separate roughly cohesive and cohesionless sediment. The observations show that there is no clear boundary between cohesive and non-cohesive sediment, the definition is usually site-specific. In general, clays ($< 2\,\mu$m) are considered to be cohesive sediment. Silt ($2\,\mu\text{m} - 63\,\mu\text{m}$) is considered to be between cohesive and non-cohesive sediment. In fact, the cohesive properties of silt are primarily caused by the existence of clay. Thus, aggregation is most important in the fine silt and clay fraction, whereas coarse silts and larger grains are little or not affected by aggregation processes.

2.2.2 Clay Structural Units and Electric Charge

Clay minerals with particles less than 2 μm are formed either anew from remnants of chemical weathering or by ions replacing other ions, which have been dissolved from existing minerals (*ismorphous substitution*). Clay minerals are assigned to the layer silicates. Depending on their crystalline structure, they are categorized into two-layer, three-layer or four-layer clay minerals, which are typically composed of plate-like particles. Typical clay minerals are kaolinite (two-layer), illite (three-layer) and montmorillonite (three-layer), shown in figure 2.2. A typical four-layer clay mineral is chlorite.

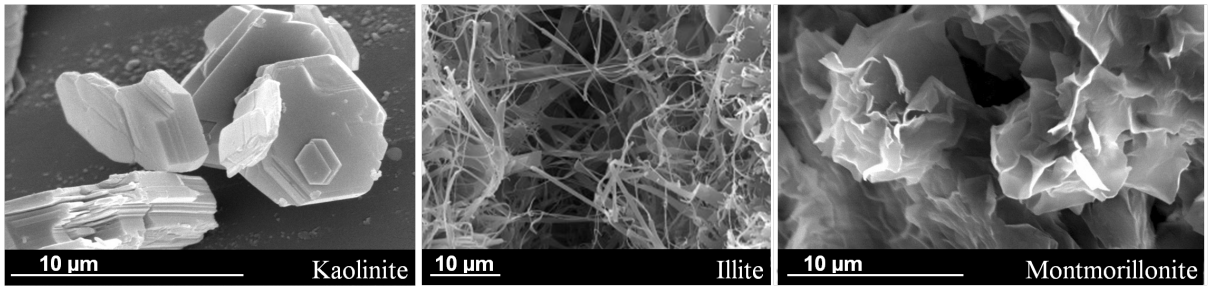

Figure 2.2: Photos of typical clay minerals: kaolinite, illite, montmorillonite (Blogs of the European Geosciences Union, http://blogs.egu.eu/divisions/sss/tag/clay-2/).

The surface area of the basal planes of clay minerals is many times larger than the surface area of their edges. Because of the layered structure and its plate-like shape, clay minerals have a high specific surface area ($^{m^2}/_{g}$), making it possible to adsorb pollutants. The layered structure of clay minerals is typically composed of two types of sheets: the silicon-oxygen sheet (Si=silicon, O=oxygen), which is characterized by a tetrahedral structure, and the aluminium-, iron- or magnesium-oxygen-hydroxide sheet (Al=aluminium, Fe=iron, Mg=magnesium, OH=hydroxide), which shows an octahedral structure. Figure 2.3 shows the structural unit of a single kaolinite plate which has a two layer structure made up of an aluminium octahedral sheet with a superposed tetrahedral sheet ($Al(OH)_6$ and SiO_4 sheets). Single mineral plates are built up as stacks of such tetrahedral and octahedral sheets. Crystalline flake-like particles exhibit a thickness of about 100 nm with plate diameters of 2 μm. Stacks of crystalline flakes can extend to large particle sizes up 100 μm or more (Winterwerp and van Kesteren, 2004).

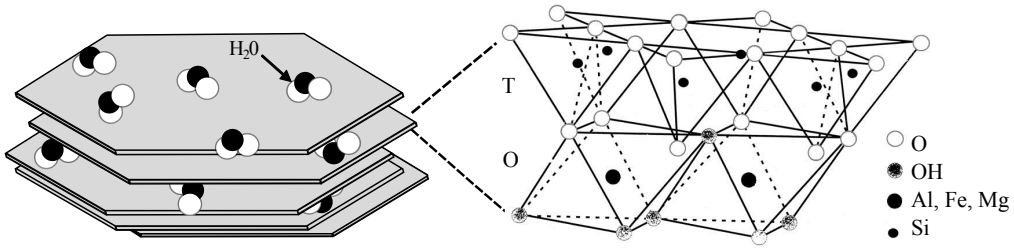

Figure 2.3: Layered structure of clay minerals composed of plate-like particles (left). Structural unit of a single mineral plate of kaolinite (enlarged view). It is a two-layer clay mineral, composed of a T=tetrahedron and a O=octahedron sheet (modified from Lagaly et al., 1997).

The cohesive properties of clay minerals are the result of the interactions between clay minerals and water. The electric charge on the phase boundary of the particle clay minerals and the ion or cation content of the water are responsible for cohesion. The two main causes for charged clay particles are isomorphous replacements within the clay crystal lattice and pH-affected charge. The flat face of crystalline particles consists of substantial negative charges as a result of higher quality central cations being replaced by other less valuable cations inside the structure of the mineral (isomorphous replacements). For kaolinite, e. g. as one of the most occurring clay minerals, isomorphous replacement of higher quality Si(IV) atoms by less valuable Al(III) atoms leads to a negatively charged lattice, causing ion exchange on these surfaces. The negative charge of the surface area is termed as *permanent*, since it is not dependent on the pH-value or the ion content of the water. The second type of surface charge is at the edge of the clay particles. This charge depends on the pH-value and can either be positive if protons are adsorbed, or negative if

desorption of the protons occurs. Since the charges of the edges depend on the pH-value and the ionic strength and therefore consequently can be either positive or negative, the term *variable* on the clay edges can be used. Because of this, clay minerals can have both negative and positive charges on the surface. Figure 2.4 shows a clay particle with a permanent negative charge on the basal planes and a variable charge on the edges in an aqueous ionic solution. The pH-value where the net total particle charge is zero, i. e. where positive and negative charge are in balance, is called the point of zero charge (PZC). The point of zero charge is an important parameter, since it means that electrophoretic mobility is zero. This point defines the maximal degree of aggregation, since no repulsion between the particles takes place.

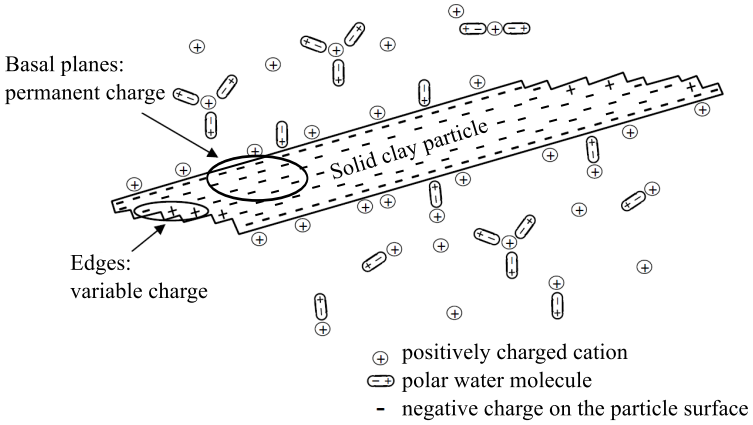

Figure 2.4: Clay particle with a permanent charge on the basal planes and a variable charge on the edges (modified from Dunn et al., 1980).

Figure 2.5 shows the effect of the pH-value of the water on the surface charge density (C/m^2) for different minerals. Each charge density curve is a result of a superposition of the constant pH-independent charge and the variable pH-dependent charge. As shown in the figure, in the neutral pH range (pH=7) most suspended solids, which are typically encountered in natural waters, are negatively charged. However, it must be noted that the illustrated curves are derived from several studies using different measuring methods. Schroth and Sposito (1997) for example, have shown that a significant variability exists among published experimental studies of the surface charge behavior of kaolinite. The pH-value at which the electrophoretic mobility is zero, ranges between 3.0 and 5.0 for kaolinite. Therefore, the curves in figure 2.5 are to be considered qualitatively.

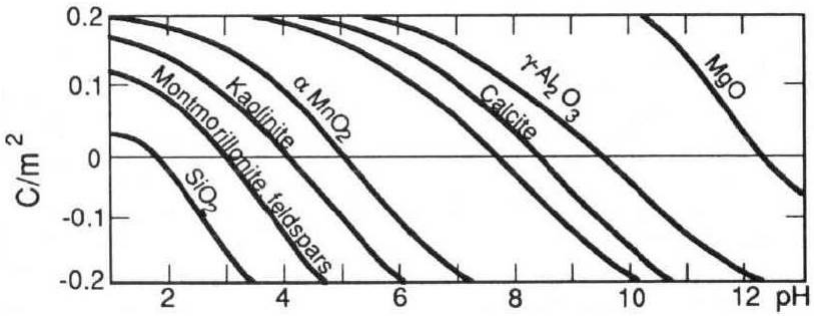

Figure 2.5: Effect of pH on surface charge (C/m^2). In the neutral pH range most suspended solids, typically encountered in natural waters, are negatively charged (Stumm, 1992).

The electric surface charge density can be estimated through experimental measurements of the adsorption of protons from an electrolyte solution. This is termed as the *cation exchange capacity* (CEC) being expressed in milliequivalents (meq) per 100 g of clay (McAnally, 2000, Sigg and Stumm, 2011). However, it must be noted, that the experimentally determined CEC depends on the pH-value and the electrolytes used. The term CEC is often used to characterize the degree of cohesion of the sediment. Table 2.3 lists the characteristic size, the CEC, and the critical salinity to aggregation for the three most common clay minerals (the impact of salt content is described further below). It can be seen that kaolinite exhibits significantly less cohesion than montmorillonite. It has a sediment cation exchange capacity which is $^1/_{27}$ to $^1/_{10}$ less than the CEC of montmorillonite and individual grains that are about 12 times larger compared to montmorillonite.

Table 2.3: Common clay minerals and their typical characteristics: grain size, CEC and salinity (modified from McAnally (2000)).

Clay mineral	Grain size (μm)	Cation exchange capacity ($^{\text{meq}}/_{100\text{g}}$)	Critical salinity for aggregation (ppt or ‰)
Kaolinite	$0.1 - 1$	$3 - 15$	0.6
Illite	$0.01 - 0.3$	$10 - 40$	1.1
Montmorillonite	$0.001 - 0.1$	$80 - 150$	2.4

The above mentioned electric charges on the clay particles are responsible for the cohesion and interactions between clay particles in an ionic solution leading to aggregation of cohesive sediments. Derjaguin, Landau, Vervey, and Overbeek (DLVO) developed a theory of colloidal stability, which currently represents the cornerstone of the understanding of interactions between colloidal particles and their aggregation behavior (Russel et al., 1989). Attraction forces lead to particle coagulation as a result of overcoming the repelling forces. Attractions occur because of van-der-Waals forces, that are pH-independent and become weaker with an increased distance from the particle surface. The electrically repulsion of two particles is caused by the *Born's repulsion* and by their evenly negatively charged surfaces. The repulsion also decreases with an increased distance from the particle surface. Hence, the interaction between two particles is governed by the resulting force (cohesive force) between two particles. If the particles distance is small, attracting forces are pitted against repelling forces.

The ionic strength of the surrounding water plays also a role in terms of the degree of sediment cohesion. The negatively charged surface of a particle is surrounded by a cloud of cations (see figure 2.6), where a high cation concentration is immediately adjacent to the negatively charged particle surface (stern layer). In the outer layer (diffuse layer) the cation concentration is reduced to the surrounding water, while the concentration of the anions is increasing. The composition of the stern layer and the diffuse layer is called diffuse double layer (DDL). If the negative charge of two clay particles decreases, the concentration of cations gets smaller. In this case the thickness of the two double layers decreases, so that the repulsive forces are reduced and particle aggregation dominates. Furthermore, organic matter can also strengthen the bonds of particles in an aggregate (see chapter 2.2.1).

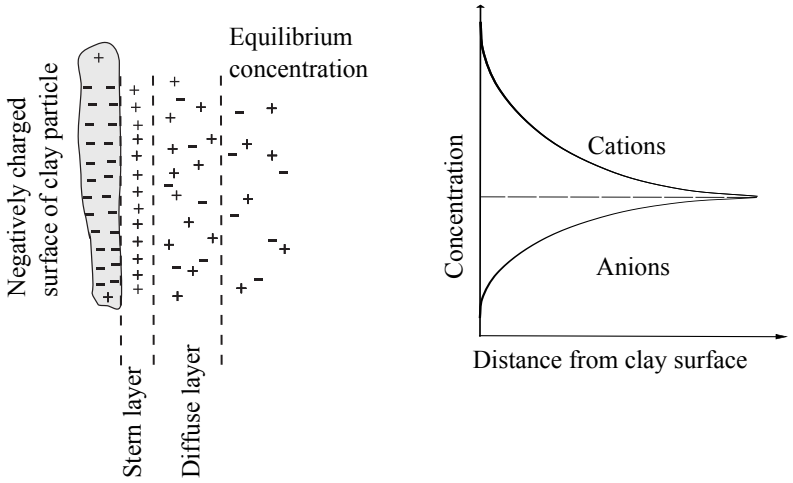

Figure 2.6: Left: diffuse double layer (DDL) composed of a stern layer and a diffuse layer at a negatively charged surface of a clay particle, right: variation in concentration of cations and anions with distance from clay surface (modified from Maggi (2005)).

In summary, the most important sediment specific properties with regard to their qualitative impact on cohesion are the following:

- **Organic matter**: Organic polymers charged as neutral particles, usually reinforce the physico-chemical bonds, holding particles together and lead to a strengthening and biogenic stabilization of the particles.
- **Particle size**: As the particles get smaller the specific surface increases. For this reason the van-der-Waal forces gain more impact, causing cohesion to increase.
- **Cation exchange capacity (CEC)**: The CEC is linked with the particle size distribution. With decreasing particle size, the pH dependent CEC is increasing. The term CEC is often used to take into account the degree of cohesion of the sediment.

Water properties influence the thickness of the double layer and therefore the cohesion in the following ways (Spork, 1997, Raudkivi, 1998, McAnally, 2000, Maggi, 2005 or Schweim, 2005):

- **Ionic strength of the water/salt content**: The double layer becomes thinner with an increasing ionic strength of the water, causing a higher degree of cohesion. With an increase of the salt content in the water, the ions are pushed closer to the boundary surface so that the thickness of the double layer decreases. Hence, the repulsive force reduces and the attraction forces dominate causing coagulation to occur. The critical ion concentration (in ppt or ‰) at which minerals cohesion begins to increase and allows aggregation, varies with the different clay minerals. Whereas Drake (1976) proposes an average salinity content of 2 ‰ as point for aggregation (discussed in Maggi (2005)), van Leussen (1994) and McAnally (2000) suggest different salt concentrations for different minerals, such as 0.6 ‰ for kaolinite, 1.1 ‰ for illite and 2.4 ‰ for montmorillonite (see table 2.3). The cohesion increases up to these critical concentrations and then is constant for higher values of salt concentration.
- **Sodium-Adsorption-Ratio (SAR)**: The effect of salts has been expressed in terms of the SAR. The SAR is defined as the ratio of the concentration of monovalent sodium cations Na^+ to the

divalent calcium Ca^{++} and magnesium Mg^{++} cations in water. A high ratio of monovalent ions compared to the divalent ions (i. e. an increasing SAR) increases the thickness of the diffuse double layer and leads to a lower degree of cohesion.

- **pH-value**: The pH-value effects the ionisation of the silicon compounds and hence the thickness of the double layer. For most clay minerals, a higher pH-value results in a reduction of cohesion, since the diffuse double layer thickness increases.
- **Temperature**: In literature the reasons for the temperature effect are discussed controversially. On the one hand, cohesion is decreasing with increasing temperature. On the other hand, the molecular motion of the particles increases with increasing temperature and decreasing viscosity. When particles collide the thickness of the double layer can be overcome. However, within the temperature ranges of natural rivers, the effect is usually considered to be small and may be dominated by biogenic or salinity effects.

Summarizing the above, it can be said that the degree of sediment cohesion, i. e. the possibility to form aggregates or flocs of many small individual particles, depends on both the pH-dependent surface charge of the particles and on the thickness of the diffusive double layer. When two particles collide, it is essential to overcome the repelling charges to form aggregates.

2.3 Flocculation Processes

2.3.1 Flocculation within the ETDC-Cycle

Fine sediment dynamics consist of a series of different individual processes which are governed by the properties of the cohesive sediments, the water flow and the fluid properties. These processes are acting together on different time scales, for example the time scale of vertical mixing, the time scale of settling and the time scale for aggregation and disaggregation. In this regard, a mere physical observation is insufficient since both chemical and biological factors have also an impact on the sediment processes and their interactions. This results in a complex water-sediment system. To illustrate these interdependencies, an overview of the different fine sediment processes, the interactions between the processes and the involving influence factors are given in figure 2.7.

In general, fine sediment processes can be described with a cycle of erosion, transport, deposition and consolidation, also known as the ETDC-cycle (Maggi, 2005). Within this cycle, cohesive sediments such as clay and silt particles are transported in the water column in suspension, since the fine sediment particles are easily suspended by water currents. Alternatively, non-cohesive sediments, such as coarser sand and gravel, are usually transported along the bottom by rolling, sliding and saltation. The suspended matter comes into the water column either with the upstream water flow or by erosion of deposited sediments due to high shear stresses.[3] During the transportation of sediments with the water flow, flocculation processes take place. On the one hand, cohesive clay particles can coagulate into larger, less dense aggregates or flocs (aggregation), consisting of numerous individual particles. On the other hand, flocculation implies also the break-up of aggregates (disaggregation) due to fluid shear stresses and particle-collision induced stresses.

[3] The portion of suspended load which is transported in the river with no interaction with the river bed is defined as wash load. It is governed by the upstream supply rate and not by the composition and properties of the bed material.

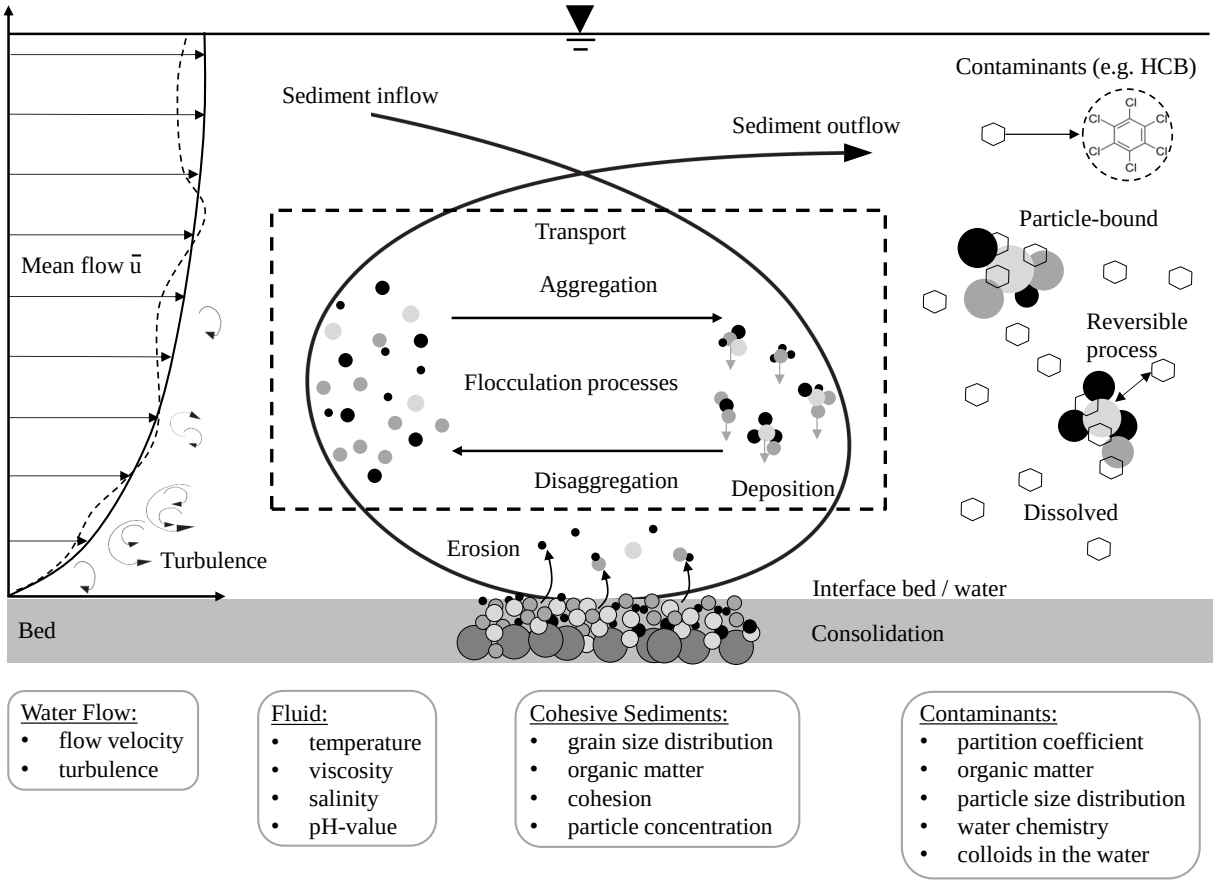

Figure 2.7: Water-sediment system described with a cycle of erosion, transport, deposition and consolidation (macro-scale processes), involved in particle aggregation/disaggregation and sorption/adsorption of contaminants (micro-scale processes). Below the scheme, the corresponding influence factors and the respective properties are presented.

Hence, in this work the term *flocculation processes* implies both, aggregation and disaggregation of flocs or particles. The term *flocs* is used for the resulting sedimentary units, i. e. for the larger aggregates composed of primary fine-grained cohesive sediments. The term *particle* describes both individual sediment grains and flocs.

With growing sediment size the particles are more likely to settle towards the bed than smaller particles. Thereby they enter a layer of high sediment concentration and high turbulence stresses. If the floc strength is strong enough to resist the high bed shear stresses, the particles will deposit to the bed. If the bed shear stress is sufficiently intense, the weaker settling aggregates are broken into smaller particles, picked up by the water flow and re-participate in the flocculation process. High bed shear stresses may also lead to erosion of already deposited aggregates. For cohesive sediments, four erosion modes can occur: entrainment, floc erosion, surface erosion and mass erosion (Winterwerp and van Kesteren, 2004).

Consolidation takes place when the accumulated cohesive sediments (deposited flocs or particles) are compressed under the influence of their own weight (self-weight consolidation). As a result pore water is expelled and the particles are forced to be closer to each other. This leads to a stabilization of the bed. In the ETDC-cycle, particles or aggregates which do not deposit on the bed will be carried out by the water flow. For a detailed overview of the processes erosion and consolidation of fine sediments, the following

literature is proposed: Parchure and Mehta (1985), Sills and Elder (1986), Winterwerp and van Kesteren (2004), Schweim (2005), Mehta (2014).

The above mentioned processes are on the one hand strongly marked by the specific sediment characteristics, e. g. the grain size distribution, the amount of organic matter and the degree of cohesion. Additionally, also the sediment concentration plays an important role. At low shear stresses, an increase in sediment concentration results in an increase of floc size due to the higher collision probability with higher concentrations. When the concentration is further increasing, the floc size decreases again as the flocs start to hinder each other while settling (see chapter 2.4.2).

On the other hand, the water flow characteristics have a major impact on the sediment behavior. The hydraulic boundary conditions, which are for example represented by the mean flow velocity and the turbulence intensity, influence the sediment transport velocity as well as the fluid shear stresses acting on the sediment particles.

In addition, the fluid properties, i. e. the salt content, the pH-value, the temperature and thus the viscosity play a role in terms of the sediment cohesion degree. Since cohesion is an important factor for undergoing aggregation (see chapter 2.2.1), these factors also affect the possibility to form larger sediment particles.

The complexity of fine sediment dynamics increases by the fact that clay minerals are able to adsorb contaminants (e. g. hexachlorobenzene (HCB)) due to their high specific surface area. Contaminants can be present in water, in both dissolved and particle-bound form. The adsorption and desorption of persistent contaminants are reversible processes and depend on numerous factors, such as the partition coefficient (ratio of particle-bound to dissolved contaminant concentration at equilibrium), the content of organic matter in the suspended sediment, the content of colloids in the water, the water chemistry and the particle size distribution. Since flocculation processes can change the grain size distribution of the suspended sediment constantly, the distribution of contaminants on the individual grain size fractions is also exposed to continuous change.

It is obvious that fine sediment dynamics is a complex research field, even as a closed system with constant boundary conditions. Additional temporal and spatial variability of the hydraulic and hydrological conditions lead to changes of the external forces making the system even more difficult to understand. Within the above mentioned sediment processes, the main focus of this work lies on the key small-scale processes of flocculation, i. e. the aggregation and disaggregation (break-up) of particles and flocs. The objective of the next sections is therefore to provide an understanding of these small-scale processes of fine sediment dynamics and to create a conjunction to the large-scale processes such as sediment transport and sediment deposition.

2.3.2 Transport and Collision Mechanisms

Primary particles or flocs are transported in suspension at approximately the velocity of flow by three transport mechanisms: advection, diffusion and dispersion. In the following, these three processes are described.

Advection is the transport by the mean fluid flow. In rivers, sediment transport by advection is the dominant process. The mass flux due to advection, J_{advec}, by the flow velocity u in x-direction is defined as:

$$J_{advec} = u \cdot C \tag{2.7}$$

where

J_{advec}	advective mass flux in x-direction	$[\mathrm{kg/m^2 \cdot s}]$
C	suspended sediment concentration (SCC)	$[\mathrm{kg/m^3}]$

Diffusion can be differentiated into molecular and turbulent diffusion. Molecular diffusion is the thermal motion of molecules induced by concentration gradients at temperatures above absolute zero. The particles move smoothly and systematically from a region of higher concentration to one of lower concentration. Once an equilibrium concentration is reached the particles continue to move, but the process of molecular diffusion is then governed by the random walk of particles (self-diffusion). The result of the molecular diffusion is a gradual mixing of material with the effect that the distribution of particles will become uniform. The molecular diffusion can be described mathematically by Fick's law which relates the mass flux due to molecular diffusion, $J_{diff,mol}$, with the concentration gradient. The proportionality factor D_{diff} is the diffusion coefficient (diffusivity) which depends on the properties of the fluid. In one spatial dimension (e. g. x-direction), the Fick's law is defined as:

$$J_{diff,mol} = -D_{diff} \cdot \frac{\delta C}{\delta x} \tag{2.8}$$

where

$J_{diff,mol}$	molecular diffusion mass flux in x-direction	$[\mathrm{kg/m^2 \cdot s}]$
D_{diff}	diffusion coefficient	$[\mathrm{m^2/s}]$
$\frac{\delta C}{\delta x}$	gradient of the concentration in x-direction	$[\mathrm{kg/m^4}]$

The turbulent diffusion is the transport of particles by the random and chaotic eddies in a turbulent flow, which leads to a mixing of the particles within the fluid. Whereas the molecular diffusion allows mixing by the motion of particles, turbulent diffusion is characterized by the random motion of the fluid. In analogy to the molecular diffusion, turbulent diffusion follows the Fick's law by the use of a turbulent diffusion coefficient (eddy diffusion coefficient). This coefficient describes the properties of the turbulent fluid flow. The mass flux due to turbulent diffusion, $J_{diff,turb}$ in x-direction is defined as:

$$J_{diff,turb} = -D_{turb,x} \cdot \frac{\delta C}{\delta x} \tag{2.9}$$

where

$J_{diff,turb}$	turbulent diffusion mass flux in x-direction	$[\mathrm{kg/m^2 \cdot s}]$
$D_{turb,x}$	turbulent diffusion coefficient	$[\mathrm{m^2/s}]$

Turbulent diffusion occurs much more rapidly than molecular diffusion. Therefore, in consequence of the much longer time scales, molecular diffusion is often negligible.

Dispersion is a diffusion-like process, which causes the particles to mix as a result of velocity gradients. Due to the different flow velocities, initially directly adjacent particles are moving apart with the effect that concentration gradients are compensated. By analogy with the diffusion process, the mathematical

description of the dispersion process is given with a dispersion coefficient K_{disp}. The sediment mass flux due to dispersion, J_{disp} in x-direction is defined as:

$$J_{disp} = -K_{disp} \cdot \frac{\delta C}{\delta x} \tag{2.10}$$

where

J_{disp}	dispersion mass flux in x-direction	$[\mathrm{kg/m^2 \cdot s}]$
K_{disp}	dispersion coefficient	$[\mathrm{m^2/s}]$

The compensation of the concentration gradients occurs to a large extent in lateral flow direction, whereas a small part of the compensation proceeds in vertical direction. Simultaneously, turbulent diffusion contributes to a further flattening. Since both processes can not be separated, the sum of dispersion and turbulent diffusion is often described as a hydrodynamic dispersion with a combined anisotropic diffusion or dispersion tensor. In areas with very low flow velocities (e. g. in reservoirs), turbulent diffusion and concentration gradients are the dominating sediment transport mechanisms.

Apart from the three transport mechanisms mentioned above, a further mass flux of sediments due to the self-weight of the particles has to be considered. Contrary to an ideal tracer which follows the fluid flow, particles settle down under the influence of gravity. The mass flux $J_{settling}$ as a result of gravitational forces is defined in relation to the settling velocity:

$$J_{settling} = w_s \cdot C \tag{2.11}$$

where

$J_{settling}$	vertical mass flux due to self-weight of particles	$[\mathrm{kg/m^2 \cdot s}]$
w_s	settling velocity	$[\mathrm{m/s}]$

During the transport of suspended sediments, flocculation processes occur. The small particles collide with each other as they move and cohesion determines if the collision causes them to adhere to each other and form larger aggregates. Whether colliding particles stick to each other depends on the fact whether attractive forces dominate repulsion forces. With an increasing suspended sediment concentration, i. e. with an increasing number of particles in the fluid, the probability that two particles collide increases. This results in enhanced flocculation processes. Hence, both collision frequency and the degree of cohesion are essential to flocculation processes. Collisions of particles, which result in potential formation of flocs, are caused by three processes:

1. Brownian motion: this is a process which is influenced by the thermal energy of the fluid. It implies the random motion of suspended particles in a fluid that results in collisions of particles.
2. Differential settling velocities: large particles with a large settling velocity will cause collisions with smaller, slower-settling particles.
3. Turbulent stresses: due to chaotic and rapid variations of pressure and flow velocity, turbulent stresses cause particles to collide.

The rates at which particles collide due to the corresponding collision mechanisms are relatively well understood. Quantitative expressions for these collision frequency rates are reported in several reviews

(e. g. in McCave (1984), Lick and Lick (1988), Winterwerp (1998) and Lick (2009)). They are all based on the early theories of collision frequencies developed by Smoluchowski (1916). In the context of this work, an overview of these different mathematical-physical equations is given in chapter 3.2.1.

From the literature it can be concluded that in the natural environment turbulence and differential settling are the predominant mechanisms for interparticle collision, while Brownian motion can be considered as a negligible factor (Maggi, 2005). Brownian motion becomes important only when concentrations are higher than approximately 10 g/l (Burt, 1986) and for very small particles with sizes less than 1 μm (Winterwerp, 2002). Thus, Brownian motion has to be taken into account only in the very early stages of flocculation processes. Inter-particle collisions caused by turbulent stresses are cited to be the most important collision mechanism (Maggi, 2005). In particular, in high-turbulence regions the effect of fluid shear is significant. Concerning the effect of differential settling, Stolzenbach and Elimelich (1994) carried out experimental studies in a settling column. They showed that for particles which are moved by turbulence, the effect of differential settling is small. The probability that large, but less dense particles with a higher settling velocity will collide with small, but denser, slower-settling ones is rather low due to the deflection of the trajectory of the smaller particles around the larger ones. From the studies above it can be concluded that turbulent motions are assumed to be the dominant collision mechanism for further undergoing flocculation processes.

2.3.3 Modes of Particle Interactions

Apart from their size, aggregates or flocs can be characterized by their structure formation. Plate-like kaolinite particles (see figure 2.2) can form different structures after collision. Due to their permanent negative charge on their faces and the variable pH-dependent charge on their edges (see chapter 2.2.2) different modes of particle interactions in clay suspensions are possible. Depending on both the pH-value and the ionic strength of the water, Lagaly et al. (1997) mention three modes of particle interactions:

- Edge to Edge (EE)
- Edge to Face (EF)
- Face to Face (FF)

In a deflocculated dispersion, different types of interaction form sediments with different structures (see figure 2.8). The EF particle association mode shows a so called card-house structure due to negative charges on the faces and positive charges on the edges leading to electrostatic attraction between the edges and faces. A stairstep structure is formed by the overlap of particles when FF associations occur. In this case the electrical double layers are compressed and coagulation is promoted. Chain-like structures are formed as a result of EE interactions.

The EF and EE formation lead to an open, loose and easily disrupted structure with low density aggregates of large volumes. The stairstep FF structure however gives small and compact aggregates of higher densities than for the card-house or chain-like structure. Thus, the yield strength of aggregates caused by FF interactions is higher and therefore more resistant towards flow forces than the yield strength of aggregates caused by EF or EE interactions. The different modes of particle interaction depend on the pH-value and the ionic strength of the water.

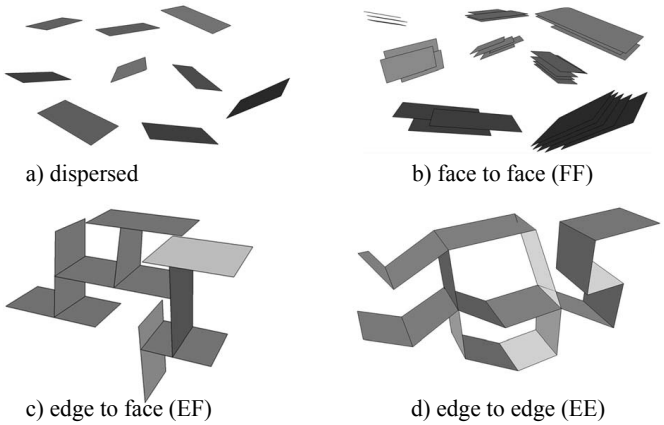

Figure 2.8: Modes of particle structures in clay suspensions: a) dispersed, b) face to face, c) edge to face, d) edge to edge (Unalan et al., 2014).

2.3.4 Floc Structure

Flocculation processes alter the properties of fine-grained sediments in terms of both the effective particle size and the structure of the growing flocs or aggregates. For the mathematically description of the irregular aggregate structure, numerous flocculation models make use of the concept of fractal geometry/fractal dimension. The fractal theory is based on the self-similarity of a structure, i. e. the fact that a growing entity shows the same structure as at its initial state (Mandelbrot, 1982). Figure 2.9 shows a two-dimensional object which illustrates the concept of self-similarity. At multiple scales of the object, the same pattern can be identified as at its initial observation: a triplet made of spherical particles of equal size. Due to the self-similarity of the structure growing fractals are treated as scale-invariant objects (Vicsek, 1992).

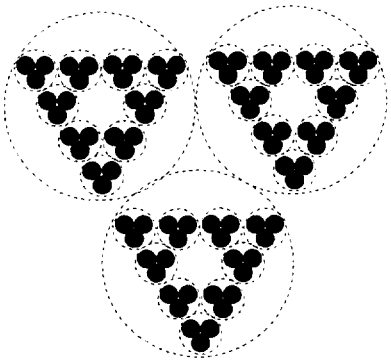

Figure 2.9: Two-dimensional object of a self-similar aggregate structure (Gregory, 1997).

Several flocculation models use the approach of fractal structures in order to model the complex and variable structure of cohesive sediment aggregates. The fractal dimension of flocs can mathematically be defined by considering a simple cube of size a_c, which represents a zero-order aggregate (see figure 2.10). The combination of 8 such primary units results in a cubic aggregate of size $a_f = 2a_c$. A further rise of 8 of such cubic aggregates ($a_f = 4a_c$) would lead to a cubic aggregate-aggregate of 64 primary units and so

on (Mehta, 2014). Based on this model concept, the number N_f of particles in a fractal aggregate of size a_f is defined by the following equation (Mehta, 2014):

$$N_f = \left(\frac{a_f}{a_c}\right)^{n_f} \tag{2.12}$$

where

N_f	number of particles in a fractal aggregate	[–]
a_f	size of the aggregate	[m]
a_c	size of the cube	[m]
n_f	fractal dimension	[–]

On this basis the fractal dimension n_f can be expressed by:

$$n_f = \frac{log\,(N_f)}{log\left(\frac{a_f}{a_c}\right)} \tag{2.13}$$

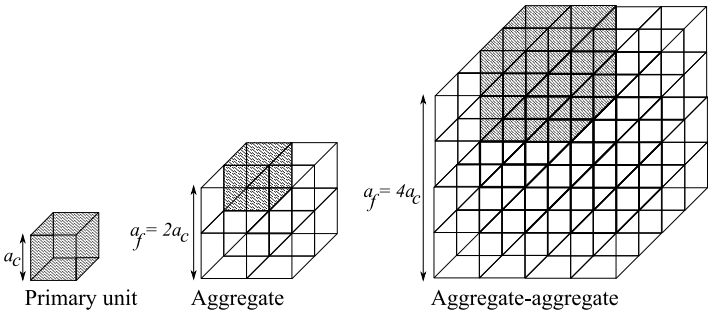

Figure 2.10: Cubic fractal structures formed from a primary cube (modified from Mehta, 2014).

The fractal dimension can take values from $n_f = 3$, indicating a compact and dense structure, to $n_f = 1$ for an irregular, open and porous structure. The smaller the fractal dimension is, the smaller is the density. For example, in figure 2.10 the fractal dimension remains constant with increasing size, exhibiting the maximum value of $n_f = 3$. The density is equal to the one of the primary particles for all cubic sizes. The fractal dimension would decrease if some of the primary units would be removed whereas the overall aggregate size remains constant.

Figure 2.11 shows two-dimensional projections of typical three-dimensional aggregates with different fractal dimensions ranging from $n_f = 1.2$ to $n_f = 2.5$. For example, if the flocs are connected on one line, the fractal dimension is about 1 (linear self-similarity), while if they are on a flat plane, the dimension is 2 (areal self-similarity). And a snowflake with equal distribution in all three spatial directions would be a value of about 3 (volumetric self-similarity).

Within flocculation models, the fractal dimension is applied either as a constant particle size independent value or as a variable fractal dimension which depends on the particle size. Numerical models including the fractal dimension often consider an overall constant fractal dimension for the whole floc size spectrum (e. g. Kranenburg, 1999, Xu et al., 2008). Typical values within estuaries and coastal waters vary from $n_f = 1.7$

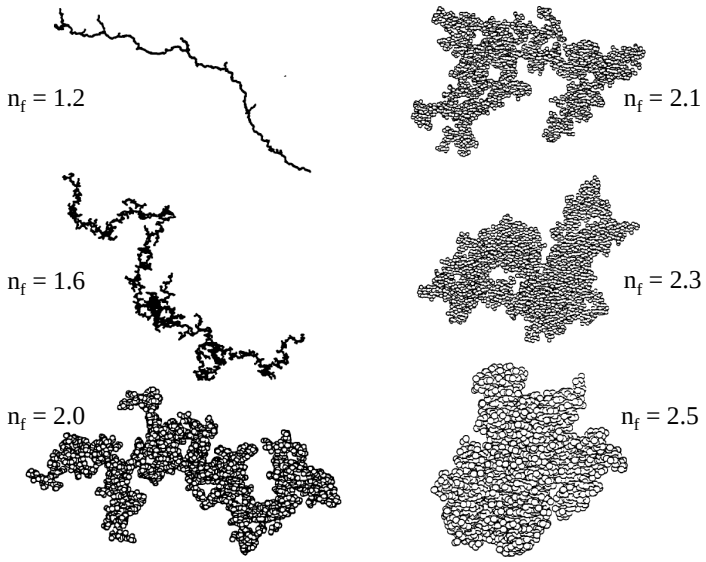

Figure 2.11: Two-dimensional projections of typical three-dimensional aggregates with different fractal dimensions n_f= 1.2 to 2.5 (from Thouy and Jullien, 1996).

to $n_f = 2.2$ (Winterwerp and van Kesteren, 2004). Thus, these models often assume an average value for the fractal dimension such as $n_f = 2.0$ for each particle size. The use of a constant fractal dimension for all particle sizes treats the aggregates as idealized and real fractal aggregates over the whole particle size spectrum. However, several previous studies proposed the concept of a variable fractal dimension since they showed improvements in predicting the floc size distribution and the floc settling velocity (e. g. Chakraborti et al., 2003, Khelifa and Hill, 2006, Maggi, 2007, Maggi et al., 2007, Son and Hsu, 2008). For three-dimensional flocs/aggregates, a variable fractal dimension decreases from the value of $n_f = 3$ for small and compact particles with particle sizes close to the primary particles to about $n_f = 1.0$ for large and irregular flocs with an open and porous structure. The suggestion to include a variable fractal dimension is based on the idea that there is a transition during the growth from the smaller Euclidean primary particles to larger real fractal aggregates. This leads to a decrease of the fractal dimensions as floc sizes are increasing (Maggi, 2007). According to this theory, primary particles should have a value of $n_f = 3.0$, whereas large flocs should have fractal dimensions of about $n_f = 2.0$ and smaller. Once the flocs have reached a certain size, they can be treated as real fractals. In this case, the value of their fractal dimension is constant and depends only on the flow conditions or the particle concentration.

Two ranges of behavior were observed in terms of the fractal dimension of flocs at a constant turbulent shear rate by Kumar et al. (2010). In the first region, for floc sizes less than 200 μm, a variable fractal dimension was needed to describe the submerged specific gravity as a function of floc size. In the second region, for floc sizes greater than 200 μm, a constant fractal dimension was found to suffice for the description of the submerged specific gravity. The constant fractal dimension for this second region was $n_f = 2.3$ for fresh water flocs and $n_f = 1.95$ for salt water flocs.

Khelifa and Hill (2006) propose a power law function of the floc diameter for describing the variable fractal dimension. Their formulation is based on 26 different data sets of settling velocity with floc sizes

ranging between 1.4 μm and 25,500 μm. According to Khelifa and Hill (2006) the fractal dimension n_f depends on the floc size D_f, the primary particle size D_g and the exponent β_{fc} :

$$n_f = 3 \cdot \left(\frac{D_f}{D_g} \right)^{\beta_{fc}} \tag{2.14}$$

with

$$\beta_{fc} = \frac{log(n_{fc}/3)}{log(D_{fc}/D_g)} \tag{2.15}$$

where

D_f	diameter of the aggregate/floc	[m]
D_g	diameter of the grain particle	[m]
n_{fc}	characteristic fractal dimension	[–]
D_{fc}	characteristic floc size	[m]

Khelifa and Hill (2006) recommend the typical values for n_{fc} and D_{fc} to be $n_{fc} = 2.0$ and $D_{fc} = 2000\,\mu$m, if they are not measured or calculated. However, they also showed that the predicted floc density is very sensitive to the parameter n_{fc}. For example, if a characteristic floc size D_{fc} was measured, but no information about the corresponding floc structure in terms of the characteristic fractal dimension n_{fc} is available, this fractal dimension has to be determined.

When estimating the floc structure it has to be considered that the magnitude of the fractal dimension depends on the mechanism by which aggregates grow. Flocs produced by particle-cluster aggregation have higher fractal dimensions than those formed by cluster-cluster aggregation, even if they are of the same size (see figure 2.12). In the case of particle-cluster aggregation, a particle is able to penetrate into a cluster before encountering and sticking with another particle. In an encounter of two clusters the first contact is likely to occur before the clusters have inter-penetrated to a significant content, which leads to a much more open structure (Gregory, 1997). Thus, in case of uncertainty regarding the characteristic value n_{fc}, the range of n_{fc} has to be considered when calculating the exponent β_{fc}.

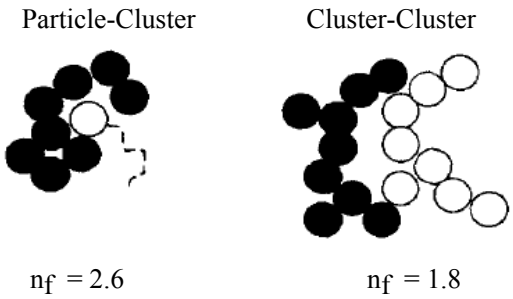

Figure 2.12: Schematic diagram of particle-cluster (left) and cluster-cluster (right) aggregation with the corresponding fractal dimensions n_f (modified from Gregory (1997)).

The fractal self-similar structure of flocs has the crucial consequence that the floc density decreases with increasing floc size. Whereas the density of non-fractal objects ($n_f = 3.0$) is independent of aggregate size, large fractal aggregates can exhibit very small densities. Mineral grains exhibit typical densities of about 2650 $^{kg}/_{m^3}$. However, large porous aggregates show typical densities in the range of 1060 to 1300 $^{kg}/_{m^3}$,

very close to that of water (McAnally, 2000). The density ρ_f of an aggregate of size D_f and with a fractal dimension n_f can be described by the following semi-empirical equation (Kranenburg, 1994):

$$\rho_f = (\rho_g - \rho_w) \cdot \left(\frac{D_g}{D_f}\right)^{3-n_f} + \rho_w \tag{2.16}$$

where

ρ_f	density of the aggregate/floc	$[\mathrm{kg/m^3}]$
ρ_g	density of the grain particle	$[\mathrm{kg/m^3}]$
ρ_w	density of the fluid	$[\mathrm{kg/m^3}]$

2.3.5 Impact of Turbulence

In chapter 2.1 it was shown that turbulent flow is a complex phenomenon in fluid dynamics due to its chaotic behaviour. In terms of aggregation and disaggregation, the turbulent structure of flow is important in two opposing ways: turbulence increases the number of collisions between suspended particles, thereby increasing the probability of floc growth and floc size. However, at the same time, it decreases the floc size by the break-up process with high turbulent shear stresses. Many studies have been carried out on the effect of turbulence on the flocculation process, mainly in the field of sanitary and chemical engineering. Argaman and Kaufmann (1970) were one of the first authors who studied the simultaneous effect of turbulence on aggregation and floc-break-up. In order to describe the collision mechanism between suspended particles in a turbulent flow, the authors developed complex mechanistic flocculation models. These models are characterized by various numerical parameters which have to be determined by flocculation tests, difficult floc size measurements and turbulence measurements. Dyer (1989) proposed a conceptual model of floc size which builds on the assumption that flocculation is mostly determined by concentration and turbulence shear stresses. In figure 2.13 the ambivalent effect of shear stress on floc size is qualitatively illustrated based on the work of Dyer (1989).

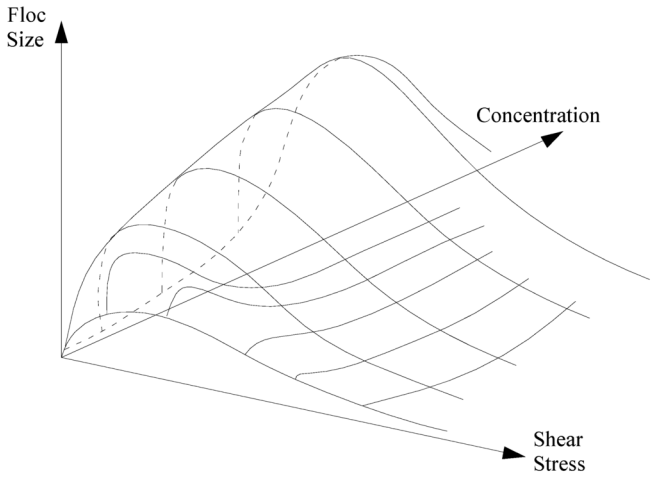

Figure 2.13: Conceptual flocculation diagram showing the relationship between floc size, suspended sediment concentration and shear stress (Dyer, 1989).

With increasing shear stresses the floc diameter initially increases due to a higher collision frequency, resulting in an increase of the settling velocity at low turbulent stresses. This is the case until floc breakup because of fluid shear becomes more important and floc sizes decrease again. The figure also shows an increase in floc size with sediment concentration at low shear stresses due to the higher occurrence of collisions with higher concentrations. The floc size then decreases as hindered settling becomes important (see chapter 2.4.2). At high shear stresses the impact of concentration decreases and disaggregation of flocs dominates. Based on the complex flocculation model of Argaman and Kaufmann (1970), van Leussen (1994) developed a heuristic formula for the settling velocity w_s, which describes the ambivalent effect of turbulence:

$$w_s = w_{s,0} \cdot \frac{1 + aG_t}{1 + bG_t{}^2} \tag{2.17}$$

where

$w_{s,0}$	reference settling velocity	[m/s]
G_t	velocity gradient in turbulent flow	[1/s]
a, b	empirical coefficients	[–]

The units of the parameters in equation 2.17 clarify that the formula is dimensionally incorrect demonstrating the empirical relationships between the variables. This has to be taken into account when comparing different settling velocity formulas. In equation 2.17, the effect of turbulence is captured by the absolute velocity gradient G_t (see chapter 2.1.2). The equation describes the dominance of aggregation effects at small shear stresses, while floc break-up dominates at larger shear stresses. The simple formula by van Leussen (1994) has been successfully applied in numerical studies for the simulation of suspended sediment concentration (e. g. Malcherek (1994), Weilbeer (2005)).

In terms of the interactions between flocs and turbulence, the various length scales of a turbulence spectrum influence the floc dynamics differently. Whereas the largest eddies primarily induce the mixing and dispersion of the sediment particles in the water column, the smallest eddies will be of utmost importance concerning the turbulent interaction between the sediment particles and the fluid flow. Collisions between particles are promoted by eddies of a size similar to those of the colliding particles. In literature, both laboratory experiments and field measurements have demonstrated that the Kolmogorov micro-scale of turbulence (see chapter 2.1.2) is an adequate reference for the maximum size of the fragile macro-flocs (van Leussen, 1997). For flocs larger than the Kolmogorov micro-scale, deformation or fracture occur as a result of the turbulent shear stresses. According to Winterwerp (1998), typical values of the Kolmogorov micro-scale in estuaries range from $100 - 1000\,\mu$m depending on the water depth and the flow velocity.

In natural flows, different turbulent intensities should be differentiated over the water depth with relatively high and low turbulence kinetic energy (see figure 2.14). In a zone close to the bed, the strongest turbulence intensity can be found, associated with highest velocity gradients and the highest energy dissipation. Hence, according to equation 2.5, the Kolmogorov micro-scale also varies over the water depth, resulting in the smallest micro-scale eddies near the bed, where the maximum shear forces act on the particles and flocs. Flocs which are strong enough to resist this bottom shear stresses will settle to the bed. Flocs of lower strength will be broken up into smaller units and be re-entrained into suspension by the hydrodynamic lift forces. In lower turbulence zones, the broken aggregates will again participate in the aggregation process. This continuous process of aggregation and disaggregation is presented on the right side in figure 2.14. The different levels of turbulent shear stresses over the water depth lead to a vertical gradient in floc size

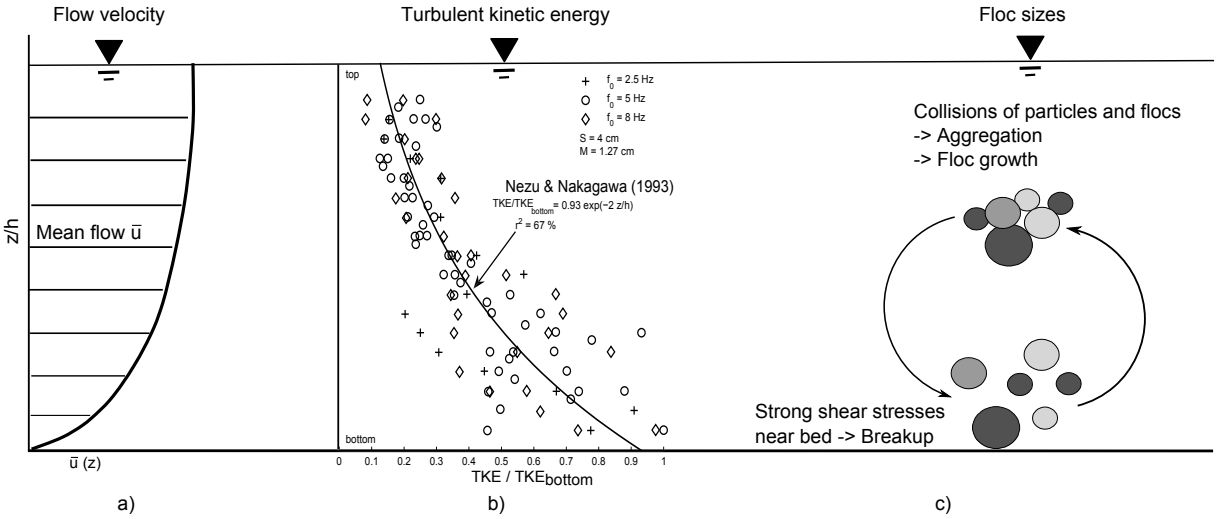

Figure 2.14: a) Logarithmic mean velocity profile over water depth, b) vertical distribution of the turbulent kinetic energy *TKE* in a differential turbulence column (modified from Kühn (2007), c) schematic picture of continuous process of aggregation and breakup of flocs in a turbulent flow (modified from van Leussen (1997)).

at equilibrium stage, i. e. when aggregation and disaggregation processes are in balance. Kühn (2007) conducted floc size measurements over the water depth in a differential turbulence column reproducing a natural turbulence profile in rivers. It was shown that at equilibrium, the vertical floc size distribution can be approximated by a linear decrease in floc size towards the bottom. In regions of higher turbulence intensity, i. e. in a zone close to the bottom, smaller particle sizes were measured than in the upper part of the water column, since the strong turbulent shear stresses led to an enhanced disaggregation of the aggregates. It has to be noted that the vertical gradient in floc size, as indicated in figure 2.14, can only occur if the flocculation time is smaller than the settling and mixing time of the sediments. This will be ensured when the residence time of the flocs in the upper part of the water column is large enough.

A quasi-equilibrium situation for the floc size distribution is reached when floc growth is equal to floc break up. The equilibrium floc size depends on the turbulence intensity and on the ratio between the residence time of the flocs in the water column (e. g. the water depth) and the flocculation time. Figure 2.15 shows the floc size as a function of the shear rate (velocity gradient G_t) and the water depth. At a water depth of 4, 2 and 1 metre (solid lines) the floc diameter is increasing with the shear rate parameter G_t at small G_t, followed by a decrease in floc size at larger G_t. Figure 2.15 is qualitatively similar to the diagram in figure 2.13. The dashed line represents the equilibrium floc size diameter, i. e. when a balance between particle aggregation and disaggregation is reached. However, at small shear stresses, flocs typically can not reach the equilibrium, because the bottom of the settling column will be reached before the equilibrium size is reached. Winterwerp (1998) attributes the effect to the significantly increased floc size at low shear stresses which in turn results in an increase of the settling velocity. The effect will be greater with a smaller water depth, as the residence time will be lower. Therefore, the residence time of the flocs in the column becomes the limiting factor. At high shear stresses, the flocs do not get very large as they tend to break-up. For this case, their residence time in the water column is large enough to reach equilibrium size.

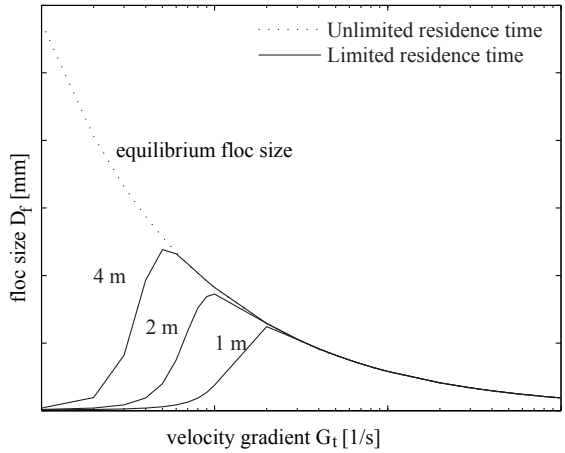

Figure 2.15: Effect of limited residence time on the relation between floc size D_f and the velocity gradient G_t (modified from Winterwerp (1998)).

2.4 Settling and Deposition

In the previous chapter it was shown that turbulence plays a major role in terms of aggregation and disaggregation mechanisms. It was also pointed out that the largest scales of turbulence induce the mixing and dispersion of the sediment particles. Both facts get relevant when describing the essential investigation parameters in sediment engineering - the settling and deposition behavior of fine sediment particles. The floc settling is governed by the level of turbulence and the transport by the mean fluid flow, i. e. advection. If the turbulence intensity and the fluid flow velocity are decreasing, the sediment flocs and particles deposit and sedimentation takes place. Except the hydraulic forces, also the floc properties are significant when estimating the deposition of flocs. The floc size, its shape and the floc structure have an impact on the settling of individual fragile flocs as well. These properties are affected by aggregation and disaggregation processes, which in turn are to a major degree influenced by turbulence. Further, the properties of the primary particles play an important role in terms of the rheological sediment characterization. Attributes of the sediment mixture, as the suspended sediment concentration, the sediment cohesion or the amount of organic matter, present further influencing factors for the sediment deposition.

To describe the deposition behavior of fine sediments the parameter *settling velocity* is usually used. The various numbers of impact factors imply that the settling velocity can be expressed theoretically by different parameters. As a consequence, it is difficult to define a unique definition for the settling velocity. Nevertheless, it is possible to derive a specific approach or modeling technique for a particular problem, for example in the sector of water quality or within siltation studies. This leads to specific settling velocity formulas for the respective applications.

Even laboratory measurements of the settling velocity of samples taken from suspensions in situ may not necessarily yield the accurate value for the characteristic settling velocity of this suspension. As sediment flocs can be destroyed by sampling and/or transport to the laboratory, even under well-controlled conditions in the laboratory the particle size distribution may vary compared to in situ floc sizes. However, the use of in situ instruments yields data pertaining to a certain location and time frame, thereby limiting

the scope of in situ measurements. Nevertheless, both laboratory studies and in situ measurements are essential for a better understanding of the cohesive sediment dynamics.

In this section, first the settling velocity of an individual grain particle in still water is described theoretically according to Stokes law. Based on this, the settling velocity of individual fractal flocs in still water at low suspended sediment concentration is presented. For high-concentrated suspensions, when hindered settling takes place, an empirically based expression depending on the suspended sediment concentration is described. The last part of this chapter presents a theoretical formula and description for the calculation of the deposition rate of cohesive sediments in still water.

2.4.1 Settling Velocity in Still Water

Grain Particle

The settling of individual particles in suspensions depends on different particle characteristics like the size, the shape and the particle density, as well as on the water viscosity. The settling velocity of an idealized, spherical particle in still water can be derived by a force balance between the particles submerged gravity force $F_g{}'$ and the drag force F_d (Raudkivi, 1998):

$$F_g{}' = (\rho_g - \rho_w) \cdot g \cdot \frac{\pi}{6} \cdot {D_g}^3 \tag{2.18}$$

$$F_d = \frac{1}{2} \cdot \rho_w \cdot {w_{s,g}}^2 \cdot C_D \cdot \frac{\pi}{4} \cdot {D_g}^2 \tag{2.19}$$

where

$F_g{}'$	submerged gravity force	$[\mathrm{kg \cdot m/s^2}]$
F_d	drag force	$[\mathrm{kg \cdot m/s^2}]$
$w_{s,g}$	settling velocity of the grain particle	$[\mathrm{m/s}]$
C_D	drag coefficient	[–]

For an idealized, spherical particle, the settling velocity becomes:

$$w_{s,g} = \sqrt{\frac{\rho_g - \rho_w}{\rho_w} \cdot g \cdot \frac{1}{C_D} \cdot \frac{4}{3} \cdot D_g} \tag{2.20}$$

The drag coefficient C_D is a function of the particle shape, the surface texture and the particles Reynolds number $Re_g = w_{s,g} \cdot D_g/\nu$. For spherical particles in the Stokes' regime (i. e. $Re_g \ll 1$), Stokes' solution for the drag coefficient yields (Stokes, 1850):

$$C_D = \frac{24}{Re_g}; \qquad Re_g \ll 1 \tag{2.21}$$

where

Re_g	particle Reynolds number	[–]

For higher Reynolds numbers $Re_g \geq 1$, different approaches and theoretical treatments to predict the drag coefficient can be found in literature (Roberson and Crowe, 1993).

Equation 2.20 in combination with equation 2.21 yields the well-known Stokes' settling velocity for spherical particles in still water:

$$w_{s,g} = \frac{{D_g}^2}{18\nu} \cdot g \cdot \left(\frac{\rho_g - \rho_w}{\rho_w} \right); \qquad Re_g \ll 1 \tag{2.22}$$

Equation 2.22 is based on the sphericity of the particles. The particle shape is considered on the one hand by the definition of the volume in equations 2.18 and 2.19, and on the other hand by the drag coefficient. However, in natural rivers the particles exhibit grain shapes which may differ strongly from an idealized spherical shape. To take into account deviations from this spherical shape, McNown and Malaika (1950) introduced the shape factor FF, which depends on the longest, the middle and shortest axis of a sediment particle. For natural sediments, the median shape factor is proposed to be $FF \cong 0.7$. Taking into account this shape factor in the definition of the drag coefficient, for Reynolds numbers $Re_g < 2 \cdot 10^5$, C_D becomes (McNown and Malaika, 1950):

$$C_D = \frac{24}{Re_g} + 2.7 - 2.3FF; \qquad Re_g < 2 \cdot 10^5 \tag{2.23}$$

where

FF form factor of a sediment particle [–]

Thus, the settling velocity for natural and con-cohesive particles with a median shape factor $FF = 0.7$, for Reynolds numbers $Re_g < 2 \cdot 10^5$, results in (Zanke, 1982):

$$w_{s,g} = \frac{11\nu}{D_g} \left(\sqrt{1 + 0.01 \cdot \frac{\rho_g - \rho_w}{\rho_w} \cdot \frac{g \cdot {D_g}^3}{\nu^2}} - 1 \right); \qquad Re_g < 2 \cdot 10^5 \tag{2.24}$$

Another form of the drag coefficient, which includes the influence of higher Re_g, is based on empirical data and is expressed by Schiller and Naumann (1933):

$$C_D = \frac{24}{Re_g} \left(1 + 0.15 Re_g^{0.687} \right); \qquad Re_g < 800 \tag{2.25}$$

Fractal Floc

Assuming that the fluid flows around and not through the flocs, the above mentioned equations for individual grain particles can also be applied for flocs of cohesive sediments. This assumption is not trivial. Johnson et al. (1996) studied the flow through flocs by experiments with latex micro-spheres and by numerical simulations. Flocs were treated as self-similar fractal entities showing an increased permeability, thus an increased flow through the floc with increasing floc size due to larger pore sizes. From their studies they concluded that the settling velocity of porous permeable flocs is slightly larger compared to impermeable flocs. However, the explanation for these observations remains unclear. With increasing permeability one would expect lower settling velocities due to an increase in the friction affected floc surface. Gregory (1997) refers to the permeability in the context of the fractal dimension. Fractal aggregates with a fractal dimension greater than $n_f = 2$ show a slight permeability, whereas with decreasing fractal dimensions the permeability rapidly increases. On the contrary, studies conducted by

Moudgil and Vasudevan (1988) and Stolzenbach and Elimelich (1994) show that flow through flocs will not be of significant importance.

For the determination of the settling velocity, it can be concluded that flocs can be treated as porous, but effectively impermeable entities. Based on this approximation and using equation 2.20, an implicit formula for the settling velocity of an individual spherical fractal floc in still water can be expressed (Winterwerp, 1998):

$$w_{s,f} = \frac{(\rho_g - \rho_w)}{\rho_w} \cdot \frac{g}{18\nu} \cdot {D_g}^{(3-n_f)} \cdot \frac{{D_f}^{(n_f-1)}}{1 + 0.15{Re_f}^{0.687}} \tag{2.26}$$

where

$w_{s,f}$	settling velocity of the floc	[m/s]
Re_f	floc Reynolds number	[–]

Equation 2.26 is derived from equation 2.20 by the substitution of the particle grain diameter D_g by the floc diameter D_f, and the substitution of the particle grain density ρ_g by the floc density ρ_f (and using equation 2.16). Furthermore, in equation 2.26 it is assumed that the drag coefficient for single grain particles defined in equation 2.25 is also valid for flocs, because the drag coefficient of a fragile floc is difficult to predict and therefore no data on drag coefficients for falling flocs are available. By considering the Stokes' solution for the drag coefficient (equation 2.21) and applying this drag coefficient also for flocs, the settling velocity of a spherical fractal floc becomes:

$$w_{s,f} = \frac{(\rho_g - \rho_w)}{\rho_w} \cdot \frac{g}{18\nu} \cdot {D_f}^2 \cdot \left(\frac{D_g}{D_f}\right)^{(3-n_f)} \tag{2.27}$$

For solid Euclidean particles, i. e. for $n_f = 3.0$, equation 2.27 is reduced back to the standard Stokes' settling relation in equation 2.22, which does not consider the fractal dimension and thereby does not not take into account a decreased floc density with increasing floc size.

Summarizing the above, the settling velocity of a spherical fractal floc in equation 2.27 is calculated in still water depending on the following sediment parameters: the floc size D_f, the size of the primary particles D_g, the primary particle density ρ_g ($= 2650\,\mathrm{kg/m^3}$) and the fractal dimension n_f ($= 1.0 - 3.0$). In addition, the density of the water ρ_w (often set to $\rho_w = 1000\,\mathrm{kg/m^3}$), the kinematic viscosity ν (often set to $\nu = 1.25 \cdot 10^{-6}\,\mathrm{m^2/s}$) as well as the acceleration of gravity g ($= 9.81\,\mathrm{m/s^2}$) are included in the settling velocity formula. Again it has to be noted that the settling velocity formula based on equation 2.27 is valid when assuming spherical and impermeable flocs. Settling velocity formulas which also consider these two factors can be found for instance in Strom and Keyvani (2011).

Figure 2.16 illustrates modeled settling velocities based on equation 2.26 by the use of different constant fractal dimension $n_f = 1.7$, 2.0 and 2.3, together with several measured data on settling velocity and floc size (Winterwerp, 1999). Figure 2.16 shows that equation 2.26 adequately fits the measured data. For particles up to a few $100\,\mu$m, the best agreement was found for a fractal dimension $n_f = 2.0$. For floc diameters larger than $1000\,\mu$m, the impact of the floc Reynolds number Re_f is increasing, thus the deviation to a simple power law behavior gets higher as well. For this purpose, Winterwerp (1999) refers to the limited validity of equation 2.26 beyond a few mm. The figure also shows that for a given floc size a decrease in fractal dimension results in lower settling velocities, since the floc density decreases with

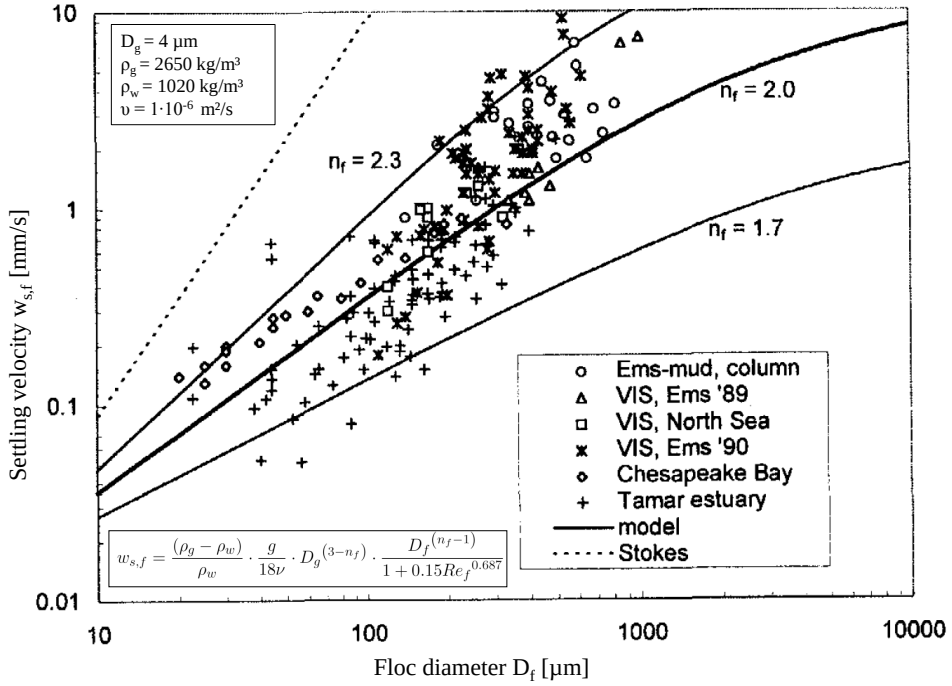

Figure 2.16: Relation between settling velocity and floc diameter (Winterwerp, 1999).

lower values for the fractal dimension. Adopting $n_f = 3.0$ would fit the standard Stokes' settling solution (dashed line) and thereby estimating too high settling velocities compared to measured values.

2.4.2 Influence of Sediment Concentration on Settling Velocity

The presented settling velocity in equation 2.26 was derived for the free settling of an individual fractal floc in still water. However, the equation has limitations with respect to the volumetric concentration of the cohesive sediment suspension. When the concentration is increasing, interactions between the particles and flocs in the fluid modify the settling behavior, since the flocs start to hinder each other while settling. Hence, equation 2.26 is valid only for low suspended sediment concentrations. Another limiting factor of this equation is the difficult prediction of the essential floc parameters in order to calculate a correct floc settling velocity. On the one hand the floc size, which depends on several factors, like cohesion, turbulence and concentration has to be known. On the other hand, the floc structure has to be determined by the value definition for the fractal dimension. As a consequence of the difficult prediction of these parameters, the settling velocity for a given material is often determined by measurements (Burt, 1986, Raudkivi, 1998).

An alternative empirical based solution which is widely used to simulate cohesive sediment deposition implies the correlation between the measured settling velocity in the laboratory and the suspended sediment concentration. For relatively low concentrations, the following power function can be applied (Raudkivi, 1998):

$$w_s = mC^n \tag{2.28}$$

where

m, n empirical coefficients [–]

w_s represents a median settling velocity corresponding to 50 % of solids by weight settled out. m and n are empirical coefficients which have to be determined from laboratory data.

At higher concentrations, when hindered settling takes place, the influence of particle concentration on the effective fall velocity can be expressed by the following power function (Raudkivi, 1998):

$$w_s = w_0 \left(1 - kC\right)^{\beta_{Re}} \tag{2.29}$$

where

w_0	settling velocity of an individual floc or particle	[m/s]
k	parameter depending on sediment composition	[–]
β_{Re}	function of the particles Reynolds number	[–]

w_0 is the settling velocity of an individual floc or particle, k depends on the sediment composition and β_{Re} is a function of the particles Reynolds number ($2.5 < \beta_{Re} < 5.5$). Figure 2.17 illustrates the dependency of the settling velocity on the sediment concentration by data obtained in laboratory using a sediment mixture from Severn Estuary mud. The reported limits of the onset of hindered settling vary widely, depending on the sediment composition, from about 3 g/l to 15 g/l (Raudkivi, 1998). Up to a concentration of 3 g/l the settling velocity is increasing with increasing sediment concentration. This effect can be attributed to two factors: with increasing suspended sediment concentration the collision probability of the particles and flocs is increasing. This results in enhanced flocculation processes and larger aggregates, which imply higher settling velocities. However, increasing flow velocities can lead to erosion of larger particles from the bed. These particles are then mobilised in suspension and thereby leading to a change in sediment sizes towards larger particle and floc sizes, which imply higher settling velocities. Hence, it is not necessarily aggregation processes that cause the increase in settling velocity with increasing suspended sediment concentration (Winterwerp and van Kesteren, 2004). At higher concentrations, at the onset of hindered settling, the effective settling velocity decreases due to the upflow of the water as it is displaced by the descending particles. With respect to the application of these equations it is important to note that the coefficients m, n, k and β_{Re} are determined on the basis of field or laboratory measurements and are representative for a certain sediment mixture and for specific hydraulic boundary conditions.

In chapter 2.3.5, an approach (equation 2.17) was presented to relate the settling velocity to a turbulent shear parameter, expressed by the velocity gradient G_t, and to a reference settling velocity $w_{s,0}$. The reference velocity $w_{s,0}$ is often linked to equation 2.28 or 2.29 (Weilbeer, 2005, Baugh and Manning, 2007, Manning, 2008a):

$$w_s = mC^n \cdot \frac{1 + aG_t}{1 + bG_t{}^2} \tag{2.30}$$

and

$$w_s = w_0 \left(1 - kC\right)^{\beta_{Re}} \cdot \frac{1 + aG_t}{1 + bG_t{}^2} \tag{2.31}$$

As previously mentioned at the beginning of this chapter, there is no unique formula for the settling velocity of flocs, since it is affected by various factors. As a result, existing approaches consider merely

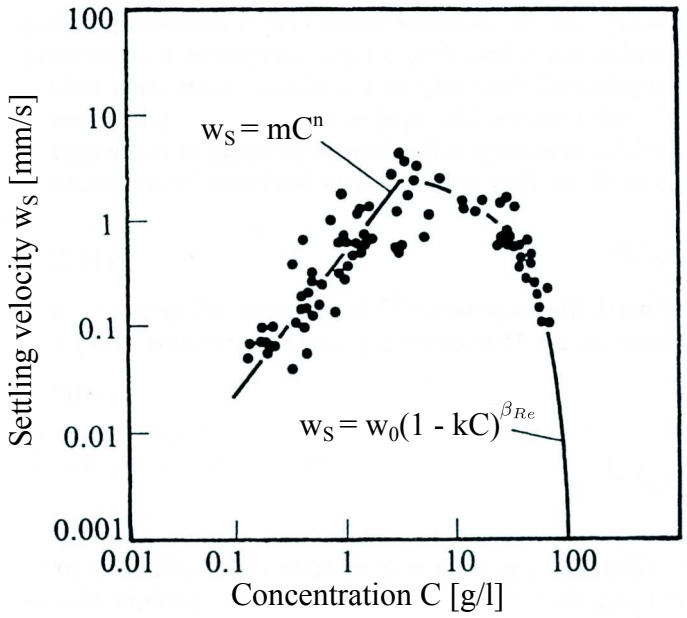

Figure 2.17: Median settling velocity w_s as a function of the sediment concentration C, based on data from Severn Estuary (UK) mud with $m = 0.513$, $n = 1.29$, $k = 0.008$, $\beta_{Re} = 4.65$ and $w_0 = 2.6\,\mathrm{mm/s}$ (Raudkivi, 1998).

certain aspects among the many influencing factors. In this work, two general approaches for calculating the floc settling velocity were presented. One approach is a theoretically based formulation depending on the particle and floc diameter while taking into account the fractal structure of flocs. The other approach uses an empirically based equation depending on the sediment concentration. In literature various other settling velocity approaches can be found. In general, they can be differentiated with respect whether they describe w_s as a function of the particle diameter (e. g. Lick et al., 1992, Cheng, 1997) or by the suspended sediment concentration (e. g. Rasmussen and Larsen, 1996, Reuter et al., 2003). They also vary in their complexity. An overview of further selected settling velocity formulas can be found in Hillebrand (2008).

2.4.3 Deposition Rate

In order to simulate large-scale processes as cohesive sediment transport and deposition, the settling velocity of the falling particles and flocs is one important parameter. Based on the settling velocity, the deposition rate, i. e. the settling flux towards the bottom, can be calculated. The deposition rate, which is expressed by the change of mass of suspended sediment per unit area with time, can be calculated by using the deposition formula based on Krone (1962):

$$\frac{dh\overline{C}}{dt} = -D_{dep} = -w_{s,char} C_b \left(1 - \frac{\tau_b}{\tau_d}\right) \qquad \text{for } \tau_b < \tau_d \tag{2.32}$$

where

h	water depth	[m]
$\overline{C}$	depth-averaged concentration	[kg/m³]
t	time	[s]
D_{dep}	deposition rate	[kg/m²·s]
$w_{s,char}$	characteristic settling velocity	[m/s]
C_b	near-bed concentration	[kg/m³]
τ_b	bed shear stress	[N/m²]
τ_d	critical shear stress for deposition	[N/m²]

Assuming that the vertical gradient in suspended sediment concentration is small due to very small settling velocities, the near-bed concentration C_b in Krone's equation is often set equal to a depth-averaged concentration $\overline{C}$. The Krone equation was derived for low concentrations of suspended sediment using mud from the San Francisco Bay in a laboratory flume. It is a popular formula in cohesive sediment transport models for low sediment concentrations. Under low sediment concentration conditions, it can be assumed that the flocculation time of cohesive sediment particles is large. In the case that the flocculation time T_f is larger than the settling time T_S ($T_f/T_S > 1$), vertical gradients in floc size are not expected to occur extensively. The floc size is mainly determined by the near-bed turbulent flow conditions. Therefore, for low sediment concentrations, variations in flocculation over the water depth with time are not significant (Hill et al., 2001). Hence, the settling velocity in equation 2.32 is often set to a constant, characteristic value in both time and space. In contrast, for high sediment concentrations the flocculation time gets smaller than the settling time ($T_f/T_S < 1$), thus aggregation can result in larger floc sizes in the upper part of the water column compared to floc sizes near the bed. This results in a vertical gradient in floc size, as it was indicated in figure 2.14 in chapter 2.3.5.

The product $w_s C_b$ represents the flux of suspended particles to the bed surface, whereas the product $(1 - \tau_b/\tau_d)$ is interpreted as the probability that an arriving aggregate would be retained on the bed. It is often referred to as the fraction of flocs whose yield strengths are too weak to withstand the large shear stresses near the bed and therefore will be broken and resuspended. According to Krone (1962) a critical shear stress for deposition τ_d exists. If the bed shear stress τ_b is below this value ($\tau_b < \tau_d$) all sediment will eventually deposit, while at at higher values ($\tau_b > \tau_d$) no sediment is able to deposit. The critical shear stress for deposition depends on the sediment composition and the shear strengths of depositing aggregates and has to be determined. From experimental measurements Krone (1962) defines values for τ_d to be in the range of 0.060 to 0.078 N/m².

Based on sedimentation experiments in a rotating annular flume, it could be shown in many studies, that contrary to Krone's experiments, not all sediment deposited when $\tau_b < \tau_d$ and an equilibrium concentration was found (e. g. Mehta and Partheniades, 1975, Lau, 1994, Haralampides et al., 2003, Stone and Krishnappan, 2003, Krishnappan, 2007, Hillebrand, 2008). Figure 2.18 shows the resulting concentration versus time for four different bed shear stresses based on sedimentation experiments in a rotating circular flume by Stone and Krishnappan (2003).

For all cases, the data show that, after 20 minutes of full mixing of the sediment and the subsequent lowering of the flume speed to a constant bed shear stress, the sediment concentration decreases suddenly in the beginning and then decreases gradually towards a steady-state value, i. e. an equilibrium concentration. This value was found to be a function of the applied shear stress in the flume. The distribution in floc size is the cause of the observed decrease in sediment concentration: for a given bed shear stress, first the larger particles of the suspension implying higher settling velocities settled from the water column

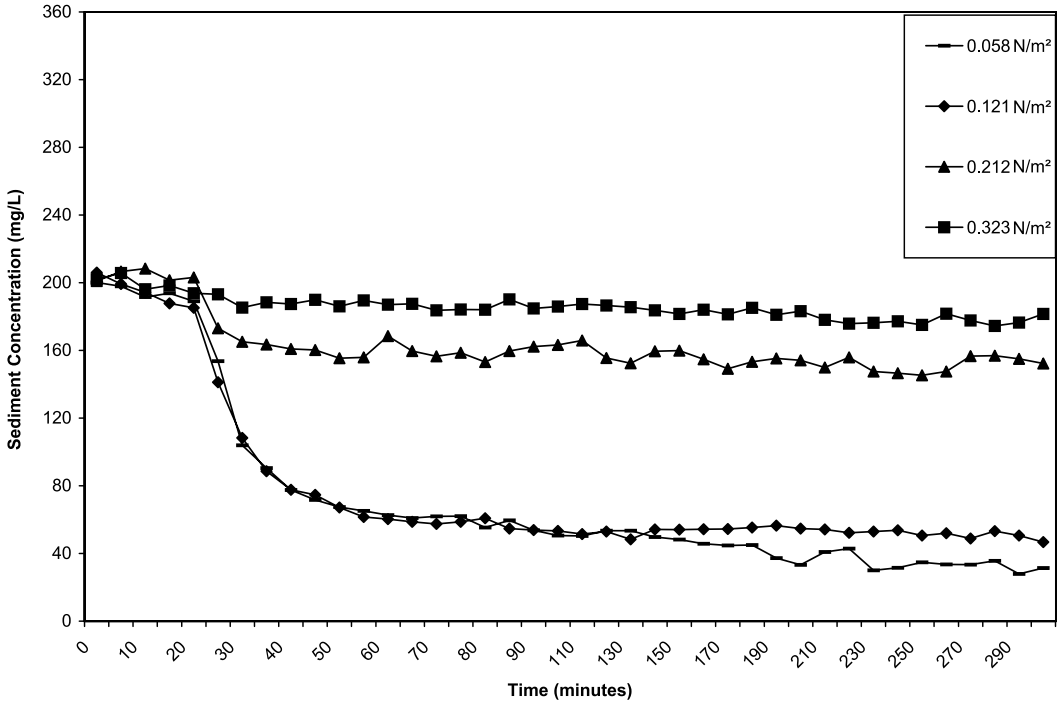

Figure 2.18: Results of depositional experiments: Concentration of suspended sediments vs. time as a function of bed shear stress (Stone and Krishnappan, 2003).

leaving only the finer particles in suspension. This results in a decrease of the median diameter with time. Smaller particles with lower settling velocities exhibit smaller critical shear stresses for deposition and can therefore be transported in suspension more easily. As a consequence, the sediment concentration decreases very slowly. Choosing the same sediment type and the same initial sediment concentration while decreasing the bed shear stress, the deposition rate would increase according to equation 2.32. This effect results in lower values for the equilibrium concentration with decreasing bed shear stresses.

Several experiments were carried out to analyze the question if sedimentation and erosion can occur simultaneously for cohesive sediments. Measured data from some studies suggest the idea that erosion and deposition can occur at the same time. Contrary, other laboratory studies indicate that erosion does not occur simultaneously with deposition. This paradigm in cohesive sediment dynamics was studied by Partheniades (1965, 1968) who carried out three experiments in a rotating circular flume. Two of the three experiments indicated that erosion does not occur during deposition, whereas one experiment could only be explained by the fact that a certain part of the fine fraction was eroded. The latter assumption is supported by observations from Krone which are based on deposition experiments in a straight flume (1962, 1993). Field measurements analyzed by Sanford and Halka (1993) indicate that the paradigm of mutually exclusive erosion and deposition is valid under laboratory conditions, but not for field observations.

On the basis of the observations reviewed in this chapter, it can be concluded that physical processes in cohesive sediment dynamics, in particular flocculation processes, are not fully understood yet. The results obtained from different researchers vary partly, sometimes even are contradictory. The discrepancies may be caused by different experimental conditions and measurement techniques, nevertheless also indicate the significant processes' complexity accompanied by limitations for cohesive sediment engineering.

3 Computational Fluid Dynamics Modeling of Flocculation Processes

The chapter above illustrated that aggregation and floc break-up processes strongly influence the transport and settling of cohesive sediment particles and flocs involving changes in particle properties. It was also shown that flocculation is a multi-layered process which is affected by several physical, biological and chemical factors. Due to the complex physical phenomena associated with cohesive sediments, flocculation processes are not fully understood yet. A better understanding of these mechanisms is a prerequisite to predict the transport and fate of fine-grained sediments accurately or to evaluate the risk regarding particle-bound contaminants.

In order to make long term predictions of cohesive sediment deposition or to quantify the impact of particle-bound contaminants, and for the purpose of studying complex fine sediment mechanisms, computational fluid dynamics (CFD) sediment transport models are increasingly used as simulation and research tools. The CFD sediment transport models are typically applied to enable the calculation of the macro-scale sediment processes like sediment transport and deposition physically as accurate as possible. A realistic and precise sediment transport modeling means that also the key sediment processes at micro-scale have to be taken into account and included in the model. In that regard, and in particular when the model focus lies on the small-scale processes, flocculation plays a major role. Hence, the inclusion of an explicit treatment of flocculation processes in numerical sediment transport models is essential in order to provide relevant knowledge for the understanding of the physico-chemical and biological coherences related to fine sediment dynamics.

Currently, due to its complexity and still existing research gaps, numerical modeling of flocculation processes represents a major challenge in morphodynamics and sediment engineering. Both empirically and mathematically/physically based flocculation algorithms used in numerical models exhibit different degrees of complexity depending on the number of influencing factors that are taken into account. All flocculation models are based on and calibrated by the use of measurement data from laboratory experiments and/or field studies. A good agreement between the simulation results and the measured data is a prerequisite for further application of the flocculation model in a 1D, 2D or 3D hydrodynamic sediment transport model.

The aim of this work was to gain insight into flocculation processes and its process complexity. For this purpose, the 3D sediment transport model SSIIM (Olsen, 2014) was used and should be extended by the implementation of a flocculation algorithm which enables the simulation of aggregation and disaggregation processes of cohesive sediments. In future, the implemented flocculation model is expected to serve as a research tool for the simulation of aggregation and floc break-up processes at micro-scale. Additionally, it is supposed to be applied for the modeling of sediment processes at macro-scale where the cohesive properties of the fine sediments influence the model results. Within this work, the objective was on the one

hand to apply the algorithm for analyzing and modeling flocculation processes in a physical model in the annular flume (see chapter 5). Finally, on the other hand the flocculation model was used for applications in sediment engineering where the cohesive properties of sediments are relevant for the sediment transport. In this work, the Iffezheim hydropower reservoir in Germany was used as a real test case for the practical application of the flocculation algorithm (see chapter 6).

In this chapter a review on numerical modeling of flocculation is given from literature. In the first part it is described how flocculation models are currently coupled within CFD sediment transport models. Subsequently, fundamental mathematical formulations and descriptions of aggregation and disaggregation mechanisms are presented. Due to the lack of understanding in flocculation processes in general, and floc break-up mechanisms in particular, different approaches for modeling disaggregation are described. The chapter closes with a comparative study of several existing flocculation models. The aim of this study was to choose a flocculation algorithm which considers the most relevant physico-chemical influential factors and which is also suitable for the implementation in SSIIM.

3.1 Coupling of Flocculation Models within CFD Sediment Transport Models

Flocculation models are commonly implemented within CFD sediment transport models. The coupling of both models aims on the simulation of cohesive sediment transport by advection and turbulent diffusion, and sediment deposition or erosion while simultaneously aggregation and disaggregation mechanisms are considered. The interaction of flocculation and sediment transport/vertical settling is currently modeled on the basis of two approaches: the transport and settling stage is calculated by the three-dimensional, unsteady advection-diffusion equation, while a flocculation model is used for predicting the particle size and concentration distribution due to aggregation and disaggregation. For a particle size distribution which is characterized mathematically by multiple particle size classes, the advection-diffusion equation for each sediment size class i is given by:

$$\frac{\partial C_i}{\partial t} + U_j \frac{\partial C_i}{\partial x_j} + w_{s,i} \frac{\partial C_i}{\partial z} = \frac{\partial}{\partial x_j} \left(D_{turb} \frac{\partial C_i}{\partial x_j} \right) \tag{3.1}$$

where

C	suspended sediment concentration (SCC)	$[\mathrm{kg/m^3}]$
t	time	$[\mathrm{s}]$
U_j	flow velocity in j-direction	$[\mathrm{m/s}]$
w_s	settling velocity	$[\mathrm{m/s}]$
D_{turb}	turbulent diffusion coefficient	$[\mathrm{m^2/s}]$

Equation 3.1 describes the change in concentration of individual sediment size classes over time due to mass fluxes by advection, turbulent diffusion and settling (see chapter 2.3.2). For the one-dimensional case in the vertical z-direction and by neglecting mass fluxes due to advection, the equation can be simplified to:

$$\frac{\partial C_i}{\partial t} = \frac{\partial}{\partial z}\left(D_{turb}\frac{\partial C_i}{\partial z} - w_{s,i}C_i\right) \tag{3.2}$$

According to equation 3.2, the concentration is not changing in time if there is a balance between the rate of upward turbulent diffusion and the settling rate. For solving the advection-diffusion equation initial and boundary conditions are necessary. Initial conditions at time $t = 0$ imply the specification of the concentration of each sediment size class as a function of the vertical z-direction. The corresponding boundary conditions are the zero net sediment flux at the water surface, $z = 0$ (top boundary):

$$D_{turb}\frac{\partial C_i}{\partial z} - w_{s,i}C_i = 0\Big|_{z=0} \tag{3.3}$$

whereas at the bed, $z = h$, a depositional flux is equated to the difference between the deposition flux F_{dep}, caused by particle settling and the erosion flux F_e, due to turbulent diffusion:

$$F_{dep} - F_e = w_{s,i}C_i - D_{turb}\frac{\partial C_i}{\partial z} = \dot{C}_i\Big|_{z=h} \tag{3.4}$$

where

F_{dep}	deposition flux	$[\mathrm{kg/m^2 \cdot s}]$
F_e	erosion flux	$[\mathrm{kg/m^2 \cdot s}]$

In the case that the bed shear stress τ_b exceeds the critical value of bed shear stress for erosion $\tau_{e,i}$, particle or floc erosion would occur. However, the erosion flux F_e is often assumed to be zero in numerical deposition models of fine sediments, in agreement with the postulation that cohesive sediments do not undergo simultaneous deposition and erosion (see chapter 2.4.3). In this case, the net rate F_{dep} at which particles of size class i are deposited to the bed ($z = h$) is given by:

$$F_{dep}(z = h) = \begin{cases} 0 & \tau_b > \tau_{d,i} \\ w_{s,i}C_{b,i}\left(1 - \frac{\tau_b}{\tau_{d,i}}\right) & \tau_b \leq \tau_{d,i} \end{cases} \tag{3.5}$$

No depositional flux of size class i at the bed will occur when the bed shear stress τ_b exceeds the critical shear stress for deposition $\tau_{d,i}$. In the case that the bed shear stress is below the critical shear stress for deposition ($\tau_b \leq \tau_{d,i}$), the depositional flux is calculated by using equation 2.32 according to Krone (1962) (see chapter 2.4.3).

The sediment concentration C_i and the settling velocity $w_{s,i}$ of each sediment size class are the linking parameters between the advection-diffusion equation and a separate flocculation model. CFD cohesive sediment transport models of multiple size classes i, that include a separate flocculation model, are usually solved in two steps within each time step and for each computational cell. In figure 3.1, the flowchart demonstrates a possible calculation process in such models. Its sequence is not representative of all CFD models, but is a prime example for the SSIIM model which was used within this work.

For a specific time step t_n, first the concentration in each sediment size class from the previous time step t_{n-1} is used to calculate a new concentration $C_i(t_n)$ as a result from advection, turbulent diffusion and deposition or erosion. The first (time-dependent) term in the advection-diffusion equation is computed on

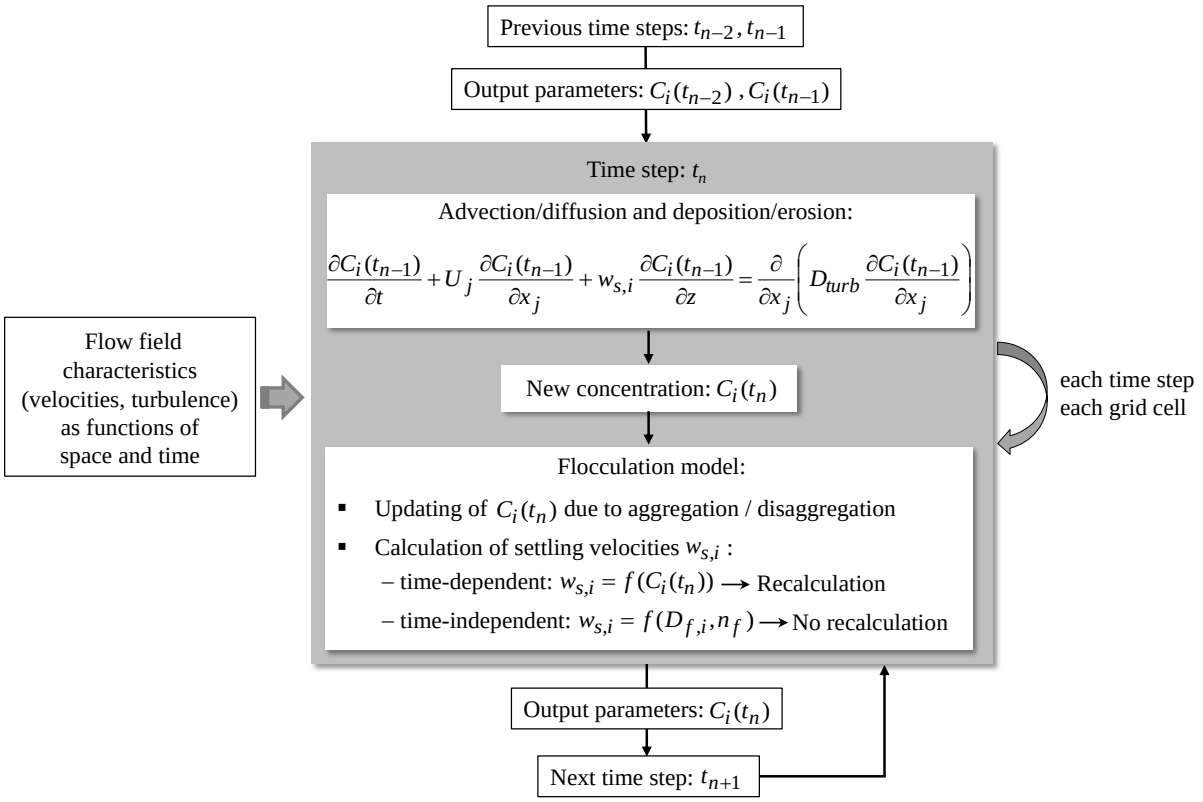

Figure 3.1: Flowchart representing a possible sequence of the calculation processes in a CFD cohesive sediment transport model of multiple size classes i including a flocculation model.

the basis of known values from the previous time step t_{n-2} and from values of time step t_{n-1}. Secondly, the flocculation model is used to update the new concentration $C_i(t_n)$ in each sediment size class due to class-by-class sediment mass changes caused by aggregation and disaggregation. Additionally, the settling velocity of each sediment size class $w_{s,i}$ is typically calculated within the flocculation computation. The settling velocity can be calculated either as a variable parameter which changes with the time-dependent sediment concentration (e. g. according to equation 2.28 or 2.29) or as a steady, time-independent value that is a function only of predefined and non changing values for the respective particle sizes $D_{f,i}$ and the fractal dimension n_f (e. g. according to equation 2.26). In the case of a time-dependent settling velocity, the settling velocity values have to be recalculated for each time step and each grid cell. Using a time-independent settling velocity, no recalculation is required and the values remain constant for the whole simulation time. The above described computation process is repeated for the next time step t_{n+1}, in which again the calculated sediment concentrations from the time steps t_{n-1} and t_n serve as input data. The flow field characteristics, i. e. the flow velocities and turbulence parameters influence both, the transport/settling and the flocculation processes. These parameters are obtained from solving the Navier-Stokes-equations (see chapter 2.1.1) and by the use of the applied turbulence model (see chapter 4.1.2) within the water flow modeling. The water flow parameters are functions of space and time and serve as a continuous data input for the cohesive sediment transport calculation.

3.2 Flocculation Models

3.2.1 Mathematical Formulations for Aggregation

A complete flocculation model should include the calculation of both aggregation and disaggregation mechanisms. Within the modeling of flocculation processes a number of empirical and mathematical algorithms have been developed, which can be differentiated whether they simulate aggregation only, or both aggregation and disaggregation. Nearly all flocculation models, which simulate aggregation solely, are based on one fundamental coagulation equation derived originally by Smoluchowski (1916). The Smoluchowski equation describes the kinetics of aggregation in a diffusion field theoretically in terms of binary collisions:

$$\frac{dn_l}{dt} = \frac{1}{2} \sum_{i+k=l} \alpha_{a,ik} \beta_{ik} n_i n_k - n_l \sum_{i=1}^{i=s} \alpha_{a,il} \beta_{il} n_i \tag{3.6}$$

where

n_i, n_k, n_l	number concentration for particles of size i, k, l per unit volume	$[1/m^3]$
$\alpha_{a,ik}, \alpha_{a,il}$	aggregation factor between two particles of size i and k, and size i and l	[–]
β_{ik}, β_{il}	collision frequency function between two particles of size i and k, and size i and l	$[m^3/s]$

Equation 3.6 expresses the change rate of the number of particles of discrete particle size l per unit fluid volume as a result of particle collisions. The first term on the right hand side describes the increase in particles of size l due to aggregation of two particles of size i and k, whose total volume is equal to the volume of a particle of size l. The factor $1/2$ in front of this term ensures that over the summation the same collision is not counted twice. The second term on the right hand side defines the loss of particles of size l by aggregation of these particles with all other particle sizes ranging from the smallest particles in size class $i = 1$ to the largest particles in size class $i = s$.

The aggregation factor α_a, which is often cited as collision efficiency, takes values from zero to one ($0 < \alpha_a \leq 1$). It represents the probability of cohesion after collision of two particles. α_a is usually used to account for the effect of particle cohesiveness, i. e. for physico-chemical forces and electrochemical properties of the sediment-water mixture and other coagulative mechanisms such as chemical and/or organic coatings on sediment particles. The aggregation factor can therefore be expressed as the weight fraction of suspended sediment that is strongly cohesive (e. g. particle sizes with elemental grain diameters less than 20 μm (see table 2.2)). Since α_a is influenced by many factors and due to the lack of effective methods to determine this factor, the aggregation coefficient is usually expressed as an empirical coefficient. However, in this context Maggi (2005) refers to work from Friedlander (1957) and Pruppacher and Klett (1978), who both investigated collision efficiency by generic mathematical formulations. Based on Friedlander (1957) the collision efficiency $\alpha_{a,ik}$ for two particles of sizes D_i and D_k is given by:

$$\alpha_{a,ik} = 1 - \frac{3}{2(1 + D_i/D_k)} + \frac{1}{2(1 + D_i/D_k)^3} \tag{3.7}$$

Pruppacher and Klett (1978) derived a similar equation:

$$\alpha_{a,ik} = \frac{(D_i/D_k)^2}{2(1 + D_i/D_k)^2} \tag{3.8}$$

The original formulation by Friedlander (1957) is deduced from theoretical considerations regarding the prediction of rates of heat and mass transfer from single spheres and cylinders to fluids in laminar motion. Based on the model of Friedlander (1957), Pruppacher and Klett (1978) described a simpler formulation for the collision efficiency, which shows an increase of $\alpha_{a,ik}$ with increasing ratio D_i/D_k. However, in most published studies, due to the lack of information about the physico-chemical properties of the used sediment, the aggregation factor is set as a constant value which does not depend on floc size. It is usually used as a calibration parameter, in combination with the collision frequency function.

In equation 3.6, the collision frequency functions β_{ik} and β_{il} express the measure of probability that two particles collide with each other in unit time. The classical Smoluchowski expression takes only Brownian motion as the relevant collision mechanism between two particles into account. Enhancements of the Smoluchowski equation were done by involving also fluid shear and differential settling as collision mechanisms. The collision frequency functions, given for the three different collision mechanisms Brownian motion, fluid shear and differential settling, take on the following functional forms (e. g. Saffman and Turner, 1956, McCave, 1984, Tsai et al., 1987, McAnally, 2000, Maggi, 2005):

$$\beta_{B,ik} = \left(\frac{2}{3}\frac{\kappa_B T}{\mu}\right)\frac{(D_i + D_k)^2}{D_i D_k} \qquad \text{Brownian motion} \tag{3.9}$$

$$\beta_{S,ik} = \frac{G}{6}(D_i + D_k)^3 \qquad \text{Fluid shear} \tag{3.10}$$

$$\beta_{D,ik} = \frac{\pi}{4}(D_i + D_k)^2 \cdot |w_{s,i} - w_{s,k}| \qquad \text{Differential settling} \tag{3.11}$$

where

$\beta_{B,ik}$	collision frequency function between two particles of size i and k due to Brownian motion	$[\mathrm{m^3/s}]$
$\beta_{S,ik}$	collision frequency function between two particles of size i and k due to fluid shear	$[\mathrm{m^3/s}]$
$\beta_{D,ik}$	collision frequency function between two particles of size i and k due to differential settling	$[\mathrm{m^3/s}]$
κ_B	Boltzmann constant	$[1.3806488{\cdot}10^{-23}\,\mathrm{J/K}]$
T	absolute Temperature	[K]
μ	dynamic viscosity of fluid	$[\mathrm{kg/m{\cdot}s}]$
D_i, D_k	diameter of colliding particles of size i and k	[m]
G	velocity gradient	$[1/\mathrm{s}]$
$w_{s,i}$, $w_{s,k}$	settling velocity of particles of size i and k	$[\mathrm{m/s}]$

The velocity gradient is either $G_l = du/dz$ for laminar fluid shear, or $G_t = \sqrt{\epsilon/\nu}$ for turbulent fluid shear according to Camp and Stein (1943) (see equation 2.6). The total collision frequency $\beta_{sum,ik}$ can be expressed as a linear superposition of the aforementioned terms:

$$\beta_{sum,ik} = \beta_{B,ik} + \beta_{S,ik} + \beta_{D,ik} \tag{3.12}$$

Smoluchowski (1916) proposed six simplifying assumptions in order to solve the equations, describing the aggregation process more manageably. Thomas et al. (1999) gave an overview of these assumptions:

- Laminar flow conditions.
- Particle collisions will result in aggregation only. No disaggregation of flocs due to collision-induced stresses and flow shear stress will occur.
- Collisions involve only two particles. The probability of three or more particles colliding simultaneously is negligible.
- Mono-dispersed suspension, i. e. all particles exhibit the same size.
- All particles show a spherical shape which remains constant during the whole aggregation mechanism. The particles are treated as solid Euclidean particles, therefore not taking into account the fractal structure of flocs.
- The aggregation factor α_a is unity for all collisions, meaning that all collisions will result in attachment.

The assumptions above oversimplify the real flocculation process, thus may lead to potential errors, under- or overestimations when modeling cohesive sediment dynamics. Hence, subsequent developments and modifications of the Smoluchowski model include further or more detailed physico-chemical aspects associated with flocculation, such as: effect of flow shear and/or differential settling on the collision frequency, disaggregation due to flow shear stresses and collision-induced stresses, greater number of colliding particles and consideration of specific floc properties (e.g. shape, fractal structure, cohesiveness).

In addition, the particle size spectrum can be described more realistically. Aggregation models using mono-dispersed particle assumptions, as it is realized in the Smoluchowski model, are actually only valid during the initial stages of flocculation. As flocs grow, larger aggregates are formed becoming also involved in the collisions. Hence, many flocculation models describe a distribution of particle sizes in a hetero-dispersed suspension by the definition of discrete size class intervals, e. g. $1-2\,\mu$m, $2-4\,\mu$m, $4-8\,\mu$m. Contrary to a definition of individual particle sizes[1], this method allows to reduce the number of differential flocculation equations, resulting in shorter computation times. Likewise, less sediment characteristics have to be provided over a given range of particle sizes.

A detailed summary of some results regarding amendments and enhancements of the Smoluchowski equation which are related to every assumption mentioned above can be found in the review papers from Thomas et al. (1999) or Zhu (2014). However, since the properties of sediment particles are indeed complex in nature, and with respect to computing power capacity and involving running times, some of the simplifying assumptions depicted above are still used currently in advanced, more developed flocculation models.

3.2.2 Mathematical Formulations for Disaggregation

Smoluchowski (1916) assumed that flocs do not break-up once formed. However, floc size and mass distribution is determined by the balance of the opposing mechanisms of aggregation and disaggregation, the latter being caused by fluid shear and collision-induced stresses. Basically, a floc will break-up if

[1] e. g. $1\,\mu$m, $2\,\mu$m, $3\,\mu$m, $4\,\mu$m in arithmetic series, or $1\,\mu$m, $2\,\mu$m, $4\,\mu$m, $8\,\mu$m in geometric series.

the shear stress acting on the aggregate, either from the surrounding flow or from collision with other aggregates, exceeds the strength of the floc. The floc strength is affected e. g. by shape, size, density and structure of the floc. Experimental results from Krone (1963) have shown that as aggregate size increases, both aggregate density and yield strength decrease. McAnally (2000) points out that aggregate strength is a function of the grain-to-grain cohesion, the size and orientation of particles within the aggregate, the organic content and to a lesser degree of salinity and pH-value. The floc yield strength determines if an aggregate is able to withstand disaggregation forces. The strength of a fractal floc τ_f is estimated as follows (Kranenburg, 1994, Mehta, 2014):

$$\tau_f = K_F \left(\frac{\rho_f - \rho_w}{\rho_w} \right)^{\frac{2}{3-n_f}} \tag{3.13}$$

where

τ_f	strength of a fractal floc	[N/m²]
K_F	empirical sediment dependent coefficient	[N/m²]
n_f	fractal dimension	[–]

The parameter K_F is a parameter, which depends on the physico-chemical properties of the sediment and the water. The floc density can be calculated as a function of floc size and fractal dimension, according to equation 2.16. The equation shows that with decreasing floc density and fractal dimension, the floc yield strength also decreases. This means, when the floc structure becomes less dense, i. e. more fragile/weak, the flocs become more susceptible to undergo disaggregation. In the case, that fluid shear or collision-induced stresses exceed the floc yield strength, the floc will be disaggregated into smaller particle sizes. In chapter 3.2.3, different approaches for calculating these stresses are described. In the following, general expressions for the time rate of change of the number of particles of a specific size as a result of disaggregation due to fluid shear and particle collisions are illustrated.

Disaggregation due to Fluid Shear

A general expression for the time rate of change of the number of particles of a discrete particle size l, which results from disaggregation due to fluid shear, is given as follows (e. g. Tsai et al., 1987, Lick and Lick, 1988, McAnally, 2000):

$$\frac{dn_l}{dt} = -B_l n_l + \sum_{m=l+1}^{i=s} \gamma_{ml} B_m n_m \tag{3.14}$$

where

n_m	number concentration for particles of size m per unit volume with $m = l+1$	[1/m³]
B_l, B_m	coefficient characteristic of sediment and particles of size l and m	[1/s]
γ_{ml}	probability that a particle of size l will be formed after disaggregation of a particle of size m	[–]

The first term on the right-hand side represents the rate at which l size particles are lost to smaller sizes due to shear-induced disaggregation of these particles. The second term on the right-hand side represents the rate at which l size particles are gained by shear-induced disaggregation of flocs larger than l.

The coefficients B_l and B_m depend generally on the chemical and physical characteristics of the sediment, the given fluid shear stress and on the individual properties of the particles of size l and m (e. g. particle diameter, effective density of the floc, floc yield strength). Lick and Lick (1988) summarised that numerous basic theoretical analyses by different researchers have been carried out in order to determine this quantity (e.g. Argaman and Kaufmann, 1970, Parker et al., 1972). The resulting theories include very complex functions of floc and fluid properties. Some of them are roughly defined or not measurable. Thus, due to the lack of sufficient information, the determination of the functional form of B_l or B_m is highly difficult.

The quantity γ_{ml} is the probability that a particle of size l will be formed by disaggregation of a larger particle of size m. In literature, different assumptions in terms of the mode of breakup distribution among the particle sizes were made. Lick and Lick (1988), for example, give three fragmentation distribution functions: breakup of a floc into two smaller particles of equal size, breakup of a floc into two particles whose size ratio is fixed, or breakup of a floc into n particles of equal size. McAnally (2000) proposes another hypothesis of the mode of floc breakup, based on the simple assumption that each floc is formed by a number of smaller particles of uniform size each. In this case, each floc can breakup into two smaller flocs of sizes i and j, such that $i + j = m$. No preferred mode of backup is used in this assumption, thus each possible mode of breakup has the same probability. As a result, for all particles of size m greater than size l, γ_{ml} can be expressed as follows (Lick and Lick, 1988, McAnally, 2000):

$$\gamma_{ml} = \frac{2}{m-1} \tag{3.15}$$

Disaggregation due to Particle Collisions

A general formula for the time rate of change of n_l as a result of disaggregation due to collisions of two particles can be written as:

$$\frac{dn_l}{dt} = -n_l \sum_{i=1}^{i=s} P_{il}\beta_{sum,il}n_i + \sum_{m=l+1}^{i=s} \gamma_{ml}n_m \sum_{i=1}^{i=s} P_{im}\beta_{sum,im}n_i \tag{3.16}$$

where

P_{il}, P_{im} probability of disaggregation of size i into size l or m [–]

The first term on the right-hand side represents the rate at which l size particles are lost by disaggregation collisions between l size particles and all other particles. The second term on the right-hand side represents the rate of increase of particles of size l by disaggregation collisions between all i size particles and m size particles, where m is greater than l.

The quantities P_{il} and P_{im} represent the probability of disaggregation of the particles of size i into size l or size m, respectively. Values for the probability of disaggregation have to be determined empirically as a function of both shear and sediment concentration (McAnally, 2000).

3.2.3 Different Approaches for Modeling Disaggregation

Equations 3.6, 3.14 and 3.16 can be combined into one equation, which represents a complete focculation model. It expresses the time rate of change of number of particles of discrete size l by both aggregation and disaggregation, the latter being caused by fluid shear as well as by collision-induced stresses:

$$\begin{aligned}\frac{dn_l}{dt} =& \frac{1}{2}\sum_{i+k=l}\alpha_{a,ik}\beta_{sum,ik}n_i n_k - n_l\sum_{i=1}^{i=s}\alpha_{a,il}\beta_{sum,il}n_i && \text{aggregation}\\ &- B_l n_l + \sum_{m=l+1}^{i=s}\gamma_{ml}B_m n_m && \text{disaggregation by fluid shear}\\ &- n_l\sum_{i=1}^{i=s}P_{il}\beta_{sum,il}n_i + \sum_{m=l+1}^{i=s}\gamma_{ml}n_m\sum_{i=1}^{i=s}P_{im}\beta_{sum,im}n_i && \text{disaggregation by particle collisions}\end{aligned} \tag{3.17}$$

The input parameters required to solve the complete mathematical equation 3.17 are, on the one hand the parameters accounting for aggregation, i. e. the aggregation factor α_a and the three frequency functions β_B, β_S and β_D. On the other hand, the parameters accounting for the growth limiting effect by disaggregation, i. e. the coefficients B and P, and the probability distribution function γ have to be defined. In order to model aggregation, the aggregation coefficient α_a has to be determined as a value between 0 and 1, whereas the frequency functions (equations 3.9 to 3.11) are relatively well understood and mathematical formulations can be found in literature. Thus, the definition of the aggregation-specific parameters seems to be feasible. However, the disaggregation parameters are far more difficult to approximate, since the relation between floc strength and their mode of break-up mechanisms under stress is affected by many factors. Hence, these coefficients have to be determined by experiments. Due to the lack of understanding in floc break-up processes, in particular the modeling of disaggregation mechanisms still represents a difficult issue in flocculation modeling, on which several studies have been published.

Within these studies, disaggregation is modeled on the basis of different assumptions and model objectives. On the one hand, the model objective is to simulate the change in the number of particles due to disaggregation, given by the equations 3.14 and 3.16. On the other hand, the model purpose is to estimate representative floc sizes, e. g. the maximum or equilibrium floc size, both parameters describing growth limiting by disaggregation.

Two kinds of models have been accepted in literature to describe breakup of flocs due to flow shear stresses in turbulent flows, depending on the floc's size relative to the Kolmogorov microscale (Mühle, 1993, Thomas et al., 1999): flocs with sizes smaller than the Kolmogorov microscale are predominantly subjected to the viscous forces of the turbulent flow. In this case, the surface of the floc is attributed to be disrupted by shearing stresses of the turbulent flow. This break-up mechanism is known as "surface erosion" meaning that small particles are separated from the floc surface. Flocs which exceed the Kolmogorov microscale are in the inertial sub-range of a turbulent flow. In this case, due to fluctuating pressure gradients across the particles or flocs, they may be split into pieces of comparable size, known as "large-scale fragmentation" or fracture. Based on these ideas and under the assumption that flocs possess homogeneous and isotropic structures, scaling relations between floc strength and floc size were predicted. However, as illustrated in chapter 2.3.4 flocs are known to be fractal objects. By experimental work, Yeung and Pelton (1996) suggested to relate floc strength with floc compactness reflected by the fractal dimension, rather than with

floc size. The authors found that more compact flocs with higher fractal dimensions favored break-up by surface erosion, whereas flocs characterized by lower fractal dimensions were more likely to undergo large-scale fragmentation.

In spite of these differences, one major factor, which is used in nearly all disaggregation models to describe the influence of flow shear on floc break-up is the velocity gradient G. For laminar flow, with the assumption of a linear velocity distribution over the entire surface of a particle, the following approach for the maximum flow shear stress acting on the surface of a spherical particle is used (with $G_l = {}^{du}/_{dz}$) (Krone, 1963):

$$\tau_u = \frac{\mu}{8}\frac{du}{dz} \qquad \text{laminar flow} \tag{3.18}$$

where

τ_u flow shear stress $[{}^{\mathrm{N}}/_{\mathrm{m}^2}]$

For turbulent flows, the velocity gradient $G_l = {}^{du}/_{dz}$ in laminar flow is substituted by the velocity gradient $G_t = \sqrt{{}^{\epsilon}/_{\nu}}$ (Camp and Stein, 1943). G_t depends on the turbulent dissipation rate ϵ and the kinematic viscosity ν (see equation 2.6).

Saffman and Turner (1956) estimated the coagulation rate of drops in turbulent clouds in which they considered the nature of the flow field around a drop. By assuming that the maximum floc size is in the order of the smallest eddies of Kolmogorov size and that the linear velocity gradient ${}^{du}/_{dz}$ obeys a Gaussian distribution, the authors derived the following equation (Saffman and Turner, 1956, Jones and Perry, 1979):

$$\tau_u = \frac{\mu}{8}\sqrt{\frac{2\epsilon}{15\pi\nu}} \qquad \text{turbulent flow} \tag{3.19}$$

Substitution of the term $\sqrt{{}^{\epsilon}/_{\nu}}$ by the turbulent velocity gradient G_t yields:

$$\tau_u = \frac{\mu}{8}\sqrt{\frac{2}{15\pi}}G_t \approx 0.0258\mu G_t \tag{3.20}$$

Delichatsios and Probstein (1974) developed a coagulation model which considers flocs and particle sizes smaller and larger than the Kolmogorov microscale. They derived new mathematical expressions which differ from Saffman and Turner (1956) for particles smaller than the Kolmogorov microscale only in the leading coefficients.

In the floc break-up model of Winterwerp (1998), fractal flocs with dimensions of the Kolmogorov length scale or smaller are considered. At this scale, disruptive stresses due to viscous forces are dominant. For the description of turbulence-induced shear stresses in the viscous regime (e. g. $Re_\eta \approx 1$) Winterwerp (1998) proposes the following approach:

$$\tau_u = \mu\frac{du}{dz} \approx \mu G_t \equiv \mu\sqrt{\frac{\epsilon}{\nu}} \tag{3.21}$$

The above mentioned formulations show that the definition of the turbulent velocity gradient G_t, originally derived by Camp and Stein (1943), remained a key parameter in terms of predicting flow shear stresses on particles due to turbulence effects. The theories differ only in the proportionality constants.

In some break-up models, the turbulent velocity gradient is also used in relationship with the maximum floc size or the rate of break-up (e.g. Parker et al., 1972, Tambo and Hozumi, 1979). These models commonly indicate the existence of a critical value of the velocity gradient, above which the aggregation mechanism is attributed to be reduced, e. g. the maximum floc size is reached. The basic form of the relationship between the maximum floc diameter $D_{f,max}$ and the velocity gradient G_t is given as follows (Thomas et al., 1999):

$$D_{f,max} = \frac{K}{{G_t}^{n_b}} \tag{3.22}$$

where

$D_{f,max}$	maximum floc diameter	[m]
K	constant	[m/s]
n_b	constant	[–]

Parker et al. (1972) have defined the constants K and n_b for two alternative break-up modes (erosion and fracture) and for two turbulence regimes (viscous subrange and inertial subrange). They proposed that the surface erosion rate of primary particles from aggregates was proportional to ${G_t}^2$ in the viscous subrange (i. e. particles smaller than the Kolmogorov microscale), and proportional to ${G_t}^4$ in the inertial subrange (i. e. particles larger than the Kolmogorov microscale).

Coufort et al. (2008) derived a simple expression representing the relation between maximum floc size with the viscous dissipation rate of turbulent kinetic energy. For a fixed aggregate strength, they give the following equation to determine the maximum floc size, regardless of the fact whether the aggregate is in the viscous subrange or in the inertial subrange:

$$D_{f,max} \approx \epsilon^{-\frac{1}{4}} \tag{3.23}$$

Both equations 3.22 and 3.23 express that the maximum floc size decreases as turbulence increases, indicating that the applied fluid shear stresses are high enough to cause break-up as the predominant mechanism.

Beyond the maximum floc size, the median floc size is another representative size definition in order to characterize the spectrum of particle sizes. Lick et al. (1993) relate the median floc size to sediment concentration and turbulence by the following power function:

$$D_{f,median} = B_D (C G_t)^{m_D} \tag{3.24}$$

where

$D_{f,median}$	median floc size	[m]
B_D	constant: 9 for fresh water, and 10.5 for sea water	[–]
C	suspended sediment concentration (SCC)	[g/cm³]
m_D	constant: -0.56 for fresh water, and -0.4 for sea water	[–]

Winterwerp (1998) added a concept for the equilibrium floc size, which is the maximum size attained in steady state conditions and represents a balance between aggregation and disaggregation (i. e. $^{D_f}/_{dt} = 0$). Winterwerp (1998) derived the equilibrium floc size $D_{f,e}$ to:

$$D_{f,e} = D_g + \frac{k_A C}{k_B \sqrt{G_t}} \tag{3.25}$$

where

$D_{f,e}$	equilibrium floc size	[m]
D_g	diameter of the grain particle	[m]
k_A	dimensional aggregation parameter	[m²/kg]
k_B	dimensional floc break-up parameter	[s^1/2/m²]

The dimensional aggregation parameter k_A and the floc break-up parameter k_B are functions of non-dimensional coefficients and several parameters (e. g. fractal dimension, primary particle size, particle density, dynamic viscosity and yield strength of flocs). From equation 3.25 it follows that the equilibrium floc size is proportional to $^1/\sqrt{G_t}$, and therefore is consequently a function of the turbulence intensity. Moreover, equation 3.25 shows that for very small velocity gradients, the equilibrium floc size $D_{f,e}$ becomes very large.

Thomas et al. (1999) refer to further flocculation models (e. g. Wiesner, 1992, Dharmappa et al., 1994), in which floc break-up is considered by the definition of an upper limit on floc size. In these models, the value of the maximum floc size depends on the assumed mode of break-up, e. g. whether the largest flocs are assumed to be in the order of the Kolmogorov microscale or larger than it.

The above considerations show that a lot of work has been published on modeling disaggregation due to turbulence-induced shear stresses. Nearly all these formulations have in common that flow shear is expressed as a function of the turbulent velocity gradient G_t. The models vary in their complexity, since the knowledge of floc break-up modes and the involved mechanisms and influencing factors is still insufficient.

In contrast to floc break-up by flow shear stresses, model approaches for disaggregation due to collision-induced shear stresses are less frequently used or completely neglected, respectively. In principle, a two-body floc collision can lead to break-up, if the collision-induced shear stress experienced by the particles exceeds the strength of at least one of the two colliding particles. In the flocculation model based on Winterwerp (1998), the effect of disaggregation due to inter-particle collisions was omitted on the basis that flocs with a small excess density will contribute to the effect of collisions only to a small degree. Likewise, Winterwerp (1998) argued that turbulent shear flow acts continuously, contrary to break-up by collisions.

McAnally (2000), however, points out from his analyses that both flow-induced shear stresses and collision shear stresses can be important within the range of particle sizes and flow intensities typical of estuarial

flows. Thereby, collision-induced shear is supposed to be more important for larger particles and higher energy dissipation rates, i. e. for higher turbulence conditions.

Verney et al. (2011) concluded from theoretical analyses and experiments that for the experimental test range of parameters and boundary conditions,[2] fluid shear has a minimal effect on disaggregation, while collisions between particles are the dominant mechanism for disaggregation. However, they also confirm the assertion by McAnally (2000) that for lower concentrations and shear stresses, disaggregation due to fluid shear may become significant. The mathematical formulation for the collision-induced shear stress experienced by a particle based on McAnally (2000) is given in chapter 4.2.2.

3.3 Comparison and Evaluation of Flocculation Models

The Smoluchowski model for aggregation combined with a formulation for floc break-up are the basis for a complete flocculation model. By the use of equation 3.17 several models simulating flocculation processes have been proposed. However, with regard to present knowledge gaps on flocculation behavior in natural systems and due to inadequate or non-existent measurement data, in applied cohesive sediment transport modeling not all the terms in equation 3.17 are always present. Computing power capacity and running times induce additionally conceptual improvements and/or simplifications of complex flocculation algorithms. Concerning these aspects, various flocculation models for applied cohesive sediment modeling purposes can be described by their degree of complexity and how accurate these models are able to simulate physical processes. In the following, based on the simplest approach to treat the aggregates as solid, Euclidean entities and thus not taking into account flocculation processes, three different methods how to include flocculation effects in numerical models are presented in ascending order of complexity (see figure 3.2). Each flocculation model (FM) is based on a given range of particle size classes i. On the basis of the presented literature review one flocculation algorithm was chosen within this work. It should enable the simulation of both aggregation and disaggregation physically very closely and should be technically appropriate for the implementation in the 3D sediment transport program SSIIM.

No consideration of flocculation: solid particles

The most basic and simplest approach to model cohesive sediment transport is to set a constant characteristic settling velocity for each particle size class in both time and space. By using the settling velocity formula based on Stokes (1850) no calibration parameters are required. This strong simplification implies that each particle is treated as a solid Euclidean entity, rather than a fractal floc. The effects of turbulence, suspended sediment concentration or cohesion on flocculation processes are excluded. Thus, flocculation effects on the particle sizes are neglected. In some models, the settling velocity values calculated according to Stokes, in particular the settling velocity for the coarser and less dense particles, are adjusted by model calibration.

FM 1: considering floc structure

In order to model the complex and variable structure of cohesive sediment aggregates, the settling velocity formula by Winterwerp (1998) can be used. Contrary to Stokes formulation, Winterwerp considers the fractal structure of flocs, with the consequence that floc density decreases as floc size increases. This approach involves only one parameter to calibrate, the fractal dimension n_f. This floc model does not take

[2] The experiments were conducted on suspended sediments at a concentration of 93 $^{mg}/_{l}$, with shear rates of from 0 to 12 $^{1}/_{s}$ and maximum floc sizes up to 1500 μm.

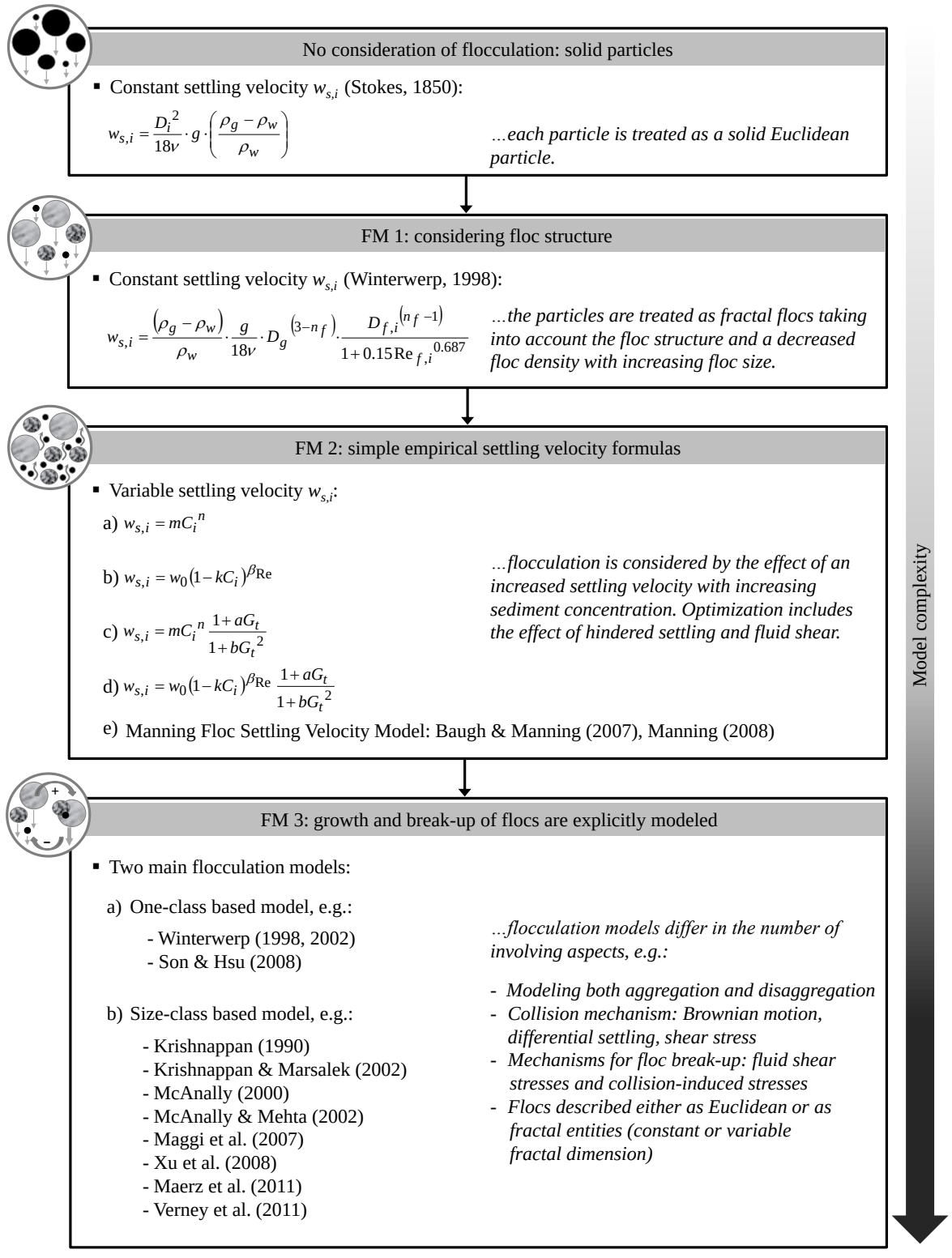

Figure 3.2: Examples for different flocculation models (FM) derived from literature and illustrated in ascending order of complexity.

into account any interaction in terms of aggregation or disaggregation between the particles. Flocculation is merely modeled with respect to its effect on the fractal structure property.

FM 2: simple empirical settling velocity formulas
A widely used method for modeling flocculation is the application of a variable, empirical settling velocity formulation. Measured data are used to relate flocculation to suspended sediment concentration. Based on the simple equation 2.28 different floc modeling stages are possible:

In **case (a)**, flocculation effects are modeled through an increase in settling velocity with increasing sediment concentration C (given by equation 2.28). A higher sediment concentration is related to a higher particle collision probability. This results in greater aggregation, thus larger aggregates with higher settling velocities. In this case two empirical coefficients, m and n, have to be determined. This approach does not include the important effects of turbulence or higher sediment concentrations that cause particles to hinder each other while settling. Hence, model improvements of this equation comprise the following stages:

In **case (b)**, the simulation includes hindered settling by using equation 2.29, which contains three calibration parameters: w_0, k and β_{Re}.

In **case (c)**, the effect of more frequent collisions, represented by the concentration C, in combination with the ambivalent effect of turbulence, represented by the turbulent velocity gradient G_t, is considered by using equation 2.30. This approach requires the determination of 4 calibration parameters: m, n, a and b. This simple approach was successfully used by Malcherek (1995) within a three-dimensional numerical study on the suspended sediment concentrations of the Weser estuary. Weilbeer (2005) used this formula within the three-dimensional modeling of sediment dynamics in the Ems estuary.

In **case (d)** the effect of turbulence in combination with hindered settling is considered by using equation 2.31. This is the most complex empirical formulation for the settling velocity, since 5 calibration coefficients: w_0, k, β_{Re}, a and b need to be defined.

In **case (e)** flocculation is also modeled by the use of an empirically based floc settling velocity model derived by Manning (2008b). It is based on the concept of larger macroflocs ($D_f > 160\,\mu$m) and smaller microflocs ($D_f < 160\,\mu$m). The flocculation model consists of three algorithms: equations are given for the settling velocity of the macroflocs, the settling velocity of the microflocs and one equation that represents the ratio of the macrofloc to microfloc suspended sediment concentration. The settling velocity of the fragile macroflocs, which are very sensitive to break-up, depends on turbulent shear stress and sediment concentration. This algorithm indicates an increase in settling velocity at low shear stresses, since flocculation is enhanced by flow shear, whereas for higher shear stresses for the same concentration floc break-up occurs. The settling velocity of the smaller microflocs, which represent the building components of the macroflocs, varies only in response to turbulent shear stress. The combination of the three equations allows to describe the mass settling flux of flocculated cohesive sediment at each point in the water column. The floc settling velocity model was compared to real observations and with a number of alternative settling velocity expressions (e. g. constant settling velocity and simple power regression relationship between the mean settling velocity and the suspended sediment concentration). The use of a constant settling velocity led to strong under- or overestimations of the observed concentrations. The power law fit reasonably well with observed concentrations, however the use of the Manning flocculation algorithm further increased the amount of vertical variation in the simulated suspended concentrations. In addition, it allowed a better reproduction of the lateral suspended concentration pattern observed in situ. Baugh

and Manning (2007) implemented the Manning floc settling velocity model into a 3D computational model of estuarine hydraulics and sediment transport (TELEMAC3D) for applications of the Lower Thames estuary.

FM 3: growth and break-up of flocs are explicitly modeled
In order to represent the processes of aggregation and disaggregation more realistically, various empirical and analytical mathematical flocculation algorithms have been developed on the basis of the Smoluchowski equation together with a floc break-up function. Instead of using a variable settling velocity formula, as mentioned above, such models explicitly consider the growth and break-up of flocs by calculating the time rate of change of number concentration of each particle size. In literature two main flocculation models are described of increasing complexity: (a) one-class based model and (b) size-class based model.

(a) One-class based model: Winterwerp (1998) constructed a one-class based model, which simulates flocculation of an individual fractal floc with a characteristic diameter for the whole floc size population. Actually, flocculation produces a distribution of particle sizes, however a varying number of size fractions is not accounted for in this model. By linear addition of terms for aggregate-forming collisions (first term) and disaggregation by shear only (second term), Winterwerp (1998) derived a differential equation which calculates changes in characteristic floc diameter over time in a Lagrangean reference frame:

$$\frac{\partial D_f}{\partial t} = k_A C G {D_f}^2 - k_B G^{3/2} {D_f}^2 (D_f - D_g) \tag{3.26}$$

where k_A and k_B (see equation 3.25 above) are constants which have to be determined empirically. The formulation for aggregation is obtained from literature on basis of the Smoluchowski equation. For modeling floc break-up, Winterwerp (1998) proposed a simple break-up function which was derived by following small, homogeneous clouds of particles on their trajectory through the fluid. The simple linear combination of the aggregation and disaggregation term implies a simultaneous aggregation and floc break-up without mutual interactions. For small values of floc sizes, the aggregation term dominates, whereas for large floc sizes break-up dominates. Equation 3.26 is based on the following assumptions: flocs have dimensions of the Kolmogorov microscale or smaller, only disaggregation due to turbulence is simulated, the effect of particle collisions on floc break-up is omitted, the fractal dimension is set to an average value of $n_f = 2$, and hindered settling due to higher sediment concentrations is supposed to play no role within the measured range of settling velocities and sediment concentrations. The settling velocity is calculated according to equation 2.26, assuming fractal, spherical flocs. For equilibrium conditions, i. e. ${dD_f}/{dt} = 0$, Winterwerp (1998) defined the equilibrium floc size $D_{f,e}$ given above in equation 3.25.

Application of this flocculation model in a numerical transport model was realized in further studies from Winterwerp (2002) by translation of the Lagrangean reference frame into an Eulerian coordinate system. The modified model represents a single-fraction equation, thus a mono-dispers system of particles. Consequently, the computed floc size and settling velocity are considered as characteristic values, e. g. as the median or mean floc size and settling velocity. The modified formula includes also a hindered settling equation to take into account high sediment concentrations. The flocculation model was implemented into a 1D-CFD model to simulate cohesive sediment processes in a reach of the turbidity maximum in the Ems estuary (Netherlands). Son and Hsu (2008) adopted a flocculation model which is based on the studies of Winterwerp (1998). Contrary to Winterwerp, they took into account a variable fractal dimension instead of a fixed one.

The main feature of one-class based models is the use of a single characteristic floc size. Hence, the major advantage of these models is the reduction of computation time and model complexity compared to size-class based models, representing the floc size distribution in terms of a number of discrete size classes.

(b) Size-class based models: Size-class based models were developed by several authors (e.g. Krishnappan, 1990, McAnally, 2000, Maggi, 2007, Xu et al., 2008, Maerz et al., 2011, Verney et al., 2011). Two types of size-class based models can be distinguished: the first one uses as many classes as particles are created (e. g. Maggi, 2007). This can result in hundreds of classes yielding large computation times when implemented in 2D/3D CFD models. The second type of model uses size classes which are defined by mean sizes (or mean masses) and lower and upper boundaries (e. g. McAnally and Mehta, 2002). This method allows the number of size classes to be reduced, thus less computation time is needed. Size-class based models also differ in their physical model accuracy, i. e. in the number of involving floc characteristics and processes, as well as whether these flocculation models were applied in 1D/2D or 3D cohesive transport models. The main properties of the size-class based models listed in figure 3.2 are described shortly hereinafter.

Krishnappan (1990) applied a flocculation model within a 1D settling model in order to simulate the measured settling of sediment mixtures under flocculated conditions in still water. Therefore, in this flocculation model no turbulence effect was considered. The model approach calculates the motion of sediment particles in two stages, a single-grain settling stage and a flocculation stage. The one-dimensional unsteady advection-diffusion equation was used to model the settling, whereas the coagulation equation was applied to simulate aggregation. Floc model complexity was reduced, because only aggregation due to differential settling was modeled, as no flow was involved, and Brownian motion is generally assumed to be negligible. Disaggregation due to particle collisions was ignored and floc break-up caused by fluid shear had no relevance due to still water conditions. The settling velocity was calculated by using the Stokes' equation, hence flocs were treated as solid Euclidean particles not taking into account the fractal structure. The flocculation model was extended to dynamic turbulent conditions, including its effect on collision frequency functions and growth limiting by Krishnappan and Marsalek (2002).

McAnally (2000) derived a multi-class flocculation model which is a combination of a statistical and a deterministic, physics-based representation of aggregation and disaggregation processes. The flocculation algorithm allows aggregation of flocs due to collisions caused by Brownian motion, differential settling and turbulence. Flow-induced stresses due to turbulence as well as collision-induced shear stresses may lead to disaggregation of flocs, if these stresses exceed the floc yield strength. The floc structure was accounted for by including the fractal dimension. The flocculation algorithm was tested against flocculation data from laboratory mixing chamber experiments with no deposition, and flume experiments in which deposition occured. For the latter the flocculation algorithm was implemented in a one-dimensional advection-diffusion equation for multiple grain sizes.

Maggi (2007) proposed a population balance equation which describes the time evolution of the floc size distribution, in combination with a modified model describing the floc geometry by using a variable and constant fractal dimension. The one-dimensional modeling of flocculation was developed for calculating experiments in a settling water column. An oscillating three-dimensional grid in the settling column produced a homogeneous turbulence field generating flocculation. The flocculation model considered aggregation and floc break-up, the latter caused by fluid shear only. For mathematical simplicity, the collision mechanisms of Brownian motion as well as differential settling were neglected, hence only turbulent

shear was taken into account. The floc break-up terms were modeled by using the parametric expression derived by Winterwerp (1999).

Xu et al. (2008) developed a multi-class model for predicting floc size distribution by including both aggregation and disaggregation. For simulating aggregation the Smoluchowski framework was applied, including turbulence and differential settling as collision mechanisms. Disaggregation due to turbulent shear only (no disaggregation caused by particle collisions) was modeled on the basis of the break-up kernel derived by Winterwerp (1998). The flocculation model assumes a fractal treatment of flocs by applying a constant average fractal dimension of $n_f = 2$ within the break-up function. For calculating the settling velocity, an empirical relationship was used which comprises the effects of variable floc densities due to fractal structure. The flocculation simulation was compared with settling column experiments carried out by Winterwerp (1998). Within the study, in contrast to many other cohesive sediment transport models, beyond the processes deposition, diffusion and flocculation, also the erosion process was considered. Consequently, Xu et al. (2008) postulate that erosion and deposition can occur simultaneously in the laboratory. The flocculation algorithm was implemented in a 1D vertical sediment transport model in order to simulate floc size variations over tidal cycles.

Maerz et al. (2011) derived a size class-based model which considers the following physical approximations: aggregation is represented by using the Smoluchowski equation, while the floc break-up term is based on the formulation by Winterwerp (1998). Floc break-up occurs due to fluid shear only, while disaggregation due to particle collisions is not taken into account. Furthermore aggregation due to differential settling and Brownian motion is neglected, and therefore turbulent shear is included as the only collision mechanism. The model includes a constant fractal dimension to take into account the fractal structure. An average settling velocity of the observed particle distribution was calculated according to equation 2.26 derived by Winterwerp (1998). The model was validated by laboratory experiments and it was shown that it could reproduce the dynamics of the average diameter fairly well. The implementation of the flocculation model in a cohesive sediment transport model has not been realized within the studies.

Verney et al. (2011) developed a size-class based flocculation model to simulate changes in floc population during an idealized tidal cycle observed from laboratory experiments. The focus of the flocculation model was set on providing key information on aggregation/disaggregation and their modeling, whereby floc settling or floc advection were neglected (so called 0D size-class based model), and thus the overall concentration remained constant. The aggregation term expressed through the Smoluchowski equation was modeled under the assumption that fluid shear is the dominant collision mechanism, while differential settling and Brownian motion were not taken into account. Disaggregation was considered to be caused by both mechanisms, fluid shear as well as particle collisions. The break-up terms due to turbulent shear are based on equations proposed by Winterwerp (2002). The mathematical formulations include for example a fragmentation probability equation and a function for the fragmentation rate determined by the floc yield strength. The floc yield strength in turn depends on the physico-chemical properties of the floc and on organic matter. Because there are still uncertainties concerning the break-up modes of flocs, several distribution functions of broken flocs due to turbulent shear were tested within the studies. The floc structure was estimated by using a constant fractal dimension over the size range as well as a variable fractal dimension which decreases with increasing floc size.

Evaluation of the Flocculation Models

All of the size-class based flocculation models described above can be potentially implemented in applied cohesive sediment transport models. However, only a few flocculation models were applied in a 1D vertical

model, e. g. by Krishnappan and Marsalek (2002) and Xu et al. (2008). None of the size-class based models were included in a 2D or 3D transport model. The reasons are different, e. g. greater costs in computational time, high degree of model complexity, difficulty to parameterize the various coefficients due to missing measured data and the currently existing uncertainties in the understanding of flocculation processes. One-class based models which use a single characteristic floc size need less computational time than size-class based models which explicitly simulate growth and break-up of flocs by adopting a number of size classes. Therefore, they are more suitable for a coupling with applied 3D engineering transport models. However, such models use some physical simplifications and provide limited knowledge on the floc population. Hence, the question is how accurate the models reproduce observed trends of a whole floc size distribution compared to size-class based models.

Flocculation models which have been successfully applied within three dimensional computational models, e. g. by Malcherek (1995), Weilbeer (2005) and Baugh and Manning (2007), comprise less complex, empirically based settling velocity formulas. The question is whether it is entirely sufficient to use a simple power law model or a fixed (mean) settling velocity. The settling velocity formulations are calibrated by using measured data collected under particular conditions in laboratory or in situ and by using particular measurement devices. Other measurement devices and methods are likely to result in different data sets, thus different calibration parameters. Spearman and Roberts (2002) point out that the development of the power law model was based on studies using the Owen tube/gravitational analysis method. These studies have shown a strong relationship between sediment concentration and settling velocity. However, more recently in situ video techniques are applied to estimate settling velocity. This method shows settling velocities many times higher than the gravitational method (Spearman and Roberts, 2002). Therefore, in addition to the significant process complexity, due to uncertainties in terms of settling velocity measurements, the question arises if this model approach is consistently able to reproduce observed pattern in floc size distributions physically correctly.

The major aim of this work was to improve the understanding of the fine sediment processes which are highly affected by flocculation processes involving changes in particle properties. The knowledge of the key aggregation and disaggregation mechanisms is the basis for predicting the transport and deposition of fine-grained sediments in an accurate way. Within this work, for the purpose of studying complex fine sediment mechanisms, the three-dimensional model SSIIM was used as a simulation and research tool. In view of the overall work objective to gain insight into the flocculation mechanisms and its process complexity, the secondary aim was to extend the software by a flocculation model which is physically as accurate as possible for the description of particle aggregation and floc break-up. In this respect, a size-class based model seemed to be the most suitable flocculation model. Since it provides detailed information on floc populations, the floc dynamics can be investigated physically very closely. In the long-term, the extended model should be applied for different cohesive sediment related issues. On the one hand it should be used for modeling flocculation processes observed in the laboratory in terms of fundamental investigations, on the other hand it should be applied for practical applications in sediment engineering. Since boundary conditions (e. g. range of suspended sediment concentrations, shear stresses, particle sizes or water chemistry) may differ for the respective issue, also the dominant sub-processes and influencing factors, which are associated with flocculation, may differ depending on the issue. For these reasons, it has to be ensured that the flocculation model is able to reproduce many effects/influencing factors. This provides the opportunity to use the flocculation algorithm for a broad range of applications and boundary conditions in future numerical cohesive sediment studies.

On the basis of these considerations, among the different size-class based models, a flocculation approach was chosen which considers the most physical sub-processes and floc characteristics, and is also technically feasible for the coupling with SSIIM 3D. In this work the flocculation approach derived by McAnally (2000) was implemented in SSIIM representing a combination of a statistical and a deterministic, physics-based representation of aggregation and disaggregation processes. The flocculation algorithm allows aggregation due to Brownian motion, differential settling and fluid shear, whereas disaggregation is accounted for by turbulence-induced fluid shear and particle collisions. The fractal structure of flocs is considered by the parameter fractal dimension. The implementation of the selected flocculation algorithm in the software program SSIIM and its main mathematical and physical concept are presented in the next chapter.

4 Implementation of a Flocculation Algorithm in SSIIM 3D

Within this work the flocculation model based on McAnally (2000) has been implemented in the three-dimensional sediment program SSIIM (Olsen, 2014). In this chapter first a brief overview of the CFD software SSIIM and its theoretical principles for hydraulic and sediment modeling are presented. Afterwards the main mathematical terms and physical descriptions of the implemented flocculation model are given.

4.1 Numerical Sediment Transport Model SSIIM 3D

4.1.1 Model Overview

The three-dimensional numerical sediment transport program SSIIM 3D is an open source software developed at the Norwegian University of Science and Technology, Trondheim (NTNU). SSIIM is an abbreviation for **S**ediment **S**imulation **I**n **I**ntakes with **M**ultiblock option (Olsen, 2014). The program is primarily used for teaching and research purposes in hydraulic/sediment engineering. The main theoretical principles of the water flow and sediment computation are described briefly below. For a more detailed and full description of SSIIM, the User's Manual (Olsen, 2014) is recommended. Fundamentals in computational fluid dynamic modeling and hydraulic/sediment engineering are reported comprehensively for example in Pope (2000), Wu et al. (2000), Ferziger and Peric (2002) or Hirsch (2007).

There are two main versions of the program: SSIIM 1 uses a structured grid and is easier to use as the grid is simpler. If wetting/drying processes are the model purposes and the model geometry is complex, it is necessary to utilize SSIIM 2, that uses an unstructured grid. For SSIIM 2 a nested grid option was developed, which is used for resolving finer scale problems in some parts of the geometry. Also, the grid editor includes the possibility of generating and connecting multiple blocks. This is not possible for the structured grid editor in SSIIM 1 which only works on one block.

As many other numerical models, SSIIM consists of three parts: a pre-processor, a solver and a post-processor. The pre-processor includes tools for the generation of the computational grid and input data. The post-processing implies the viewing and presentation of the computed model results. This can be done via the user interface of the program or by exporting the results to other post-processing software packages as Tecplot or Para View. The computation itself can include the calculation of water velocity, sediment flow, bed level changes, water level changes, temperature and/or water quality. Hereinafter, the numerical algorithms and solving methods for the water flow and sediment flow computation are summarized.

4.1.2 Water Flow Calculation

Navier-Stokes Equations
The Navier-Stokes equations (see equation 2.1) are used to obtain the flow velocities and pressure field in a turbulent flow. In SSIIM, they are solved on a three-dimensional, non-orthogonal grid. The default algorithm in SSIIM neglects the transient term. For transient calculations the user can include this term by setting a time step and the number of inner iterations for each iteration. Also the gravity term is not included in the standard solution of the Navier-Stokes equations in SSIIM. The user can include gravity in case of free-surface calculations, e. g. for modeling spill ways and flood waves with steep fronts.

Discretization
The partial differential Navier-Stokes equations can not be solved by analytical methods. Therefore, numerical methods are required which deliver approximate solutions of the differential equations. The numerical methods comprise an algorithm that discretizes the governing differential equations in space and time and therefore provides an approximate solution. Several methods for space discretization can be applied. The three classical used discretization methods in computational fluid dynamics are the finite volume method (FVM), the finite difference method (FDM) and the finite element method (FEM):

- The FVM solves the partial differential equations in the form of discrete algebraic equations. The model domain is decomposed into a number of finite control volumes, where the variable (e. g. velocity, pressure) is calculated at a node inside each control volume cell. The temporal change of a variable in a cell is a function of the variable in the neighbouring cells. It is quantified by balancing the fluxes through the volume surfaces and the sources/sinks inside the volume. Since the flux entering a given volume is identical to that leaving the adjacent volume, the FVM satisfies the conservation laws.
- The FDM solves the partial differential equations by approximating them with difference equations. Finite difference expressions approximate the derivative terms in the partial differential equations by means of Taylor series expansion around grid points.
- The FEM subdivides a whole domain into smaller subdomains, so called finite elements. By using specific weight functions at each element node, approximated values for the requisite flow variables are calculated.

SSIIM uses the finite volume method for the spatial discretization on a three-dimensional grid. A main advantage of the FVM is its application for unstructured and complex grids. There are a number of different discretization schemes available for the control-volume approach. The approaches differ in how the concentration on a cell surface is calculated. A first-order (POW) or a second-order (SOU) upwind scheme are implemented in SSIIM. Using the first-order upwind scheme, the variable values on the cell surfaces are estimated from the upstream cell. The concentration in the cell is computed as a function of the weighted average concentrations in the six direct neighbouring cells. The second-order upwind scheme uses twelve surrounding cells. The use of the POW scheme is expected to give more stable solution, but may result in too diffusive results. The second-order upwind scheme avoids the false diffusion, but may tend to overestimate occuring eddies. Within this work, the first-order scheme was used for all calculations. The numerical methods are described in detail by Olsen (1991).

For transient computations, two approaches can be used for time discretization: the explicit and implicit method. For the explicit method, the value at a node at time $n+1$ is computed from the known values at

nodes from the previous time step n. The implicit method calculates the value at a node at time $n+1$ from known values at nodes from the previous time step n and additionally from unknown values at the neighbouring nodes at time $n+1$. The implicit method gives more stable results, especially when using longer time steps. The explicit solution is easier to solve than the implicit method. In SSIIM an implicit time discretization is implemented.

Turbulence Modeling
A turbulent flow regime represents an essential phenomenon in natural rivers or hydraulic systems, which is characterized by a random and chaotic flow and the formation of eddies of various scales (see chapter 2.1.2). Since turbulent flows show very complex properties, they are difficult to model. Three common turbulence models are used in CFD modeling which are listed briefly below:

- Direct numerical simulation (DNS): the Navier-Stokes equations are solved directly without modeling. The whole range of turbulent scales is resolved, from the smallest dissipative scales (Kolmogorov microscale) up to the macroscales, which contain most of the kinetic energy. Since all spatial and temporal scales of turbulence must be resolved in the computational mesh, DNS requires a very high temporal and spatial three-dimensional discretization. The limitations of DNS are therefore the treatment of simple geometries and a low Reynolds number.

- Large eddy simulation (LES): only the unsteady large scales of turbulence are resolved explicitly in the Navier-Stokes-equations. The impact of the small scales is approximated by using a separate subgrid-scale model. The subgrid-scale model simulates the energy transfer between the large scale, directly resolved eddies and the small scale, not modeled eddies. LES is suited for the modeling of complex flows with large-scale turbulence structures. It is a compromise between DNS and RANS concerning modeling effort and model accuracy.

- Statistical turbulence models: the Navier-Stokes equations are considered as time-averaged equations, known as Reynolds Averaged Navier-Stokes (RANS) equations. Reynolds decomposition means, that the instantaneous quantities are separated into a mean (time-averaged) component and a velocity fluctuation component (see figure 2.1 in chapter 2.1.2). The resulting time-averaged Navier-Stokes equations will contain additional turbulent stress terms, known as Reynolds stress terms. Statistical turbulence models are used to model these Reynolds stresses. There are two different approaches for modeling the Reynolds stresses, the Reynolds stress models and the eddy-viscosity models. Since Reynolds stress models are computationally intensive, eddy-viscosity models are used frequently in engineering CFD modeling. These models simulate the eddy-viscosity ν_t, which is introduced with the Boussinesq approximation. The eddy-viscosity is no material property, but depends on the turbulent flow condition. Different models exist to calculate this quantity, which vary in the number of additional differential equations to be resolved. A common used statistical turbulence model is the k-ϵ model, which requires two more equations for modeling the eddy-viscosity. The k-ϵ model calculates the turbulent eddy-viscosity as:

$$\nu_t = C_\mu \frac{TKE^2}{\epsilon} \tag{4.1}$$

  where

ν_t	turbulent eddy-viscosity	$[m^2/s]$
C_μ	empirical constant	[–]
TKE	turbulent kinetic energy	$[m^2/s^2]$
ϵ	turbulent dissipation rate	$[m^2/s^3]$

The value for the empirical constant C_μ is usually set to $C_\mu = 0.09$. The turbulent kinetic energy and the energy dissipation are modeled through two additional differential equations. They can be found in the User's Manual (Olsen, 2014).

The k-ϵ model is the most frequent model in CFD modeling, because of its strength in the universal applicability. In SSIIM, the k-ϵ model is the default turbulence model and was used for all conducted computations within this work.[1]

Pressure and Wall Laws

To find the unknown pressure term in the Reynolds-averaged Navier-Stokes equations, SSIIM uses the Semi-Implicit Method for Pressure-Linked Equations (SIMPLE) (Patankar, 1980) as the default method. The basic principle is to guess a pressure field in the computation domain field. The following continuity defect is used to obtain an equation for the pressure correction. In the next iteration step, this pressure correction equation is then added to the pressure equation, so that the continuity is satisfied. When changes in the water and bed levels were calculated within this work, an adaptive grid was used to model these changes. The grid was then moved vertically according to the computed free water surface and bed level changes. The free surface was computed using the pressure computed with the SIMPLE method when solving the Navier-Stokes equations.

In natural rivers which often are characterized by hydraulic rough conditions, the velocity gradient towards the wall is usually very steep. The definition of boundary layer conditions is therefore an important factor in CFD modeling. A large number of grid cells would be required to resolve the velocity gradients. Hence, instead wall laws are used for cells close to the boundary. Wall laws describe the velocity profile between the wall and the centre of the cell closest to the boundary. The default wall law in SSIIM uses an empirical logarithmic formula for rough boundaries (Schlichting, 1979):

$$\frac{U(y)}{u_*} = \frac{1}{\kappa} ln \left(\frac{30y}{k_s} \right) \tag{4.2}$$

where

$U(y)$	flow velocity at a distance y from the wall	$[m/s]$
u_*	shear velocity	$[m/s]$
κ	von Karman's constant	[–]
y	distance between the wall and the centre of the bed cell	[m]
k_s	wall roughness	[m]

[1] In SSIIM also other turbulence models are implemented and can be specified by the user, for example the k-ω model.

The von Karman's constant κ is equal to 0.4, and the wall roughness k_s is usually equivalent to the maximum sediment size. This wall law is valid for $(u_* k_s)/\nu > 70$. In case of smooth walls, a two-layer wall law is used:

$$\frac{U(y)}{u_*} = \frac{1}{\kappa} ln\left(\frac{y u_*}{\nu}\right) \qquad \text{for } \frac{y u_*}{\nu} > 11 \tag{4.3a}$$

$$\frac{U(y)}{u_*} = \frac{y u_*}{\nu} \qquad \text{for } \frac{y u_*}{\nu} < 11 \tag{4.3b}$$

Smooth wall laws are valid for $(u_* k_s)/\nu < 5$ (Nikuradse, 1933). Within this work, a smooth wall law formulation was used for all calculations in the annular flume with SSIIM 1 (see chapter 5). Rough boundaries were used for all calculations in the Iffezheim reservoir with SSIIM 2 (see chapter 6).

4.1.3 Sediment Transport Calculation

Bed Load Transport

For modeling bed load transport several empirical bed load transport formula are available. They are all developed under different flow conditions and for different sediment characteristics by conducting flume experiments. Hence, these formulations give different results for each case study and should, as a consequence, be used within their range of validity. For the default case, SSIIM calculates bed load transport according to the formula by van Rijn (1984a) which was developed for mostly uniform sand particles[2]:

$$q_{bed,i} = 0.053 \frac{\left[\frac{\tau_b - \tau_{c,i}}{\tau_{c,i}}\right]^{2.1}}{\left[D_i \left(\frac{(\rho_g - \rho_w) g}{\rho_w \nu^2}\right)^{1/3}\right]^{0.3}} \tag{4.4}$$

where

q_{bed}	dimensionless bed load transport	[-]
τ_b	bed shear stress	[N/m²]
τ_c	critical bed shear stress for erosion	[N/m²]
D	particle size	[m]

In the default SSIIM algorithm, the bed shear stress τ_b is calculated from the turbulent kinetic energy TKE:

$$\tau_b = \sqrt{C_\mu} \cdot \rho_w \cdot TKE = 300 \cdot TKE \tag{4.5}$$

The turbulent kinetic energy TKE is computed by the k-ϵ model, with the constant $C_\mu = 0.09$ (see above). The critical bed shear stress $\tau_{c,i}$ for movement of the bed particles is computed by using a parameterization of the Shields (1936) curve.

Suspended Load Transport

Suspended load is calculated by solving the transient advection-diffusion equation 3.1 for each sediment size class i separately. In SSIIM, the diffusion coefficient D_{turb} is equal to the turbulent eddy viscosity ν_t which is calculated from the k-ϵ turbulence model. An empirical formula for the equilibrium sediment

[2] In SSIIM it is also possible to use different bed load sediment functions, e. g. the Wu (1969) or Meyer-Peter and Müller (1949) formula.

concentration $C_{bed,i}$[3] close to the bed is specified as boundary condition for the sediment transport of cohesionless sediment material, based on the equation of van Rijn (1984b):

$$C_{bed,i} = 0.015 \frac{D_i}{a_{ref}} \frac{\left[\frac{\tau_b - \tau_{c,i}}{\tau_{c,i}}\right]^{1.5}}{\left[D_i \left(\frac{(\rho_g - \rho_w) g}{\rho_w \nu^2}\right)^{1/3}\right]^{0.3}} \tag{4.6}$$

where

C_{bed}	equilibrium sediment concentration close to the bed	$[\mathrm{m^3/m^3}]$
a_{ref}	distance from the bed to where $C_{bed,i}$ is computed (half the bed cell height)	[m]

If erosion of cohesive fine sediments in the silt and clay fraction is computed to account for cohesion, the critical shear stress computed by Shields (1936) can be increased by a correction factor. Alternatively, algorithms can be coded which explicitly calculate the critical shear stress for cohesive sediments. Model approaches which calculate the critical shear stress of cohesive sediments can be found for example in Mitchener and Torfs (1996), Sanford and Maa (2001) or Ternat et al. (2008).

In SSIIM it is possible to convert the calculated concentration from van Rijn (1984b) into a sediment pick-up (entrainment) rate. However, is has to be considered that this concentration is derived for cohesionless sediments. With respect to an improved physical system description, in this work the equation from van Rijn (1984b) was replaced by using the equation of Ariathurai and Arulanandan (1978) which was originally derived for calculating the erosion rate of cohesive sediments. By transforming the originally erosion rate equation into an equation for calculating the equilibrium sediment concentration, the following equation was implemented in SSIIM (beddll.dll):

$$C_{bed,i} = \frac{M_e \left(\frac{\tau_b}{\tau_{c,i}} - 1\right)}{w_{s,i} \cdot \rho_g} \tag{4.7}$$

where

M_e	erosion coefficient	$[\mathrm{kg/m^2 s}]$

In literature different values for the dimensioned erosion coefficient M_e can be found, as it is a site- and sediment-specific empirical parameter. Spork (1997) sets M_e to $2.7 \cdot 10^{-5}$, whereas Amos et al. (1996) define higher values of M_e in the order between $4.9 \cdot 10^{-4} - 4.0 \cdot 10^{-3}$. In this work, the erosion coefficient was set to $M_e = 2.7 \cdot 10^{-4}$. The resulting sediment pick-up rate $F_{R,i}$ of size class i is then computed by the following equation:

$$F_{R,i} = C_{bed,i} \cdot w_{s,i} \cdot \rho_w \tag{4.8}$$

where

$F_{R,i}$	sediment pick-up rate	$[\mathrm{kg/m^2 s}]$

[3] In SSIIM the sediment concentrations are given in volume concentrations instead of mass concentrations (for example, a volume concentration of $0.001\,\mathrm{m^3/m^3}$ with a specific sediment density of $2650\,\mathrm{kg/m^3}$ is equivalent to a mass concentration of $0.001 \cdot 2650 = 2.65\,\mathrm{g/l}$).

Equation 4.8 is only used in the case that the actual bed shear stress τ_b exceeds the critical shear stress τ_c. If the bed shear stress is smaller than the critical shear stress, the sediment concentration C_{bed} at the bed gets zero and no entrainment rate is calculated. In this case only the deposition rate $D_{dep,i}$ for each size class is calculated as the product of the settling velocity $w_{s,i}$ times the sediment concentration C_i.

The bed level changes Δz are computed based on the computed sediment deposition rate and the pick-up rate for all the size fractions:

$$\Delta z = \sum \left(w_{s,i} C_i - F_{R,i} \right) \Delta t / r \tag{4.9}$$

where

Δz	bed level changes	[m]
Δt	time step	[s]
r	conversion factor between volume of sediment particles and volume of deposits on the bed	[kg/m³]

The equations above show, that SSIIM in general is able to calculate fine sediment transport and deposition by solving the advection-diffusion equation for each sediment size fraction. In previous studies, particle deposition in a laboratory flume was measured and computed in SSIIM (Olsen and Skoglund, 1994). However, the particles were too coarse for flocculation to occur. If fine sediments are modeled in SSIIM, each size fraction has to be characterized by a predefined particle diameter, a respective sediment concentration and settling velocity. Each size class interacts independent of the other fractions and no aggregation and disaggregation mechanisms between the particles can occur (see figure 4.1, above model).

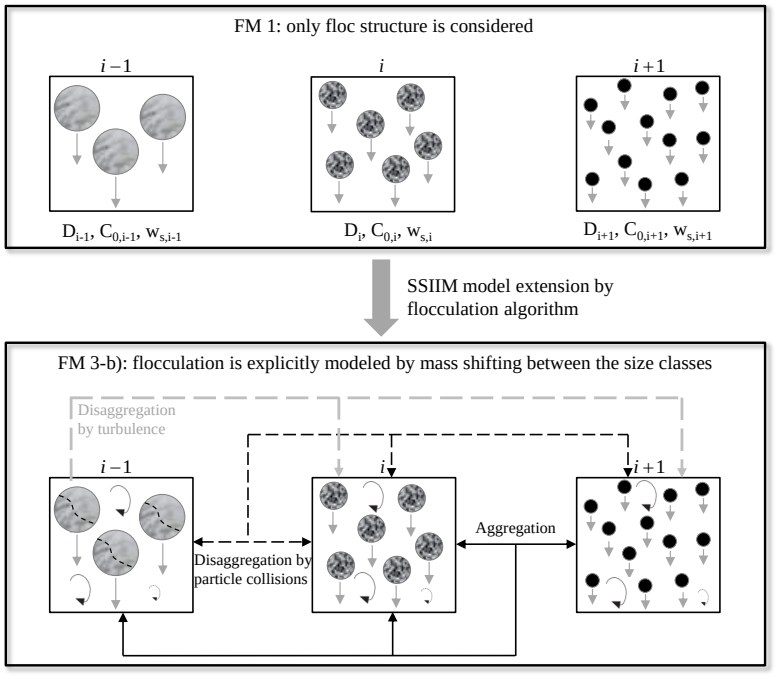

Figure 4.1: SSIIM model extension by an explicit flocculation model.

In the case that flocculated sediment particles should be modeled, flocculation effects can only be modeled indirectly by taking into account the floc structure in the settling velocity formula (e. g. by using the

Winterwerp (1998) settling velocity equation). This simplified flocculation approach would correspond to flocculation model FM 1 described in chapter 3.3. However, as already mentioned in chapter 3.3, this model approach considers only one parameter, the floc structure. Any interactions in terms of aggregation or disaggregation between the particles are not simulated. Therefore, the objective of this work was to extend SSIIM by a physically realistic flocculation model which allows an explicit modeling of floc growth and floc break-up by particle mass shifting between the size classes (denoted as flocculation model FM 3 in chapter 3.3). On the basis of the comparative studies of different flocculation models in chapter 3.3, a size-class based model derived by McAnally (2000) was chosen to be implemented in SSIIM. The flocculation algorithm allows aggregation and disaggregation due to particle collisions and fluid shear leading to a shifting of sediment mass between the classes. The individual mathematical equations and physical descriptions of the implemented flocculation model are presented in the next section.

4.2 Implemented Flocculation Algorithm

The flocculation model based on McAnally (2000) was originally derived in order to develop an improved, analytic physics-based representation of aggregation and disaggregation processes, taking into account sediment and flow characteristics in estuarial waters. In the following, the main mathematical terms and physical descriptions of the flocculation model are presented. In order to get a better overall understanding of the flocculation algorithm, some of the concepts and formulations presented in the previous chapters are repeated. For a full overview and detailed consideration of the flocculation model the reader is referred to the original source from McAnally (2000).

The presented flocculation algorithm has been implemented in SSIIM by the use of the programming language C++. The numerical flocculation algorithm is embedded in a DLL (Dynamic Link Library) and therefore represents an extension of SSIIM (flocdll.dll).

4.2.1 Sediment Particle Characteristics

McAnally (2000) uses the sediment particle mass as the fundamental descriptor of a sediment particle. Various other parameters can be determined from the particle mass property, as described below. The continuous spectrum of particle sizes, ranging from the largest flocs/aggregates of size class $j = 1$ to the smallest, primary grains of size class $j = s$, is described by a finite set of discrete mass class intervals, defined as follows:[4]

Class index:	$j = 1$ to s	
Class lower limit on particle mass:	$M_j(lower)$	$(^{kg}/_{particle})$
Class upper limit on particle mass:	$M_j(upper)$	$(^{kg}/_{particle})$

The total sediment mass within each class can change with time by different processes (see figure 4.2):

1. Increase or decrease from fluxes by advection and diffusion.

[4] Due to technical reasons within the implementation in SSIIM, in this work size class $j = 1$ was defined containing the largest particles. In the origin work from McAnally (2000) however, size class $j = 1$ was defined containing the smallest particles.

2. Increase from fluxes by erosion or decrease from fluxes by deposition.
3. Increase by aggregation of particles from smaller classes.
4. Increase by disggregation of particles from larger classes.
5. Decrease by aggregation or disaggregation of particles within the class.

Wheras items 1 and 2 are calculated within the sediment flow calculation by using the advection-diffusion equation (see equation 3.1), items 3 to 5 are computed by the flocculation algorithm.

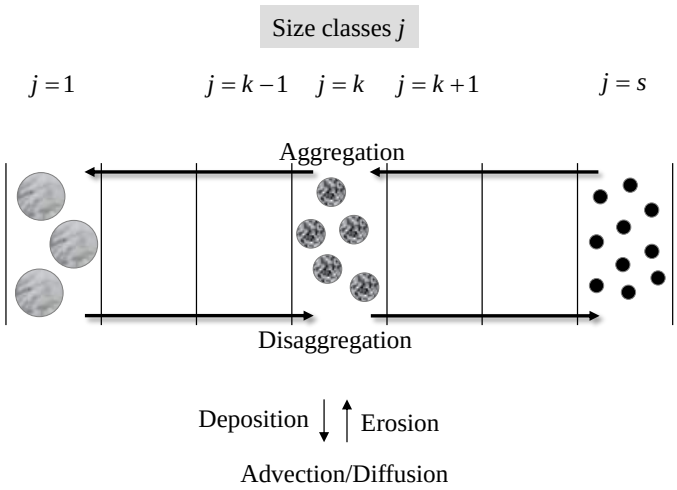

Figure 4.2: Sediment mass fluxes within size classes j by aggregation and disaggregation, deposition/erosion, advection and diffusion (modified by McAnally (2000)).

Based on predefined sediment size classes, represented by the particle diameter D_j, the density of each particle size class ρ_j can be determined by the following equation:

$$\rho_j = \text{smaller of } \begin{cases} \rho_g \\ \rho_w + B_\rho(C,G_c,S,T) \left(\frac{D_g}{D_j}\right)^{3-n_f} \end{cases} \tag{4.10}$$

The particle density of the smallest and compact primary particles of size D_g in size class $j = s$ corresponds to the sediment grain density ρ_g ($= 2650\,\mathrm{kg/m^3}$). The density of larger, less dense particles in size classes $j < s$ is computed on the basis of the particle diameter D_j, the fractal dimension n_f ($= 1.0 - 3.0$) and the empirical sediment- and flow-dependent density function $B_\rho(C,G_c,S,T)$. The function depends on the sediment concentration C, the turbulence parameter G_c (which accounts for collision-inducing flow forces), the salinity S and the temperature T. Since B_ρ is difficult to measure and has not yet been quantified, McAnally and Mehta (2000) set a theoretical value of $B_\rho = 1650\,\mathrm{kg/m^3}$. In that case, the particle density depends only on the particle size and the floc structure expressed by the fractal dimension. From equation 4.10, it can be seen, that an increase in particle size leads to a decrease in the particles density, since ongoing flocculation is related with more water-filled pore space. On the other hand, higher values of the fractal dimension cause a higher floc density, as they imply a more compact and massive floc structure.

The (average) sediment particle mass M_j ($^{\mathrm{kg}}/_{\mathrm{particle}}$) of each size class is determined from the particle density and the (average) particle size, assuming that all particles are approximately spherical:

$$M_j = \rho_j \cdot \pi \cdot \frac{D_j^3}{6} \tag{4.11}$$

As mentioned above, each (average) particle mass M_j is represented through a mass class interval, which contains particles with the smallest particle mass $M_j(lower)$ and the largest particle mass $M_j(upper)$ of this class. Based on a simple linear mean formulation of M_j, the mass class interval is calculated by:

$$M_j = \frac{M_j(lower) + M_j(upper)}{2} \tag{4.12}$$

This allows the calculation of the class limits based on the particle mass:

$$M_j(upper) = \frac{M_j + M_{j-1}}{2} \tag{4.13a}$$

$$M_j(upper) = M_{j-1}(lower) \tag{4.13b}$$

The settling velocity for each class is computed using the formula of Winterwerp (1998), a modified Stokes' settling expression which considers flocs as fractal objects. It is computed for each size class and depends on floc size and floc density, the latter is calculated according to equation 4.10. Winterwerp's settling velocity for spherical fractal flocs is given in equation 2.27. Transformation of this equation and substitution of D_f by D_j, yields the following formula for the settling velocity:

$$w_{s,j} = \frac{D_j^2}{18\nu} \cdot g \cdot \frac{\Delta\rho_j}{\rho_w} \tag{4.14}$$

where $\Delta\rho_j$ is the density difference of the respective floc in class j and water:

$$\Delta\rho_j = \rho_j - \rho_w \tag{4.15}$$

The simple settling velocity equation does not take into account sediment concentration and flow characteristics, since the flocculation algorithm considers these effects on a class-by-class basis.

The particle strength τ_j, i. e. the resistance to disaggregate due to collision-induced stresses and fluid shear, is given by an adaption of equation 3.13:

$$\tau_j = B_\tau(C,G_c,S,T) \left(\frac{\Delta\rho_j}{\rho_w} \right)^{\frac{2}{3-n_f}} \tag{4.16}$$

where B_τ replaces the coefficient K_F in equation 3.13. B_τ is an empirical sediment- and flow-dependent stress function, similar to the coefficient B_ρ, mentioned in equation 4.10. Since no explicit formulation is known for B_τ, the coefficient is usually fit to experimental data by calibration. In case of missing measured data, McAnally and Mehta (2000) set B_τ to a constant value ranging from order 1 to 10^4 $^{\mathrm{N}}/_{\mathrm{m}^2}$. The wide range of values shows, that the strength of a fractal floc can vary by several orders of magnitude. Equation 4.16 illustrates that the floc structure, expressed by the fractal dimension n_f, also affects the

particles' strength. Compact particles with a high fractal dimension show a high yield strength, whereas lower values for n_f imply weaker particles/flocs, which can be broken up more easily due to flow shear or collision-induced shear stresses.

The sediment properties mentioned above are computed at the beginning of the flocculation modeling and remain constant during the entire model run.

4.2.2 Mass Fluxes due to Particle Collisions and Flow Shear

Number of Colliding Particles

Collisions of two or more particles either lead to aggregation if the collision-induced stresses are less than the yield strengths of the colliding particles, or contribute to disaggregation of one or both particles if the collision-induced stresses exceed the particles' yield strengths. Floc break-up can also occur due to flow shear without any particle interaction. Most flocculation models consider collisions of two particles. McAnally (2000) analyzed collisions of two, three and four particles. The explicit formulations for morebody collisions aimed to reproduce flocculation processes physically more correct than if they are omitted. McAnally (2000) found, that the frequency of three-body collisions in turbulent flow is not larger than 2 % of the frequency of two-body collisions for floc diameters up to 1 mm and sediment concentrations up to 10 g/l. For smaller flocs at lower sediment concentrations, this frequency decreases rapidly. Four-body collisions will contribute to an even smaller fraction (1 % or less of the number of three-body collisions). The calculations showed that three-body collisions make only a small contribution to the total movement of sediment mass among the classes during the early stages of aggregation. However, near equilibrium size, three-body collisions play a greater role, since disaggregation of particles becomes important.

McAnally (2000) carried out calculations with two-body collisions only and with additional three-body collisions. For both calculations the same boundary conditions were applied. It was shown, that both calculations resulted in essentially identical growth rates during the first quarter-hour, then they diverged. Also, both calculations achieved nearly the same equilibrium diameter. However, the calculation with the two-body collisions achieved equilibrium more rapidly, since the calculation with additional three-body collisions contributes more to disaggregation than to aggregation. As a result, if the equilibrium diameter or the aggregation rate in the initial stages of flocculation should be examined, two-body collisions will be sufficient. The mass change rate associated with four-body and higher collisions was not calculated, but is expected to be a minor factor in the aggregation rate (McAnally, 2000).

Apart from the studies of McAnally (2000), only a few studies exist about more-body collisions. The analyses from Lick and Lick (1988), Burban et al. (1989), and Lick et al. (1992) indicate, that disaggregation due to three-body collisions is required in order to explain an observed decrease in median floc size as the sediment concentration increases.

Based on the studies considering three-body collisions and higher order collisions, the influence of these collisions is assumed to play a minor role in flocculation processes. Thus, with respect to less computation time, within this work only two-body collisions were modeled.

Collision Frequency

Depending on a predefined mass concentration of particles in each class C_j ($^{kg}/_{m^3}$), the initial number concentration of particles n_j ($^{1}/_{m^3}$) is approximated via the equation:

$$n_j = \frac{C_j}{M_j} \tag{4.17}$$

The collision efficiency N_{ik} ($^{1}/_{m^3 \cdot s}$), i. e. the number of collisions involving two particles from size class i and k is given by:

$$N_{ik} = \alpha_a(\beta_{B,ik} + \beta_{S,ik} + \beta_{D,ik})n_i n_k \tag{4.18}$$

where α_a is the weight fraction of suspended sediment that is strongly cohesive (see chapter 3.2.1). $\beta_{B,ik}$, $\beta_{S,ik}$ and $\beta_{D,ik}$ express the collision frequency functions for the processes Brownian motion, fluid shear and differential settling (see chapter 3.2.1). According to equations 3.9, 3.10 and 3.11, McAnally (2000) points out the following modified collision frequency functions:

$$\beta_{B,ik} = \left(\frac{2}{3}\frac{\kappa_B T F_c}{\mu}\right)\frac{(D_i + D_k)^2}{D_i D_k} \tag{4.19}$$

$$\beta_{S,ik} = \left(\frac{\pi F_c^2}{4}\sqrt{\frac{2}{15\pi}}\right)\sqrt{\frac{\varepsilon}{\nu}} \cdot (D_i + D_k)^3 \tag{4.20}$$

$$\beta_{D,ik} = \left(\frac{\pi F_c^2}{4}\right)(D_i + D_k)^2 \cdot |w_{s,i} - w_{s,k}| \tag{4.21}$$

The functional form of the three equations represents a modified concept of collisions efficiency expressed in equations 3.9, 3.10 and 3.11. McAnally (2000) defines $F_c\,(-)$ as a new non-dimensional correction factor for the "collision sphere diameter". Figure 4.3 illustrates that in case of two spherical particles of size class i and k. These particles will encounter if the center of particle k intrudes within the collision sphere of particle i. The collision sphere diameter will be reduced when taking into account the effect of water and ions which are trapped between converging particles and resist collision (McAnally and Mehta, 2000). F_c represents this reduction in the collision sphere diameter by taking values between 0 and 1. A reduced collision sphere of diameter decreases the collision efficiency. This effect is represented by including the correction factor F_c in equations 4.19, 4.20 and 4.21.

In fact, the collision diameter function F_c depends on the suspension size distribution, which changes over the entire period of flocculation processes. A representative value for F_c is calculated according to the following equation:

$$F_c = 0.987 f_c \Pi_c^{0.0975} \tag{4.22}$$

where the parameter $f_c\,(-)$ accounts for the variation of F_c and ranges from 0 to 1. McAnally and Mehta (2000) give an operational form for f_c (not given here) as a function of sediment concentration and fluid flow. The parameter was also observed to vary with the sediment characteristics, but has not been accomplished yet. Due to these uncertainties, McAnally (2000) considers f_c to be a placeholder equal to 1. In this work, f_c was assumed to be 1 as well, as the parameter is not yet fully defined and to reduce model complexity.

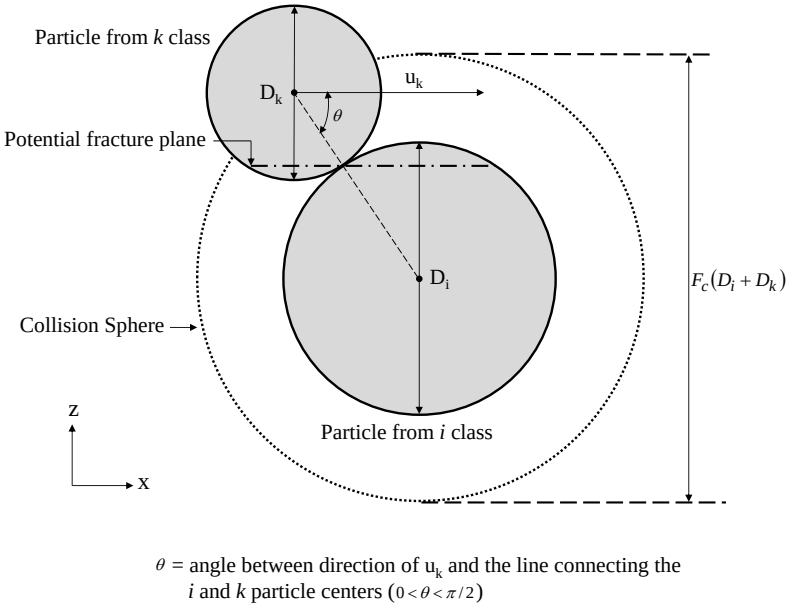

Figure 4.3: Two-body particle encounter of i and k class particles (modified from McAnally, 2000).

The non-dimensional term Π_c $(-)$ is given by:

$$\Pi_c = \left[\frac{\frac{D_g}{D_1} \cdot \frac{S}{S_0} \left(1 - 0.875 \frac{T}{T_0}\right) \frac{CEC}{CEC_0}}{\frac{\Delta\rho_i D_i^3}{\Delta\rho_k D_k^3} \cdot \frac{u_i (D_i + D_k)}{\nu}} \right] \tag{4.23}$$

Π_c takes into account the ionic composition of the water and particle related characteristics. Equation 4.23 depends on several parameters: the grain diameter D_g, the reference diameter D_1, the salinity of the water S, the reference salinity S_0, the fluid temperature T (degrees Celsius), the reference temperature T_0, the sediment cation exchange capacity CEC, the reference cation exchange capacity CEC_0 and the i class particle velocity u_i relative to the k particle. The multiplicity of parameters indicate the difficulty to predict the collision efficiency of colloidal suspensions. In this work, the term of Π_c was simplified by setting the enumerator of the equation to 1. In that case, Π_c depends on the densities and particle sizes of the two colliding particles i and k, the kinematic viscosity of the water ν and the relative velocity u_i. u_i $[\mathrm{m/s}]$ is given by the sum of the three velocities.:

$$u_i = \begin{cases} \frac{\kappa_B T}{3\pi\mu D_i D_k} & \text{Brownian Motion} \\ \frac{D_i + D_k}{2} \sqrt{\frac{2\varepsilon}{15\pi\nu}} & \text{Flow Shear} \\ |w_{s,i} - w_{s,k}| & \text{Differential Settling} \end{cases} \tag{4.24}$$

Stresses on Particles

The shear stress experienced by the k aggregate during a collision with a particle from size class i is given by :

$$\tau_{ik,k} = \frac{8 u_i^2 M_i M_k}{\pi F_p D_k^2 (D_i + D_k)(M_i + M_k)} \tag{4.25}$$

where F_p (–) is the relative (non-dimensional) depth of interparticle penetration during a collision. The value of F_p is a function of particle momentum, particle density, and the number and strength of interparticle bonds of the colliding particles. It is greater than 0 and less than 0.5. As an exact value for F_p is not available, it is assumed to be ≈ 0.1 based on analyses by Krone (1963). The shear stress for the i class particle is obtained by replacing ${D_k}^2$ by ${D_i}^2$. Equation 4.25 shows, that the collision-induced shear stress increases with increasing relative velocity u_i, and therefore with increasing energy dissipation rate ϵ (see equation 4.24). The functional form of equation 4.25 is derived by a straightforward application of Newton's second law. A detailed derivation of equation 4.25 can be found in McAnally (2000).

The collision-induced shear stress is the smallest for two given particles, if the collision velocity vector passes near the center of both particles, i. e. $\theta = 0$. If the angle θ increases (see figure 4.3), the shear stresses increases as well, since the same collision force is applied over a smaller shear surface. However, due to present insufficient knowledge about particle strength, an approximated value of $\theta = \pi/4$ is assumed.

The flow-induced shear stresses on a particle in turbulent flow are calculated according to the approach proposed by Winterwerp (1998) (see equation 3.21)[5]:

$$\tau_u \approx \mu \sqrt{\frac{\epsilon}{\nu}} \tag{4.26}$$

McAnally (2000) concluded from analyses that both flow-induced shear stresses and collision-induced shear stresses play an important role within the range of particle sizes and flow intensities typical of estuarial flows. However, collision-induced shear stresses are supposed to be more important for larger particles and higher dissipation rates.

Flow-induced Disaggregation

A i-class particle will break-up by flow-induced shear stresses (without interaction with other particles), if the turbulence-induced shear stresses τ_u exceed the particle strength τ_i. The particle of mass M_i will disaggregate into two particles of masses $M_{l1'}$ and $M_{l2'}$, which are not automatically of equal size.

$$\text{If } \{\tau_i < \tau_u\} \quad M_i \Rightarrow \begin{cases} M_{l1'} = M_i - \Delta M_i^0 \\ M_{l2'} = \Delta M_i^0 \end{cases} \tag{4.27}$$

As a consequence of mass shifting due to disaggregation, the following changes in concentration ΔC ($\mathrm{kg/m^3}$) can be calculated:

$$\Delta C_i = -\, M_i n_i \tag{4.28a}$$

$$\Delta C_j = +\, p_j \, (l = i : s) \, M_i n_i \qquad j = i \text{ to } s \tag{4.28b}$$

The mass of the broken particles is removed from the original size class i and is distributed among this size class i and all smaller size classes ($j = i$ to s) according to a probability mass function p. The probability mass function is described below. Equation 4.28 shows, that the break-up process by fluid shear is modeled as a time independent process. If the shear strength of the i-class particle is exceeded by fluid shear stresses, *all* particles from size class i will be disaggregated. However, this does not imply that all particle

[5] In the origin work from McAnally (2000) flow-induced shear stresses according to Krone (1963) are assumed (see equation 3.18).

mass is removed from size class i, since the broken mass is distributed among this broken size class and all smaller size classes.

Collision Outcomes due to Two-body Collisions

If two particles i and k collide, different types of collision outcomes can be described (see figure 4.4). The collision outcomes are based on both, the assumption that every collision results in cohesion at the particle contact point and it is supposed to split into two fragments, in case that a particle breaks after collision. By these assumptions there is a limited set of possible collision outcomes, which are categorized by the number of colliding particles (= 2), whether aggregation only (A) or both aggregation and disaggregation (D) occur, and by the number of particles resulting from the collision ($1 - 3$).

In the following descriptions the class subscript notation represents the relative size of the colliding particles. Size class subscript k denotes the smaller colliding particle which is represented by a larger size class (e. g. $k = 5$). Size class subscript i denotes the larger particle which is represented by the smaller size class (e. g. $i = 2$). The configuration of size classes is shown in figure 4.2. Subscript j denotes the preselected size intervals and subscripts beginning with l denote a particle of any size.

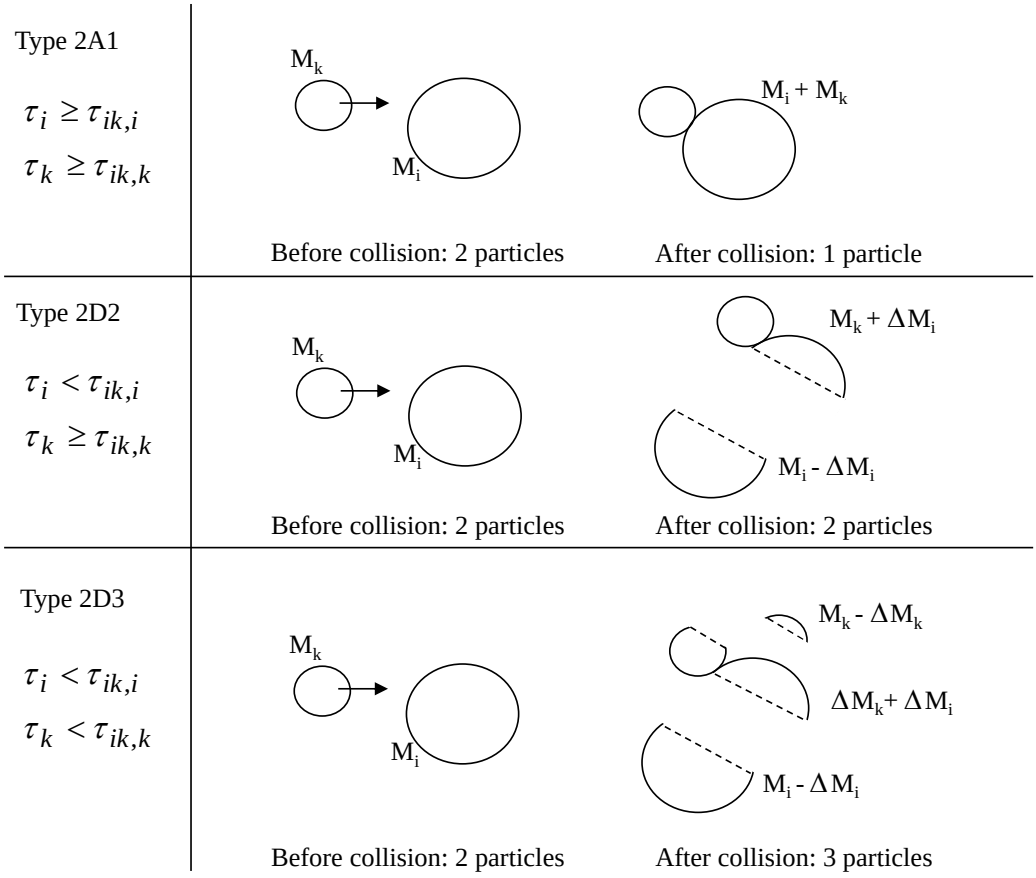

Figure 4.4: Collision outcomes depending on the strength of the particles τ_i and τ_k compared with the collision induced forces $\tau_{ik,i}$ and $\tau_{ik,k}$ (modified by McAnally (2000)).

Type 2A1
In a collision, in which both particles' yield strengths τ_i and τ_k are greater than the collision-induced shear stresses $\tau_{ik,i}$ and $\tau_{ik,k}$, these two particles will aggregate into one new larger particle. The mass of the new particle corresponds to the sum of the two colliding particles $M_i + M_k$. This set of condition is written as:

$$\text{If} \left\{ \begin{matrix} \tau_i \geq \tau_{ik,i} \\ \tau_k \geq \tau_{ik,k} \end{matrix} \right\} M_i \rightarrow M_k \Rightarrow M_{l'} = M_i + M_k \tag{4.29}$$

The new formed l' particle of mass $M_{l'}$ will not necessarily be equal to one of the representative class masses. The new particle's class index $j = l$ is that for which $M_{l'}$ is greater than the class lower limit and less or equal than the class upper limit. This is expressed as:

$$l = J\{i + k\} = \text{CLASS}\{M_j(\text{lower}) < (M_i + M_k) \leq M_j(\text{upper})\} \tag{4.30}$$

After the aggregation collision, mass of the i and k class particles will no longer exist in the classes and is therefore removed from these classes. The rate of mass concentration changes $\dot{C}\,(\mathrm{kg/m^3 s})$ for these classes is computed as follows:

$$\dot{C}_{j=i}(ik) = -M_i N_{ik} \tag{4.31a}$$
$$\dot{C}_{j=k}(ik) = -M_k N_{ik} \tag{4.31b}$$

The removed mass from size class i and k is subjected to size class j which is defined according equation 4.30:

$$\dot{C}_{j=l}(ik) = +(M_i + M_k) N_{ik} \tag{4.32}$$

Type 2D2
In case that only one particle's yield strength τ_i is less than the collision-induced shear stress $\tau_{ik,i}$, a fragment of the weaker particle breaks off while bonding to the non-breaking particle. In this case the smaller non-breaking particle will undergo aggregation, whereas the larger, weaker one will disaggregate. The collision will result in two new particles. This type of collision is written as:

$$\text{If} \left\{ \begin{matrix} \tau_i < \tau_{ik,i} \\ \tau_k \geq \tau_{ik,k} \end{matrix} \right\} M_i \rightarrow M_k \Rightarrow \begin{cases} M_{l1'} = M_i - \Delta M_i \\ M_{l2'} = M_k + \Delta M_i \end{cases} \tag{4.33}$$

where ΔM_i = mass of the fragment which breaks from the i particle and bonds with the k particle. The mass concentration change rates for the i and k size class particles are given accordingly to Type 2A1 in equation 4.31.

The angle in figure 4.3 can vary from 0 to $\pi/2$. By assuming the collision force at the point of contact and the inertial resistance at the center of the particles, the maximum shear stress will occur in a potential fracture plane ranging from the particle edge to its center. Thus, the broken fragment of the i class particle ΔM_i may imply a mass between zero (and therefore fall into the smallest size class $j = s$), and

a maximum of $M_i/2$. Over many collisions this mass will vary over that whole range and will average $3/16M_i$. The resulting average mass change rates are computed as follows:

$$\dot{C}'_1 = + \left(M_i - \frac{3}{16} M_i \right) N_{ik} \tag{4.34a}$$

$$\dot{C}'_2 = + \left(M_k + \frac{3}{16} M_i \right) N_{ik} \tag{4.34b}$$

The mass $M_{l1'}$ can be as small as $(M_i/2)$ and as large as M_i. Therefore, the particle of mass $M_{l1'}$ can fall into any class from $l1 = i$ to $J\{i/2\}$[6]. The mass $M_{l2'}$ will be larger than M_k and smaller than $(M_k + M_i/2)$. Thus, $M_{l2'}$ can fall into any class from $l2 = J\{k + i/2\}$ to k. Over many collisions the probability that either $M_{l1'}$ or $M_{l2'}$ will fall into any jth class is assumed to be the result of a random distribution of fragment sizes over their possible mass classes. Therefore the mass concentration change rate for each of the involved classes will be given by equation 4.31 plus:

$$\dot{C}_j(ik) = p_j \left(l1 = i : J\left\{\frac{i}{2}\right\} \right) \dot{C}'_1 + p_j \left(l2 = J\left\{k + \frac{i}{2}\right\} : k \right) \dot{C}'_2 \qquad j = 1 \text{ to } s \tag{4.35}$$

where $p_j(l = i1 : i2)$ is the probability mass function for the likelihood that C' will fall into a given class from $i1$ to $i2$. By assuming that all particle sizes within the range of possible sizes are equally likely, the probability mass function is given by:

$$p_j(l = i1 : i2) = \frac{M_j(upper) - M_j(lower)}{M_{i1}(max) - M_{i2}(min)} \tag{4.36}$$

i. e. a particle of mass M_l with a minimum possible size class $i1$ and a maximum possible size class $i2$ has a probability $p_j(l = i1 : i2)$ of falling into sediment class j, with $j \in [i1{:}i2]$.

Type 2D3

In case that both particles' yield strengths τ_i and τ_k are less than the collision-induced shear stresses $\tau_{ik,i}$ and $\tau_{ik,k}$, both particles will disaggregate. As a result three new particles are created, since the fragments ΔM_i and ΔM_k are bonded at the point of contact (see figure 4.4). Two particles will consist of the free fragments of the i and k particle and a third will consist of the other fragments of the i and k particle which are bonded at the point of contact. Using the same logic as for Type 2D2 the following equations are derived:

$$\text{If} \left\{ \begin{matrix} \tau_i < \tau_{ik,i} \\ \tau_k < \tau_{ik,k} \end{matrix} \right\} M_i \rightarrow M_k \Rightarrow \begin{cases} M_{l1'} = M_i - \Delta M_i \\ M_{l2'} = M_k - \Delta M_k \\ M_{l3'} = \Delta M_k + \Delta M_i \end{cases} \tag{4.37}$$

[6] In this case equation 4.30 is interpreted as $J\left\{\frac{i}{2}\right\} = \text{CLASS}\{M_j(\text{lower}) < (\frac{M_i}{2}) \leq M_j(\text{upper})\}$.

$$\dot{C}_1' = + \left(M_i - \frac{3}{16} M_i \right) N_{ik} \tag{4.38a}$$

$$\dot{C}_2' = + \left(M_k - \frac{3}{16} M_k \right) N_{ik} \tag{4.38b}$$

$$\dot{C}_3' = + \left(\frac{3}{16} M_i + \frac{3}{16} M_k \right) N_{ik} \tag{4.38c}$$

The mass concentration change per class is given by equation (4.31) plus:

$$\begin{aligned} \dot{C}_j(ik) = p_j \left(l1 = i : J \left\{ \frac{i}{2} \right\} \right) \dot{C}_1' + p_j \left(l2 = k : J \left\{ \frac{k}{2} \right\} \right) \dot{C}_2' \\ + p_j \left(l3 = J \left\{ \frac{i}{2} + \frac{k}{2} \right\} : s \right) \dot{C}_3' \end{aligned} \tag{4.39}$$

4.2.3 Size Distribution Changes Algorithm

The equations given above were implemented in SSIIM 3D and used to enable the calculation of the particle size distribution of a suspended fine sediment suspension by the processes aggregation and disaggregation, that are caused by two-body collisions and fluid shear. The procedure in SSIIM for calculating overall changes in particle size distribution caused by advection/diffusion and erosion/deposition while simultaneously considering flocculation processes can be summarized as follows (see figure 4.5):

1. Define particle sizes D_j (or particle mass) distribution:
   - ρ_j by equation (4.10) in each class j
   - M_j by equation (4.11) in each class j
   - $M_j(lower)$ and $M_j(upper)$ by equation (4.13) in each class j
   - $w_{s,j}$ by equation (4.14) with (4.15)
   - τ_j by equation (4.16) with (4.15)
2. Define an initial mass concentration distribution $C_j(t = 0)$ and calculate n_j by equation (4.17) in each class.
3. Conditions of the fluid and flow as functions of space and time: temperature T, fluid density ρ_w, viscosity ν and dissipation rate ε.
4. Particle concentration flux by size class $\dot{C}_{j,flux}$ from advection/diffusion and erosion/deposition (by advection-diffusion equation 3.1).
5. Flow-induced shear stresses on each particle class τ_u by equation (4.26).
6. Collision diameter function F_c by equation (4.22) (with equation (4.23) and (4.24)).
7. Number of two-body collisions, N_{ik}, and the associated collsion-induced shear stresses, τ_{ik}, by equations (4.18) and (4.25), respectively (with equations (4.19), (4.20) and (4.21)).

8. Aggregation/disaggregation mass concentration change rates from collisions, $\dot{C}_j(ik)$ by appropriate equations (4.29) to (4.39); the equations ared selected on basis of comparison of imposed stresses with particle strengths.

9. Dissaggregation mass concentration change rates from flow-induced stresses, $\dot{C}_{j,shear} = \Delta C_{j,shear}/\Delta t$ by equation (4.28), with Δt = time step.

10. The total rate of change of sediment mass concentration by size class:

$$\dot{C}_{j,sum} = \frac{\dot{C}_j(ik)}{2} - \dot{C}_{j,shear} + \dot{C}_{j,flux} \tag{4.40}$$

where division of the right hand side term by 2 compensates for recounting of the same collisions by the permutations of the i and k particles.

11. Calculation of the new mass concentration in each class, $C_{j,new}$, and the associated number concentration, $n_{j,new}$:

$$C_{j,new} = C_{j,old} + \dot{C}_{j,sum}\Delta t \tag{4.41}$$

$$n_{j,new} = \frac{C_{j,new}}{M_j} \tag{4.42}$$

12. back to 3.

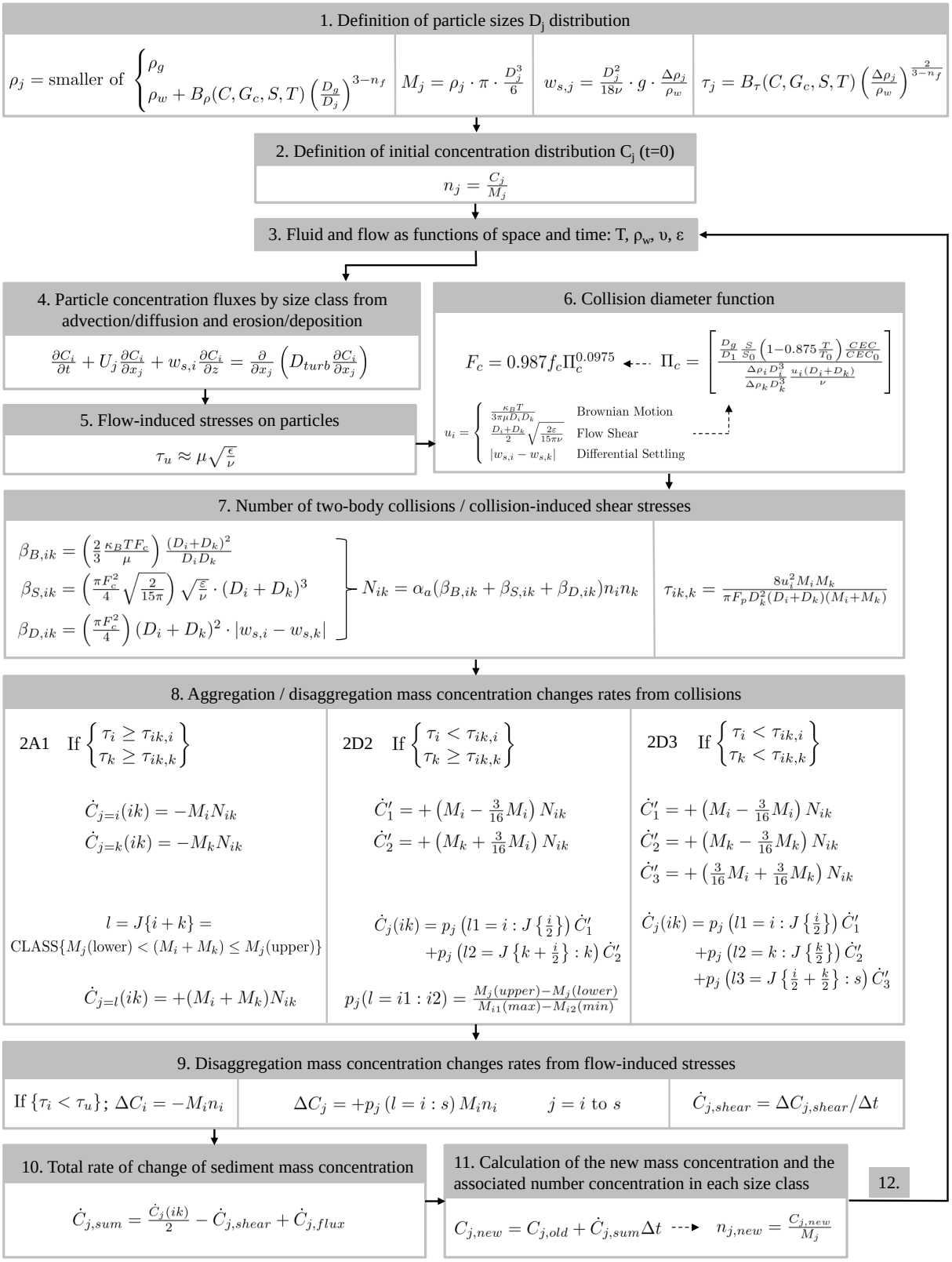

Figure 4.5: Procedure for calculating overall changes in particle size distribution in SSIIM by aggregation/disaggregation processes involving advection/diffusion and erosion/deposition.

5 Modeling Flocculation Processes in the Open Annular Flume

In the long-term, the objective of the implemented flocculation algorithm in SSIIM is to use it firstly for practical issues in sediment engineering to simulate cohesive sediment processes in rivers. Sediment transport and deposition are strongly influenced by the changing sediment particle properties induced by flocculation. Therefore, the model extension represents a major contribution towards a physically more realistic simulation of cohesive sediment transport. Secondly, the objective of the algorithm implementation is to use the model extension for research purposes in fluid dynamics, which focus explicitly on the small-scale processes aggregation and disaggregation. It was shown that flocculation is affected by several physico-chemical factors and that there is still a lack of understanding of the different involving mechanisms. The flocculation model could serve here as a research tool for further investigations on flocculation.

However, prior to any application of the flocculation algorithm on natural and complex water-sediment systems, a testing and validation of the algorithm by the use of measured data is required. For testing the flocculation algorithm, data of high temporal resolution are required. Therefore, usually, not field measurements are used, but data from laboratory experiments where boundary conditions are well known and constant over the whole experiment time.

Within this work, experimental data from previous studies in an open annular flume (Klassen, 2009) were used to validate the implemented flocculation algorithm in SSIIM. The application of the flocculation algorithm for the simulation of the laboratory experiments was conducted by modeling the temporal development of the measured floc sizes and the suspended sediment concentration. The question here is how accurately the measured laboratory data in the open annular flume can be simulated. The implemented flocculation algorithm is based on several empirical calibration coefficients depending on the sediment and flow characteristics. These model coefficients often are difficult to parameterize due to missing measured data or as a consequence of the wide range of values. In order to evaluate the uncertainty of these parameters on the model results, sensitivity analyses are essential and indispensable for further applications of the flocculation algorithm in sediment engineering. The following numerical investigations focus on the question how accurate cohesive sediment experiments in the open annular flume can be simulated in SSIIM by applying the implemented flocculation model and which parameters are sensitive towards modeling flocculation and deposition of cohesive sediments in the annular flume.

In this chapter, firstly, the open annular flume is described by its function, and characterized by its hydraulics which are analyzed by measurement data and numerical modeling. Subsequently, the experimental techniques and methods, followed by the measurement results of the cohesive sediment studies in the annular flume are presented. The focus of this chapter lies on the sensitivity analyses for the numerical modeling of flocculation and deposition in the annular flume. These numerical analyses and simulation results are presented and discussed in the third part. The chapter closes with an evaluation of

the numerical sensitivity studies with respect to the consequences on the application of the implemented flocculation algorithm for natural river systems.

5.1 Open Annular Flume

5.1.1 Function and Setup

Laboratory investigations on cohesive sediments aim to analyze the transport characteristics of fine cohesive sediments under controlled conditions. For these kinds of studies, annular flumes are a commonly used type of test rig as the flocculation processes are not interfered with by pumps and an infinite flow can be generated (Parchure and Mehta, 1985, Haralampides et al., 2003, Krishnappan, 2006, Hillebrand, 2008, Klassen, 2009). At the Karlsruhe Institute of Technology (KIT) in Germany two annular flumes with a free water surface were developed for laboratory studies on cohesive sediment transport within the research work of Hillebrand (2008). The flumes differ only in scale, but not in their general functionality. Both flumes consist of a circular water-filled basin with a closed inner cylinder which is set in rotation by an engine. The gap between the outer non-rotating cylinder and the inner rotating cylinder represents the annular flume (see figure 5.1). The rotating inner cylinder constitutes the moving boundary of the water body and generates the water flow by friction. The basin diameter of the small flume is 1.20 m, the diameter of the large flume is 3.60 m. The width of the cross sections is 0.375 m for both flumes, which yields an inner radius of 0.225 m in the small flume and 1.425 m in the large flume. The water depth can be chosen arbitrarily up to 0.60 m.

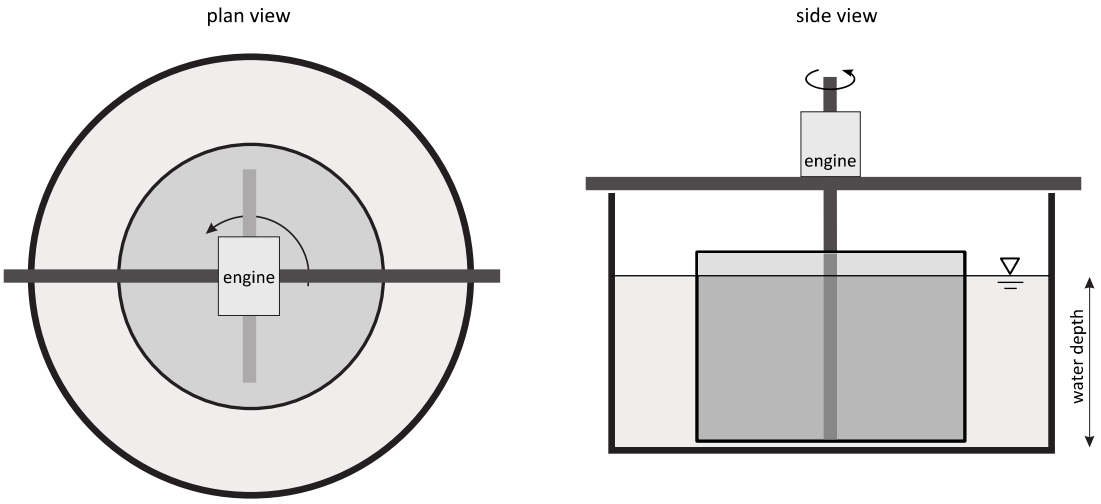

Figure 5.1: Simplified sketch of the open annular flume (Hillebrand and Olsen, 2010).

The bottom of the small flume is built of PVC and the outer wall of plexiglass. The inner cylinder of the large flume is made from stainless steel plates, while the bottom and outer wall are made of concrete coated with paint. Thus, the technical roughness of both flumes is less than 0.001 m with the roughness of the large flume exceeding the roughness of the small flume to some extent (Hillebrand and Olsen, 2010).

5.1.2 Flow Field Measurements and Simulation in SSIIM

The first step towards simulating cohesive sediment experiments in the annular flumes is to analyze their hydraulics. The knowledge of the hydraulics by means of measurements and numerical simulation is the basis for a scientifically reliable modeling of laboratory experiments on fine sediment flocculation processes and deposition in the annular flume. Within previous cohesive sediment experiments (Klassen, 2009), several floc size and suspended sediment concentration measurements were conducted in both flumes. These floc size measurements provide the possibility to test and validate the implemented flocculation algorithm in the annular flume. For the application of the implemented flocculation algorithm in simulating floc sizes, measured data from one experiment in the small flume were used in order to reduce CPU time compared to a simulation in the large flume. The chosen experiment in the small annular flume was carried out at a rotational frequency of the inner cylinder of $f = 22\,\mathrm{min}^{-1}$, while the water depth was kept constant at 0.28 m.

For this setup of boundary conditions in the flume, measurement data of the flow field were available from previous annular flume studies by Hillebrand (2008). Hillebrand conducted three-dimensional flow field measurements for different rotational frequencies of the inner cylinder in both annular flumes using Acoustic Doppler Velocimetry (ADV). ADV ensures simultaneous three-dimensional measurements at high temporal resolutions so that the average flow field as well as the turbulence characteristics can be recorded. Due to the dimensions of the probe and the distance between probe and measurement volume, velocities could not be measured near the water surface and in the immediate vicinity of the side walls. For a detailed description of the flow field measurement technique in the flumes the reader is referred to Hillebrand (2008).

The numerical simulation of the hydraulics was realized in SSIIM 1 using a structured grid. Based on previous model sensitivity studies towards different wall law formulations, carried out by Hillebrand and Olsen (2010), a smooth wall law formulation (see equation 4.3) was applied in the numerical model. The smooth wall law was mainly valid as roughness Reynolds numbers $(u_* \cdot k_s)/\nu$ were determined to be in the order of 2 to 10. Therefore, no calibration procedure for the wall roughnesses was needed. The moving boundary, i. e. the inner cylinder was implemented by transforming the wall law into a source term for the velocities and turbulence equations in the cells bordering the rotating wall.

The structured 3D grid of the numerical model is made up of hexahedral cells. The computation grid and a vertical slice through the grid in y-z-direction are shown in figure 5.2. The grid has 300 x 20 x 12 cells in the streamwise, lateral and vertical direction, respectively. This results in a total of 72,000 3D cells with horizontal dimensions between 0.47 cm and 1.9 cm. In the vertical direction the grid is mostly uniform with cell sizes of 1.9 cm x 2.8 cm. At the bottom and at the water surface the grid is refined in two layers, with smaller cell sizes of 1.9 cm x 1.4 cm. This computation grid of the small annular flume was also applied for the simulation studies of flocculation processes which are presented in chapter 5.3.

In the following, the measured data on flow velocities and turbulence carried out by Hillebrand (2008) are presented together with the simulation results in SSIIM. Since the annular flume amounts to an infinite flow with no inflow or outflow areas, in the following, fluid flow analyses in only one arbitrary cross-section normal to the side walls are presented. By measurements and simulation it was verified that the hydraulics are the same in every other cross-section of the flume. The subsequent figures show velocities and turbulence at three profiles in the flume cross-section at a distance from the inner rotating

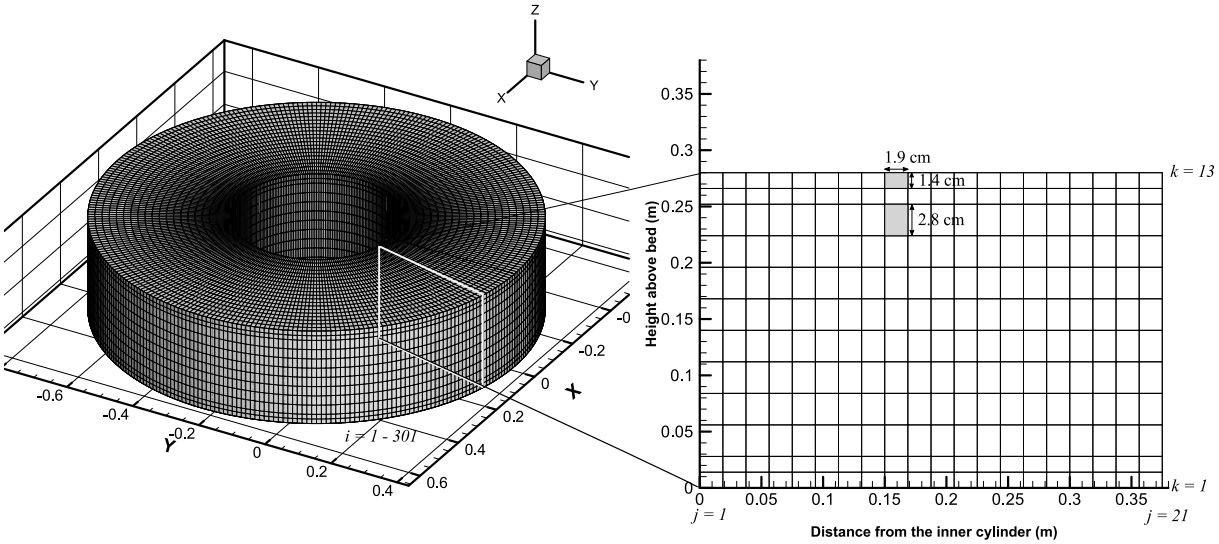

Figure 5.2: 3D computational grid of the small annular flume and a cross-section of the computational mesh in y-z-direction (enlarged view).

cylinder of 8.8 cm, 18.8 cm and 28.8 cm, corresponding to approximately 25 %, 50 % and 75 % of the cross-section width, respectively.

Flow Velocities

The flow velocities are analyzed on the one hand by the longitudinal flow velocities in the main flow direction (x-direction) since they determine the suspended load transport by advection (see chapter 2.3.2). On the other hand, the vortex-structures of the secondary currents in the lateral and vertical direction (y- and z-direction) are described, as they affect the distribution of the suspended particles within the cross-section.

Figure 5.3 shows the longitudinal flow velocities u tangential to the side walls, which approximate the main fluid flow. Both measured velocities and calculated results show that the longitudinal velocities decrease with increasing distance from the inner moving boundary.

The highest longitudinal flow velocities (not shown in figure 5.3 for reasons of clarity) are immediately near the moving wall, where the flow is generated. Here the flow velocities correspond to the reference velocity of the moving inner cylinder $U_{ref} = f \cdot 2\pi r = 51.8\,\mathrm{cm/s}$. The longitudinal velocities decrease along the cross-section to zero flow velocity at the outer non rotating wall due to the no-slip condition. The differences between measurement and simulation in velocity magnitude are the highest near the moving wall. From here up to approximately the middle of the cross-section, the velocities are slightly underpredicted by the simulation. With increasing distance from the inner cylinder the differences in magnitude decrease and the simulated results fit the measured velocities very well. Measured values and simulation results show that the tangential fluid flow is relatively uniform over the water depth. Contrary to typical two-dimensional fluid flows, no logarithmic velocity profile occurs. The observed trends in measured values and model results in the small annular flume are supported by further simulation studies from Hillebrand and Olsen (2010) which are not shown here.

Figure 5.4 shows the secondary currents as a result from the flow velocity components in the lateral and vertical direction. The secondary currents in the annular flume occur due to the curve and the rotation

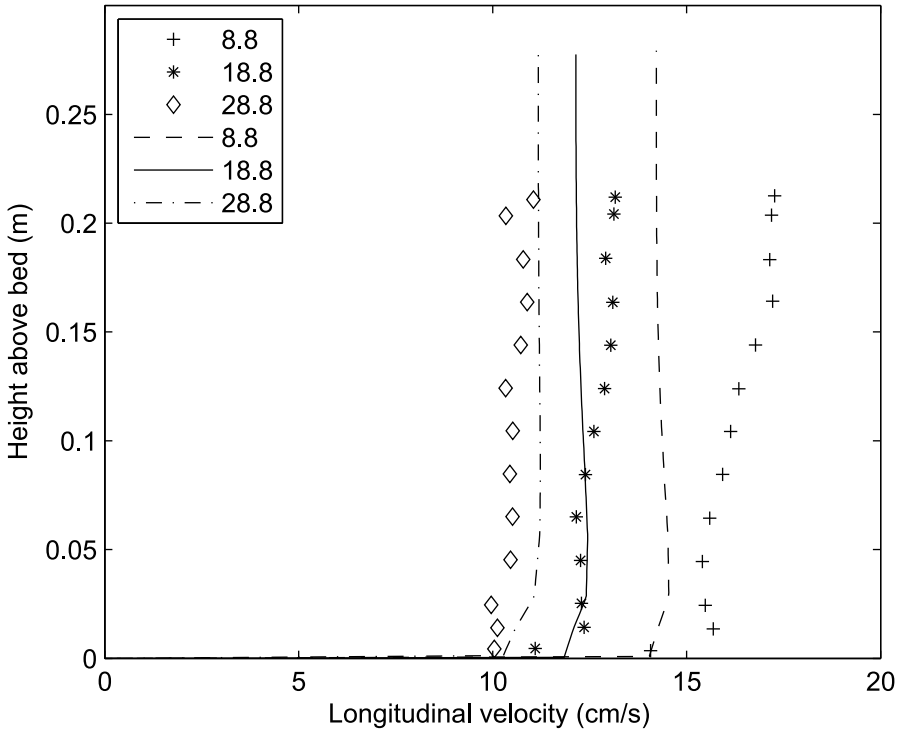

Figure 5.3: Longitudinal velocities u in x-direction in the small annular flume for $f = 22\,\mathrm{min}^{-1}$. Markers indicate measured values, lines indicate simulation results in SSIIM. Distances from the inner cylinder (in cm) along the flume cross-section are given by the numbers in the legend.

of the annular flume. It has to be taken into account in figure 5.4 that different scales for the reference velocity vectors have been used in the simulation and measurement graphic. The lengths of the reference velocity vectors have been chosen such that the model results and measured values could become more comparable in terms of the flow pattern and less the magnitude of the velocities in the cross-section. The magnitudes of the individual flow components v and w in lateral and vertical direction are compared in figure 5.5.

From figure 5.4 it can be seen that simulation and measurement show a three-dimensional flow pattern in the open annular flume characterized by a main vortex structure. In the simulation the vortex center is located slightly below the middle of the cross-section hight and approximately a quarter of the cross-section width away from the moving boundary. Lateral simulated velocities are highest near the bed across the entire cross-section width and show approximately zero values in the remaining cross-section. The simulated vertical velocities have highest values near the side walls with maximum values at the mid-height near the inner rotating wall. In figure 5.5 it can be seen that for a distance of 8.8 cm at mid-height, where approximately the vortex center is located, the vertical velocity gets zero. Below this point the vertical velocity vectors shows in negative direction (towards the bottom) and above in positive direction (towards the free surface). In comparison to the simulation, in the measurement data the main vortex is located at approximately the same height, but further away from the moving boundary at approximately the middle of the flume width (see figure 5.4). The measurements also show an additional minor vortex structure near the bottom. In contrast to the simulation, the measured lateral velocities are highest towards the water surface and decrease towards the bottom.

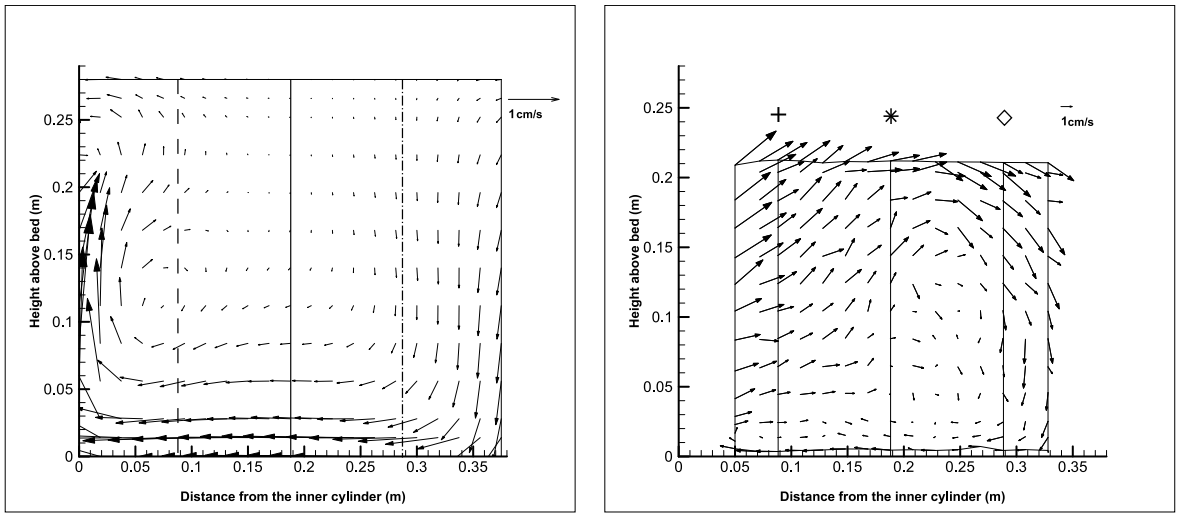

(a) Simulation (b) Measurement

Figure 5.4: Simulated and measured secondary currents in the small annular flume for $f = 22\,\mathrm{min}^{-1}$. The vertical lines show the respective three profiles at which simulated and measured magnitudes of the lateral (v) and vertical (w) velocity components are compared with in figure 5.5.

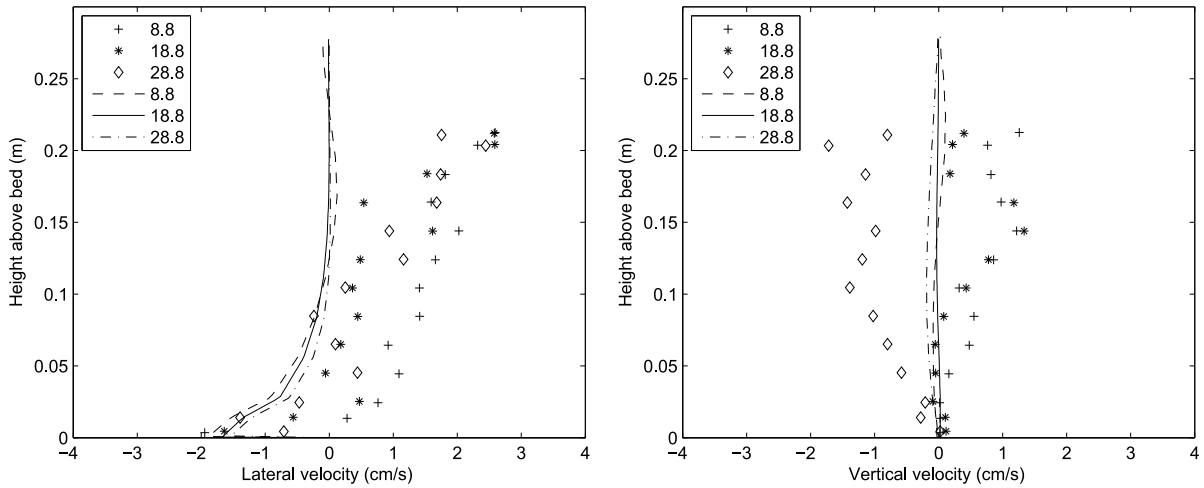

(a) Lateral velocities v in y-direction (b) Vertical velocities w in z-direction

Figure 5.5: Lateral and vertical velocities in the small annular flume for $f = 22\,\mathrm{min}^{-1}$. Markers indicate measured values, lines indicate simulation results in SSIIM. Distances from the inner cylinder (in cm) along the flume cross-section are given by the numbers in the legend.

The measured lateral velocities exceed the simulated values over the whole water depth except the region near the bottom almost along the entire cross-section width. Near the bottom, however, the simulation calculates higher lateral velocities. The vertical velocities are underestimated by the simulation within the measured cross-section area. In spite of these discrepancies, both measurement and the numerical model show an apparent secondary current, which shows outward near the surface and inward near the

bed similar to the secondary current in river bends. The secondary currents are a major characteristic of the open annular flow pointing out that the flow field is clearly three-dimensional.

Turbulence Characteristics

The fluid flow in the annular flume is highly turbulent. The turbulent kinetic energy (see chapter 2.1.2) is often used as a turbulence parameter to estimate the mixing and dispersion intensity of the sediment particles by the largest turbulent eddies. In figure 5.6 the simulated and measured turbulent kinetic energy in the small annular flume is shown in the three profiles.[1] It can be seen that the turbulent kinetic energy values from the measurements are overpredicted by the model by a factor of approximately up to five. The differences between measured and simulated *TKE*-values are highest near the moving inner cylinder, where the turbulent kinetic energy is produced in the annular flume. Near the outer non-rotating wall the differences in magnitude decrease due to a strong turbulent kinetic energy gradient along the flume width in the simulation. Even though absolute values differ, simulation and measurement show similar characteristics. The *TKE*-values are highest near the surface and decrease towards the bottom. Furthermore, the simulated turbulent kinetic energy shows the highest values near the moving boundary, where the turbulence is produced, and decreases towards the outer non-rotating wall. This tendency along the flume width is not observed in such a clarity in the measurements.

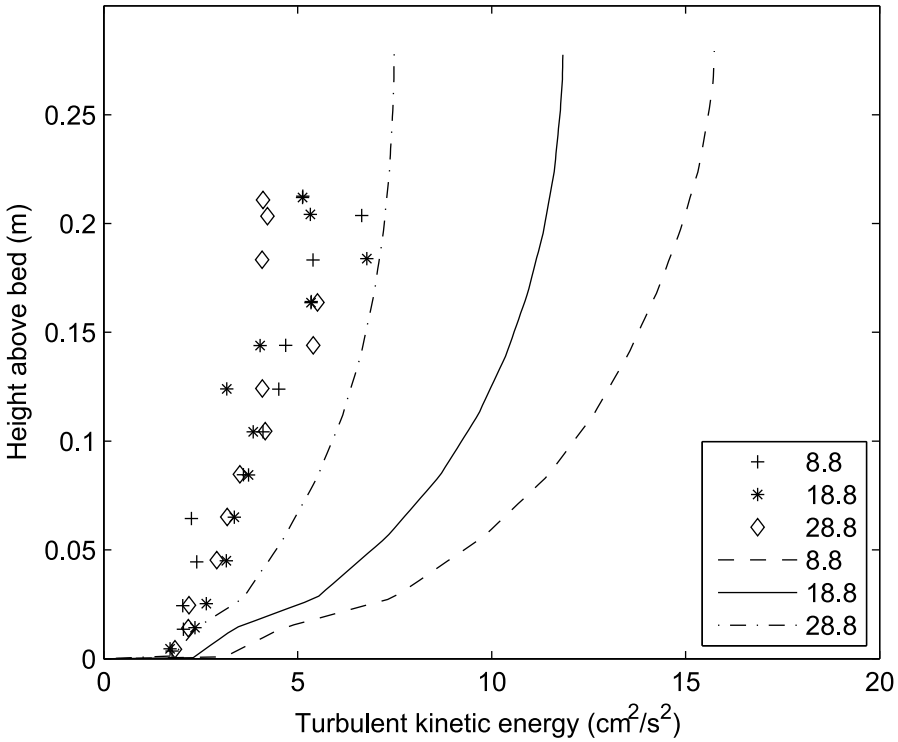

Figure 5.6: Turbulent kinetic energy *TKE* in the small annular flume for $f = 22\,\mathrm{min}^{-1}$. Markers indicate measured values, lines indicate simulation results in SSIIM. Distances from the inner cylinder (in cm) along the flume cross-section are given by the numbers in the legend.

In terms of the turbulent interaction between the sediment flocs and the flow, the smallest eddies of turbulence are of utmost importance. It was shown in chapter 2.3.5 and 3.2.3 that in literature the

[1] The measured turbulent kinetic energy is obtained from the mean-square velocity fluctuations in each direction by the use of equation 2.4. The simulated turbulent kinetic energy is calculated by the k-ϵ model.

ambivalent effect of turbulence on sediment aggregation and disaggregation processes is often captured by the turbulent velocity gradient G_t, which depends on the turbulent dissipation rate ϵ and the kinematic viscosity ν (see equation 2.6). Within the implemented flocculation algorithm in SSIIM, the turbulent dissipation rate is used as a turbulence parameter to calculate the flow-induced and collision-induced shear stresses on the particles and to compute the collision frequencies (see diagram in figure 4.5). Hence, in order to understand and interpret the impact of turbulence on the measured and simulated flocculation processes in the annular flume, the turbulent dissipation rate is evaluated in figure 5.7.

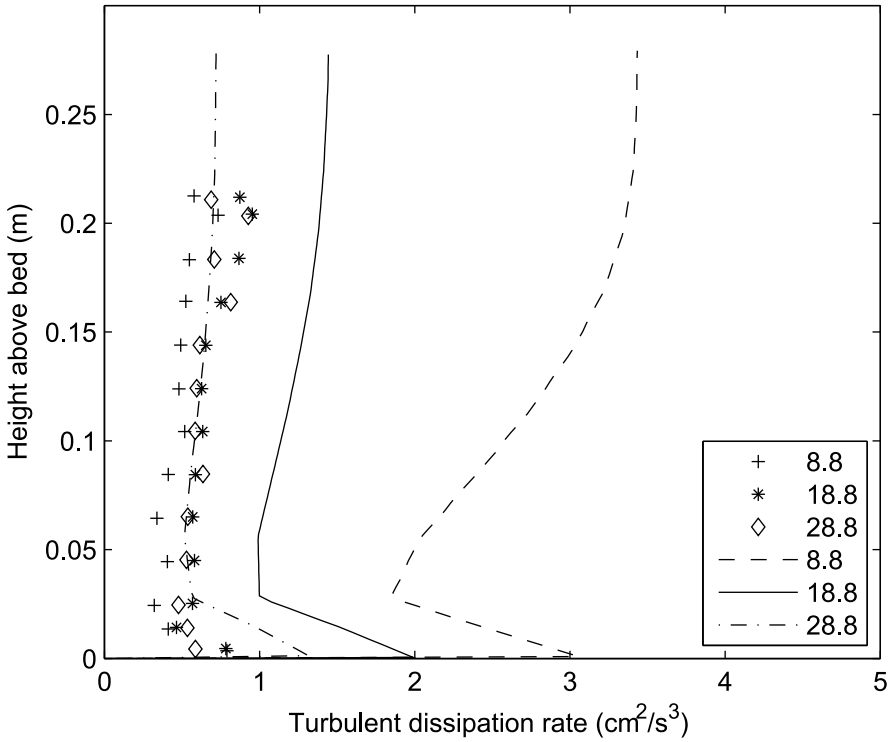

Figure 5.7: Turbulent dissipation rate ϵ in the small annular flume for $f = 22\,\mathrm{min}^{-1}$. Markers indicate measured values, lines indicate simulation results in SSIIM. Distances from the inner cylinder (in cm) along the flume cross-section are given by the numbers in the legend.

The lines show simulated ϵ-values calculated from the k-ϵ model in SSIIM. In order to determine the turbulent dissipation rate from measurements, velocity measurements of high temporal and spatial resolution are required which have to be recorded simultaneously. Since a simultaneous recording of velocities in different measurement points was not possible with the used ADV measuring device, the assumption of an isotropic turbulence ($\overline{u'^2} = \overline{v'^2} = \overline{w'^2}$) was made. It allows to determine the local energy dissipation rate by means of ADV data with high temporal resolution at only one measurement point. Then, by the application of Taylor's hypothesis (also known as *frozen turbulence*) it is possible to derive spatial turbulent structures from temporal ones (e. g. Tennekes and Lumley, 1972). The use of the Taylor's hypothesis enables to calculate the *Taylor mircoscale*, which is a turbulence length scale. The calculation of the Taylor microscale in turn allows then to compute the energy dissipation rate from measured velocity values at only one point. The aforementioned method was applied within the work of Hillebrand (2008) to calculate the energy dissipation rate from measured velocity values and is not presented in detail here.

Figure 5.7 shows that the simulated dissipation rates calculated in SSIIM overpredict the measured values along a wide range of the flume width. The discrepancies between simulation and measurement results increase with decreasing distance from the moving cylinder, e. g. at a distance of 8.8 cm from the inner cylinder the simulated dissipation rates are about 4 to 6 times larger than the measured values. With increasing distance from the moving wall these discrepancies decrease, similarly as it was observed for the turbulent kinetic energy in figure 5.6. While in the simulation the dissipation rate gradient is relatively strongly pronounced from the highest values near the inner cylinder to lower dissipation rates at the outer wall, the measured values do not show this tendency. At the nearest evaluated profile at a distance of 8.8 cm from the rotating cylinder they even show lower values than in the other two profiles. However, the characteristics in the shape of the profiles are similar for both. Measured values and simulation results decrease from the water surface towards the bottom, whereas near the flume bottom the dissipation rate increases again showing the highest values here. Nevertheless, these tendencies are more distinct in the simulation results.

In summary it can be concluded, that relatively good agreement was found for the longitudinal flow velocities in the main flow direction. Also the secondary currents were observed as a major characteristic in the annular flume by the simulation and the measurements pointing out the three dimensionality of the flow field. However, absolute velocity values differ in both the lateral and vertical flow direction. Discrepancies are most significant in the determination of the magnitude of the turbulent kinetic energy and the turbulent dissipation rate, but general characteristics of the distribution are similar. The presented figures clearly show that both simulation and measurements indicate a complex three-dimensional flow field in the annular flume.

The described flow field characteristics are supported by further computed and measuring data for different rotational frequencies of the inner moving cylinder (not shown here). The investigations have shown that the velocity field is self-similar within the studied range of reference velocities, i. e. that the flow velocities for different rotational frequencies scale by the reference velocity, while the main flow field pattern remains the same.

When elaborating possible reasons for the observed differences in the measurement and simulation results, one might initially identify the model roughness as a potential source for discrepancy. However, previous investigations by Riesterer (2007) and Hillebrand and Olsen (2010) have shown that in a realistic range of relatively low roughnesses, the roughness value has a minor effect on the model results. Another reason could be the grid resolution in SSIIM. In this work the computational grid is based on 300 x 20 x 12 cells (see figure 5.2). Hillebrand and Olsen (2010) have used an approximately twice finer grid in all three directions while the other boundary conditions were the same. Their simulation results support the presented hydraulic characteristics when using a coarser grid. Hence, it can be concluded that the grid resolution was chosen sufficiently fine enough to compute the complex flow field in an accurate way. The most significant discrepancies were found in the determination of the turbulence characteristics. The reasons for this could on the one hand be attributed to the reliability of the measured values, as the measurements were conducted non-automatically and measurement conditions were not always favorable. On the other hand, Hillebrand and Olsen (2010) mention that k-ϵ models are considered to systematically overpredict turbulent kinetic energy under specific conditions (Joubert et al., 2005, Tian et al., 2005). Another reason could be that the assumption of an isotropic turbulence for calculating the turbulent energy dissipation rate ϵ might not have been justified or that the measurement frequency was not sufficient to capture turbulence characteristics in an accurate way.

The simulated and measured flow field analyses above inevitably raise the question, whether the measured or modeled values better represent the true values in the small annular flume. This question can not be answered adequately within this work and needs to be adressed in further numerical and measurement studies. The necessity of further scientific analyses becomes even more obvious when comparing the hydraulics in the two annular flumes of different scale. Several previous studies in the annular flume mentioned above (Riesterer, 2007, Hillebrand, 2008, Hillebrand and Olsen, 2010), have shown that the difference in radius between the two flumes induces significant differences in their hydraulic characteristics. For example, for the same reference velocity of the inner cylinder and the same boundary conditions in both flumes, the flow velocities in the small flume are lower than those in the large flume, while the turbulent kinetic energy exceeds that in the large flume. It could be shown in previous comparative cohesive sediment transport studies in the two flumes (Klassen, 2009) that these scale effects have a decisive influence on the deposition behavior of the sediments.

Within this work, the presented analyses of the hydraulics by means of measurements and simulation serve as a basis for further successfully modeling laboratory experiments on flocculation and deposition of cohesive sediments in the test case of the small annular flume. The knowledge about the differences in the flow field characteristics is a crucial prerequisite for a further comparison of modeled flocculation processes with measured ones, since aggregation and disaggregation mechanisms are significantly affected by the hydraulic conditions. In the next section, the cohesive sediment measurement techniques and experimental results in the small annular flume are presented. The measured results on cohesive sediment transport are used to compare these data with the results of the numerical modeling by adopting the implemented flocculation algorithm.

5.2 Fine Sediment Experiments

5.2.1 Technique and Methods

For the validation and testing of the implemented flocculation algorithm, measured laboratory data from one experiment in the small annular flume were used which was carried out within previous studies in the two flumes (Klassen, 2009). In the experiment, the temporal development of floc sizes, affected by flocculation processes, as well as the suspended sediment concentration were measured at one point in the middle of the height of the water level ($h = 0.14\,\mathrm{m}$) and in the middle of the flume width. Figure 5.8 shows the arrangement of the measuring devices in the small flume. The experiment was carried out in tap water. In order to simplify the complex system of natural sediments, which normally contain significant amounts of different clay minerals and a certain range of organic material (see chapter 2.2.1), industrially processed kaolinite was used. Kaolinite is a typical representative for clay minerals and is part of the mineral class of the layer silicates. The chemical characteristics of this mineral were already described in chapter 2.2.2. In the experimental studies, the used kaolinite had a medium grain diameter of $D_g = 2.1\,\mu\mathrm{m}$.

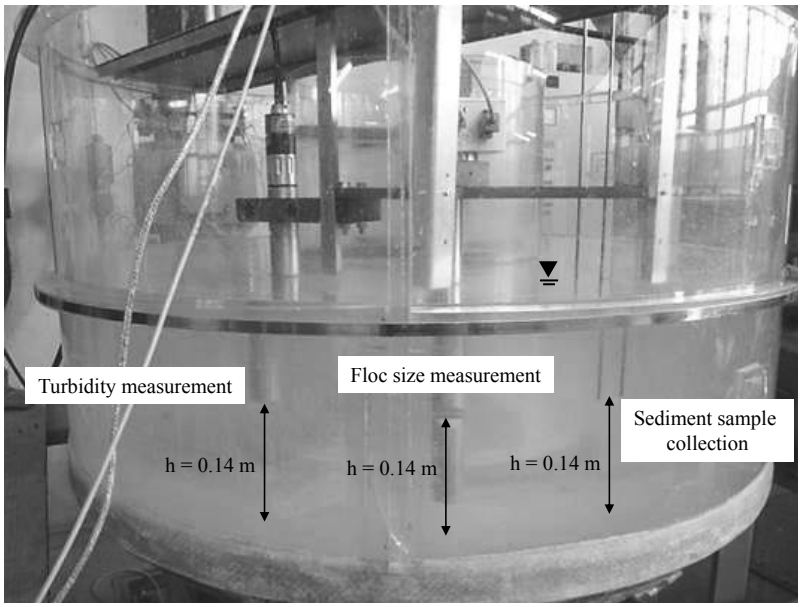

Figure 5.8: Arrangement of the measuring devices in the small flume.

Experimental Procedure

Prior to the start of the experiment, a dry amount of sediment was weighed to achieve an initial concentration of $C_0 = 500\,\mathrm{mg/l}$. After adding tap water, the sediment-water-suspension was mixed intensively using a laboratory stirrer. A high stirrer frequency was used to break up possible flocs due to mixing. Before adding the sediment suspension in the annular flume, tap water was filled inside the flume to a height of 0.28 m. The rotational frequency of the inner cylinder was set to $22\,\mathrm{min}^{-1}$. The sediment suspension was then added near the inner rotating cylinder to achieve a fast mixing of the suspension due to the high flow velocities and turbulence intensity at the rotating wall. At the beginning of the measurements a high frequency of sediment samples was necessary due to the rapid turbidity decrease. In the further experiment the sampling was based on the degree of the turbidity decrease. Concurrently, particle sizes were measured within an interval of 15 minutes over the whole experiment duration. An overview of the boundary conditions for the cohesive sediment experiments in the small annular is presented in table 5.1.

Table 5.1: Boundary conditions for the cohesive sediment experiments in the small annular flume.

Rotational frequency	Flume width	Water depth	Water medium	Industrially processed sediment	Initial concentration
$f = 22\,\mathrm{min}^{-1}$	$b = 0.375\,\mathrm{m}$	$h = 0.28\,\mathrm{m}$	Tap water	Kaolinite, $D_g = 2.1\,\mu\mathrm{m}$	$C_0 = 500\,\mathrm{mg/l}$

Measurement of the Suspended Sediment Concentration

For measuring the suspended sediment concentration the turbidity was recorded continuously (every 30 seconds) combined with taking sediment samples. The turbidity measurement was conducted by using a turbidity sensor which records the scattering light in a 90 degrees angle. An accumulation of air bubbles or sediment on the sensor surface was prevented by an ultrasound source integrated in the sensor, so that incorrect measurement results could be avoided. As the turbidity depends on the sediment concentration

as well as on the particles sizes and floc structure, sediment samples were taken at regular time intervals. The gravimetric determination of the sediment concentration together with the associated turbidity values allows then the derivation of a functional correlation between measured turbidity values and the suspended sediment concentration.

Measurement of Floc Sizes

In order to verify flocculation processes, floc sizes were measured simultaneously with an interval of 15 minutes. For that, in situ measurements were conducted without taking sediment samples from the suspension. The disadvantage of sampling is that sediment particles may be destroyed or altered during transport. However, in situ methods require a certain amount of particles in the measuring volume over the entire measuring time in order to characterize the particle size distribution in an adequate way. The investigations on floc sizes were carried out by using the In-Line microscope Aello 7000. The floc size measuring system consists of a 38 cm wide stainless-steel pipe with a 8 mm wide slot acting as the measuring volume (see figure 5.9). On the one side of the slot, the illumination device is placed, which provides the backlighting for the pictures. On the other side of the slot, a microscope objective and a CCD-camera with a resolution of 1024 x 768 pixels are positioned. At the end of the stainless-steel pipe, a box for camera electronics and electronic connections is located.

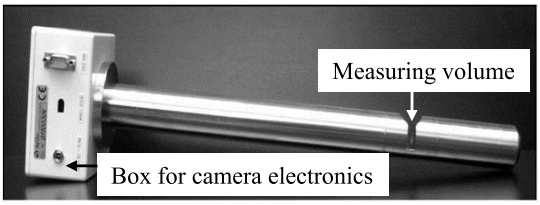

Figure 5.9: Aello In-Line Microscope for measuring floc sizes.

An image recognition software analyses the pictures and calculates characteristic parameters of the particle size distribution, e. g. the mean diameter D_m, the particle diameter D_{16} or D_{84}. Thereby only those particles and flocs are detected by the software which are in the focal plane and exhibit a uniform surface and a sharp border. As a consequence, only particles which are completely visible in the picture are analyzed. Figure 5.10 shows a recorded picture by AELLO and the corresponding analyzed picture from the software with the detected particles.

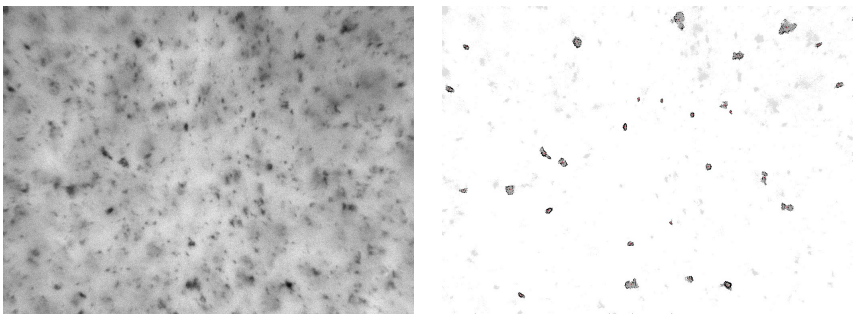

(a) Recorded picture by AELLO (b) Detected particles by the software

Figure 5.10: Recorded picture by AELLO and analyzed picture from the software.

By the assumption of a spherical form of the particles, the software determines the projected area of each detected particle and calculates the resulting particle's diameter. Based on all detected particle sizes, a representative diameter for the particle size distribution is defined. Within this work, the arithmetic mean diameter D_m is used as a representative parameter for characterizing the particle size distribution. It is based on the diameter of approximately 1000 measured particles.

For the subsequent discussion and evaluation of the measured and simulated floc sizes it is important to know the limitations of the used measurement device. The limitations on the AELLO analyze system are:

- Due to the detection process of the pictures (only particles with a uniform surface and sharp border are detected) and the limited picture field size, only particles in the size range between $3\,\mu\text{m} - 450\,\mu\text{m}$ can be measured.
- The particle detection depends on the optical properties of the flocs. With increasing experiment duration, soilings on the measurements window are expected, which will affect the picture quality. Further, aggregation and disaggregation processes may lead to a reduced picture quality, so that the picture is no longer optimally illuminated and does not display a sufficient contrast. In these cases, not all particle size ranges can be analyzed by the evaluation software.
- For the calculation of a representative particle parameter (e. g. D_m) a certain number of particles is required. Within this work, the calculation of the D_m is based on approximately 1000 measured particles. In the case that the particle concentration in the measuring volume is too low (e. g. when almost all particles or flocs have deposited), a long recording time is necessary in order to capture the required number of particles. A long recording time in turn does not allow the measurement of possible changes in the particle size distribution. In contrast, too high sediment concentrations (e. g. when adding the suspension in the annular flume) may also lead to a reduced picture quality due to the shadow casting of the particles. This effect can result in too coarse detected particles from the software.
- For the calculation of the particle diameter a spherical form of particles is assumed. Different particle forms result in inaccuracies of the measurement results.

5.2.2 Results

In figure 5.11 (a) the measured suspended sediment concentrations and in figure 5.11 (b) the corresponding measured particle diameters D_{10}, D_m and D_{90} from the selected experiment in the small annular flume are shown over the entire duration of the experiment of about 70 hours. The first 5 hours of the experiment are shown in figure 5.12 in enlarged view. It can be seen that within the first 5 hours of the experiment, the sediment concentration decreases most rapidly, from an initial value of $C_0 = 500\,\text{mg/l}$ to about $330\,\text{mg/l}$. Subsequently, the concentration gradient reduces and the sediment mass deposits slower. After about 60 to 70 hours only approximately 7 % ($33\,\text{mg/l}$) of the initial sediment material is in suspension, i. e. almost the whole sediment mass has deposited.

The temporal development of the particle sizes indicates flocculation processes: the first measured mean particle diameter D_m was recorded two minutes after adding the sediment suspension in the flume to $D_m = 9.3\,\mu\text{m}$ ($D_{10} = 4.8\,\mu\text{m}$, $D_{90} = 16\,\mu\text{m}$). Since the size of the primary particles of kaolinite is $D_g = 2.1\,\mu\text{m}$, only aggregation processes can be related to this significant increase in particle size in the

order of approximately a factor of 4.5. In the time period of the first 5 hours the maximum mean floc diameter is reached after 17 minutes to $D_m = 11\,\mu$m ($D_{10} = 5.4\,\mu$m, $D_{90} = 18.9\,\mu$m), accounting for further aggregation processes. Then the mean diameter is decreasing to a value between $D_m = 7.5$ to $8.0\,\mu$m ($D_{10} = 4.4\,\mu$m, $D_{90} = 10.5$ to $13.6\,\mu$m). The decrease in floc size can be caused by the settling of the larger flocs, leaving the smaller particles in suspension.

After about 5 hours the particle sizes increase again and a steady-state condition is reached in which the mean particle size remains approximately constant with time ($D_m = 9$ to $10\,\mu$m) since aggregation and floc break are assumed to be in equilibrium. The abrupt increase in floc size after 5 hours might be caused by floc erosion of the deposited sediment particles. Individual deposited particles could have been disrupted from the surface of the bed by flow-induced bed shear stresses. Thereby the particles will get into suspension again and re-participate in the flocculation process. By aggregation of these eroded particles, larger floc sizes might be created, which will result in an increase of the measured mean floc size. However, this is only an attempt to explain the observed phenomenon in the small annular flume. For a complete understanding of the involved processes in the experiment, further and detailed measurements of floc sizes in the annular flume are required. It is interesting to note that the abrupt increase in floc size after about 5 hours was also observed for another rotational frequency of the inner cylinder in the small annular flume (Klassen, 2009) providing a verification of the measurement data.

The indicated decrease of the particle sizes after 60 hours is likely to arise from a reduced picture quality associated with the long experiment time. In the case of a reduced picture quality, not all particle size ranges can be analyzed by the evaluation software (see chapter 5.2.1). This might result in the indicated shifting of the detected particle sizes, although there is no decrease in floc size from a physical point of view, since floc growth and floc break-up processes are assumed to be in equilibrium at this stage of the experiment.

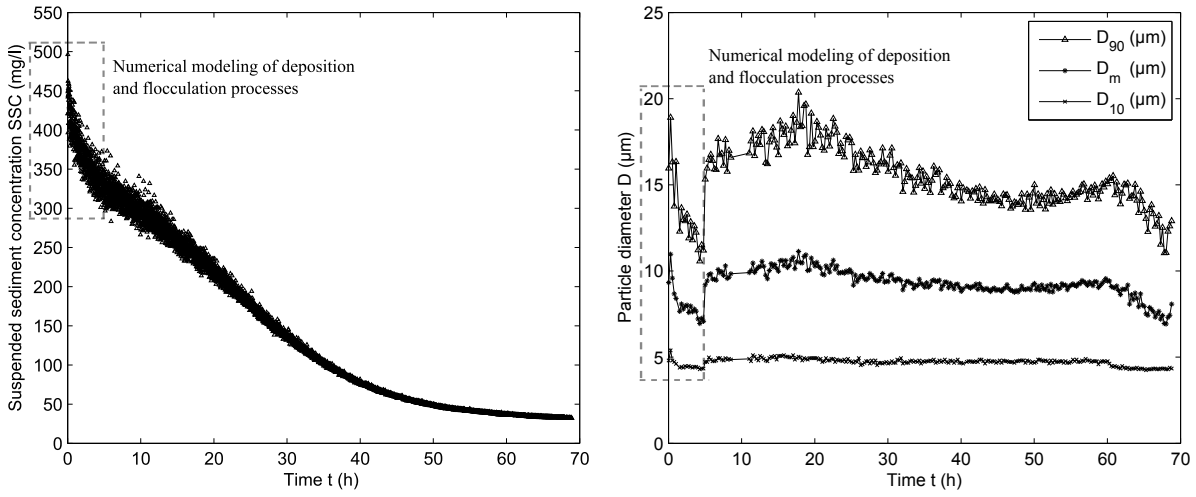

(a) Measured SSC over 70 hours

(b) Measured particle diameters over 70 hours

Figure 5.11: Measured suspended sediment concentrations (a) and particle diameters (b) over a time of approx. 70 hours at the center of the cross section in the small annular flume. The dashed lines show the timespan of the experiment (first 5 hours) which was analyzed within numerical sensitivity studies by the application of the implemented flocculation algorithm in SSIIM.

When modeling the measured deposition and flocculation processes, a short time step is required, since the aggregation and disaggregation mechanisms take place on small time scales. This implies that the analyze of flocculation processes over a period of 70 hours by numerous comparative sensitivity calculations is associated with excessive computational times. For this reason, the numerical modeling was limited in time. Several numerical studies have shown that the predicted flocs size distribution differs significantly from the primary particle size distribution during the initial periods of sediment settling. Within the numerical flocculation studies of Krishnappan (1990), the flocs were formed during the initial period of the first hour. After this initial period, the flocculation process slowed down and the settling became predominant. Winterwerp (1998) also showed that the increase in floc size is most significant in the initial stages. When a final equilibrium floc size is reached, i. e. when an equilibrium between aggregation and floc breakup and a steady state of the particle size distribution is achieved, the floc growth rate decays rapidly. The observed trends are supported by further flocculation investigations (e. g. Tsai et al., 1987 Lick et al., 1992, Son and Hsu, 2008, Xu et al., 2008).

Based on the assumption that flocculation processes are most significant after adding the sediment into the annular flume, the numerical modeling was limited to the first 5 hours of the experiment for most of the sensitivity calculations. Figure 5.12 shows the measured data for the selected time frame in enlarged view. However, certain selected long-term deposition and flocculation computations were also carried out over the entire time of the experiment (see chapter 5.3.3).

In figure 5.13, two representative pictures of the particles, captured by the Aello In-Line Microscope can be seen for two measurement points within the first 5 hours: 17 minutes after adding the sediment suspension in the annular flume, yielding a maximum mean floc size of $D_m = 11\,\mu$m, as well as 2.8 hours after starting the experiment, resulting in a mean particle diameter of $D_m = 7.6\,\mu$m. By merely viewing the pictures, no clear deviations in floc sizes are visible for the two different times. The differences in measured floc sizes can only be identified by the image evaluation software (see figure 5.12 (b)).

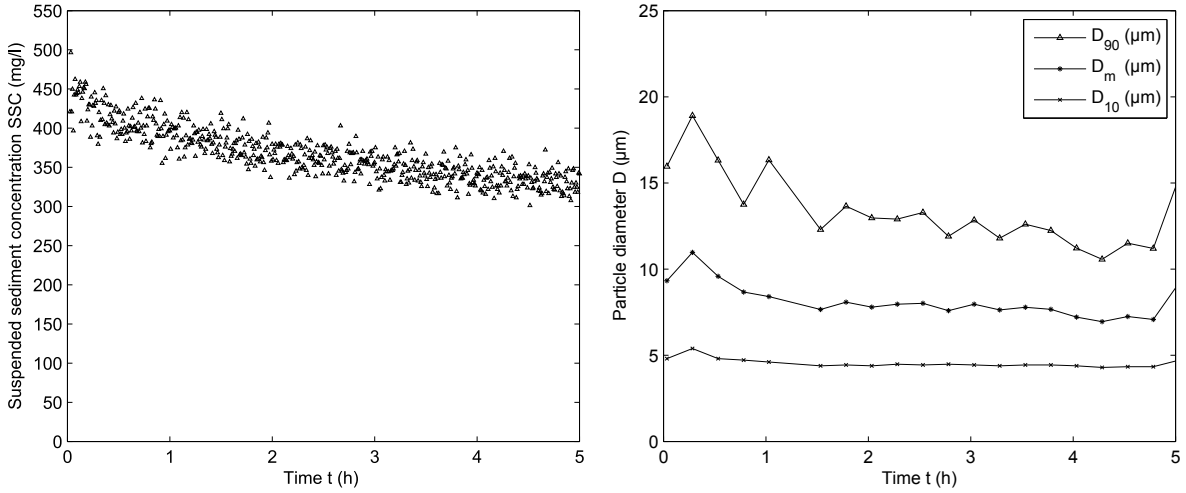

(a) Measured SSC over 5 hours

(b) Measured particle diameters over 5 hours

Figure 5.12: Measured suspended sediment concentrations (a) and particle diameters (b) over a time of approx. 5 hours at the center of the cross section in the small annular flume.

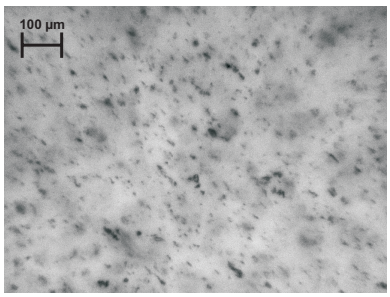

(a) 17 minutes after adding the sediment suspension in the annular flume: $D_{50} = 11\,\mu$m

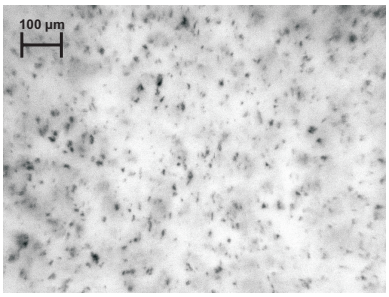

(b) 2.8 hours after adding the sediment suspension in the annular flume: $D_{50} = 7.6\,\mu$m

Figure 5.13: Pictures of the particles captured by the Aello In-Line microscope.

5.3 Numerical Modeling of Flocculation Processes in the Open Annular Flume

5.3.1 Definition of Parameters and Initial/Boundary Conditions

The numerical modeling of deposition and flocculation in the annular flume was conducted with SSIIM 1 by using the computation grid described in chapter 5.1.2. For solving the advection-diffusion equation and the equations in the implemented flocculation algorithm, initial and boundary conditions have to be defined as well as different parameters and coefficients. Table 5.2 shows an overview of the parameters and the initial/boundary conditions.

Table 5.2: Definition of parameters and initial/boundary conditions for modeling deposition and flocculation in the annular flume for the reference case run.

Parameter or initial/boundary condition	Definition	Sensitivity study
1. Time step Δt (sec)	1	(5.3.2.2)
2. Number of size classes N (–)	10	
3. Particle size spectrum (μm)	see table 5.3	
4. Initial conc. C_0 (mg/l)	$C_0 = 500$ mg/l, see table 5.3	(5.3.2.3)
5. Aggregation coefficient α_a (–)	1.0	(5.3.2.4)
6. Particle yield strength coefficient B_τ (N/m^2)	1.0	(5.3.2.5)
7. Fractal dimension n_f (–)	with $D_{fc} = 15.0\,\mu$m, $n_{fc} = 1.4$	(5.3.2.1)
8. Settling velocity w_s formula (mm/s)	Winterwerp (1998)	
9. Exclusion/inclusion of erosion	exclusion	(5.3.2.6)

The respective values and definitions in table 5.2 are illustrated for the reference case run. In the following, these parameters and settings are briefly described.

1. **Time step**: A small time step of 1 sec was used, since growth and break-up processes of flocs occur at small time scales compared to the processes transport and deposition.

2. **Number of size classes**: The application of the flocculation algorithm requires the definition of a discrete number of particle size classes and the corresponding particle sizes. In these studies, a size class-based (SCB) model was used to describe the particle size spectrum (Maerz et al., 2011, Verney et al., 2011). The SCB model is based on the population equation system that describes the floc population in N discrete size classes. In this work, the particle size spectrum in the annular flume was represented by $N = 10$ size classes.

3. **Particle size spectrum**: Each of the size class corresponds to a specific particle size D_j and an average sediment particle mass M_j. Each average particle mass in turn is represented by a mass class interval, which contains particles with the smallest particle mass $M_j(lower)$ and the largest particle mass $M_j(upper)$ of this class, respectively (see chapter 4.2.1). According to the SCB model, the particle sizes were logarithmically distributed starting from the smallest primary particle diameter D_g to the maximum floc size D_{max} by using the following equation (Maerz et al., 2011):

$$D_j = D_g^{1+\frac{j-1}{N-1}\cdot\left(\frac{\log_{10}(D_{max})}{\log_{10}(D_g)}-1\right)} \tag{5.1}$$

   Taking into account the size of the primary particles of kaolinite, the minimum particle diameter was set to $D_{10} = D_g = 2.1\,\mu$m. The maximum floc size was defined according to the largest measured floc sizes. In figure 5.14 all measured flocs sizes of about 22,000 detected particles within the first 5 hours of the experiment are shown. It can be seen that most particles were found in the range between 4 and 10 μm. Due to the limitations of the camera resolution, the smallest particle sizes were detected to about 4 μm. However, it should be noted that probably smaller particles were in suspension which could not be detected by the software. The largest flocs have a size in the range between 30 to 50 μm. Hence, the coarsest particle size class was set to $D_1 = D_{max} = 35\,\mu$m. Based on these two representative particle sizes, the other particle sizes D_2 to D_9 were calculated by the use of equation 5.1. In table 5.3 the chosen particle sizes, the corresponding average particle masses and the mass class intervals are listed for the reference case.

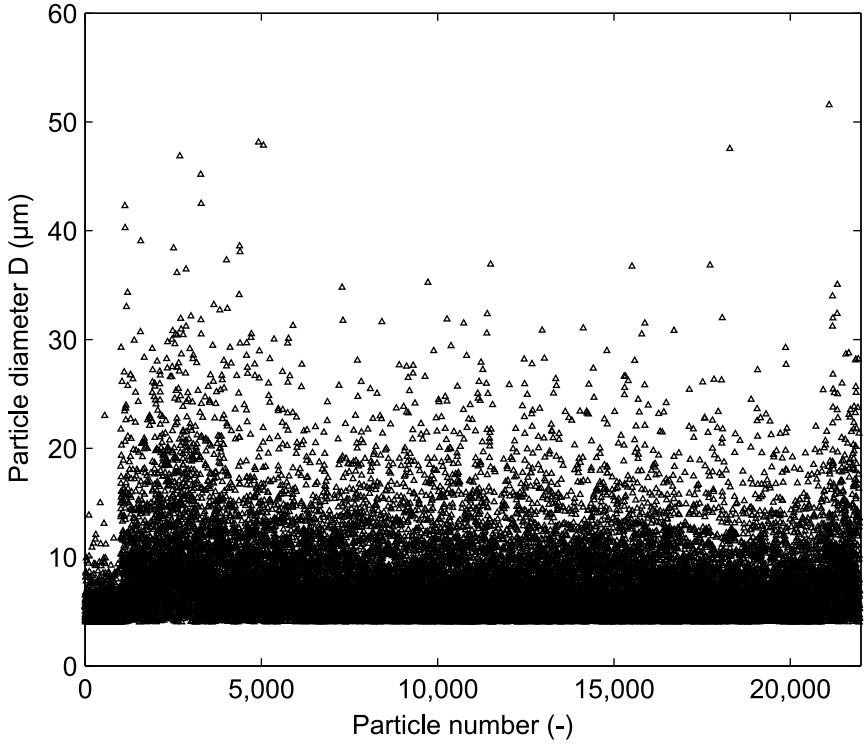

Figure 5.14: All measured particle sizes in the first 5 hours of the experiment based on approx. 22,000 detected particles.

Table 5.3: Sediment particle characteristics for the reference case run in the annular flume.

Class index	Diameter	Smallest mass	Average mass	Largest mass	Initial conc.	Fractal dimension	Density	Yield strength	Settling velocity
j	D_j (μm)	M_j(lower) (kg)	M_j (kg)	M_j(upper) (kg)	$C_{0,j}$ (mg/l)	$n_{f,j}$ (–)	ρ_j (kg/m^3)	τ_j (N/m^2)	$w_{s,j}$ (mm/s)
1	35.0	1.5724e-11	2.2582e-11	6.7705e-11	25	1.0	1006	0.0057	0.0032
2	25.6	6.1959e-12	8.8661e-12	1.5724e-11	25	1.1	1015	0.0111	0.0043
3	18.7	2.4822e-12	3.5257e-12	6.1959e-12	20	1.3	1038	0.0219	0.0058
4	13.6	1.0262e-12	1.4387e-12	2.4822e-12	20	1.5	1089	0.0437	0.0072
5	9.9	4.4560e-13	6.1370e-13	1.0262e-12	25	1.6	1194	0.0897	0.0084
6	7.3	2.0480e-13	2.7750e-13	4.4560e-13	25	1.9	1389	0.1927	0.0089
7	5.3	9.7800e-14	1.3200e-13	2.0480e-13	65	2.1	1699	0.4537	0.0085
8	3.9	4.6400e-14	6.3500e-14	9.7800e-14	125	2.4	2102	1.3448	0.0072
9	2.8	2.0700e-14	2.9200e-14	4.6400e-14	120	2.7	2483	10.0135	0.0051
10	2.1	0	1.2100e-14	2.0700e-14	50	3.0	2650	∞	0.0031

4. **Initial concentration**: In table 5.3 the respective initial concentrations in each size class are illustrated, which were defined randomly among the size classes to achieve a total initial concentration of $C_0 = 500\,\mathrm{mg/l}$. The given concentration distribution results in an initial floc size of 7.7 μm. The initial concentration was not distributed uniformly in the model domain, but in the three uppermost layers of the computation grid ($k = 10 - 13$), over the entire flume width ($j = 1 - 21$), and in four arbitrary cells in the longitudinal flow direction ($i = 81 - 85$). The objective of that initial concentration distribution in the model domain was to achieve a very close reproduction of the

experimental procedure from the laboratory, where the sediment suspension was added at the water surface.

5. **Aggregation coefficient**: The aggregation coefficient α_a was defined to the maximum value of 1.0, since it was assumed that the suspended sediment is strongly cohesive due to a very small primary grain diameter of $D_g = 2.1\,\mu$m.

6. **Particle yield strength coefficient**: Since no values for the empirical stress function B_τ were available, for the reference case the parameter was set to the minimum value found in literature, namely to $1.0\,\mathrm{N/m^2}$. The sensitivity towards higher values was analyzed in subsequent computations.

7. **Fractal dimension**: The floc structure was accounted for to calculate the particle's density (see equation 4.10), the particle's yield strength (see equation 4.16) and the collision-induced shear stresses (see equation 4.25). In these studies, a size dependent, variable fractal dimension n_f according to Khelifa and Hill (2006) was applied to take into account the fractal geometry of flocs (see equations 2.14 and 2.15). The characteristic floc size D_{fc} was set to $15.0\,\mu$m and the characteristic fractal dimension n_{fc} to 1.4. The resulting calculated fractal dimensions, the floc densities and the particle yield strengths for each size class are shown in table 5.3.

8. **Settling velocity formula**: The fractal structure was also accounted for to calculate the settling velocity. The settling velocity equation 2.27 according to Winterwerp (1998) was used, which considers the floc structure property in order to compute the floc density. The calculated settling velocities for each size class depending on the fractal dimension are shown in table 5.3. It has to be noted that the particle mass, the fractal dimension, the particle density, the yield strength and the settling velocity depend on the values for D_{fc} and n_{fc}. The values in the table are given for $D_{fc} = 15.0\,\mu$m and $n_{fc} = 1.4$. Other values for these two parameters will lead to different particle characteristics.

9. **Exclusion / inclusion of erosion**: In order to simplify the numerical modeling, suspended load was computed by the assumption that erosion and deposition do not occur simultaneously. Hence, an artificial exclusion of erosion processes was realized in SSIIM by the definition of higher critical shear stresses $\tau_{c,i}$ than the calculated bed shear stress τ_b for all the size fractions. In this case, the equilibrium sediment concentration at the bed $C_{bed,i}$ gets zero, and therefore also the sediment pick-up rate becomes zero, i. e. no entrainment rate is calculated in SSIIM (see equations 4.7 and 4.8).

All the definitions and assumptions mentioned above were applied for the reference case run in SSIIM. Due to the complex processes interactions there are still uncertainties and open questions in cohesive sediment dynamics in general, and in flocculation processes in particular. These uncertainties are reflected by the numerous number of empirical calibration parameters which, in case of missing measured data, have to be determined over a wide range of values. In order to evaluate the uncertainty of these parameters on the model results, sensitivity analyses are essential and a prerequisite for further applications of the implemented flocculation algorithm in sediment engineering. Within the testing and validation of the implemented flocculation algorithm in the annular flume, the impact of different parameter definitions on the model results was investigated. The results of the reference model configuration were used to compare different sensitivity simulations with experimental results. The major parameters, boundary/initial conditions and processes which were varied within these studies are denoted in table 5.2. These include: the time step Δt, the initial suspended sediment concentration in each size class $C_{0,j}$ (respectively, the

initial floc size), the aggregation coefficient α_a, the particle yield strength coefficient B_τ, the characteristic fractal dimension $n_{f,c}$ and the impact of taking into account also the erosion process within the simulation. In the next sections, the computation results of the reference case and of the follow-up sensitivity simulations are presented. Hereby, the computation results of the reference case are presented in the context of the description of the respective sensitivity study. Some individual results of the sensitivity studies have been already published in Klassen et al. (2013) and Klassen et al. (2015).

5.3.2 Sensitivity Analyses

5.3.2.1 Fractal Dimension

In the implemented flocculation algorithm the floc structure is described and mathematically expressed by applying the concept of fractal geometry/fractal dimension n_f (see chapter 2.3.4). The fractal dimension plays a major role in terms of the flocculation and deposition behavior since it influences the floc density, the floc yield strength and the particle collision-induced shear stresses (see chapter 4.2). The floc density in turn influences the settling velocity. The smaller the fractal dimension, the more fragile and less dense the particles are (see figure 5.15). With smaller fractal dimensions, the floc density, the yield strength and the settling velocity decrease. At the same time the collision-induced shear stresses acting on two colliding particles also decrease. Lower collision-induced shear stresses in turn facilitate aggregation by particle collision rather than disaggregation. This means, that the fractal dimension influences the collision outcome due to two-body collisions as well, i. e. whether type 2A1, 2D2 or 2D3 occur (see chapter 4.2.2).

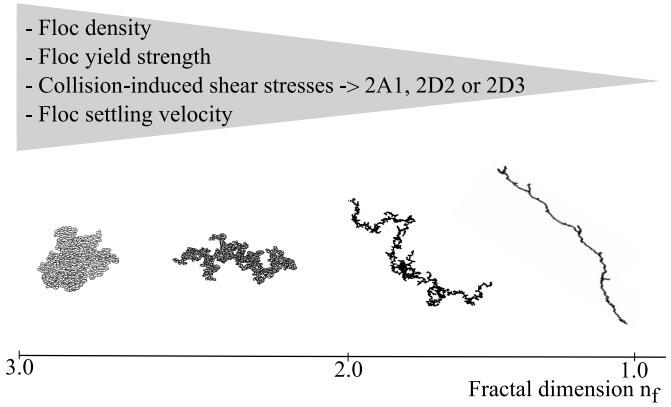

Figure 5.15: Decrease of floc density, floc yield strength, collision-induced shear stresses and floc settling velocity with decreasing fractal dimension n_f.

The numerical modeling of the annular flume experiments was conducted by the application of a variable, size dependent fractal dimension according to Khelifa and Hill (2006) (see chapter 2.3.4). In addition to the floc size D_f and the primary grain size D_g, the value of the fractal dimension n_f depends on two other parameters: the characteristic floc size D_{fc} and the characteristic fractal dimension n_{fc}. Khelifa and Hill (2006) recommend values of $D_{fc} = 2000\,\mu$m and $n_{fc} = 2.0$, if they are not measured or calculated. However, they also showed that the model results are sensitive to the parameter n_{fc}, taking values between 1 to 3. Thus, in case of uncertainty regarding the characteristic values, the range of n_{fc} has to be considered in models describing flocculation processes. In the presented studies, several values for

the characteristic fractal dimension were applied to take into account the effect of variations of n_{fc} on the flocculation processes (and therefore variations of the fractal dimension). n_{fc} was set to 1.4 (for the reference case), 1.7, 2.0, 2.3 and 2.6. The choice of these values is based on values which are commonly used in flocculation models. According to the measured particle diameters shown in figure 5.14, the value for the characteristic floc size was estimated to $D_{fc} = 15.0\,\mu$m and remained fixed for all computations. Figure 5.16 shows the calculated fractal dimensions n_f for the whole particle size spectrum depending on the value of the characteristic fractal dimension n_{fc}. For comparison, also the recommended values of Khelifa and Hill (2006) were applied.

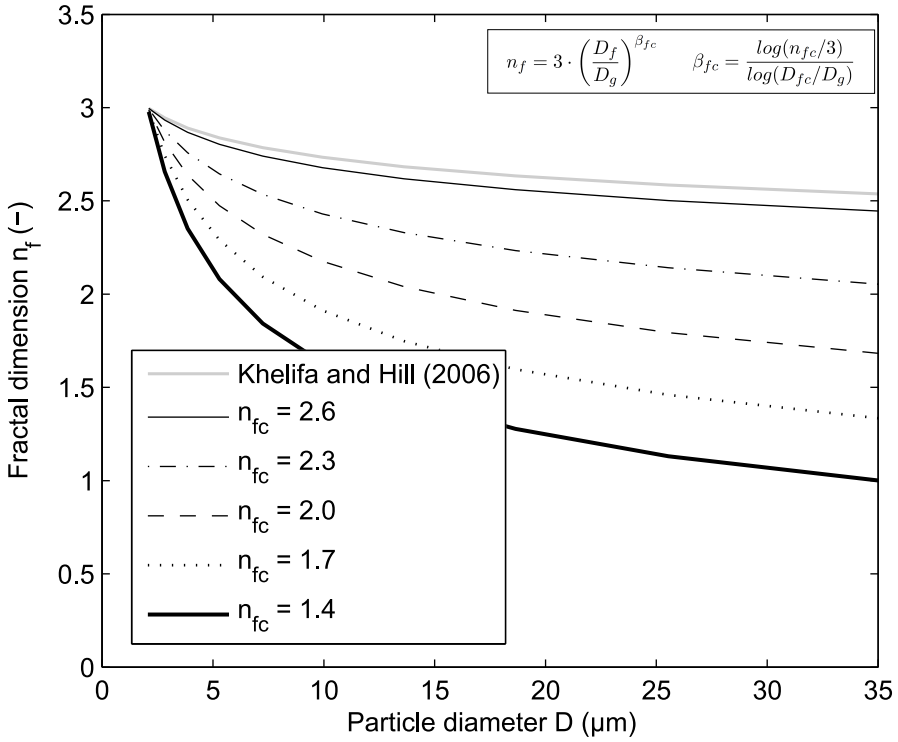

Figure 5.16: Calculated fractal dimensions as a function of particle size by using different characteristic fractal dimension n_{fc} ($D_{fc} = 15.0\,\mu$m) (Khelifa and Hill (2006): $n_{fc} = 2.0$, $D_{fc} = 2000\,\mu$m).

It can be seen that for all curves the fractal dimension decreases continuously from the maximum value of $n_f = 3$ for the smallest and solid, primary particles of size class $D_{10} = 2.1\,\mu$m to lower fractal dimensions as the size of flocs increases. The fractal dimension of the coarsest and weakest particles of size class $D_1 = 35\,\mu$m depends on the value of the characteristic fractal dimension. The higher n_{fc}, the higher the fractal dimensions for the whole floc size spectrum, i. e. the more compact and dense the particles are. Using the recommended values of Khelifa and Hill (2006) yields the most compact and dense particles with the highest fractal dimensions ranging between 2.5 and 3.0. In contrast, the reference case with $n_{fc} = 1.4$ results in fractal dimensions between 1.0 to 3.0. This floc size spectrum is therefore characterized by more porous and fragile flocs, which can break up into smaller flocs and particles more easily. From figure 5.16 it can be seen that the application of $n_{fc} = 2.6$ and $D_{fc} = 15\,\mu$m yields similar fractal dimensions for the used floc size spectrum as the recommended values of Khelifa and Hill (2006). This leads to the assumption, that these two settings will yield similar modeling results.

Table 5.4 shows the calculated particle densities for each size class (see equation 2.16), depending on the characteristic fractal dimension n_{fc}. It can be seen that the particle densities increase with higher values of n_{fc} since the particles get more compact with higher fractal dimensions. The table also depicts the decrease of floc density with increasing particle size.

Table 5.4: Particle densities ρ_j ($^{kg}/_{m^3}$) for each size class, depending on the characteristic fractal dimension n_{fc}.

Class index j	Diameter D_j (μm)	$n_{fc} = 1.4$	$n_{fc} = 1.7$	$n_{fc} = 2.0$	$n_{fc} = 2.3$	$n_{fc} = 2.6$
1	35.0	1006	1015	1039	1113	1343
2	25.6	1015	1034	1079	1190	1471
3	18.7	1038	1075	1150	1305	1625
4	13.6	1089	1155	1269	1466	1802
5	9.9	1194	1298	1451	1673	1995
6	7.3	1389	1526	1701	1919	2189
7	5.3	1699	1844	2004	2179	2369
8	3.9	2102	2201	2314	2417	2517
9	2.8	2483	2521	2556	2587	2615
10	2.1	2650	2650	2650	2650	2650

Figure 5.17 shows the calculated settling velocities according to Winterwerp (1998) by using different characteristic fractal dimensions. By comparison of the settling velocities it can be seen that the use of the recommended values of Khelifa and Hill (2006) yields the highest settling velocities in the range between $0.003\,^{mm}/_{s}$ and $0.24\,^{mm}/_{s}$, since the particle sizes imply the highest fractal dimensions and therefore the highest densities. The use of the lowest characteristic fractal dimensions $n_{fc} = 1.4$ results in the lowest settling velocities in the range between $0.003\,^{mm}/_{s}$ and $0.0089\,^{mm}/_{s}$. Consequently, for example for the coarsest particles of size $D_1 = 35\,\mu$m, the settling velocity values differ from each other by approximately a factor of 76.

The figure shows an increase in settling velocity with increasing particle sizes. However, for $n_{fc} = 1.4$, 1.7 and 2.0 the increase vanishes at a particle size of $7.3\,\mu$m, $9.9\,\mu$m and $18.8\,\mu$m, respectively. Beyond this floc size range with maximum settling velocity, the settling velocity is decreasing when the floc sizes increase further. The decrease in the settling velocity is caused by the simultaneous decrease of the density of flocs when their size becomes larger (see table 5.4). In addition, the drag force increases when the floc size increases and thereby reduces the settling velocity. For $n_{fc} = 2.3$ and 2.6, and for the values of Khelifa and Hill (2006) the settling velocity increases over the whole particle size range. In these cases, the increase in particle size dominates over the effect of a reduced density for the whole particle size range. For $n_{fc} = 1.4$, 1.7 and 2.0 however, the effect of a reduced floc density dominates over an increased particle size when a certain particle size is reached. This point is reached sooner, the lower the fractal dimension is.

It is obvious that the significant differences in the settling velocities will affect the computed deposition behavior of the suspended sediments. In figure 5.18 the measured and simulated suspended sediment concentrations over time in the same point (in the middle of one arbitrary cross-section, at the half of the water depth) are shown. First of all it can be seen that the simulation is very sensitive to different

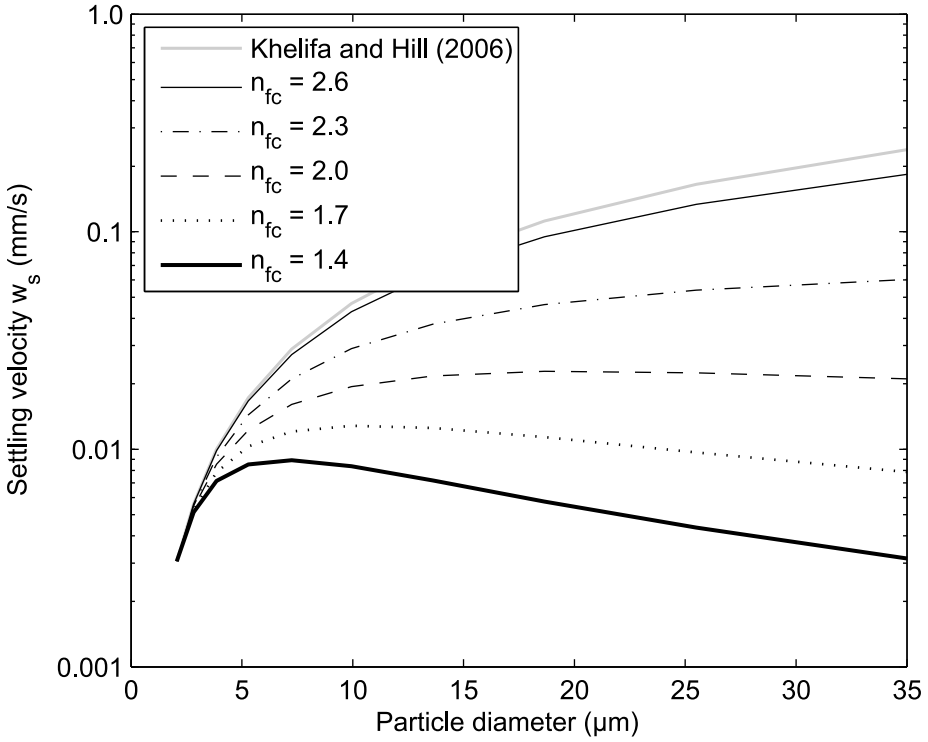

Figure 5.17: Calculated settling velocities according to Winterwerp (1998) as a function of particle size by using different characteristic fractal dimension n_{fc} ($D_{fc} = 15.0\,\mu$m) (Khelifa and Hill (2006): $n_{fc} = 2.0$, $D_{fc} = 2000\,\mu$m).

characteristic fractal dimensions. The concentrations are decreasing faster with higher values of n_{fc} (and therefore higher values of the fractal dimension n_f). These modeling results seem plausible because higher values of n_{fc} lead to higher settling velocities of the particles.

Using the values of Khelifa and Hill (2006) results in an almost complete deposition of the whole sediment mass after approximately 4 hours. In this case, the measured sediment concentrations are strongly under-predicted by the simulation. The application of $n_{fc} = 2.6$ yields, as previously expected, similar results since the settling velocities are in a similar value range. However, for instance for the reference case ($n_{fc} = 1.4$), after 5 hours there is still a sediment concentration of about 300 mg/l in suspension in the annular flume. This order of magnitude is roughly equivalent to the measured remaining sediment concentration after 5 hours (about 300 mg/l), and therefore yields the best agreement with the measured data compared with the other simulation results. Nevertheless, the initial decrease of the sediment concentration as it is indicated in the experiment is not simulated in the same way by any of the simulation results. In order to analyze how different parameter and boundary definitions in the numerical model potentially influence the initial decrease of the concentration, further sensitivity studies were carried out. These follow-up studies are presented in the sections below.

The numerical computations show that the simulation is very sensitive to the fractal dimension. Tendencies between simulated and measured suspended sediment concentration are most similar by using a characteristic fractal dimension of 1.4. This leads to the assumption that most of the particle sizes are characterized by a very fragile and open structure which can comparatively easily be disrupted either by turbulence or collision-induced shear stresses. On the basis of the recorded pictures of the suspended

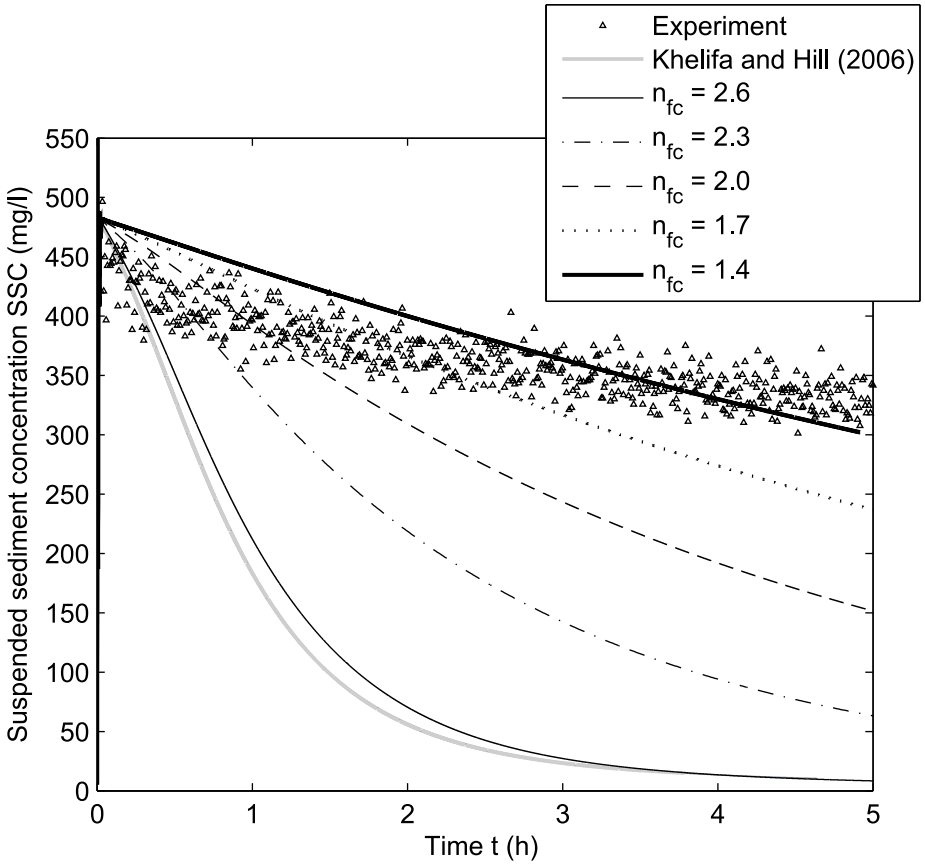

Figure 5.18: Measured and calculated suspended sediment concentrations over time by using different characteristic fractal dimension n_{fc} ($D_{fc} = 15.0\,\mu$m) (Khelifa and Hill (2006): $n_{fc} = 2.0$, $D_{fc} = 2000\,\mu$m).

sediment particles in figure 5.13, the structure of the detected flocs can not be estimated sufficiently reliably. Therefore advanced image analyses techniques and/or other additional measured values would be required. However, if the assumption of fragile flocs is right, these flocs and particles should be disrupted relatively easy. This in turn implies that computed particle diameters should on average be smaller when setting n_{fc} to 1.4 than by the application of higher fractal dimensions. A possibility to confirm the assumption of an open and porous structure, is to look on the computed particle diameters. If the development of the simulated floc diameters is in good agreement with measured floc sizes for $n_{fc} = 1.4$ as well, this would corroborate the assumption of porous and open kaolinite particles.

In figure 5.19, the measured mean diameter and the calculated mean diameters by using different characteristic fractal dimensions are presented over 5 hours. In the experimental results, the peak of the mean floc diameter (=11 μm) after 17 minutes indicates aggregation. Then a decrease of the mean diameter follows which is likely caused by the deposition of the larger particles. This increase in floc size followed by a decrease in aggregate size appears also for all calculation results. Thus, aggregation processes are simulated for all calculation runs.

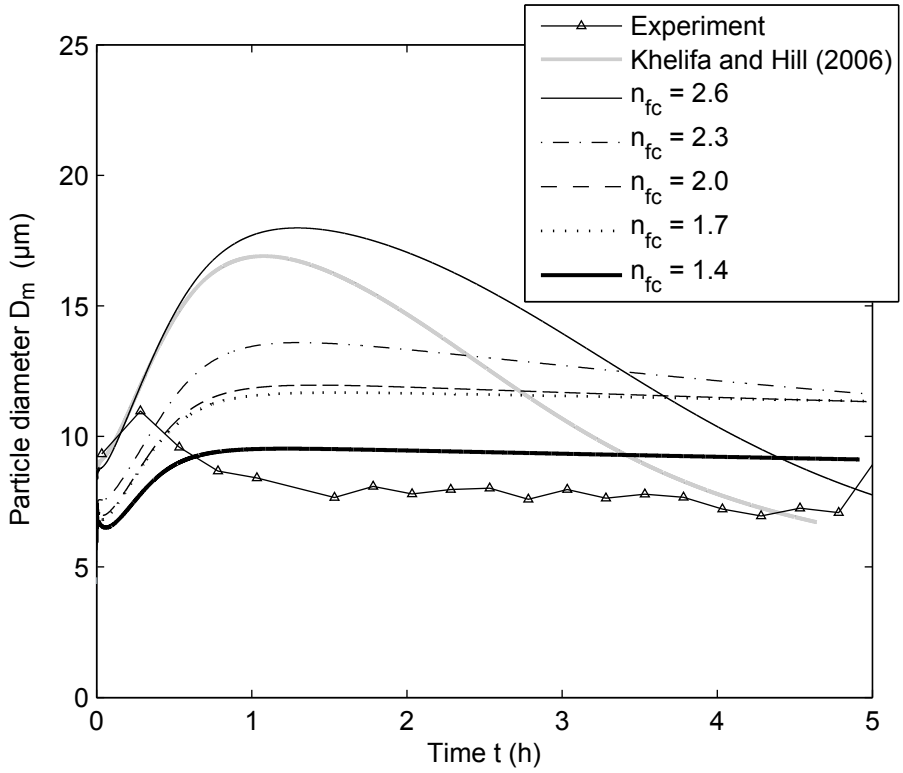

Figure 5.19: Measured and calculated mean particle diameters over time by using different characteristic fractal dimension n_{fc} ($D_{fc} = 15.0\,\mu$m) (Khelifa and Hill (2006): $n_{fc} = 2.0$, $D_{fc} = 2000\,\mu$m).

In figure 5.19, the value of the characteristic fractal dimension determines the maximum floc size, the time to achieve the maximum floc size and the slope following the peak. The best result in comparison to the experiment is reached for a characteristic value of $n_{fc} = 1.4$. For this case, the mean diameter is increasing to a maximum value of 9.5 μm, as aggregation processes take place, and then is decreasing only very slightly. For $n_{fc} = 2.6$ in contrast, the mean diameter increases to a maximum value of 18 μm due to aggregation, then the mean particle size is decreasing much steeper compared to $n_{fc} = 1.4$. The

stronger decrease in particle size results from the deposition of the larger, faster-settling particles leaving the smaller, lower-settling particles in suspension. The higher maximum mean diameters for higher values of n_{fc} can be attributed to the more flow resistant particles, since these particles imply higher yield strengths and therefore can not be disaggregated that easily in smaller entities.

Table 5.5 shows the particle yield strengths of each size class depending on the characteristic fractal dimension, and the possible collision outcomes due to two-body collisions. Table 5.6 shows the minimum and maximum flow-induced shear stress τ_u in the model domain, as well as the shear stress in the grid cell of the model results. By comparison of the fluid shear stresses with the particle yield strengths, the particle sizes which can potentially be disaggregated by fluid shear, i. e. whose yield strengths are smaller than the fluid shear stress, are highlighted in table 5.5. Particle size classes which will be disrupted by fluid shear in every grid cell, i. e. whose yield strength is smaller than the minimum fluid shear, are highlighted in dark grey. Size classes which will break up by turbulence in the output cell are highlighted in lighter grey. And particle size classes which may be disaggregated by the maximum fluid shear stresses in one of the grid cells in the model domain are marked in light grey.

Table 5.5: Particle yield strengths τ_j ($^{\mathrm{N}}/_{\mathrm{m}^2}$), depending on the characteristic fractal dimension n_{fc}. The last row shows the possible collision outcomes due to two-body collisions. Size classes which can be broken up by flow-induced shear stresses are highlighted.

Class index j	Diameter D_j (μm)	$n_{fc} = 1.4$	$n_{fc} = 1.7$	$n_{fc} = 2.0$	$n_{fc} = 2.3$	$n_{fc} = 2.6$
1	35.0	0.0057	0.0063	0.0074	0.0100	0.0211
2	25.6	0.0111	0.0125	0.0149	0.0209	0.0486
3	18.7	0.0219	0.0249	0.0307	0.0451	0.1185
4	13.6	0.0437	0.0509	0.0650	0.1021	0.3155
5	9.9	0.0897	0.1079	0.1447	0.2492	0.9665
6	7.3	0.1927	0.2432	0.3516	0.6943	3.7832
7	5.3	0.4537	0.6200	1.0153	2.5193	24.1875
8	3.9	1.3448	2.1528	4.5194	17.6917	526.9841
9	2.8	10.0135	25.7287	113.6357	1744.7061	1550677.0850
10	2.1	non-breakable				
Collision outcomes		2A1	2A1	2A1	2A1	2A1

Table 5.6: Calculated flow-induced shear stresses τ_u ($^{\mathrm{N}}/_{\mathrm{m}^2}$) on the particles within the whole model domain.

Flow-induced shear stresses $\tau_u \approx \mu\sqrt{\frac{\epsilon}{\nu}}$	($^{\mathrm{N}}/_{\mathrm{m}^2}$)
Minimum	0.0071
In output cell ($i = 250$, $j = 10$, $k = 6$)	0.0133
Maximum	0.0459

Table 5.7 shows the minimum and the maximum collision-induced shear stresses $\tau_{ik,k}$ on the particles depending on the characteristic fractal dimension. Even the comparison of the maximum collision-induced shear stress with the respective floc yield strengths values shows that all particles' yield strengths are

higher than the maximum collision-induced shear stresses for all applied characteristic fractal dimensions, partly by some orders of magnitude. Hence, two colliding particles will always aggregate into one new larger particle (collision outcome: type 2A1). Consequently, modeled disaggregation of flocs is caused only by fluid shear stresses due to turbulence.

Table 5.7: Minimum and maximum collision-induced shear stresses $\tau_{ik,k}$ ($^{N}/_{m^2}$) on the particles depending on the characteristic fractal dimension n_{fc}.

Collision-induced shear stresses $\tau_{ik,k}$	$n_{fc} = 1.4$	$n_{fc} = 1.7$	$n_{fc} = 2.0$	$n_{fc} = 2.3$	$n_{fc} = 2.6$
Minimum ($^{N}/_{m^2}$)	3.250e-9	4.803e-9	1.077e-8	4.250e-8	5.521e-8
Maximum ($^{N}/_{m^2}$)	2.349e-4	2.369e-4	2.427e-4	2.615e-4	5.705e-4

For example, adopting $n_{fc} = 2.6$ leads to more compact particles, which can not be disrupted by flow-induced stresses that easily, compared to weaker and more open particles with lower fractal dimensions. For $n_{fc} = 1.4$ the four largest size classes (marked in grey) with the lowest yield strengths will undergo disaggregation in those grid cells, where the yield strengths are smaller than the fluid shear stresses. Size classes 5 to 10 are always strong enough to withstand the fluid stresses. The first four and weakest size classes are subjected to disaggregation by fluid-shear and contribute to a shifting of particle mass in the smaller size classes. In the case of $n_{fc} = 2.6$, only the coarsest and weakest size class $D_1 = 35\,\mu$m can disaggregate. Thus, the mass shifting in smaller size classes due to turbulence-induced disaggregation is not that significant compared to $n_{fc} = 1.4$. This is the reason that higher fractal dimensions result in larger mean diameters.

In figure 5.19, the steeper slope of the declining D_m curve for higher fractal dimensions is a result of the higher particle densities, leading to higher settling velocities of the particles. For example, the application of the values of Khelifa and Hill (2006) yields a maximum mean diameter of 16.9 μm, similar to the maximum mean diameter for $n_{fc} = 2.6$ ($D_m(max) = 18\,\mu$m). For both cases only the coarsest particles D_1 can be broken by fluid shear. Also for both cases only collision outcome of type 2A1 will occur. This means that two colliding particles will aggregate into one new larger floc (see chapter 4.2.2). Therefore, only the different settling velocities are the reason for the deviating calculated mean diameter curves. The higher settling velocities, when adopting Khelifa and Hill (2006), lead to a faster settling of the larger particles, which, as a consequence, are no longer available for further undergoing aggregation. In this case, deposition dominates over aggregation earlier, so that the maximum mean diameter is smaller than for $n_{fc} = 2.6$. The higher settling velocities, when using Khelifa and Hill (2006), are also the reason for the steeper slope beyond the maximum floc size.

It can be summarized that by adopting a characteristic fractal dimension of $n_{fc} = 1.4$ the best agreement with the measured floc sizes is obtained. For higher fractal dimensions the calculated particle sizes are over-predicted up to a factor of about 2. The best agreement with measured sediment concentrations was also found for $n_{fc} = 1.4$ (see figure 5.18). The results corroborate the assumption of an open and porous floc structure of kaolinite particles under the given flow and fluid conditions in the annular flume. An open, loose and easily disrupted structure in turn indicates that the kaolinite particles form a so called card-house structure (edge to face mode) or a chain-like structure (edge to edge mode) (see chapter 2.3.3).

Simulated Flocculation Processes by Shifting of Particle Mass between the Size Classes
The flocculation processes are computed in SSIIM by shifting mass between the size classes. In the following, this is illustrated exemplarily in figure 5.20 for the case of $n_{fc} = 1.4$. Using $D_{fc} = 15.0\,\mu$m and $n_{fc} = 1.4$ results only in the aggregation type 2A1, i. e. two colliding particles are always strong enough to resist the collision-induced shear stress and form larger aggregates. Disaggregation is only caused by flow-induced stresses, which can lead to a break-up of the weakest particles of size classes 1, 2, 3 and 4 (see table 5.5). Figure 5.20 shows the temporal development of the concentrations of each size class. The decrease of the concentration of the smaller size classes 7, 8, 9 and 10 and the shifting of mass into the larger particle size classes 4, 5 and 6 illustrate aggregation of type 2A1. Size class 1 is destroyed by fluid shear in every grid cell, whereas size class 2 is disaggregated only in some of the cells, e. g. in the output cell (see table 5.5). This results in an abrupt decrease of the concentration in size class 1 and 2 in the first few seconds (that is the reason why there are no curves shown for size class 1 and 2 in figure 5.20) and in a shifting of the concentration into the smaller size classes. Particle size class 3 and 4 can also break up due to fluid forces in grid cells where the yield strengths are smaller than the respective fluid shear stress. But concurrently, mass is shifted into these classes by the aggregation processes of the smaller aggregates resulting in an increase of the concentrations. Hence, in figure 5.20 the shifting of concentrations has to be interpreted as a result of aggregation, break-up due to fluid shear, as well as simultaneously occurring deposition. These processes overlap continuously, but dominant mechanisms can be estimated over time. It can be seen that flocculation processes are most significant for about the first hour of the simulation. Afterwards aggregation and floc-break-up further occur, but are in equilibrium. Deposition of the sediment material is then dominant.

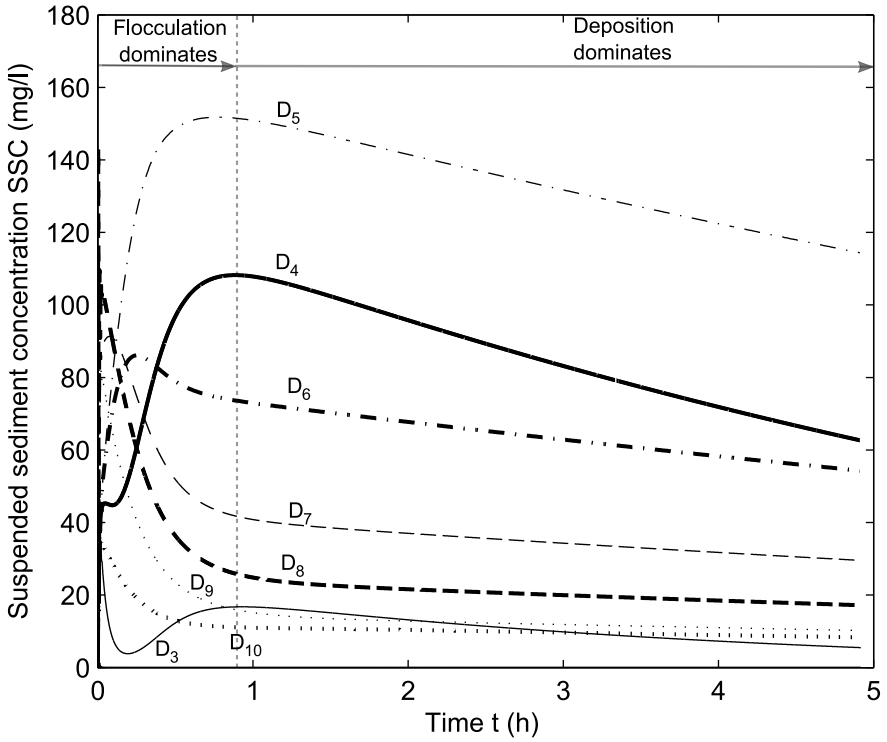

Figure 5.20: Calculated temporal development of the concentrations in each particle size class due to aggregation, flow-induced break-up and deposition by using a characteristic fractal dimension of $n_{fc} = 1.4$ ($D_{fc} = 15.0\,\mu$m).

The numerical test and validation studies presented in this chapter demonstrate that the implemented flocculation algorithm gives reasonable results, and flocculation processes in the annular flume can be modeled in a physically correct way. Within the numerical studies, it could also be shown that the flocculation and deposition behaviour is very sensitive to variations in the fractal dimension. On the one hand, the fractal dimension determines whether aggregation or disaggregation occur due to particle collisions and turbulence, and thereby strongly affects the time-evolution of the floc size distribution. On the other hand, the fractal dimension significantly influences the particle density, which in turn has a major impact on the settling velocity. Within the tested range of settling velocities it was shown that the settling velocity is a key factor when modeling the development of the suspended sediment concentration. The higher the fractal dimension of the particles, i. e. the more dense and compact the particles are, the higher the settling velocities are predicted and the faster the concentration will obviously decrease. Consequently, uncertainties regarding the fractal dimension can have a major influence on the modeled floc sizes and especially on the floc settling. Hence, reliable measurement data or theoretical expressions are required for the fractal dimension to model the complex cohesive transport processes from laboratory in an accurate way.

The presented results show, that for future research investigations on flocculation processes in laboratory it should be considered to take into account also the fractal dimension within the measurements. The estimation of the floc structure by measurement data would contribute to a better understanding of the observed processes in the laboratory. A common way to measure the fractal dimension is to use advanced optical techniques/image analysis. Experimental investigations on floc structure by the use of image analysis were for instance conducted by Spicer and Pratsinis (1996). They estimated a perimeter-based fractal dimension of the flocs by using a log-log plot of the floc perimeter and the cross-sectional area. It was found that during the initial stages of flocculation, the flocs first become more porous and open, while at steady state the floc structure becomes more compact. Flow-induced shear stresses leading to floc break-up/restructuring were given as the reason for this. Chakraborti et al. (2003) estimated the two-dimensional fractal dimension from optical sampling of flocs by using digital image processing software as well. They studied the effect of pixel resolution (ratio of circle diameter to pixel length) to determine the aggregate size and the two-dimensional fractal dimension. They found that for aggregation of an initially monodisperse suspension, the fractal dimension decrease over time in the initial stages of floc formation. Chakraborti et al. (2003) suggest to take into account these temporal changes in fractal dimensions, along with changes in aggregate size, when describing a dynamic aggregation process, and especially when modeling temporal changes in particle size distribution. Kumar et al. (2010) used measured values of the settling velocity and the floc diameter to calculate the floc submerged specific gravity, which in turn was used to compute the fractal dimension. For the definition of the floc diameter a camera system with image analyses was used. They observed two ranges of behavior in terms of the fractal dimension of flocs at a constant turbulent shear rate. In the first stages of flocculation, a variable fractal dimension was needed to describe the submerged specific gravity as a function of floc size. In the second region, when flocs have reached a certain floc size, a constant fractal dimension was found to suffice for the description of the submerged specific gravity. Various methods to measure the fractal dimension and geometric dimensions/shape factors can be found for instance in Billiones et al. (1999).

5.3.2.2 Time Step

The time step is an important factor in numerical modeling, since it affects the CPU time. Modeling flocculation requires a short time step as the small-scale mechanisms act on short time scales compared to overall processes on macro-scale, such as sediment transport or deposition. Short time steps in turn are associated with longer CPU times. When defining the time step, it has to be considered that aggregation and floc break-up occur simultaneously for all size classes in the implemented flocculation algorithm. This might lead to mass conservation errors when too large time steps are defined and therefore might cause modified model results. Hence, in order to avoid mass conservation errors or to keep them as small as possible, short time steps should be applied. The objective of this sensitivity study was to investigate how short the time step should be chosen in order to ensure that the simulation results are not affected by the time step, or respectively that mass conservation errors are in an acceptable range.

For the reference case a short time step of $\Delta t = 1\,\text{sec}$ was used. The sensitivity of the implemented flocculation algorithm towards the time step was tested by using three larger time steps (all other parameters and boundary conditions remained the same): 2 sec, 5 sec and 10 sec. Figure 5.21 shows the measured and the computed sediment concentrations. The sensitivity analysis illustrates that with a time step of 5 and 10 sec, the initial sediment concentration is inadequately predicted. The deviations from the actual defined initial concentration of $C_0 = 500\,\text{mg/l}$ are in the order of 50 and 100 mg/l, respectively. This amounts to relatively high mass conservation errors of about 10 % and 20 %, respectively. The results for the reference case with $\Delta t = 1\,\text{sec}$ and for a time step of $\Delta t = 2\,\text{sec}$ yield initial concentrations of $C_0 = 480\,\text{mg/l}$ and $C_0 = 470\,\text{mg/l}$, and therefore give much smaller mass conservation errors of about 4 % and 6 %, respectively.

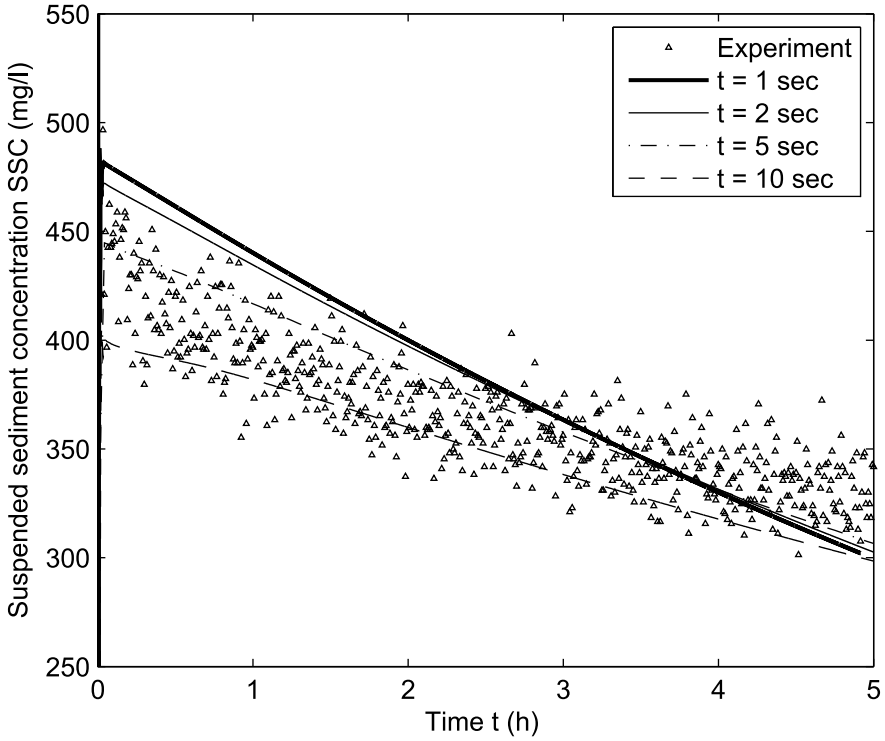

Figure 5.21: Measured and calculated suspended sediment concentrations over time by using different time steps Δt.

Figure 5.22 depicts the measured and simulated mean particle diameters. The simulated mean particle diameter increases with a larger time step, since more particles are shifted into the coarser size classes. In table 5.8, the concentrations of size class 3 ($D_3 = 18.7\,\mu$m) are examplarily shown after $t = 2\,$h, i. e. when the flocculation processes are assumed not to dominate any more, for different time steps. The comparison of $\Delta t = 1\,$sec ($C = 13\,$mg/l) with $\Delta t = 10\,$sec ($C = 69\,$mg/l) shows that the deviations amount to about 56 mg/l, i. e. for a time step of $\Delta t = 10\,$sec the concentration in size class 3 is more than 5 times higher than the concentration in this class for $\Delta t = 1\,$sec. This means that for $\Delta t = 10\,$sec more particles exist in one of the coarser size fractions which results in a higher mean diameter.

In addition, figure 5.22 shows a temporal shifting with different time steps. The peak in the computed mean diameter is reached later for larger time steps. This signifies that the aggregation process is delayed with larger time steps, whereas for smaller time steps the aggregation process occurs faster. The temporal shifting is a direct consequence of the larger time step: in the first time step a particle collision results in a shifting of particle mass into coarser size classes. In the following time step these newly formed larger particles can aggregate with other size classes and form again new particles which will be shifted in even coarser size classes. These newly formed particles in turn can collide only in the next time step, and so on. For the application of shorter time steps this process occurs much faster than for larger time steps.

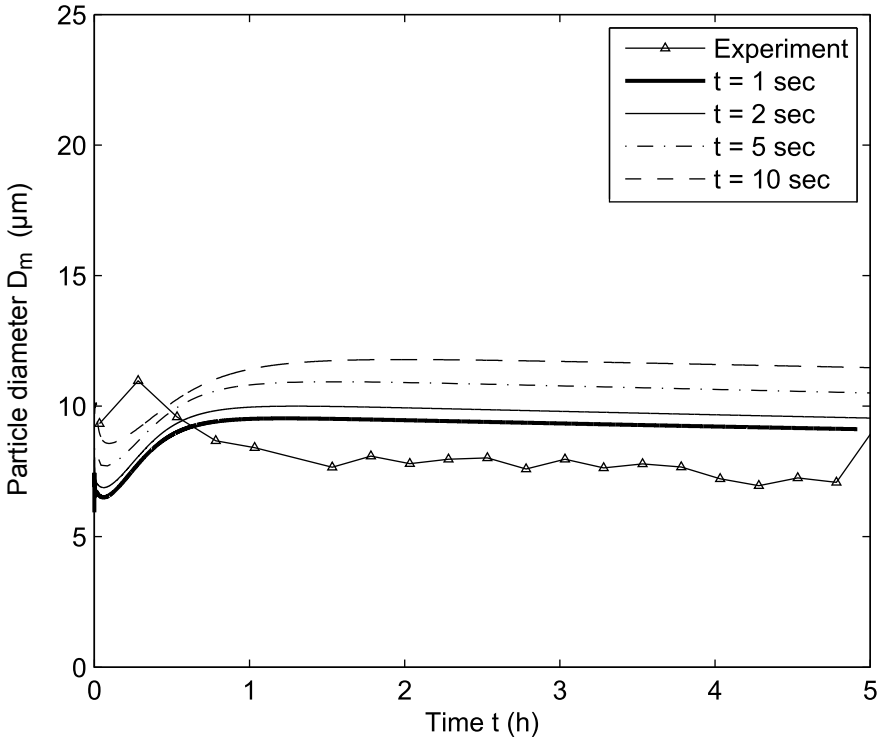

Figure 5.22: Measured and calculated mean particle diameters over time by using different time steps Δt.

Table 5.8: Calculated suspended sediment concentrations SSC after $t = 2\,\text{h}$ in size class 3 by using different time steps Δt.

Time step Δt (sec)	SSC in size class 3 ($^{\text{mg}}/_{\text{l}}$)
1	13
2	22
5	46
10	69

The sensitivity studies show that even a time step of $\Delta t = 1\,\text{sec}$ is not chosen short enough to yield an insensitivity of the model results towards the time step. There are still distinctions in simulated particle diameters and suspended sediment concentrations in comparison to a longer time step of $\Delta t = 2\,\text{sec}$. However, it can also be seen that the deviations between these two computations are not significant. A mass conservation error of 4 % for $\Delta t = 1\,\text{sec}$ was assumed to be in an acceptable range, in particular with a view to even higher CPU times when using time steps smaller than one second. For example, in the case of using $\Delta t = 1\,\text{sec}$, CPU time is around 44.5 hours for 5 hours of real time simulation (16 cores, Intel(R) Xeon(R) CPU E5-2640 v3, 2.6 GHz). A time step of $\Delta t = 10\,\text{sec}$ requires a CPU time of about 4.2 hours for the same simulation time. Due to the excessive computation time, the time step of one second was not further lowered and was applied for the follow-up sensitivity studies.

For future flocculation modeling in SSIIM, it should be investigated how the CPU time can be reduced for long-term modeling of cohesive sediments while simultaneously ensuring mass conservation. Teisson (1991) for example points out that an error of $5 \cdot 10^{-4}$ % per time step on the mass conservation of suspended sediment can lead to an error of 10 % per tide in the long term simulation of the Loire estuary, if no mass correction is considered. A satisfactory solution in this issue could be a sub-time step mentioned by Winterwerp (2002). Through a sub-time step, the advection-diffusion equation in combination with a flocculation model can be solved efficiently by the application of a smaller effective time step than that for the hydrodynamic equations and the overall processes. Verney et al. (2011) use a dynamically-adaptable varying time step, which prevents more particles aggregation or disaggregation than exist in each class, to optimize the computational costs. In future, these possible methods need to be tested for the implemented flocculation algorithm in SSIIM.[2]

5.3.2.3 Initial Floc Size

For the reference case run, initial concentrations in the size classes were chosen randomly among the size classes to achieve a total initial concentration of $C_0 = 500\,^{\text{mg}}/_{\text{l}}$ (see table 5.3). This initial concentration distribution yields an initial mean floc diameter of 7.7 μm. A different choice of initial concentrations in the size classes will result in a different initial floc size. The sensitivity towards the initial particle size

[2] Currently, in SSIIM 1 the flocculation algorithm is called as many times as the number of defined size classes for each time step and each grid cell. Actually, one single call per time step and grid cell would be sufficient to compute the mass fluxes for all size classes. For future case studies in SSIIM 1 which focus on flocculation simulation of laboratory experiments, a single call should be technically implemented in SSIIM 1 in order to reduce CPU time by a multiple. In SSIIM 2, the flocculation algorithm is called once for each time step and each grid cell and therefore runs much faster.

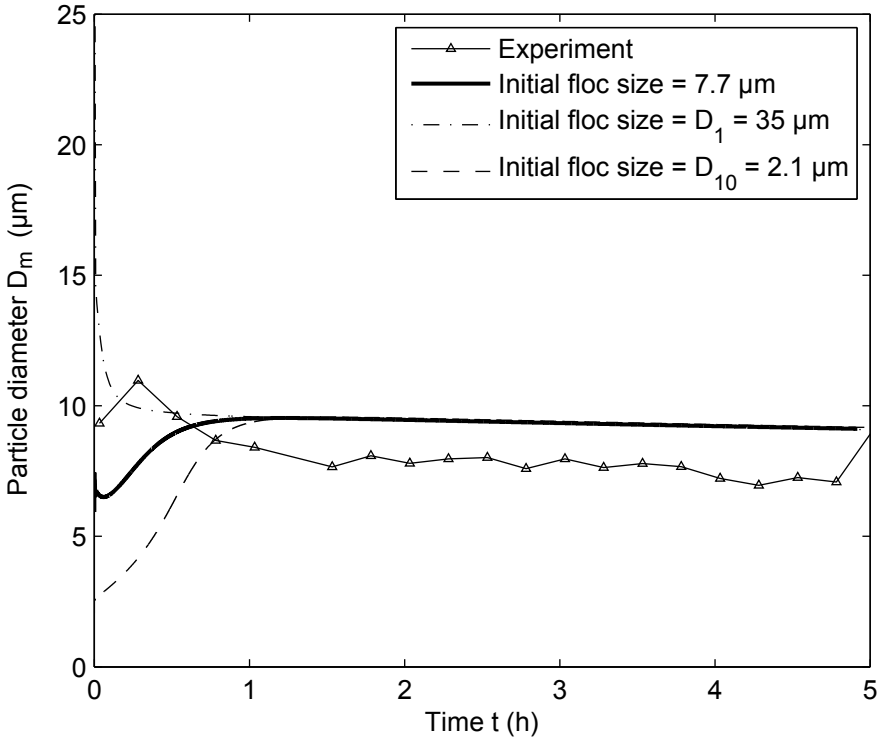

Figure 5.23: Measured and calculated mean particle diameters over time by adopting different initial floc sizes.

distribution was studied by two additional simulations for which extreme values were assumed. On the one hand, it was assumed that the initial particles consist solely of the coarsest size class $D_1 = 35.0\,\mu$m. On the other hand, the total initial concentration was allotted to the smallest size class $D_{10} = 2.1\,\mu$m.

Figure 5.23 shows the computed mean particle diameters when using different initial floc sizes. It can be seen that the initial floc size affects the time to reach an equilibrium floc size, but not the final floc size. When an equilibrium floc size is reached, the final floc sizes do not differ further. For an initial floc size of $D_{10} = 2.1\,\mu$m, an equilibrium stage is reached after about 1.1 h, whereas for an initial floc size of $D_1 = 35.0\,\mu$m aggregation and floc break-up appear to be in balance already after 0.3 h. In comparison, for the reference case with an initial floc size of 7.7 μm the flocculation processes are most significant for about the first hour of the simulation, i. e. the time period is similar to an initial floc size of 2.1 μm.

Figure 5.24 emphasizes the differences in the temporal development of the concentrations and the particle size distribution when the initial floc size is $D_{10} = 2.1\,\mu$m and $D_1 = 35.0\,\mu$m, respectively. For a better clarification in terms of the affected size classes different scales for the concentrations were used in the figures. When setting an initial particle size distribution with all particles in the finest size class 10, the aggregation process takes longer, since more size classes are affected by aggregation at the initial flocculation stage. As shown in the figure above, an equilibrium stage is reached after about 1.1 h. In contrast, when the initial particles consist only of the coarsest size class 1, the flocculation processes take place much faster and are at equilibrium after about 0.3 h. The figures show that the temporal development of the concentration as well as the particle size distribution differ until an equilibrium stage is reached.

When comparing both temporal developments in figure 5.24, it also becomes apparent that the aggregation mechanism occurs much slower than the floc break-up process due to turbulence-induced shear stresses. For example, in figure 5.24 (a) in the first time step, aggregation processes occur by shifting the total particle mass from size class 10 into size class 9 and other coarser size classes. In the next time step, aggregation leads to further mass shifting of the newly formed particle mass into even coarser size classes and so on. This aggregation process continues until some of the particle mass is shifted into size class 3. No further mass shifting into the coarser size classes 1 and 2 occurs, since *all* particles in these two weakest size classes are immediately destroyed by turbulence in the output cell (see table 5.5). This is illustrated by the absence of the concentration curves for D_1 and D_2. The aggregation mechanism is modeled as a time-dependent process which depends on the collision efficiency (see chapter 4.2).[3] In contrast, disaggregation by fluid shear is modeled as a time-independent mechanism, since *all* particles are immediately removed when the particle yield strength is smaller than the turbulence-induced shear stresses. In figure 5.24 (b) these tendencies are indicated in the initial simulation stages: in the first time step all particles are in size class 1, which all are immediately destroyed by fluid shear and shifted into size class 2 and other finer size classes. In the second time step, all newly formed particles from size class 2 will also be destroyed by fluid shear in the output cell (see table 5.5) and shifted towards smaller size classes. That is the reason why there is a rapid decrease in the concentrations in size class 1 and 2. However, after about one hour all three simulation results achieve nearly the same particle size distribution and thus the same mean floc size of $D_m = 9.6\,\mu$m.

The presented sensitivity studies show that the lack of knowledge of the initial particle size distribution is not relevant to the model results as far as the steady state is the essential study objective. Assuming that particles do not settle rapidly out of suspension and have sufficient time to reach an average, steady-state equilibrium size (i. e. the water depth or the length of the flow path are essential), flocs should theoretically grow to a similar equilibrium floc size independent of the initial size distribution for a given flow situation. If the settling velocities of the involved size fractions differ strongly, also the particle size distributions at equilibrium stage can differ significantly depending on the initial floc size. This will play a role, for example, when simulating flocculation for short flow paths or for transient sediment calculations.

The presented simulation results are supported by Son and Hsu (2008). Their model results were insensitive to the uncertainty of the initial floc size as far as the final floc size was concerned. The flocculation model from Verney et al. (2011) was also found to be only weakly sensitive to variations in the initial distribution except during the initial aggregation stage. Maerz et al. (2011) showed that the model lost the dependence on the initial conditions after 2 to 3 hours.

Figure 5.25 shows the computed sediment concentrations when using different initial floc sizes. It can be seen that different initial floc sizes result in different initial concentrations. This is caused by mass conservation errors.

[3] A time-dependent modeling applies also for particle disaggregation due to collision-induced shear stresses (i. e. for the collision outcome types 2D2 and 2D3).

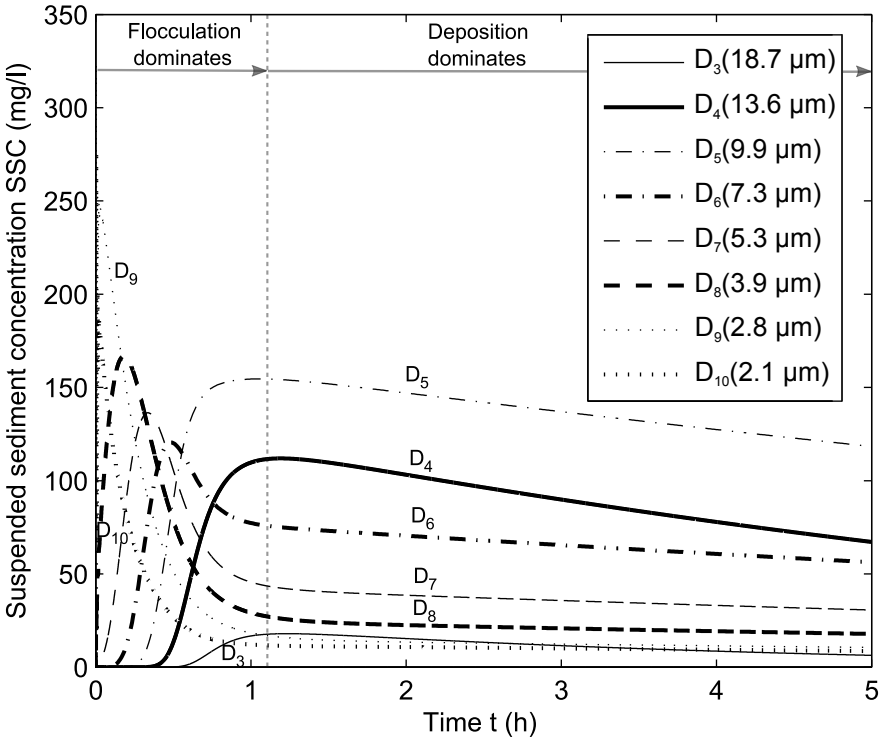

(a) Initial floc size $D_{10} = 2.1\,\mu$m

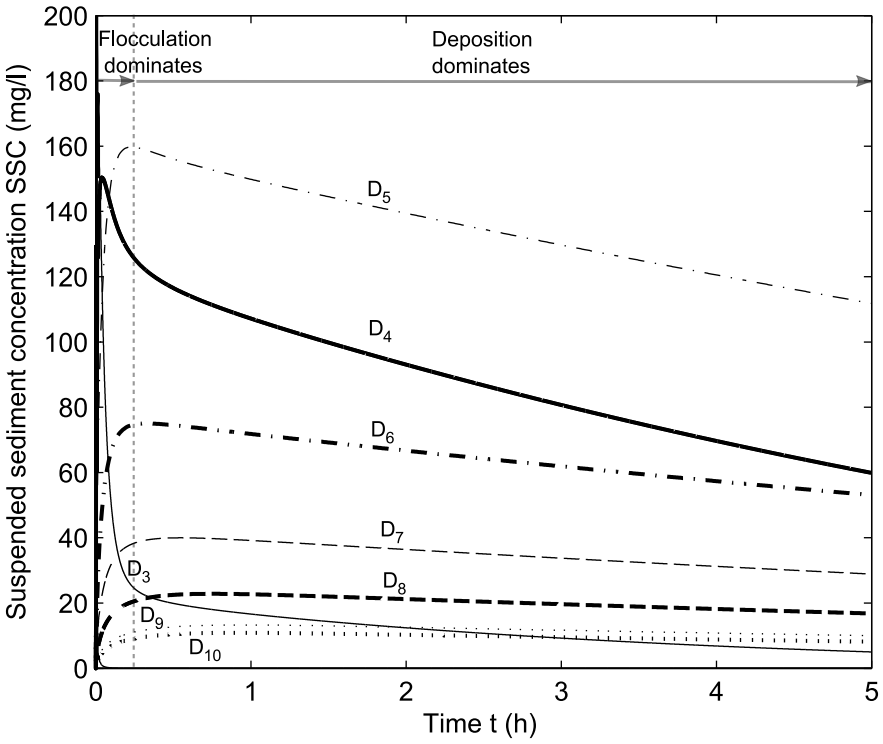

(b) Initial floc size $D_1 = 35.0\,\mu$m

Figure 5.24: Calculated temporal development of the concentrations in each particle size class due to aggregation, flow-induced break-up and deposition based on different initial floc sizes.

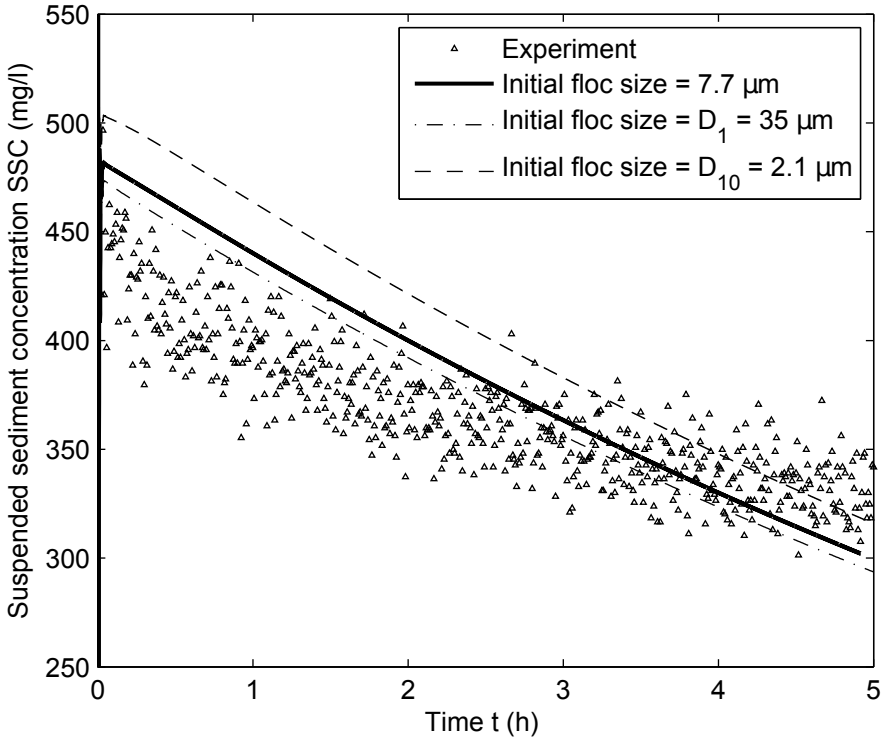

Figure 5.25: Measured and calculated suspended sediment concentrations over time by adopting different initial floc sizes.

Within the implemented size distribution changes algorithm, more particles can be removed from the affected size class than actually are available depending on the time step and the amount of particles which can be disaggregated by turbulence-induced shear stresses. In the case that a size class would receive a negative number of particles when particle mass is subtracted from the respective size class, the simulation would crash. Hence, in the herein developed and in SSIIM implemented flocculation algorithm a potential negative mass is prevented by forcing the size classes, which would get negative mass values, to zero concentrations. In this case, a lower negative mass flux for the respective size classes is computed than is theoretically determined by the flocculation algorithm. In order to compensate the reduced mass fluxes and to maintain mass conservation, also in all other classes the concentration should be lowered. However, this was not implemented yet in the flocculation algorithm and should be taken into account when modeling flocculation. For an initial floc size of $D_1 = 35.0\,\mu$m, the mass error (5 %) is slightly larger than for the reference case (4 %). If all particles consist of the finest particles with $D_{10} = 2.1\,\mu$m, the mass conservation error is zero. The results in these study clarify again that in future the flocculation algorithm has to be optimized with respect to mass conservation, especially for long-term computations.

5.3.2.4 Aggregation Coefficient

In most models, the aggregation efficiency α_a accounts for the fraction of two-body collisions that results in bonding between the colliding particles and is equal to the fraction (by weight) of sediment exhibiting cohesion (see chapter 3.2.1). Within the implemented flocculation algorithm, α_a is used to compute the collision efficiency N_{ik}, i. e. the number of collisions between two particles per volume and time step (see

equation 4.18). Thereby, it is assumed that every collision results in cohesion at the particle contact point. The number of collisions in turn determines the mass concentration changes for the affected size classes due to two-body collisions (see chapter 4.2.2).

The value for α_a can range between $\alpha_a = 0$ and 1.0. For the reference case the aggregation efficiency α_a was set to 1.0, since it was assumed that cohesive forces are strong between the particles due to a very small elemental grain diameter of kaolinite ($D_g = 2.1\,\mu$m). However, since the parameter depends not only on the degree of cohesion, but also on the water chemistry (pH, salinity, etc.), the sensitivity towards this parameter needs to be tested. In order to account for uncertainties towards this calibration parameter, the simulation results for 4 values of $\alpha_a = 1.0$, 0.7, 0.5 and 0.3 have been compared.

Figure 5.26 illustrates the calculation results in terms of the mean particle diameter. Figure 5.27 shows the temporal development of the concentrations in each particle size class for an aggregation efficiency of 0.3 and 1.0, respectively. From figure 5.26 it can be seen that the aggregation factor influences the aggregation process in terms of the temporal floc size evolution and the maximum floc size.

Adopting $\alpha_a = 0.3$ yields lower mass concentration changes in the affected size classes, thus a slower aggregation and a smaller maximum floc size compared to $\alpha_a = 1.0$. Aggregation dominates for more than two hours for $\alpha_a = 0.3$, subsequently deposition dominates (see figure 5.27 (a)). However, for $\alpha_a = 1.0$ the time required for aggregation is less than one hour, then a maximum floc size is reached (see figure 5.27 (b)). The temporal offset until equilibrium is therefore between 1 and 1.5 hours.

The temporal shift of the computed particle sizes does not significantly affect the temporal concentration development, as seen in figure 5.28. The simulation curves are almost identical. Since there are no major deviations concerning the sediment concentration distribution among the size classes and due to the fact that the settling velocities differ not significantly among the particle size spectrum, the deposition behavior is nearly the same. Hence, while the simulation results are sensitive to the aggregation efficiency in terms of the temporal development of the flocculation process and slightly in terms of the maximum floc size, the computed concentrations are insensitive towards the aggregation efficiency in the presented case study. However, this is valid only when the settling velocities of the affected particles are in a similar value range and when the sediment concentration distribution among the size classes does not vary strongly depending on α_a. If, for instance, the same computations would be carried out while applying higher fractal dimensions, this would lead to stronger differences in the calculated settling velocities among the size classes (e. g. when the settling velocities are calculated by using D_{fc} and n_{fc} values recommended from Khelifa and Hill (2006), see figure 5.17). In this case one would expect that also slightly different concentration distributions among the size classes will contribute to diverging computed sediment concentrations depending on the aggregation efficiency.

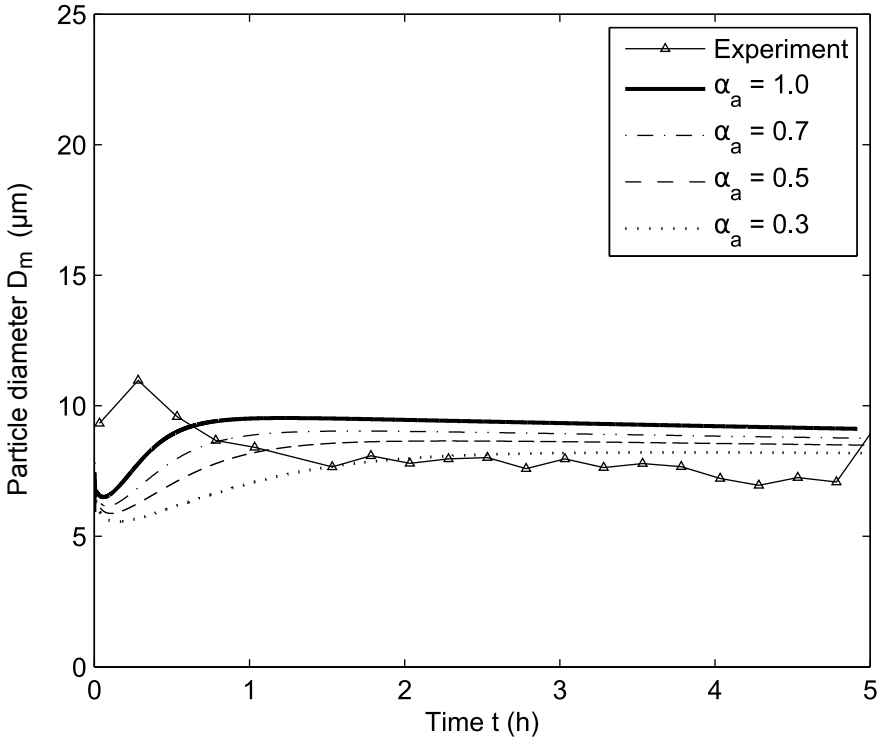

Figure 5.26: Measured and calculated mean particle diameters over time by using different values for the aggregation efficiency α_a.

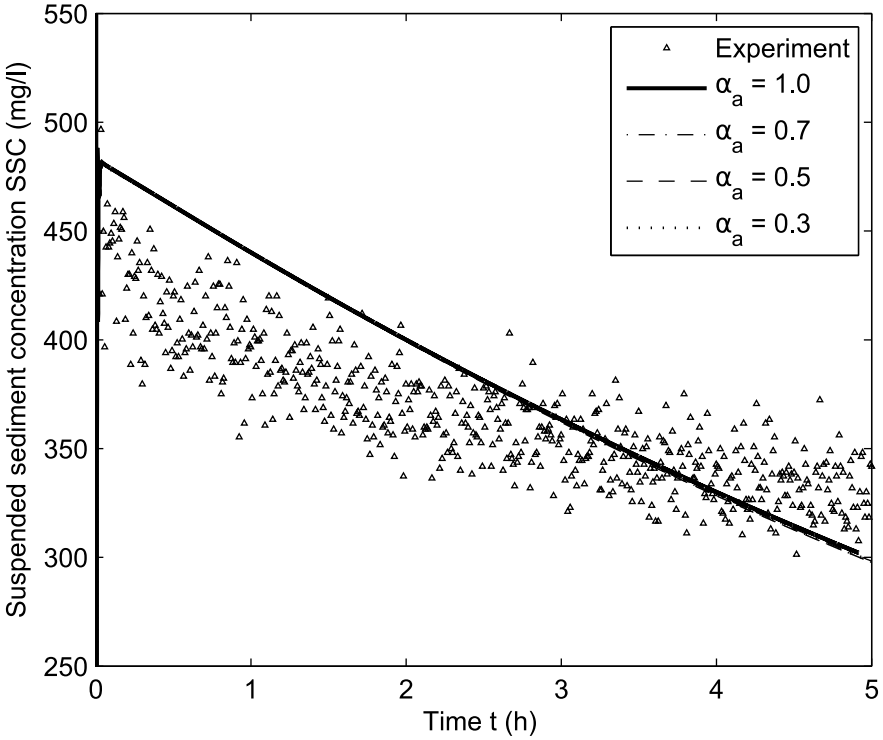

Figure 5.28: Measured and calculated suspended sediment concentrations over time by using different values for the aggregation efficiency α_a (the four simulations yield almost identical results).

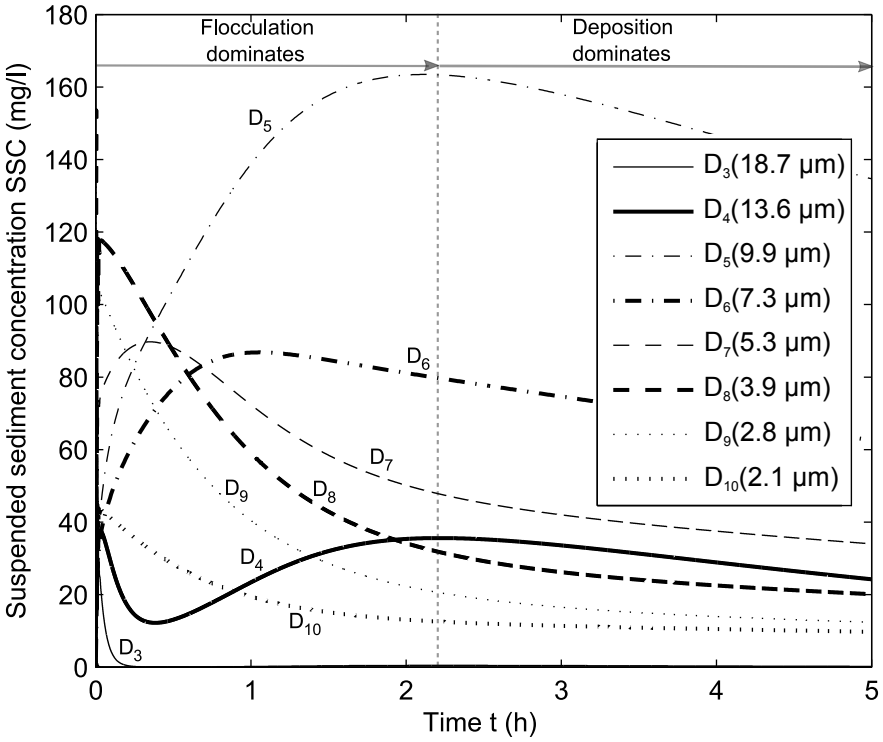

(a) Aggregation efficiency $\alpha_a = 0.3$

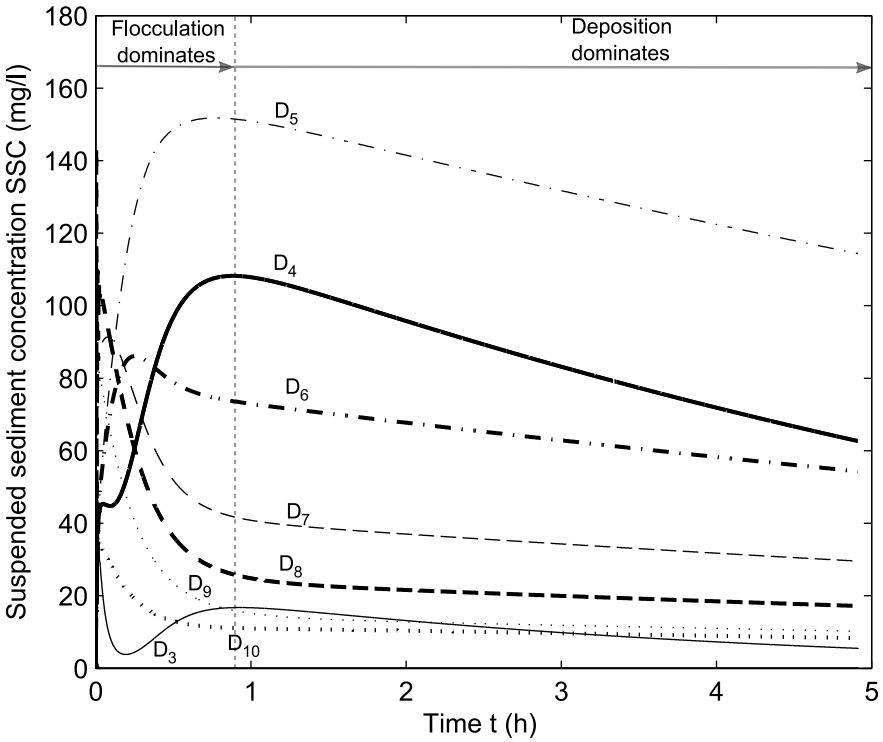

(b) Aggregation efficiency $\alpha_a = 1.0$

Figure 5.27: Calculated temporal development of the concentrations in each particle size class due to aggregation, flow-induced break-up and deposition based on different aggregation efficiencies α_a.

5.3.2.5 Particle Yield Strength Coefficient

In the implemented flocculation algorithm the particle yield strength τ_j is affected by the fractal dimension and the particle yield strength coefficient B_τ ($^{N}/_{m^2}$) (see equation 4.16). The sensitivity towards the fractal dimension was already studied in section 5.3.2.1. The parameter B_τ is an empirical sediment- and flow-dependent stress function, for which no explicit formulation is known and which varies over a wide range of values (1 to 10^4 $^{N}/_{m^2}$). Since in literature there are almost no suggestions for the value of this parameter, a sensitivity study towards this parameter was carried out. Therefore B_τ was set to $B_\tau = 1.0$, 3.0, 5.0 and 10.0 $^{N}/_{m^2}$.

Table 5.9 shows the calculated particle yield strengths in each size class depending on B_τ. Particle size classes which will be disrupted by fluid shear in every grid cell, i.e. whose yield strength is smaller than the minimum fluid shear, are highlighted in dark grey. Size classes which will break up by turbulence in the output cell are highlighted in lighter grey. And particle size classes which may be disaggregated by the maximum fluid shear stresses in one of the grid cells in the model domain are marked in light grey. It can be seen that the particle yield strengths increase with increasing B_τ. The table also illustrates that different values for B_τ do not alter the collision outcomes in these case studies. All possible particle collisions result in the aggregation type 2A1, since the particle yield strengths are always strong enough to withstand the collision-induced shear stresses. This means that two colliding particles will always form one new larger floc. However, the impact of different particle strengths gets obvious concerning the resistance to fluid shear: applying B_τ to the minimum value of 1.0 $^{N}/_{m^2}$ causes disaggregation due to flow shear of the four coarsest and weakest size classes 1, 2, 3, 4 (marked in grey). By increasing B_τ, the particle strength of each size class gets higher. Setting B_τ to 3.0 $^{N}/_{m^2}$ causes only size class 1 and 2 to break up due to fluid shear. Setting B_τ to 5.0 $^{N}/_{m^2}$ accounts for disaggregation due to flow shear only of size class 1. And for $B_\tau = 10.0$ $^{N}/_{m^2}$ all particles are strong enough to withstand the flow shear. In this case, only aggregation due to particle collisions is possible, whereas disaggregation is not possible at all. Since higher values than $B_\tau = 10.0$ $^{N}/_{m^2}$ would result in the same computation results as for $B_\tau = 10.0$ $^{N}/_{m^2}$, the sensitivity towards higher values was not further tested.

Table 5.9: Particle yield strengths τ_j ($^{N}/_{m^2}$), depending on the particle yield strength coefficient B_τ ($^{N}/_{m^2}$). The last row shows the collision outcomes due to two-body collisions. Size classes which can be broken up by flow-induced shear stresses are highlighted.

Class index j	Diameter D_j (μm)	$B_\tau = 1.0$	$B_\tau = 3.0$	$B_\tau = 5.0$	$B_\tau = 10.0$
1	35.0	0.0057	0.0172	0.0287	0.0573
2	25.6	0.0111	0.0334	0.0557	0.1114
3	18.7	0.0219	0.06569	0.1095	0.2190
4	13.6	0.0437	0.1312	0.2187	0.4374
5	9.9	0.0897	0.2691	0.4486	0.8971
6	7.3	0.1927	0.5780	0.9633	1.9266
7	5.3	0.4537	1.3610	2.2684	4.5367
8	3.9	1.3448	4.0343	6.7238	13.4475
9	2.8	10.0135	30.0405	50.0675	100.1349
10	2.1	non-breakable			
Collision outcomes		2A1	2A1	2A1	2A1

Figure 5.29 shows the simulated mean particle diameters of the sensitivity study. It can be seen that the mean floc size gets coarser with increasing B_τ. This is caused by the higher yield strengths associated with increasing B_τ, meaning that more particles can withstand the fluid shear. In consequence, disaggregation into smaller particles is limited, whereas aggregation towards larger particles is enhanced. For example, for $B_\tau = 10.0\,^{N}/_{m^2}$ only aggregation takes place, so that mass shifting from the smaller into the coarser size classes takes place until after about 1.5 h the whole sediment mass is shifted into the coarsest size class $D_1 = 35\,\mu$m, which is also clearly illustrated in figure 5.30. In this case, only shifting of mass due to aggregation takes place as a time-dependent process. If particles can also be disrupted by turbulence, i. e. with smaller B_τ values, the mass shifting occurs faster, since also disaggregation due to turbulence is modeled as a time-independent process. The more size classes are involved in the break-up mechanism, i. e. the smaller B_τ is, the sooner the maximum floc size is reached. For instance, for the reference case ($B_\tau = 1.0\,^{N}/_{m^2}$) the maximum floc size is reached already after under one hour.

It is important to note that in contrast to the initial floc size or the aggregation efficiency, B_τ does not only affect the temporal development of the flocculation processes, but also the particle size distribution in the initial stages of flocculation and at equilibrium stage. This means that to a large extent the particle size distribution depends on the possibility of undergoing disaggregation by fluid shear. For $B_\tau = 10.0\,^{N}/_{m^2}$ the whole sediment mass is shifted into the coarsest size class D_1. For $B_\tau = 5.0\,^{N}/_{m^2}$ the highest concentrations at equilibrium stage are calculated in size class D_2, whereas for $B_\tau = 3.0\,^{N}/_{m^2}$ most particles are shifted into size class D_3 (not shown here in detail). For $B_\tau = 1.0\,^{N}/_{m^2}$ most particles are computed in size class D_5 at equilibrium stage (see figure 5.20). Hence, at equilibrium stage the highest sediment concentration is found in the size class, whose particles will just not be disaggregated by turbulence.

Figure 5.29 shows that the best agreement with the measured particle sizes could be found for $B_\tau = 1.0\,^{N}/_{m^2}$. In figure 5.31 the measured and computed sediment concentrations are shown. It can be seen that with

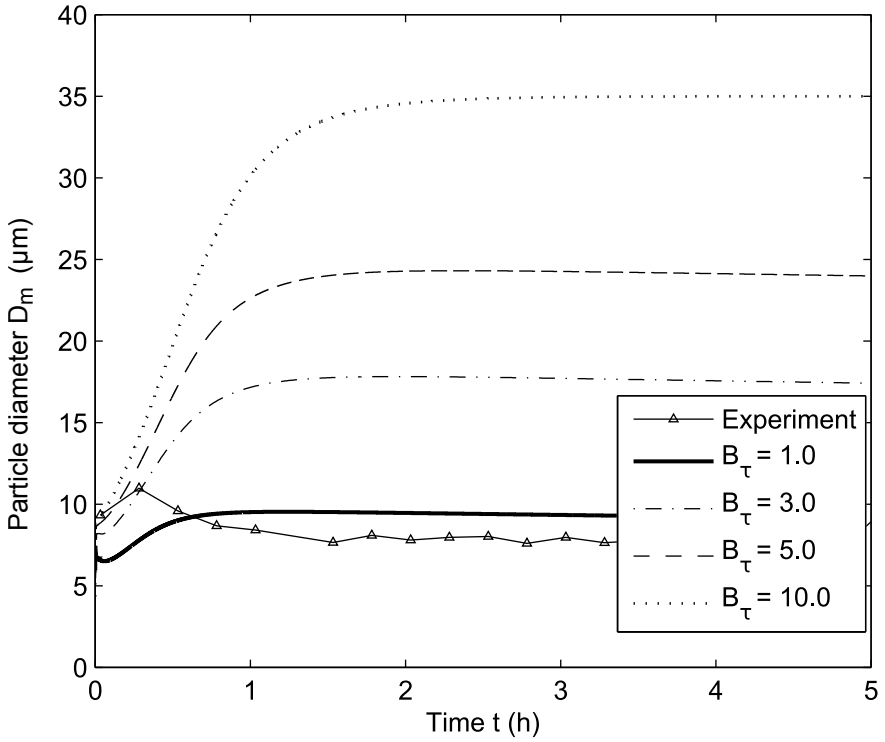

Figure 5.29: Measured and calculated mean particle diameters over time by using different values for the particle yield strength coefficient B_τ ($^{\mathrm{N}}/_{\mathrm{m}^2}$).

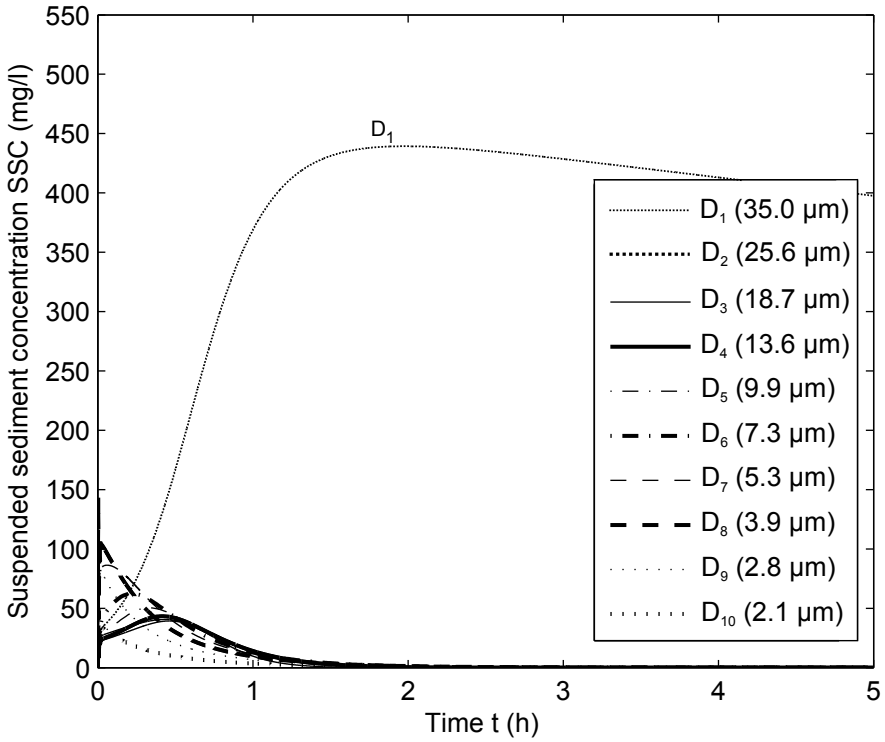

Figure 5.30: Calculated temporal development of the concentrations in each particle size class due to aggregation and deposition based on a particle yield strength coefficient of $B_\tau = 10.0\,^{\mathrm{N}}/_{\mathrm{m}^2}$.

smaller values for B_τ the sediment concentration decreases faster. This is an effect of the different simulated particle size distributions. Contrary to the previous analyses towards the aggregation coefficient α_a, the sediment concentration distribution among the size classes is significantly different when changing B_τ. For example, for $B_\tau = 10.0\,\mathrm{N/m^2}$ *all* sediment mass is shifted in size class 1 due to aggregation. This means that all particles of this size class settle down with a relatively low settling velocity of $0.0032\,\mathrm{mm/s}$, because of a very low floc density (see table 5.3). For smaller values of B_τ also a certain amount of sediment mass is shifted into other smaller size classes due to simultaneously occuring floc break-up. The smaller B_τ, the more breakable the particles are and the more sediment mass is shifted into the smaller size classes. These smaller particles in turn imply higher settling velocities than $0.0032\,\mathrm{mm/s}$, since they have a higher particle density. For instance, for the smallest value of $B_\tau = 1.0\,\mathrm{N/m^2}$, at equilibrium many particles will be shifted into the size classes 4, 5 and 6. These size classes show higher settling velocities than size class 1 (see table 5.3), and as a consequence, this concentration is decreasing faster. It has to be noted that the presented simulation results are valid for $n_{fc} = 1.4$. Other fractal dimensions will lead to different particle yield strengths and different settling velocities. For example, in the case of adopting $n_{fc} = 2.6$ and $B_\tau = 10.0\,\mathrm{N/m^2}$, the concentration would decrease more rapidly than by using $B_\tau = 1.0\,\mathrm{N/m^2}$ (and $n_{fc} = 2.6$), since the impact of a larger floc size would dominate over the effect of a reduced floc density when the particle sizes increase. Hence, the settling velocities would become larger with coarser particle sizes.

It can be concluded that there is a major impact of the value for the particle yield strength coefficient B_τ towards the flocculation process. In particular in terms of the flow-induced stresses, its influence gets very significant. On the one hand, it influences the temporal development of the flocculation process, since turbulence-induced disaggregation of particles is modeled as a time-independent process. On the other hand, it affects the computed particle size distribution. Significantly different simulated particle sizes in turn influence the deposition of the sediments, mainly when the respective settling velocities of the particles are additionally very distinct from one another.

Other parameters which influence the particle yield strength or the flow-induced shear stresses will lead to similar effects on the model results. These include for instance the fractal dimension (see section 5.3.2.1) or the formula to compute the flow-induced shear stresses on the particles in a turbulent flow. In the implemented flocculation algorithm, equation 4.26 was used for calculating these stresses. If for instance equation 3.20 is used instead, lower turbulence-induced shear stresses will cause no particle disaggregation, since all particles will be strong enough to withstand the fluid shear stresses (for the case of $n_{fc} = 1.4$ and $B_\tau = 1.0\,\mathrm{N/m^2}$).

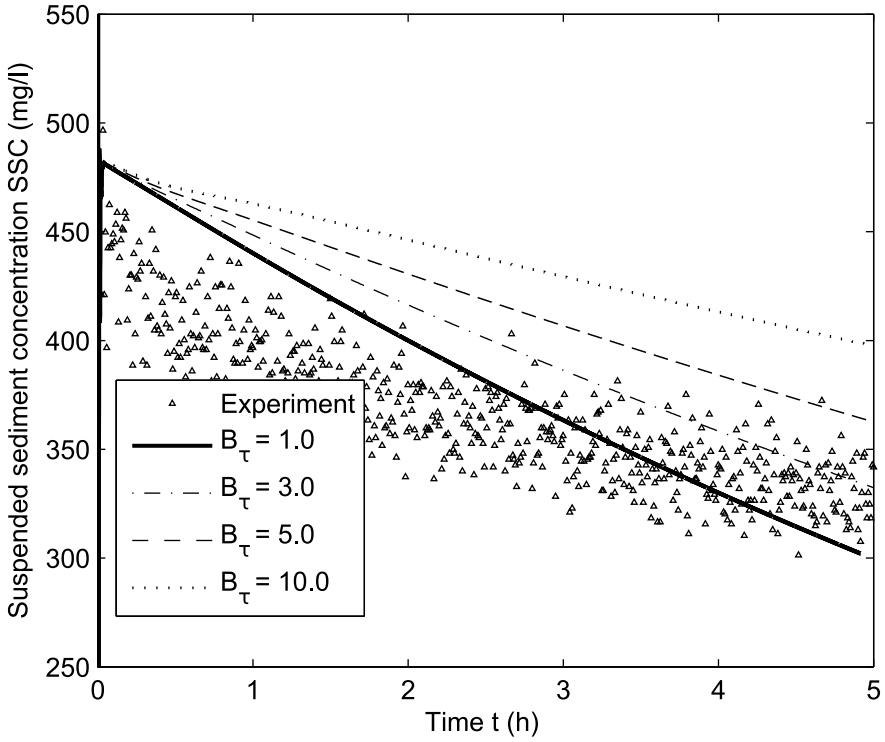

Figure 5.31: Measured and calculated suspended sediment concentrations over time by using different values for the particle yield strength coefficient B_τ ($^{\mathrm{N}}/_{\mathrm{m}^2}$).

5.3.2.6 Erosion

The previous sensitivity analyses have shown that the best agreement with measured floc diameters and sediment concentration could be found with the settings of the reference case (table 5.2). Nevertheless, the initial decrease of the sediment concentration as it is indicated from the experimental data could not be simulated in the same way by any of the simulation studies. Also the slope of the computed sediment concentration curve is steeper than in the measurements, i. e. the sediments deposit too fast. In order to achieve a better agreement with the measured data, further sensitivity studies for the annular flume were conducted. One factor resulting in a stronger initial decrease of the concentration could be that a certain (coarser) portion of the particles, which were added initially in the annular flume, do not exhibit fractal structures. These coarser particles might settle down as near-solid Euclidean spheres with $n_f = 3.0$, causing a faster initial decrease of the concentration. This aspect was verified in the model by defining the particles in the coarsest size class 1 not as fractal, but as solid entities, i. e. with a fractal dimension of $n_f = 3.0$. Accordingly, these particles were excluded from the flocculation process. On the other hand, a slower decrease of the sediment mass was realized by taking into account also potential resuspension of the deposited particles. For the sake of model simplicity, erosion of deposited fine sediments was neglected in the previous presented numerical studies. However, within the experiments of Hillebrand (2008) resuspension was observed in the annular flumes, where the turbulence and flow velocities were relatively high, i. e. near the inner rotating cylinder. In order to quantify the impact of floc erosion on the computed settling and flocculation behavior, it was assumed in the model that the deposited sediments near the inner cylinder can simultaneously be eroded by the high fluid flow forces.

Figure 5.32 shows the calculated bed shear stresses in the small annular flume. The maximum bed shear stress is near the inner rotating cylinder, where the highest flow velocities and turbulence intensities are calculated (see chapter 5.1.2), and accounts for $0.1\,\mathrm{N/m^2}$. The bed shear stresses decrease with increasing distance from the moving boundary. The erosion process was included in the model by artificially setting the critical bed shear stress to $\tau_c = 0.095\,\mathrm{N/m^2}$. In this case, only the sediments in the inner area near the moving cylinder, where the bed shear stress is higher than the predefined critical bed shear stress, can be resuspended.

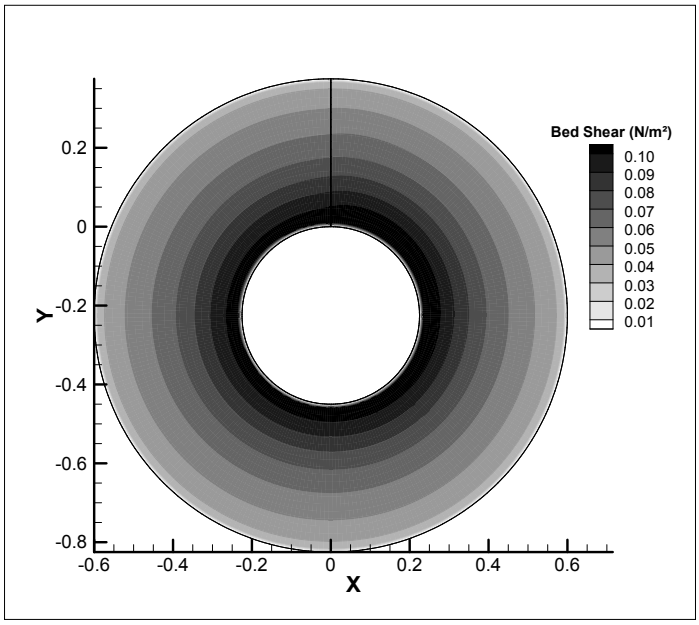

Figure 5.32: Computed bed shear stresses in the small annular flume.

Figure 5.33 illustrates the measured and the computed mean particle diameters for the reference case by excluding erosion ($\tau_c > \tau_b$) and for the case that resuspension is considered ($\tau_c = 0.095\,\mathrm{N/m^2}$). In the latter case, additionally the particles in the coarsest size class 1 were excluded from the flocculation process and specified to deposit as solid Euclidean particles with $n_f = 3.0$, i. e. with the Stokes settling velocity. The figure shows that for about the first hour of simulation the mean particle diameter is slightly higher when erosion is excluded. Then the differences go to zero, so that after 2.5 hours exactly the same D_m is calculated. Afterwards the curves differ very slowly with slightly higher particle diameters when erosion is included.

The minor differences in the computed mean particle sizes are the result of including resuspension and simultaneously excluding size class 1 from the flocculation process. For the reference case no erosion occurs and particles from size class 1 take part in the flocculation processes. These weak particles are initially destroyed by turbulence and their masses are shifted into the smaller size classes, mainly into size classes 4, 5 and 6. For the other case study ($\tau_c = 0.095\,\mathrm{N/m^2}$) the particles from size class 1 do not undergo disaggregation. These particles ($D_1 = 35\,\mu\mathrm{m}$) deposit rapidly with a relatively high settling velocity according to Stokes ($= 0.8813\,\mathrm{mm/s}$). This results in a lower mass shifting into the finer size classes compared to the reference case wit $\tau_c > \tau_b$.

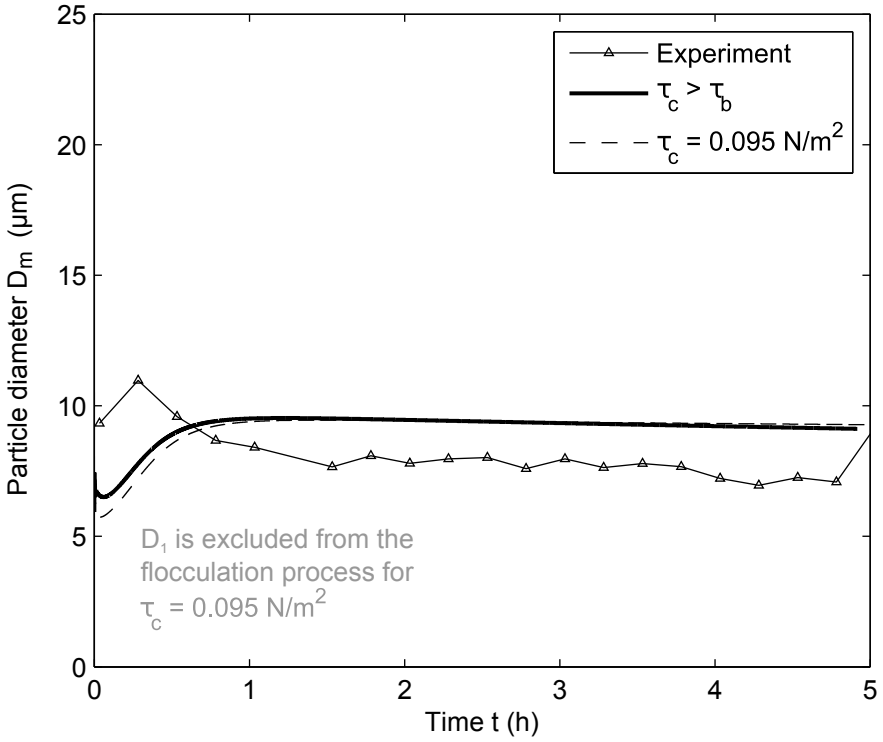

Figure 5.33: Measured and calculated mean particle diameters over time when erosion is neglected ($\tau_c > \tau_b$) and when erosion is included with $\tau_c = 0.095\,\mathrm{N/m^2}$. Additionally, for $\tau_c = 0.095\,\mathrm{N/m^2}$, the coarsest size class D_1 is excluded from the flocculation processes, but considered for the calculation of D_m.

For reasons of clarity the mass shiftings only for the the size classes 4, 5 and 6 are shown exemplarily in figure 5.34 for both study cases. For the other size classes the differences in mass shifting are very minor. The grey curves represent the mass shifting between the size classes when size class 1 is excluded from the flocculation processes and erosion is included. It can be seen that the lower masses (grey curves), especially in size class 4 and 5, are responsible for the smaller predicted mean particle diameter in the first hour. The differences in the computed mean particle diameter decrease with time and get zero at $t = 2.5\,\mathrm{h}$, since then for both runs the same concentrations exist in the respective size classes. When D_1 is excluded from the flocculation process and erosion is included, the effect of lacking mass in size class 4, 5 and 6 (due to initially deposited particles from size class 1) is counterbalanced by the effect of simultaneously occurring resuspension. That in turn results in a slower decrease of the respective concentrations in the size classes, so that there is an intersection of the two curves after 2.5 hours. The resuspended particles get involved again in the flocculation process, which leads to an increase of particle mass in the respective size classes while simultaneously sediment deposition occurs. Hence, in figure 5.34 the grey curves have to be interpreted as a simultaneously interaction of the processes flocculation, deposition and erosion.

The effect of taking into account erosion and excluding D_1 from the flocculation process also becomes evident in figure 5.35. The solid particles from size class 1 settle down independently from the other size classes very rapidly due to a comparatively high settling velocity. This results in a rapid decrease of the concentration within the first 100 seconds. Subsequently, the effect of simultaneous resuspension is responsible for the lower decrease of the sediment concentration compared to the deposition behavior from the reference case run, for which erosion is excluded. For $t = 2.5\,\mathrm{h}$, the concentration is equal for

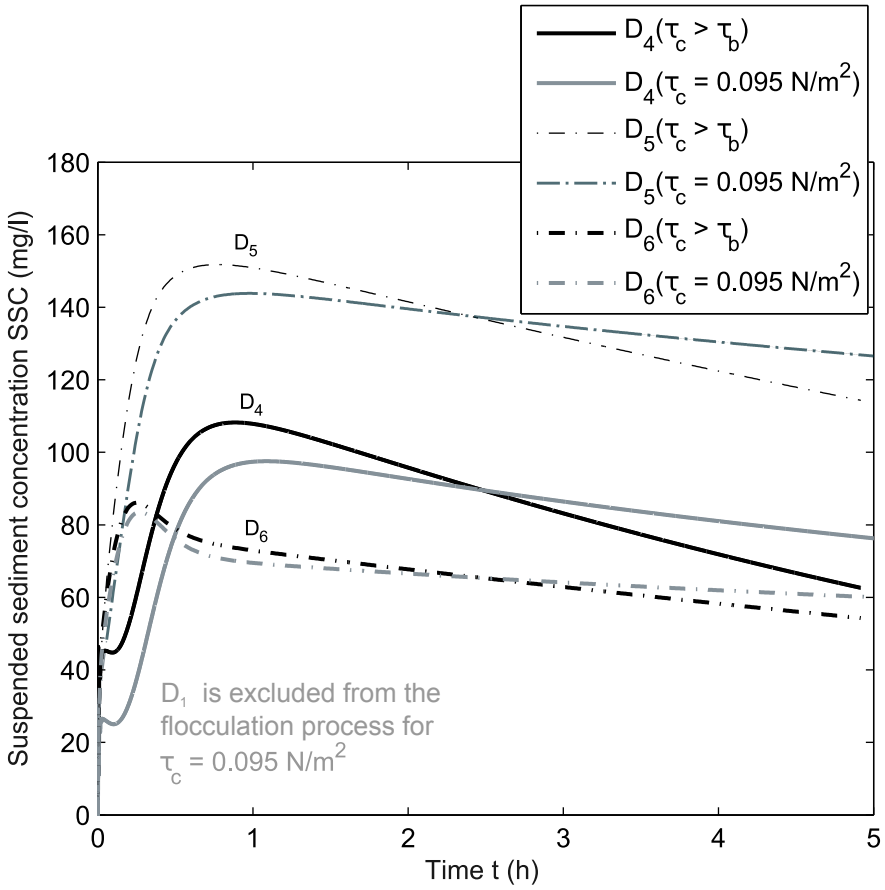

Figure 5.34: Calculated temporal development of the concentrations in the particle size classes 4, 5 and 6 when erosion is neglected ($\tau_c > \tau_b$) and when erosion is included with $\tau_c = 0.095\,\mathrm{N/m^2}$. Additionally, for $\tau_c = 0.095\,\mathrm{N/m^2}$, the coarsest size class D_1 is excluded from the flocculation processes.

both case runs, because the concentration distribution among the size classes is nearly identical at that time, as it was shown in figure 5.34.

It can be concluded that excluding the particles of the coarsest size class from the flocculation process and considering them as solid, much faster settling entities, leads to an initially significant and rapid decrease of the computed concentration. This effect will obviously be even greater for a higher defined concentration in this size class. The simulations also show that the inclusion of erosion has a considerable effect on the temporal development of the computed sediment concentration, since it leads to a decelerated deposition. The tested value for the critical bed shear stress ($\tau_c = 0.095\,\mathrm{N/m^2}$) and the exclusion of size class 1 from the flocculation process lead to a better reproduction of the measured concentrations compared to the reference case. Therefore, the definitions from the reference case, however with inclusion of floc erosion processes and excluding size class 1 from the flocculation processes, were figured out as the best and final settings for modeling cohesive sediments in the small annular flume under the specific fluid flow conditions for the first 5 hours of the experiment.

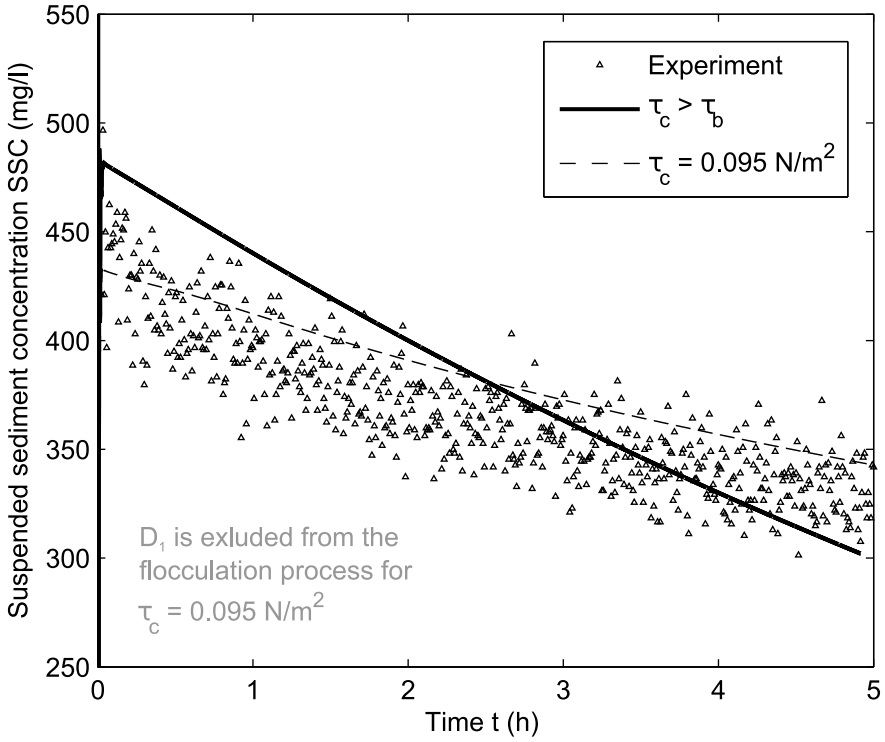

Figure 5.35: Measured and calculated suspended sediment concentrations over time when erosion is neglected ($\tau_c > \tau_b$) and when erosion is included with $\tau_c = 0.095\,\mathrm{N/m^2}$. Additionally, for $\tau_c = 0.095\,\mathrm{N/m^2}$, the coarsest size class D_1 is excluded from the flocculation processes.

5.3.3 Long-term Flocculation Modeling and Comparison with Simplified Models

The objective of the numerical studies was to analyze how unknown parameter values, boundary conditions and processes in the flocculation algorithm affect the simulation results and how accurately cohesive sediment experiments in the open annular flume can be simulated in SSIIM by the application of the implemented flocculation model. The computation results for the first 5 hours of the experiment have demonstrated that the particle size distribution in the annular flume is sensitive towards all tested parameters and boundary conditions. The studies have also shown that modeling flocculation and deposition in the annular flume depends on several unknown physico-chemical parameters pointing out the difficulty to simulate the complex processes interactions in a physically accurate and precise way.

A further question is how the parameter definitions and settings affect the long-term deposition and flocculation computations over the entire time of the experiment of about 70 hours. To investigate this issue, a long-term flocculation computation was conducted by using the same parameter definitions and settings as for the first 5 hours of simulation time, i. e. with inclusion of erosion ($\tau_c = 0.095\,\mathrm{N/m^2}$) and exclusion of the coarsest size class D_1 from the flocculation processes. However, for this case study a time step of 2 sec was applied to reduce the excessive CPU time. The modeled suspended sediment concentrations and particle sizes are shown in figure 5.36 and 5.37, respectively.

The calculated suspended sediment concentrations show a good agreement with measured data for about the first 20 hours of the experiment, then the computed sediment concentrations overpredict the measured ones. In the simulation, after 70 hours, still 15 % (76 mg/l) of the initial sediment material is in suspension,

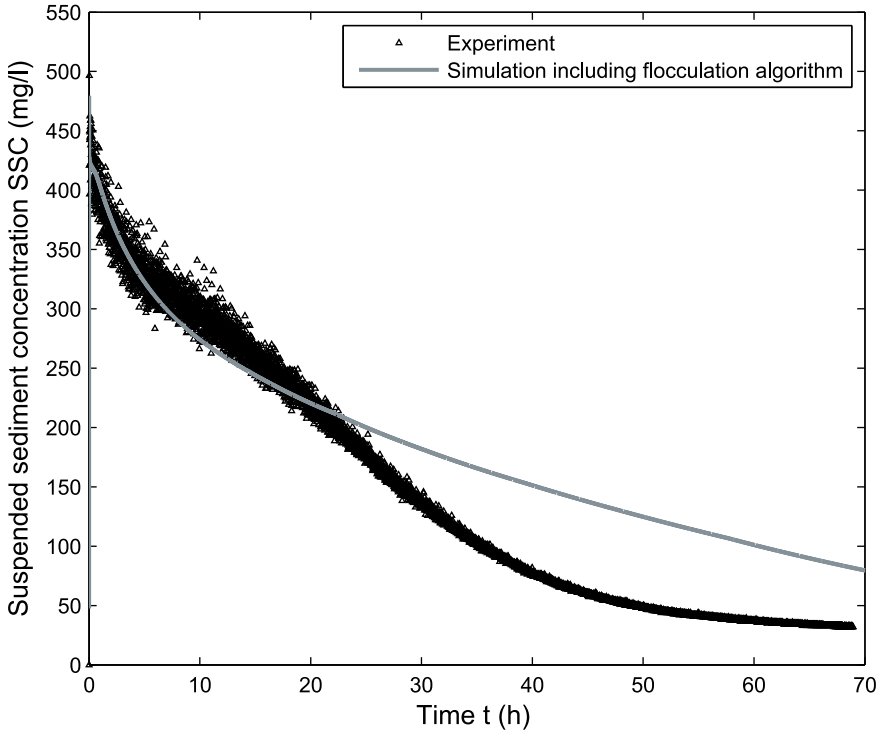

Figure 5.36: Measured and calculated suspended sediment concentrations for the final parameter definitions and boundary conditions over a time of approx. 70 hours.

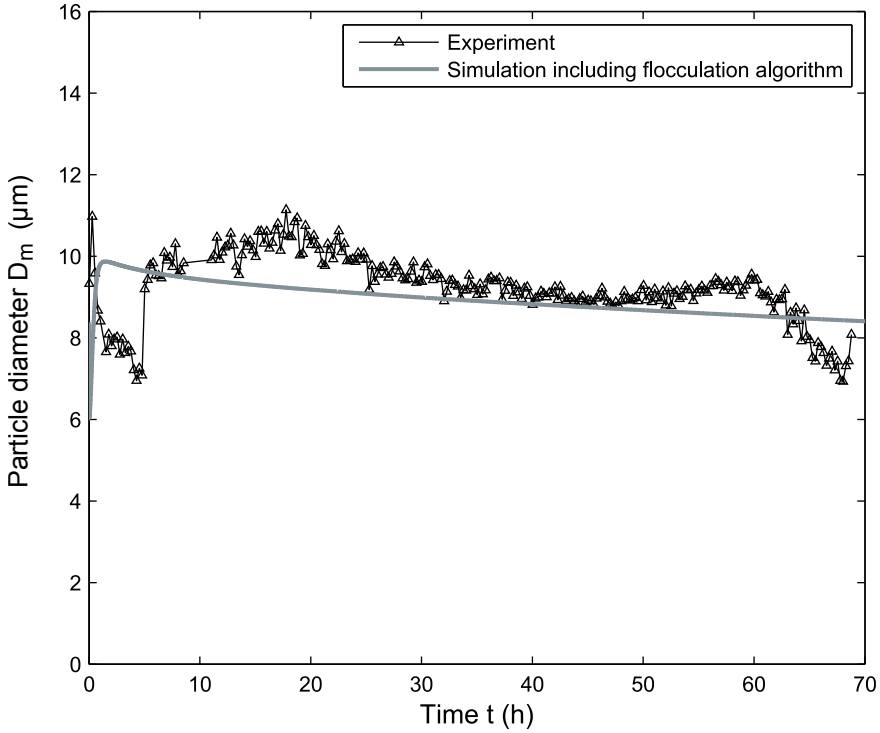

Figure 5.37: Measured and calculated mean particle diameters for the final parameter definitions and boundary conditions over a time of approx. 70 hours.

whereas this amount of sediment mass is measured already after 40 hours in the laboratory. In terms of the particle sizes, an initial increase in floc size due to aggregation processes could be reproduced by the model in a similar magnitude as for the experiment. Also the simulated mean particle diameters at equilibrium stage, i. e. when floc growth and floc break-up processes are assumed to be in equilibrium, match the measured mean particle diameters fairly well (after $t = 5\,\mathrm{h}$). However, in the laboratory there is a distinctive decrease in floc size after 17 minutes, when the particles have reached the maximum floc size of $D_m = 11\,\mu\mathrm{m}$. This significant decrease in floc size is not computed in the same magnitude by the flocculation algorithm. The simulated particle sizes rather tend to decrease continuously very slowly, after the maximum floc size of $D_m = 10\,\mu\mathrm{m}$ is reached at $t = 1.4\,\mathrm{h}$. The interesting point from the experimental data is that after 5 hours the measured particle sizes do not further decrease, as might be expected and as it is indicated by the model results. Instead of that, the mean floc size increases again fairly quickly to a more or less constant value of $D_m = 9$ to $10\,\mu\mathrm{m}$, which is not changing significantly any more for the remaining duration of the experiment. The reasons for the rapid increase in measured floc size were already discussed in chapter 5.2.2. The measured decrease of the particle sizes after 60 hours is likely caused by a reduced picture quality due to the long-term experiment, which is associated with flawed measuring data, as also identified in chapter 5.2.2. The measured floc sizes at equilibrium however fit quite well with the computed floc sizes.

The comparison of the long-term simulation with measured data shows that despite various changes in parameter definitions and initial/boundary conditions, there are still some deviations between the model results and the experiments in terms of both the suspended sediment concentration and the floc sizes. The question is to which degree the observed processes and phenomena from the experiment can be simulated physically correctly, if the implemented flocculation algorithm would be excluded from the computation. To investigate this issue, two simplified methods for modeling cohesive sediment processes were applied, which both do not include the implemented flocculation algorithm. On the one hand, the well known settling velocity formula based on Stokes (1850) was used, which treats particles as solid, Euclidean spheres with $n_f = 3$. This method represents the most basic approach with the strongest simplifications for modeling cohesive sediment processes. On the other hand, flocculation was considered indirectly by the application of the fractal dimension to calculate the settling velocity defined by Winterwerp (1998) instead of Stokes. However, in contrast to the previous computations, not a variable, but a constant fractal dimension was applied with an average value of $n_f = 2$. This average value for the fractal dimension is a commonly used method in sediment engineering to model the complex structure of cohesive sediment aggregates, when no information about the floc structure is available from measurements. By comparison, within the sensitivity studies in the previous chapter 5.3.2.1 the best agreement with measured floc sizes was achieved with a variable fractal dimension covering the whole value range from 1.0 to 3.0. According to the simulation by application of the flocculation algorithm, both simplified methods consider erosion as well.

For the application of the Stokes' settling velocity, 5 size classes from $D_1 = 20\,\mu\mathrm{m}$ to $D_5 = 1\,\mu\mathrm{m}$ were chosen. The respective initial concentrations among these size classes were defined to achieve a total suspended sediment concentration of $C_0 = 500\,\mathrm{mg/l}$, and were calibrated until an appropriate agreement with measured suspended sediment concentrations was reached. The chosen particle sizes and the calibrated initial concentrations in the size classes are shown in table 5.10. For the application of Winterwerp's settling velocity with a constant fractal dimension, the same particle size spectrum and initial sediment concentration distribution were applied as for the reference case (see table 5.2). Figure 5.38 shows the calculated settling velocities for the application of the Stokes' equation, and according to Winterwerp,

when applying a constant fractal dimension of $n_f = 2$. In addition, the settling velocities by the application of a variable fractal dimension with $D_{fc} = 15\,\mu$m and $n_{fc} = 1.4$ from the reference case run are shown in figure 5.38.

Table 5.10: Chosen particle size classes and calibrated initial suspended sediment concentrations for the application of Stokes' settling velocity (exclusion of the implemented flocculation algorithm).

Size class D_j	D_1	D_2	D_3	D_4	D_5
Particle size (μm)	20	5	3	2	1
Calibrated initial conc. C_0 (mg/l)	40	60	150	210	40

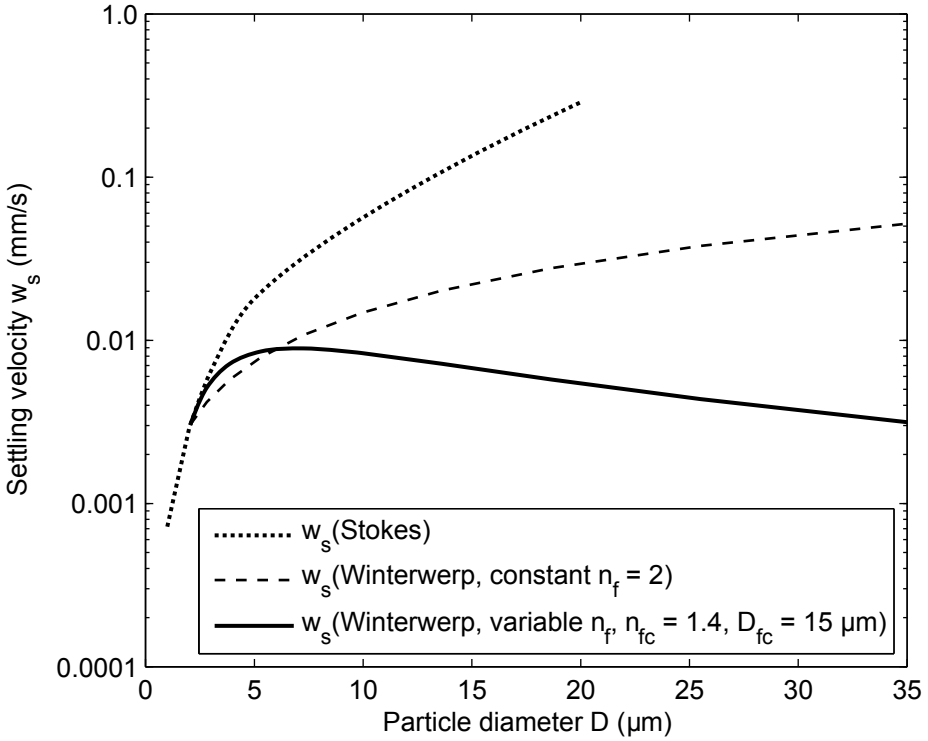

Figure 5.38: Calculated settling velocities as a function of particle size according to Stokes (1850) and Winterwerp (1998), when using a constant fractal dimension of $n_f = 2$, and a variable fractal dimension ($D_{fc} = 15.0\,\mu$m and $n_{fc} = 1.4$).

Figure 5.39 shows the measured and computed suspended sediment concentrations, and figure 5.40 the mean particle diameters for the entire duration of the experiment. From figure 5.39 it can be seen that by excluding flocculation and using the Stokes settling velocity an appropriate agreement with measured suspended sediment concentrations can be achieved. The maximum deviations between measurement and simulation are in the order of 60 mg/l in the time span between $t = 15$ to 20 h. However, from figure 5.40 it can be seen that the computed mean particle diameters strongly underpredict the measured particle sizes by a factor of up to 5. They are even smaller than the medium grain diameter of the used kaolinite ($D_g = 2.1\,\mu$m). If no aggregation processes occur, the aggregates settle down as individual solid particles ($n_f = 3.0$). This results in an abrupt decrease of the mean particle diameter due to the deposition of the two coarsest and fast-settling size fractions D_1 and D_2 leaving the smaller ones in suspension.

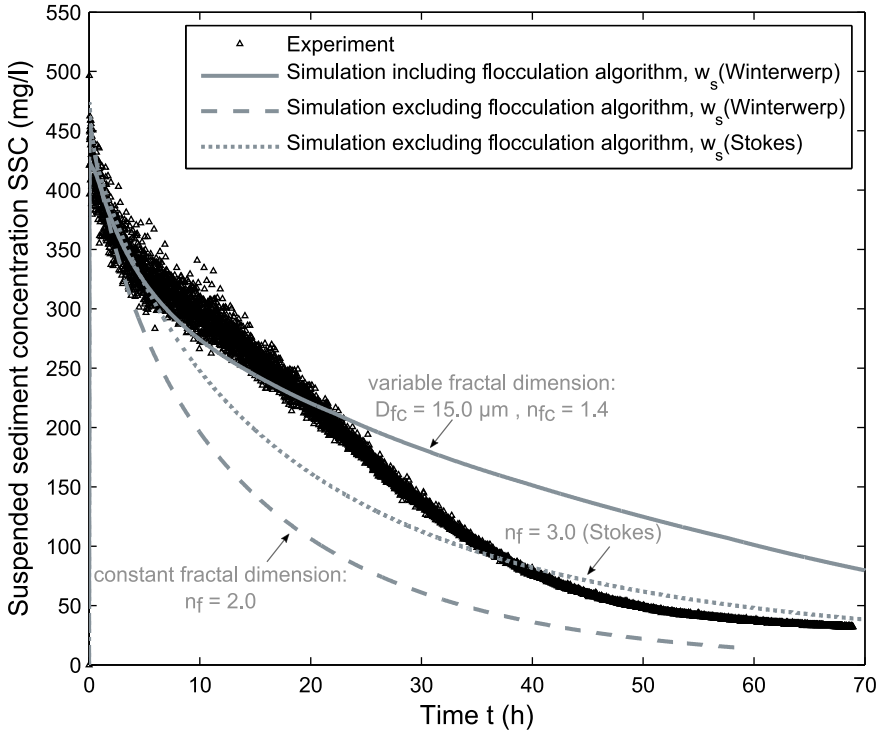

Figure 5.39: Measured and calculated suspended sediment concentrations over a time of approx. 70 hours by including/excluding the flocculation algorithm and using Winterwerp's /Stokes' settling velocity.

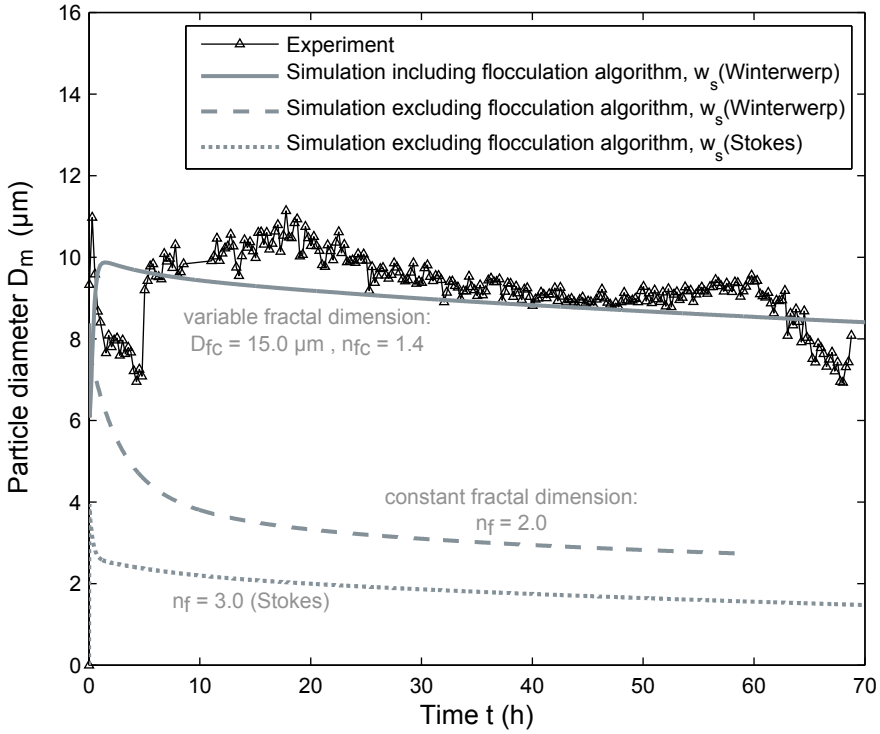

Figure 5.40: Measured and calculated mean particle diameters over a time of approx. 70 hours by including/excluding the flocculation algorithm and using Winterwerp's /Stokes' settling velocity.

Hence, while a relatively good agreement can be yield with the measured suspended sediment concentrations by calibrating the initial sediment concentrations in the size classes, insufficient and physically implausible results are obtained with respect to the particle size evolution, when excluding flocculation processes and using the well-known Stokes' settling equation.

In the case that the flocculation algorithm is excluded, but considering Winterwerp's settling velocity equation with an average constant fractal dimension of $n_f = 2.0$, both the measured sediment concentrations and the particle sizes are considerably underpredicted by the simulation. Here, two possibilities are available to achieve a better agreement with measured data. On the one hand, the initial sediment concentrations in the size classes could be varied, similar as it was done for the application of the Stokes settling velocity. On the other hand, also the calibration of the fractal dimension would provide the opportunity to achieve a better fit with the measurements. However, even if the measured concentrations could potentially be modeled in an adequate way by calibration, the question is if the predicted particle sizes would reproduce the real measured grain size evolution physically accurately.

The explicit modeling of aggregation and disaggregation processes by including the implemented flocculation algorithm and using Winterwerp's settling velocity with a variable size-dependent fractal dimension gives physically realistic results in terms of the floc size evolution. It provides a much better correspondence with measured aggregate sizes than by excluding flocculation processes. The calculated concentrations match the measured data also very well for the first 20 hours of the experiment, however subsequently the measured data are overpredicted by the model to some degree. The existing deviations in measured and calculated concentrations and particle sizes can be attributed to several reasons and are discussed in the next section.

5.4 Evaluation and Consequences on the Application of the Flocculation Algorithm for Natural Systems

The numerical studies showed that in general the flocculation algorithm gives reasonable results and aggregation and disaggregation mechanisms due to two-body collisions and fluid shear stresses can be simulated in a physically plausible way. However, the comparison of the simulation results with measured data also implied that despite various changes in parameter definitions and initial/boundary conditions there are still some deviations between measurement and experiment. There are different reasons for this, which are illustrated in figure 5.41.

The identified discrepancies in the flow field characteristics appear as one of the key reasons for the different predicted deposition and flocculation behavior in the simulation and experiment. In chapter 5.1.2, the results of the numerical model and the measurements showed that the flow field in the open annular flume is very complex. The most significant flow field discrepancies between simulation and measurement were found in the characterization of the turbulence. Whereas general characteristics of the distribution were similar, the modeled turbulent kinetic energy TKE and turbulent dissipation rates ϵ were overpredicted by a factor of up to 4 to 6. In order to get a better agreement with measured data, the consequences of lower simulated turbulent dissipation rates and turbulent kinetic energy are examined in the following.

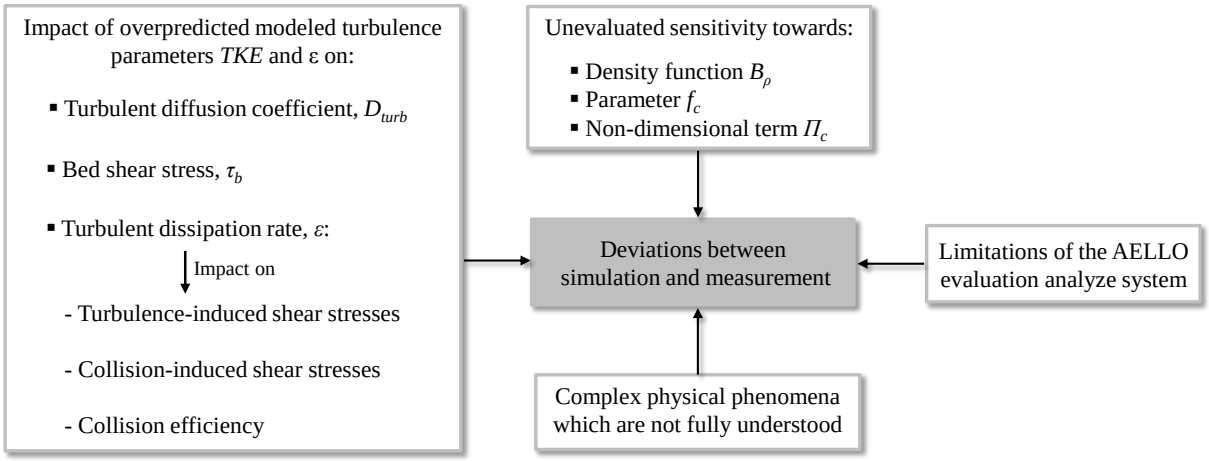

Figure 5.41: Factors for deviations between simulation and measurement by adopting implemented flocculation algorithm.

On the one hand, lower TKE and ϵ values would affect the turbulent diffusion coefficient D_{turb} in the advection-diffusion equation (3.1), since in SSIIM, D_{turb} is set equal to the eddy viscosity ν_t, which in turn depends on the square of the turbulent kinetic energy and the energy dissipation rate ($D_{turb} = \nu_t = C_\mu \frac{TKE^2}{\epsilon}$). In the case of a considerably smaller turbulent diffusion coefficient, the sediment particles are supposed to be kept in suspension for a shorter time period. On the other hand, lower values for the turbulent kinetic energy TKE would result in lower computed bed shear stresses (see equation 4.5). In the case that floc erosion is included in the simulation, less erosion would be expected. Both effects, less turbulent diffusion and erosion, would lead to faster particle deposition, so that the sediment concentration would decrease more rapidly. These mentioned consequences do not refer to changed values in the flocculation algorithm. In the implemented flocculation algorithm only the energy dissipation rate ϵ is considered as a turbulence parameter. The parameter is used to compute different variables: the turbulence-induced shear stresses, the collision-induced shear stresses (by considering that also the relative particle velocity u_i depends on flow shear), the collision frequency function due to fluid shear and therefore also the collision efficiency (see chapter 4.2). Smaller values of ϵ would imply lower flow-induced and collision induced shear stresses, and hence would reduce particle disaggregation. As a consequence, larger particle sizes are facilitated, similar to the effect which was observed for a higher particle yield strength coefficient (see chapter 5.3.2.5). Since turbulence-induced disaggregation is modeled as a time-independent process, it is assumed that smaller ϵ-values would also contribute to a slower flocculation process, since less particle size classes would immediately be disrupted. On the basis of these considerations, it can be expected that lower modeled energy dissipation rates will likely lead to a delayed flocculation process and a coarser predicted particle size distribution.

Besides the differences in the hydraulics, there are further reasons which make it difficult to reproduce the measured data exactly. There are still some uncertainties in other physico-chemical parameters in the implemented flocculation algorithm which have not yet been tested towards their sensitivity. These include, for instance, the density function B_ρ to calculate the floc density (see equation 4.10), the parameter f_c to compute the collision sphere diameter F_c (see equation 4.22) or the non-dimensional term Π_c (see equation 4.23) to take into account the ionic composition of the water and particle related characteristics. So far, within this work these parameters and terms were defined according to values proposed by McAnally and

Mehta (2000) or were simplified to reduce model complexity. Assumptions of these values and functions could lead to inaccurate model results.

Uncertainties also exist with respect to the measured floc sizes. The limitations of the used AELLO evaluation analyze system (see chapter 5.2.1) may lead to inaccuracies of the detected particle sizes as well.

In addition, also a better understanding of the mechanisms in the laboratory would contribute to a better prediction of the sediment transport and deposition. Previous comparative cohesive sediment transport studies in both annular flumes (Klassen, 2009) indicate that solely the difference in flume size contributes to a considerably different sediment deposition and flocculation behavior in the flumes while all other boundary conditions are the same.

This means that even when a better calibration is achieved for the flocculation algorithm by available data, these data would be functions of the used water/sediment type and of the prevailing hydraulic conditions. Hence, the calibrated flocculation algorithm would be applicable only for the specific water-sediment system for which it was calibrated. Other boundary conditions which imply a different type of sediment and/or other hydraulic characteristics may require other values for the parameters illustrating the process complexity.

It is assumed that the deviations between measurement and simulation are generated by a superposition of several unknown parameters, differences in the flow field characteristics, limitations of the software system and due to the still existing knowledge gaps in cohesive sediment dynamics. The sensitivity studies illustrate that the numerical modeling of flocculation and deposition processes constitutes a major challenge, even for a closed and simplified system in the laboratory, where boundary conditions are well known and constant. Uncertainties regarding several empirical calibration parameters, that imply the estimation of these parameters, can have a major influence on the simulation results when modeling flocculation processes. Hence, reliable measurement data from laboratory/field campaigns or theoretical expressions are required for those parameters to further analyze the complex cohesive transport processes in the laboratory and for further applications of the flocculation algorithm in sediment engineering.

In the longer term, the aim should be to use the flocculation algorithm for real case studies, where the properties of cohesive sediments get relevant. When modeling cohesive sediment dynamics in natural rivers, the numerical model is usually able to reproduce the water flow characteristics adequately well by calibration using a series of measured flow data. However, often poor knowledge is available in terms of the water chemistry and the sediment properties and measurement data are usually very scarce with respect to the suspended floc size spectrum, sediment cohesiveness, floc structure or the particle shape. In this case, several assumptions have to be made for the application of the implemented flocculation algorithm. The question therefore is to which degree uncertainties regarding the choice of unknown parameter values may affect the simulation results. The presented sensitivity studies highlight that the fractal behavior of flocs is the strongest assumption which is made in the flocculation algorithm, since it influences the floc size distribution and the settling velocity. Hence, even in case of a low influence on the computed floc sizes, variations in fractal dimensions can cause major variations in the floc settling velocity. Such differences could have a strong impact on the estimated suspended sediment concentrations and the settling rates in natural rivers and realistic case studies. A high sensitivity was also found towards the particle yield strength coefficient, since it influences the particle size distribution by the determination of the floc yield strength. Another conclusion is that the temporal development of flocculation processes strongly depends

on the turbulence-induced floc break-up process as a consequence of different time scales for aggregation (time-dependent) and flow-induced disaggregation (time-independent).

For the further application of the implemented flocculation algorithm in natural systems it can be concluded: if the range of the suspended particle sizes can be estimated, for example by in situ floc size measurements, it will be possible to define the sediment size classes D_j. If then no further informations of the water-sediment system are available, careful attention must be paid especially to the choice of parameters which affect the settling velocity and the particle yield strength. These imply the fractal dimension n_f and the particle yield strength coefficient B_τ. When considering a short time step and focusing on a steady-state equilibrium stage, uncertainties relating to these two parameters will show the highest impact on the model results. Hence, for a better prediction of cohesive sediment dynamics it will be necessary to enhance the knowledge about processes that influence the fractal dimension and the particle yield strength. This includes on the one hand standardized measurements of the fractal dimension, e. g. by the use of image analysis. On the other hand, the development of explicit formulations for calculating the particle yield strength coefficient is required.

6 Application of the Flocculation Algorithm on the Iffezheim Reservoir

In this work, the implemented flocculation algorithm in SSIIM was applied for a three-dimensional modeling of flocculation processes in the Iffezheim reservoir, located at the Upper Rhine river in Germany. At the Iffezheim reservoir a high amount of suspended sediments is transported with the water flow associated with an annual sediment deposition of about 115,000 m^3 upstream of the impoundment (Wasserstraßen- und Schifffahrtsverwaltung des Bundes (WSA Freiburg), 2011). As the sediment deposits are contaminated, flushing is difficult due to environmental concerns. As a consequence, these sediments need to be regularly dredged and disposed which is very costly. In order to make long-term predictions of the sedimentation rates or to evaluate the risks regarding particle-bound contaminants, knowledge of the relevant fine sediment processes is essential. Here, the inclusion of flocculation processes in the numerical sediment transport model is of particular importance, since on the one hand they affect the grain size distribution of the suspended sediments, and consequently account for the settling velocities. The settling velocities in turn govern the deposited sediment amount. On the other hand flocculation processes also alter the distribution of the adsorbed contaminants on the particle size fractions by changes of the grain size distribution.

For modeling flocculation processes in the Iffezheim reservoir, a three-dimensional sediment transport model was established in SSIIM 2, which was coupled with the implemented flocculation model. The simulations were conducted under steady-state conditions with respect to the hydraulics. Unsteady conditions were present in terms of modeling the temporal floc size evolution, while all boundary conditions and input data were kept constant during the whole simulation time. On the basis of these idealized boundary conditions, the model objective was firstly the validation of the implemented algorithm with respect to the reproduction of flocculation processes for a natural system. In order to estimate if the computed floc sizes give physically plausible results, the modeled floc size distribution was compared with measured particle sizes. Secondly, the aim was to analyze how the assumption of the boundary condition concerning the inflow particle sizes influences the modeled floc sizes. In this context, it was also investigated which impact spatially varying turbulences in the reservoir have on the computed floc sizes. The findings of these computations should finally serve as a basis for follow-up cohesive sediment computations in the Iffezheim reservoir which take into account flocculation processes.

In the first part of this chapter the Iffezheim reservoir is introduced. In this context, the problems which occur with sedimentation of contaminated sediments upstream of the reservoir are elaborated. In the second part, the numerical model in SSIIM is described. This comprises the 3D-computation grid as well as the characterization of the calibrated flow field which served as a basis for the flocculation computations. In the third part, the application of the flocculation algorithm is illustrated, including the definition of parameter values and initial/boundary conditions as well as the description and discussion of the flocculation modeling results.

All field and measurement data used within these numerical analyses are provided by the Federal Institute of Hydrology (BfG) and the Federal Waterways and Shipping Administration (WSV), Germany.

6.1 The Iffezheim Reservoir

6.1.1 Study Area

The Iffezheim barrage is located at the Upper Rhine river in South-Western Germany and was constructed between 1974 and 1978 in a German-French cooperation project. It is the most downstream impoundment along the Upper Rhine, extending from Rhine-km 309.1 (Gambsheim barrage) to Rhine-km 334.0 (see figure 6.1). The reservoir ends in three channels (see enlarged view in figure 6.1): the right channel represents the ship lock, the middle channel leads water to the hydropower plant and at the end of the left channel the weir is located. The development on migratory fish in the Rhine was realized by the construction of a fish passage.

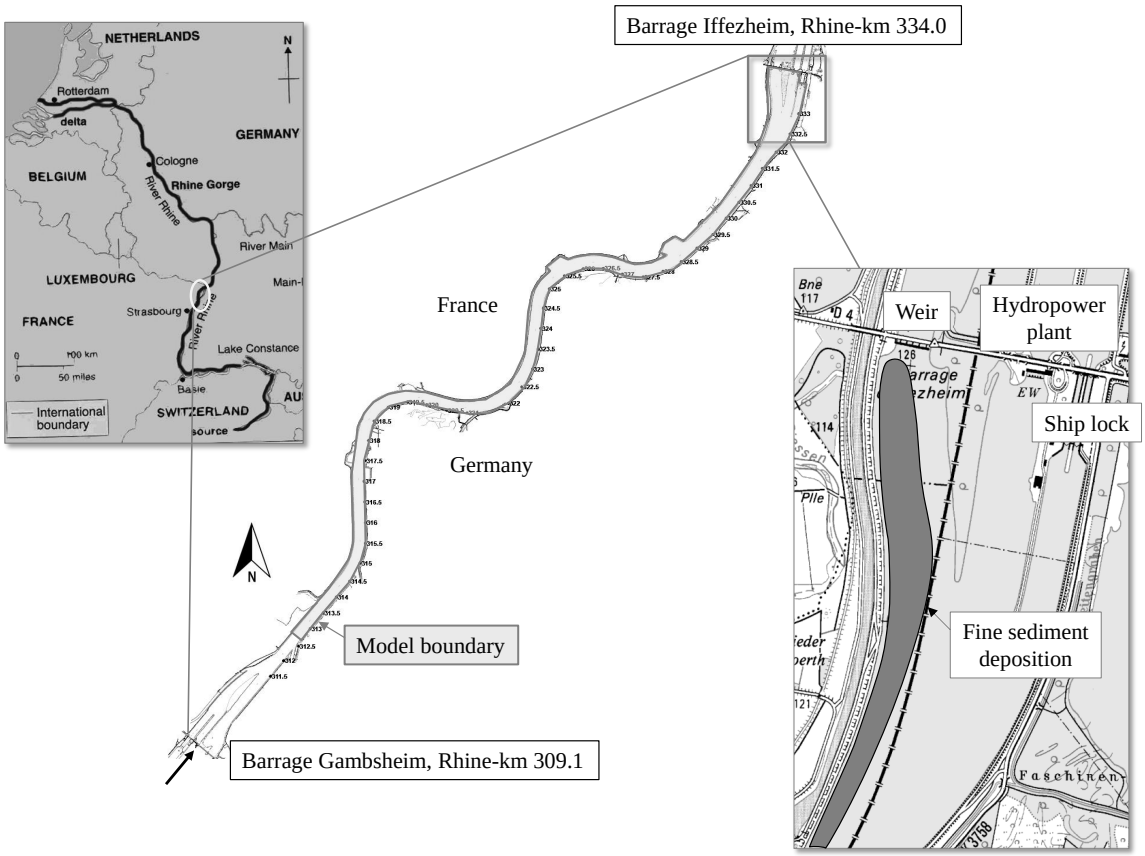

Figure 6.1: Aerial and detailed view of the Iffezheim reservoir at the Upper Rhine river in Germany.

The hydropower plant was expanded by one additional fifth Kaplan turbine in June 2013 yielding a maximum capacity of 148 MW. With the expansion of the fifth turbine the maximum discharge through the power plant channel was increased from originally 1100 $\mathrm{m^3/s}$ to 1500 $\mathrm{m^3/s}$. In general, for discharges

smaller than 1500 m^3/s, the total amount of water is fed into the turbines. For the simulation, it was assumed that during floods and higher discharges than 1500 m^3/s (originally 1100 m^3/s), the turbines are operated at full power, whereas all surplus water is channeled to the weir. The ship lock channel, as well as the fish pass, have usually only a negligible water discharge and were assumed to have zero discharge for the simulation. The average water discharge is 1240 m^3/s (LUBW Landesanstalt für Umwelt, Messungen und Naturschutz Baden-Württemberg (ed.), 2011).

6.1.2 Sedimentation of Contaminated Sediments

The annual suspended sediment load at the reservoir is around 1 million tons/year (LUBW Landesanstalt für Umwelt, Messungen und Naturschutz Baden-Württemberg (ed.), 2011). Since the spillway channel is only operated intermittently during high discharges in the river, the water velocities and turbulences are usually small in the weir channel. This causes the fine sediments to deposit upstream of the weir channel, leading to a decrease of the reservoir volume and to a threatened dam stability over time. The annual sediment deposition in the Iffezheim reservoir exhibits about 115,000 m^3 (Wasserstraßen- und Schifffahrtsverwaltung des Bundes (WSA Freiburg), 2011). The main area of the fine sediment deposition upstream of the weir channel is highlighted in figure 6.1.

Due to historic industrial emissions of particle-bound micropollutants into the Rhine, the fine sediment deposits are contaminated (Pohlert et al., 2011). Samplings and subsequent analyses of the deposited sediments have shown that the sediment is particularly highly contaminated with hexachlorobenzene (HCB)[1]. The mean HCB-concentration in 2009 was 207 $\mu g/kg_{DS}$, with a minimum value of 25 $\mu g/kg_{DS}$ and a maximum concentration of 560 $\mu g/kg_{DS}$ (Breitung, 2009). The environmental objective for HCB, that was introduced by the International Commission for the Protection of the River Rhine (ICPR), is $\leq$ 40 $\mu g/kg_{DS}$ (International Commission for the Protection of the River Rhine (ICPR), 2009). Hence, in order to ensure flood protection and with respect to the environmental quality of the river, deposited and contaminated sediment needs to be regularly dredged and disposed. This is very costly for the Federal Waterways and Shipping Administration (WSV). It becomes apparent that the objective of the responsible authorities is to find solutions for a long-term ecologically and economically optimized, sustainable sediment management. For understanding and optimizing the sediment budget in the Iffezheim reservoir, numerical sediment transport models are needed.

Within this work a three-dimensional numerical sediment transport model of the Iffezheim reservoir was developed in SSIIM to gain insight into the relevant cohesive sediment transport mechanisms. The model should be used to reproduce the flow field and the dominant cohesive sediment processes physically as precisely as possible in order to give realistic and accurate sediment deposition predictions. This means that also the key processes at micro-scale need to be included in the model. At this point, the inclusion of the implemented flocculation model plays a major role in two respects: On the one hand, the grain size distribution of the suspended sediments in the reservoir is strongly influenced by aggregation and disaggregation processes. The predicted grain sizes in turn affect the settling velocities of the particles and therefore the deposited sediment amount.

[1] Hexachlorobenzene is an organochloride with the molecular formula C_6Cl_6. It has negligible solubility in water and variable solubility in different organic solvents. HCB has been banned globally under the Stockholm Convention on persistent organic pollutants.

On the other hand, it is hypothesized that flocculation might play a factor concerning the adsorption of HCB to the suspended sediments. The suspended sediment samplings of the Upper Rhine sediments have shown that HCB contents are inhomogeneously distributed in the sediment probes of the Iffezheim barrage (Fleig et al., 2006). It was found that HCB mainly adsorbs to the coarser size fractions of the sediment ($63 - 200\,\mu$m), rather than to the finer size fractions ($< 2\,\mu$m) as it is observed from other river basins (Böhm et al., 2011). For this so-called "HCB-anomaly" aggregation processes were identified as one possible influencing factor. Since particle aggregation changes the grain size distribution towards the coarser size fractions, also the distribution of adsorbed contaminants on the size fractions is exposed to change.

The considerations above show that for an accurate cohesive sediment modeling of the Iffezheim reservoir and for future research issues in context with particle-bound contaminants, the inclusion of an explicit flocculation model is important. For these reasons, the Iffezheim reservoir served as the first real case study area for the application of the implemented flocculation algorithm on a natural water-sediment system.

6.2 Numerical Model

6.2.1 Computation Grid

The three-dimensional numerical model of the Iffezheim reservoir was developed in SSIIM 2 (see chapter 4.1). The model stretches from Rhine-km 312.6 to Rhine-km 333.9. Figure 6.1 depicts the model boundaries. The model has a length of 21.3 km, a width between 200 to 700 m and a maximum water depth of 15.5 m. For generating the grid, the bathymetry from 2008 was used computed from echo soundings with a 1.0 x 1.0 meter raster. The model domain is discretized by unstructured and non-orthogonal (hexahedral and tetrahedral) cells. The three-dimensional computation grid of the Iffezheim model and a vertical slice through the grid in the downstream part of the model are shown in figure 6.2.

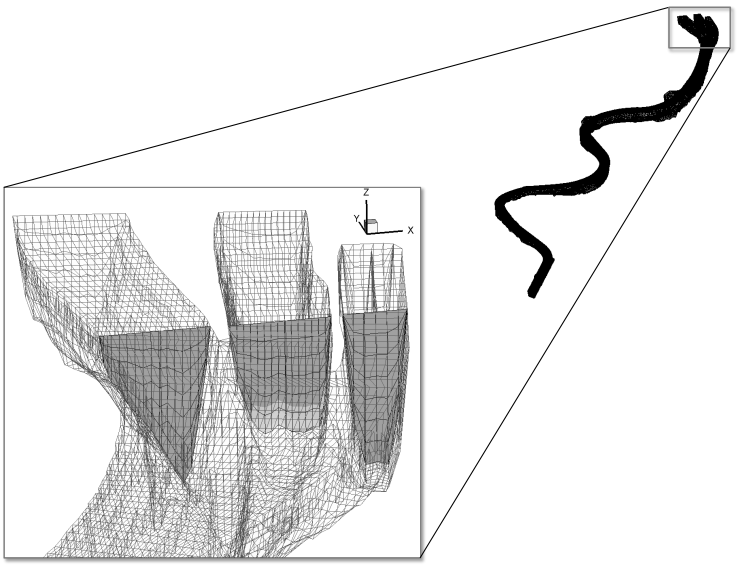

Figure 6.2: Three-dimensional computation grid of the Iffezheim model (Rhine-km 312.6 to 333.9).

The grid consists of 398 x 38 x 10 cells in the streamwise, lateral and vertical direction, respectively. As the grid is adaptive (see chapter 4.1.2), the number of cells in the vertical direction varies with the water depth. In the herein presented studies steady-state simulations were carried out in terms of the hydraulic conditions, so that the number of grid cells did not change during computation and was between 2.35 and 8.65 cells depending on the water depth. The grid contains approximately 134,830 3D cells with a cell resolution of about 7.5 x 17.5 meters in the horizontal dimension, and between 0.075 and 1.790 meters in the vertical direction.

6.2.2 Calibrated Flow Field

The knowledge of flow velocities and turbulence characteristics in the reservoir is important when making predictions of cohesive sediment transport and deposition. The hydraulic model was calibrated using ADCP (Acoustic Doppler Current Profiler) measurements of water velocities from ten cross-sections within the model domain. The measurements were conducted on November 5, 2013, i. e. after the commissioning of the fifth turbine, when the inflow discharge to the reservoir was on average $Q = 1750\,\mathrm{m^3/s}$. This discharge was used as the upstream boundary condition for model calibration. The corresponding outflow discharge through the turbines was $1500\,\mathrm{m^3/s}$, whereas the surplus of $250\,\mathrm{m^3/s}$ passed through the spillway channel. The operation of the lock channel was neglected and set to zero discharge. For the given discharge, a water level at the weir of 123.575 NN+m was used as the downstream boundary condition. The model was calibrated by adjusting the Strickler-coefficient k_{st}. The coefficient was set to $37\,\mathrm{m^{1/3}/s}$ (coarse gravel) in the upstream reaches from km 312.6 to km 318.0, increased to $42\,\mathrm{m^{1/3}/s}$ (middle gravel) between km 318.0 and km 324.0, and $45\,\mathrm{m^{1/3}/s}$ (fine gravel and sand) in the downstream reaches between km 324.0 and km 333.9, where the weir is positioned.

In figure 6.3, an overview of the spatial variation of the simulated depth-averaged horizontal velocities in the model domain is illustrated, where also the ten profiles' locations of the measurements are highlighted (km 313.0, km 314.0, km 320.0, km 321.5, km 323.0, km 326.0, km 327.0, km 329.0, km 330.945 and km 332.9). In figure 6.4, the computed depth-averaged horizontal velocities are compared with the ADCP-measurements in these ten cross-sections.

From figure 6.3 it can be seen that averaged flow velocities are the highest at the upstream model boundary (approximately $1.4\,\mathrm{m/s}$) and decrease downstream towards the Iffezheim barrage with the lowest velocities upstream of the weir (approximately $0.03\,\mathrm{m/s}$). In the two small harbour basins on the left side of the river very small flow velocities are computed. The comparison of computed with measured flow velocities in figure 6.4 shows that satisfactory reproduction of the measured flow velocities is obtained by the numerical model. The root-mean-square error (RMSE)[2] lies between $0.046\,\mathrm{m/s}$ (km 323.0) and $0.195\,\mathrm{m/s}$ (km 313.0) indicating that deviations between simulation and measurement are small. It can also be seen that good agreement is found for the velocity gradients within the profiles and at the cross profile edges. On the basis of this comparison, it can be concluded that the numerical model is sufficiently accurate to compute the flow velocities in the Iffezheim reservoir in an adequate and reasonable way.

[2]The RMSE is regularly used as a standard statistical metric in model evaluation studies. The RMSE is calculated to $RMSE = \left[\frac{1}{n}\sum_{i=1}^{n}(y_1 - y_2)^2\right]^{1/2}$, where y_1 is the measured value, y_2 the computed value and n the number of observations.

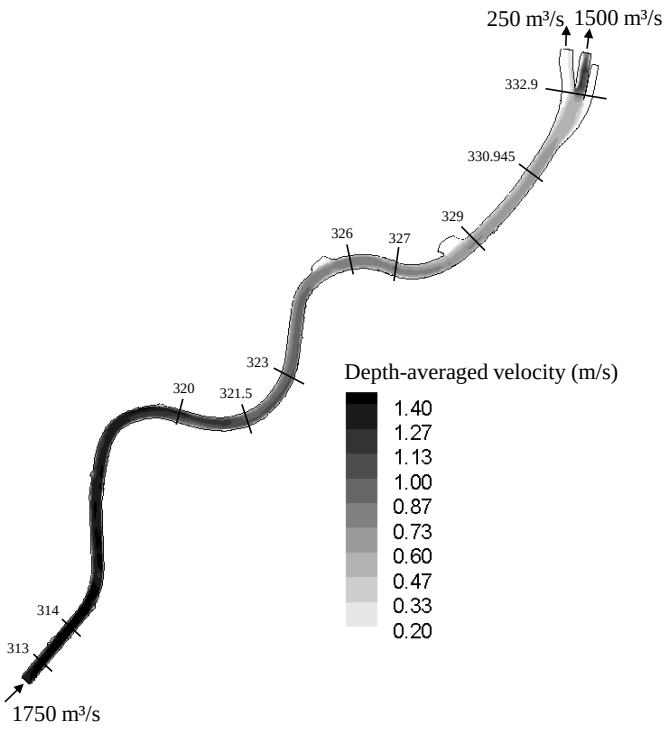

Figure 6.3: Simulated depth-averaged horizontal flow velocities in the Iffezheim reservoir for a discharge of $Q = 1750\,\mathrm{m}^3/\mathrm{s}$ and profiles' locations of the measurements.

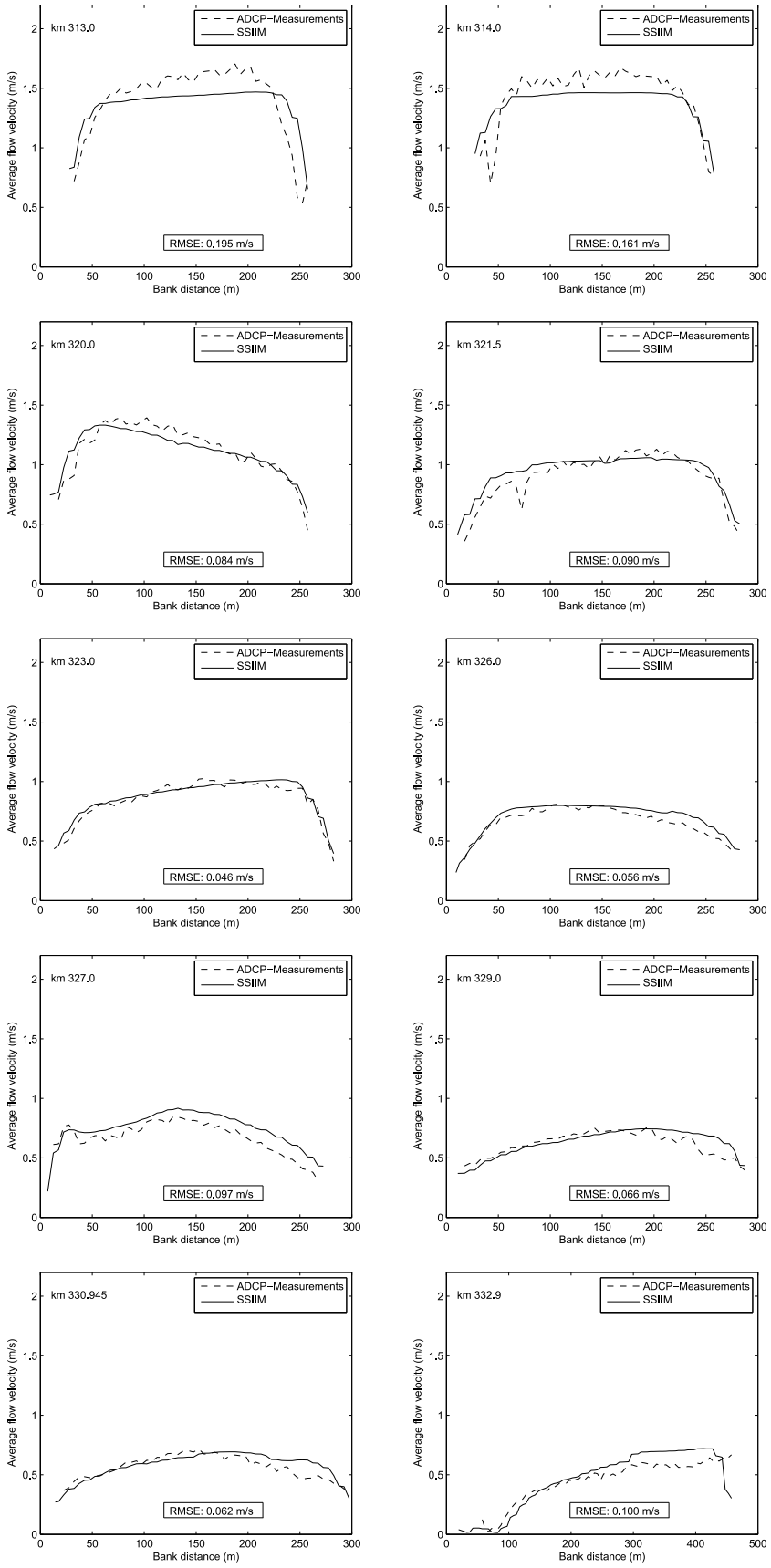

Figure 6.4: Computed and measured depth-averaged velocities in the Iffezheim reservoir for a discharge of $Q = 1750\,\mathrm{m^3/s}$.

As it was described in chapter 2.3.5, turbulence influences flocculation processes in a significant way. Since no measurement data were available with respect to turbulence parameters, the modeled turbulence characteristics were verified in terms of plausibility. Herein, the turbulent energy dissipation rate ϵ was analyzed, since it is the representative parameter for the characterization of turbulent flow structures in the implemented flocculation algorithm (see chapter 4.2). The simulated turbulent energy dissipation rates close to the river bed and at the water surface are shown in figure 6.5 for the calibrated discharge of $Q = 1750\,\mathrm{m^3/s}$. Figure 6.6 shows the turbulent dissipation rates exemplary in three vertical profiles at Rhine-km 314.0, 323.0 and 333.8 (in the weir channel).

By analogy with the computed flow velocities, it can be seen that turbulences are the highest at the upstream model boundary and decrease downstream towards the Iffezheim barrage. Figure 6.5 shows that near the river bed higher turbulent energy dissipation rates are computed than at the water surface. The maximum dissipation rates are simulated at the upstream model boundary near the river bed (in the order of $0.0134\,\mathrm{m^2/s^3}$), whereas the minimum energy dissipation can be found in the weir channel at the water surface (in the order of 2.61e-10 $\mathrm{m^2/s^3}$).

From figure 6.6, it can be seen that in all profiles a vertical gradient of the energy dissipation rate values is calculated, with the lowest values at the water surface and the maximum dissipation rates close to the river bed. In chapter 2.3.5 (figure 2.14), the vertical distribution of the turbulent kinetic energy in a differential turbulence column was illustrated representing a typical turbulence profile in natural rivers. The figure shows that the turbulent kinetic energy increases towards the bottom. Close to the river bed, the strongest turbulence intensity and consequently, the maximum flow-induced shear forces are found. This phenomenon is confirmed by the computation results.

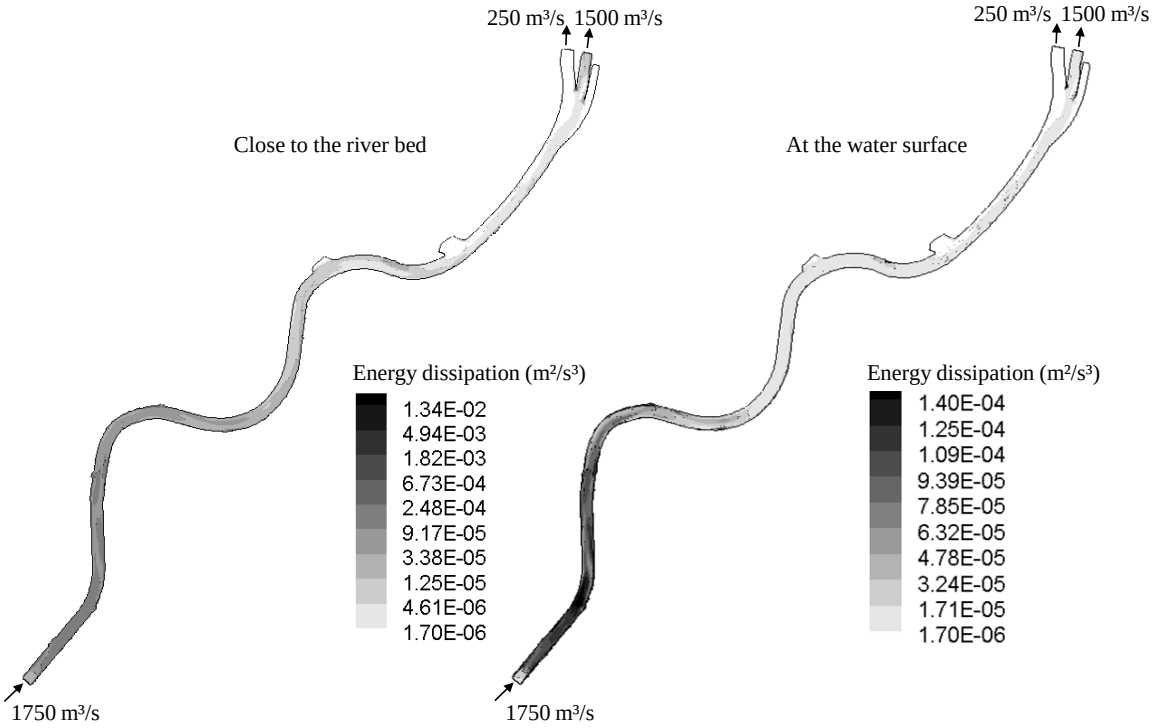

Figure 6.5: Simulated turbulent energy dissipation rate ϵ close to the river bed (left) and at the water surface (right) in the Iffezheim reservoir for a discharge of $Q = 1750\,\mathrm{m^3/s}$.

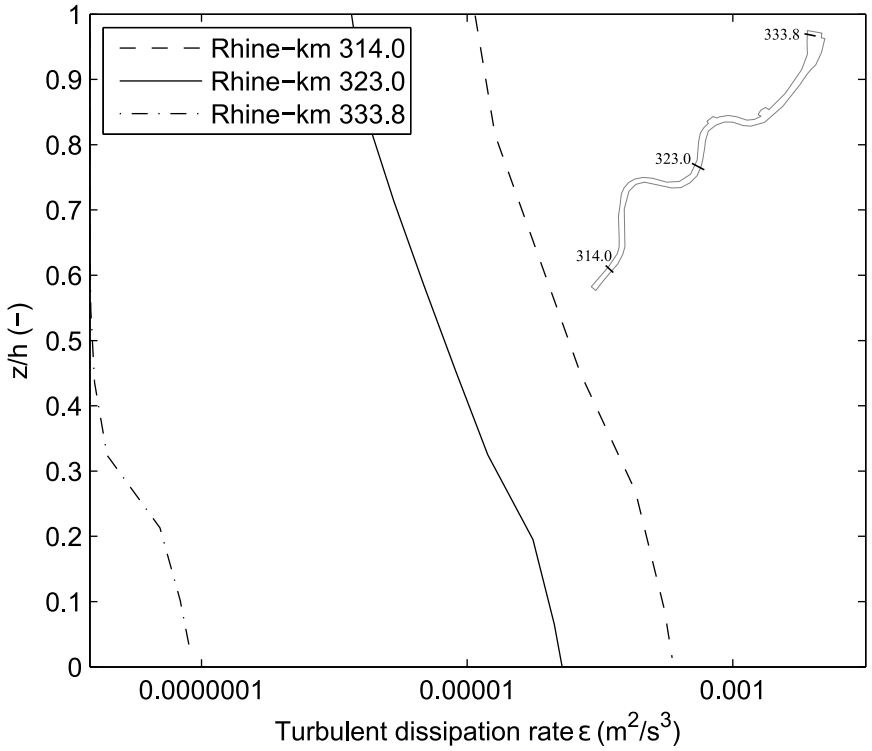

Figure 6.6: Simulated turbulent energy dissipation rate ϵ in three profiles of the Iffezheim reservoir at Rhine-km 314.0, 323.0 and 333.8 (in the weir channel) for a discharge of $Q = 1750\,\mathrm{m^3/s}$.

In figure 6.7, the computed velocity vectors at the water surface in the downstream reaches of the Iffezheim reservoir, where the reservoir gets divided into three branches, are shown. It can be seen that the water flow is fairly uniform in the middle hydropower intake channel, except for two small recirculation zones on the left side of the power plant channel. In the hydropower channel, relatively high flow velocities and energy dissipation rates are simulated. In the weir channel the flow velocities are very low (on average $0.03\,\mathrm{m/s}$), except for the area on the right bank of the weir channel. Here, higher flow velocities (on average $0.3\,\mathrm{m/s}$) are simulated and velocity vectors are oriented uniformly downstream for almost the whole length of the spillway channel. On the left side of the weir channel, a major recirculation zone with negative velocity vectors is computed. The secondary flow pattern covers the whole length of the spillway channel and roughly half of the channel width. The corresponding turbulent energy dissipation rates in the weir channel are negligibly small (see figure 6.6, Rhine-km 333.8).

The computed flow field in the weir channel, which is denoted by low flow velocities and turbulences on the left-hand side of the weir channel, is representative for a flow pattern that causes fine sediments to deposit in this area. On the right-hand side in figure 6.7, an exemplary sediment deposition pattern for the Iffezheim reservoir is shown which was derived from echosounding measurements from a three months period by the German Federal Waterways and Shipping Administration (WSV). It can be seen that a major part of the deposited sediments is found in the weir channel, where flow velocities and turbulences are relatively low.

It can be concluded that the numerical model gives plausible and appropriate results in terms of the turbulence characteristics showing the maximum energy dissipation rate values upstream of the model boundary close to the bed, whereas the lowest values are computed in the weir channel at the water surface.

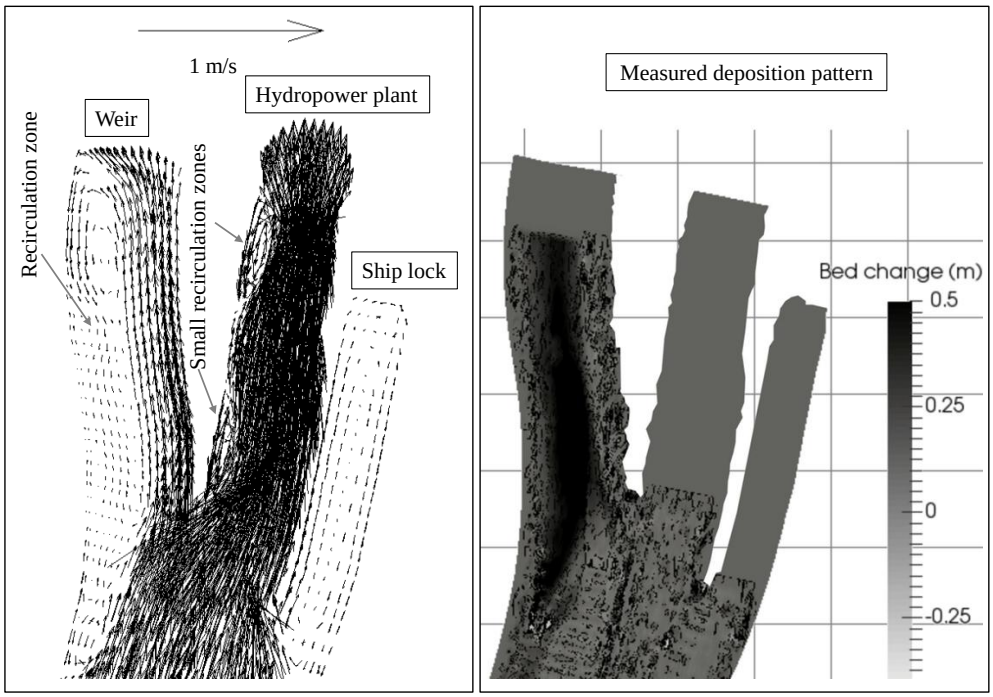

Figure 6.7: Simulated velocity vectors at the water surface in the downstream reaches of the Iffezheim reservoir for a discharge of $Q = 1750\,\mathrm{m^3/s}$ (left) and measured deposition pattern derived between two subsequent echo soundings from 5th April to 18th July 2007 (modified from Zhang et al., 2016) (right).

Within the model domain, the calculated energy dissipation rates differ up to about 7 to 8 orders of magnitude. The simulated flow field pattern in the downstream reaches of the model domain is confirmed by previous numerical studies in the Iffezheim reservoir using a discharge of similar magnitude (Hillebrand et al., 2016). The established 3D flow model in SSIIM can therefore serve as a basis for follow-up cohesive sediment computations and for the application of the implemented flocculation algorithm.

6.3 Application of the Flocculation Algorithm

For the application of the implemented flocculation algorithm on the Iffezheim model, the algorithm was transferred from SSIIM 1 into SSIIM 2. Steady-state conditions were applied in terms of the hydraulics using a constant discharge of $Q = 1750\,\mathrm{m^3/s}$. For this discharge, an averaged suspended sediment concentration of $50\,\mathrm{mg/l}$ was measured in the reservoir. The suspended sediment concentration was determined from echo intensity measurements using an ADCP instrument and calibrated by taking bottle samples (Hillebrand et al., 2012b). The concentration of $50\,\mathrm{mg/l}$ served as continuous input data at the upstream model boundary during the whole simulation time and therefore can be considered as a constant boundary condition. Based on the definitions of the discharge and the suspended sediment concentration, the flocculation algorithm was applied. Contrary to steady-state conditions in terms of the hydraulics, along the whole flow path, the flocculation simulations have to be considered as unsteady due to the temporal development of the computed floc sizes.

6.3.1 Definition of Parameters and Initial/Boundary Conditions

Table 6.1 shows an overview of the parameter definitions and settings for the application of the floc model on the Iffezheim reservoir. Table 6.2 shows the corresponding computed particle size characteristics in each of the size classes. All the definitions illustrated below were kept constant during the whole simulation time.

Table 6.1: Definition of parameters and initial/boundary conditions for modeling flocculation in the Iffezheim reservoir.

Parameter or initial/boundary condition	Definition
1. Time step Δt (sec)	15
2. Number of size classes N (–)	11
3. Particle size spectrum (μm)	see table 6.2
4. Initial conc. $C_{0,j}$ ($^{mg}/_{l}$)	see table 6.2, with $C_{0,sum} = 50\,^{mg}/_{l}$
5. Inflow conc. C_j ($^{mg}/_{l}$)	see table 6.2, with $C_{j,sum} = 50\,^{mg}/_{l}$
6. Aggregation coefficient α_a (–)	1.0
7. Particle yield strength coefficient B_τ ($^{N}/_{m^2}$)	1.0
8. Fractal dimension n_f (–)	with $D_{fc} = 50.0\,\mu$m, $n_{fc} = 2.0$
9. Settling velocity w_s formula ($^{mm}/_{s}$)	D_1 (cohesionless): Zanke (1977) $D_2 - D_{11}$ (cohesive): Winterwerp (1998)
10. Exclusion/inclusion of erosion	inclusion

The respective values and parameter definitions for the application of the flocculation model on the Iffezheim reservoir are described briefly below.

1. **Time step**: In chapter 5.3.2.2 it was elaborated that too large time steps might lead to mass conservation errors, which will increase with an increasing time step. For the flocculation computations in the Iffezheim reservoir a time step of 15 sec was used. The time step was chosen with respect to an acceptable computational time and to keep mass conservation errors to a reasonable minimum.

2. **Number of size classes**: The suspended particle size spectrum was represented by 11 size classes (see below).

3. **Particle size spectrum**: For the flocculation simulation, an assumption for the suspended particle size spectrum had to be made, since no in situ measurement data of floc sizes were available. The non-cohesive and coarsest size class was estimated to $D_1 = 130.0\,\mu$m (suspended fine sand). This size class was excluded from flocculation processes within the computations. All cohesive size classes were assumed to be in the silt fraction in the range between $D_2 = 63.0\,\mu$m to $D_{11} = 2.0\,\mu$m, with the smallest size class D_{11} representing the primary particles. The cohesive size classes were included within the flocculation computations. The respective particle size diameters of the cohesive size fractions D_3 to D_{10} were chosen in a way to ensure that the mass of a newly created aggregate/floc, which is formed by two colliding particles of the same size class, is shifted into the next coarser size class. The particle size spectrum and the average sediment particle masses of the cohesive fractions are presented in table 6.2.

4. **Initial concentration**: For the discharge of $Q = 1750\,\mathrm{m^3/s}$, an averaged suspended sediment concentration of $50\,\mathrm{mg/l}$ was measured in the reservoir. Therefore, initial to the simulation, a uniformly distributed suspended sediment concentration of $C_0 = 50\,\mathrm{mg/l}$ was defined in the whole model domain. Since the distribution of this concentration among the size classes at time $t = 0$ was not known, the initial concentrations in the respective size classes, $C_{0,j}$, had to be estimated. The specification of the initial sediment concentrations among the size classes at time $t = 0$ constitutes the initial condition for the flocculation computation. For the first simulation run, 5 % of the concentration were allocated to the non-cohesive and coarsest size class $D_1 = 130.0\,\mu\mathrm{m}$ ($C_{0,1} = 2.5\,\mathrm{mg/l}$). The remaining share of 95 % of the concentration were attributed only to the cohesive size class $D_6 = 14.6\,\mu\mathrm{m}$ ($C_{0,6} = 47.5\,\mathrm{mg/l}$) (see table 6.2).

5. **Inflow concentration**: The inflow sediment concentrations in the size classes, C_j, at the upstream model boundary represent the boundary size condition. The inflow concentrations were kept constant during the whole simulation time. Within all flocculation computations in this chapter, the inflow sediment concentrations correspond to the initial sediment concentrations, $C_{0,j}$, in the respective size classes (see table 6.2). The influence of another initial/boundary condition on the modeling results in the Iffezheim reservoir is analyzed further below in chapter 6.3.3. The sensitivity towards the initial floc size in the annular flume was illustrated in chapter 5.3.2.3.

6. **Aggregation coefficient**: Due to the lack of information about the physico-chemical properties of the suspended sediments, the aggregation factor α_a (see chapter 3.2.1) was set as a constant value which does not depend on floc size. For the cohesive size classes D_2 to D_{11}, the aggregation factor was set to $\alpha_a = 1.0$. The sensitivity analyses towards this calibration parameter in the annular flume were illustrated in chapter 5.3.2.4.

7. **Particle yield strength coefficient**: Since no values for the empirical particle yield strength coefficient B_τ (see chapter 4.2.1) were available, for the cohesive size classes D_2 to D_{11}, the parameter was set to the minimum value of $B_\tau = 1.0\,\mathrm{N/m^2}$. The sensitivity analyses towards the particle yield strength coefficient in the annular flume were presented in chapter 5.3.2.5.

8. **Fractal dimension**: The approach of Khelifa and Hill (2006) (see chapter 2.3.4) was applied to compute variable fractal dimensions for the cohesive size fractions D_2 to D_{11}. As no data about the floc structure was available from measurements, the characteristic floc size was estimated to be $D_{fc} = 50.0\,\mu\mathrm{m}$ and the characteristic fractal dimension to $n_{fc} = 2.0$. The resulting calculated fractal dimensions n_f of each size class are given in table 6.2. The influence of the fractal dimension was examined by computations in the annular flume in chapter 5.3.2.1.

9. **Settling velocity**: For the non-cohesive size class $D_1 = 130.0\,\mu\mathrm{m}$, the settling velocity equation by Zanke (1982) was used (see equation 2.24). For the cohesive fractions D_2 to D_{11}, the settling velocity formula by Winterwerp (1998) was applied taking into account the fractal structure of flocs (see equation 2.27).

10. **Exclusion/inclusion of erosion**: The grain size distribution on the bed was defined by two size fractions with grain diameters of 20 mm (coarse gravel) and 3 mm (fine gravel). These grain sizes were given uniformly over the whole model geometry and were chosen in a way to prevent sediment erosion in order to simplify the understanding of the simulated flocculation processes.

Table 6.2: Sediment particle characteristics for the Iffezheim reservoir by application of the flocculation algorithm.

Class index	Diameter	Average mass	Fractal dimension	Density	Yield strength	Settling velocity	Initial conc.	Inflow conc.
j	D_j (μm)	M_j (kg)	$n_{f,j}$ (–)	ρ_j ($^{kg}/_{m^3}$)	τ_j ($^{N}/_{m^2}$)	$w_{s,j}$ ($^{mm}/_{s}$)	$C_{0,j}$ ($^{mg}/_{l}$)	C_j ($^{mg}/_{l}$)
1	130.0	excluded from flocculation				11.42	2.5	2.5
2	63.0	1.3655e-10	1.9	1043	0.0026	0.0743	0	0
3	48.0	6.2019e-11	2.0	1071	0.0048	0.0714	0	0
4	32.7	2.0820e-11	2.1	1137	0.0115	0.0640	0	0
5	22.0	6.9855e-12	2.2	1253	0.0297	0.0534	0	0
6	14.6	2.3470e-12	2.3	1440	0.0847	0.0409	47.5	47.5
7	9.6	7.9200e-13	2.5	1710	0.2794	0.0285	0	0
8	6.3	2.6690e-13	2.6	2038	1.2044	0.0180	0	0
9	4.2	9.1300e-14	2.7	2353	9.5625	0.0104	0	0
10	2.9	3.2800e-14	2.9	2568	704.8967	0.0057	0	0
11	2.0	1.1100e-14	3.0	2650	∞	0.0029	0	0

6.3.2 Comparison of Modeled Floc Sizes with Measured Particle Sizes

The first step of the flocculation algorithm application was the validation of the implemented algorithm with respect to modeling aggregation and disaggregation mechanisms in a natural system with SSIIM 2. As a second step, in order to analyze whether the flocculation computation gives plausible results from a physical point of view, measured particle sizes from Rhine-km 330.0 were compared with the computed floc size distribution at Rhine-km 330.0.

For the first simulation run, the fraction of the cohesive sediment particles (95 %) with diameters less than or equal to 63 μm was attributed only to size class $D_6 = 14.6\,\mu$m (middle silt). The non-cohesive sediment fraction (5 %) was allocated to the coarsest size class $D_1 = 130.0\,\mu$m (fine sand). Size classes D_2 to D_5, and D_7 to D_{11} had zero sediment concentration. As mentioned above, these settings refer to both, the initial conditions at time $t = 0$ and the boundary condition in terms of the inflow concentration distribution. In figure 6.8, the predefined particle size distribution is presented together with the computed particle size distribution at Rhine-km 330.0 by the application of the flocculation model. The computed particle size distribution corresponds to a depth-averaged particle size distribution and was evaluated after the modeled floc sizes remained constant, i. e. a steady-state, time-independent situation in particle sizes was computed. In the following chapter 6.3.3, the temporal development of the depth-averaged concentrations in each particle size class is shown until a steady-state situation in modeled floc sizes is reached.

At first, figure 6.8 shows that the fraction of the non-cohesive particles from size class $D_1 = 130.0\,\mu$m, which were excluded from flocculation processes, decreased from originally 5.0 % to a negligibly small value of 0.64 %. Almost all particles of size class 1 deposit upstream of Rhine-km 330.0 due to their relatively high settling velocities (see table 6.2). The flow velocities and turbulence intensities are not

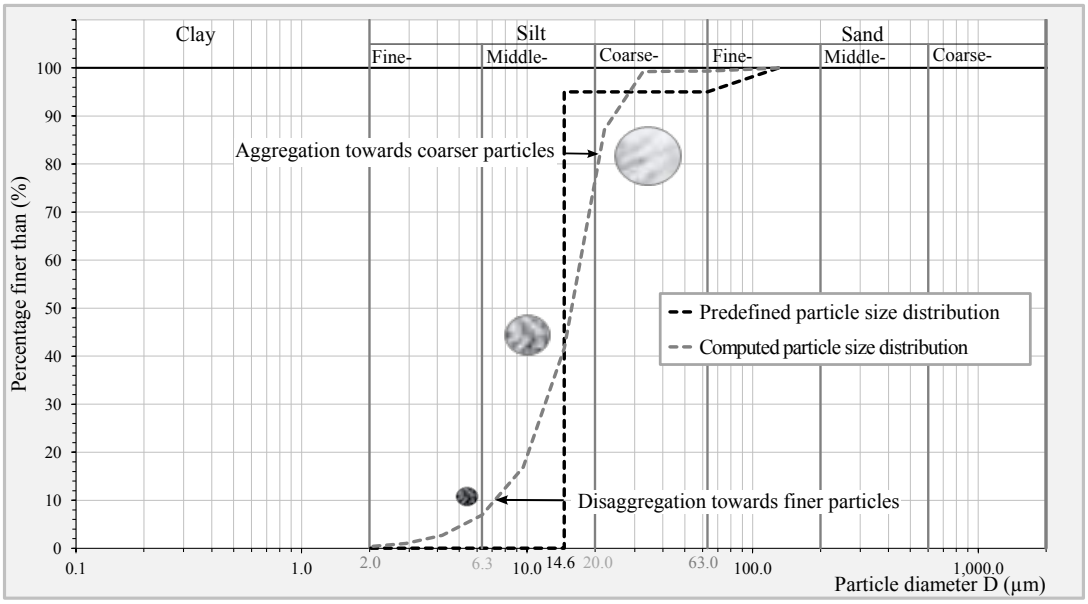

Figure 6.8: Predefined particle size distribution in the whole model domain and computed particle size distribution at Rhine-km 330.0 by application of the implemented flocculation algorithm.

high enough to keep these particles in suspension. As a consequence, only a very small fraction of the fine sand particles reach the evaluated transect at Rhine-km 330.0.

In terms of the cohesive size classes, it can be seen that the flocculation algorithm on the one hand simulates particle disaggregation, as particle mass from size class $D_6 = 14.6\,\mu$m is shifted towards the finer size classes with diameters smaller than $14.6\,\mu$m. At steady-state, 16.87 % of the sediment mass was shifted into size classes between $D_{11} = 2.0\,\mu$m and $D_7 = 9.6\,\mu$m. On the other hand, also aggregation processes are modeled which lead to a sediment mass shifting towards the coarser cohesive size classes with particle diameters larger than $D_6 = 14.6\,\mu$m. At steady-state, 57.74 % of the sediment mass consists of particles of size classes between $D_5 = 22.0\,\mu$m and $D_3 = 48.0\,\mu$m. 24.75 % from originally 95.0 % of the sediment mass remains in size class D_6, whereas no sediment mass is shifted into the coarsest cohesive size class $D_2 = 63.0\,\mu$m. Overall, the sediment mass shiftings lead to an increase in the mean cohesive particle diameter from $D_m = 14.6\,\mu$m to $D_m = 19.1\,\mu$m. Hence, for the applied settings and definitions illustrated in table 6.1, the computed particle size distribution by application of the flocculation algorithm becomes coarser than the predefined one without using the algorithm.

Previously unpublished in situ floc size measurements in the Iffezheim reservoir indicate that the in situ suspended sediment particles in the Iffezheim reservoir are flocculated and hence, are transported as coarse aggregates/flocs rather than as small individual primary particles (Stefan Haun, pers. comm.). The above presented computation results show that in the Iffezheim reservoir, in general, flocculation processes can be reproduced by the implemented algorithm when applying the parameter definitions and initial/boundary conditions from table 6.1.

In order to estimate whether the modeled floc sizes are physically reasonable and plausible, the flocculation computation from Rhine-km 330.0 was compared with measured particle sizes based on laser analyses from bottle samples at Rhine-km 330.0. The laser particle size measurements of the collected bottle samples were conducted after dispersing the particles by ultrasonic vibration (BfG, pers. comm.). This

method leads to a disruption of most of the fragile flocs into constituent primary particles. Consequently, the measurement does not reflect the real in situ size distribution of the suspended particles. In figure 6.9, the measured and computed particle volume distributions, which show the particles in the respective size class ranges by percentage of the total volume, are compared. In addition, in figure 6.10, both cumulative curves are presented which show the total volume of all size classes.

It can be seen that the proportion of the total load contributed by the smallest particles with sizes between $2\,\mu$m and $9.6\,\mu$m is larger for the measured size distribution than for the computed one. The contrast between the two distributions gets obvious, in particular for the finest particles. Whereas 17.9 % of the measured particles are smaller than or equal to $2\,\mu$m, the computed distribution contains only 0.38 % of the particles with diameters of $2\,\mu$m. For the size range between $6.3\,\mu$m and $9.6\,\mu$m, the measured and computed size distributions are very close to each other showing a slightly higher content of these particles by the measurement (10.80 %) than by the computation (9.96 %). However, the proportion of the total load contributed by the three next coarser size class ranges ($9.6\,\mu$m $-$ $14.6\,\mu$m, $14.6\,\mu$m $-$ $22.0\,\mu$m, $22.0\,\mu$m $-$ $32.7\,\mu$m) is significantly greater for the computed size distribution (24.75 %, 45.50 % and 12.11 %) than for the measured particle size distribution (8.8 %, 13.0 % and 10.40 %). In particular, for particles in the size range between $14.6\,\mu$m $-$ $22.0\,\mu$m, the flocculation simulation shows a 3.5 times higher amount of these particles than the measurement. The median grain size of the measured distribution falls within the $\leq 2\,\mu$m size class, whereas that for the computed flocculated size distribution is of the order of 12 times greater and falls within the $14.6\,\mu$m $-$ $22.0\,\mu$m size class range.

Figure 6.9 also shows that on the coarser end of the cohesive size spectrum (size class ranges $32.7\,\mu$m $-$ $48.0\,\mu$m and $48.0\,\mu$m $-$ $63.0\,\mu$m), few (0.13 %) or none sediment particles are computed at Rhine-km 330.0, whereas the measurements show a proportion of 9.3 % and 3.2 % of these particle sizes, respectively. Also the proportion of the total load contributed by the coarsest and non-cohesive size class range $63.0\,\mu$m $-$ $130.0\,\mu$m is greater for the measured size distribution (5.0 %) than for the computed particle size distribution (0.64 %).

The presented results show that for a wide range of the particle size spectrum ($2.0\,\mu$m to $32.7\,\mu$m), the modeled floc size distribution is coarser than the measured particle size distribution. However, on the coarser end of the size spectrum ($32.7\,\mu$m to $130.0\,\mu$m) the measured particle sizes exceed the modeled ones. The question is if these results are physically plausible. As it was mentioned above, it is assumed that measured particle sizes mainly reflect grain sizes of the primary particles due to particle break-up by ultrasonic vibration prior to the measurements. Since, in overall, the modeled sizes of the aggregated flocs are larger than the measured sizes of the mainly primary particles, the simulated floc size distribution is in a physically plausible value range. For the opposite trend on the coarser end of the size spectrum, where computed particle sizes are smaller than the measured ones, different reasons can be found.

Firstly, some uncertainties exist with respect to the interpretation of the measured particle sizes. It is possible that a certain proportion of the measured particle sizes may not represent primary particle sizes, but larger aggregates/flocs which have not been disrupted by the sample preparation and/or which have been newly created during the measurement. In this case, the measured particle size distribution may include both primary discrete particles as well as a certain percentage of agglomerated aggregates/flocs, and consequently does not relate only to the chemically dispersed mineral fraction. However, if flocs were newly formed during the measurement, their sizes are not representative for the in situ floc sizes. The aggregates/flocs created in situ are strongly influenced by the chemical water characteristics and the hydraulic boundary conditions in the reservoir. Since in the laboratory other boundary conditions

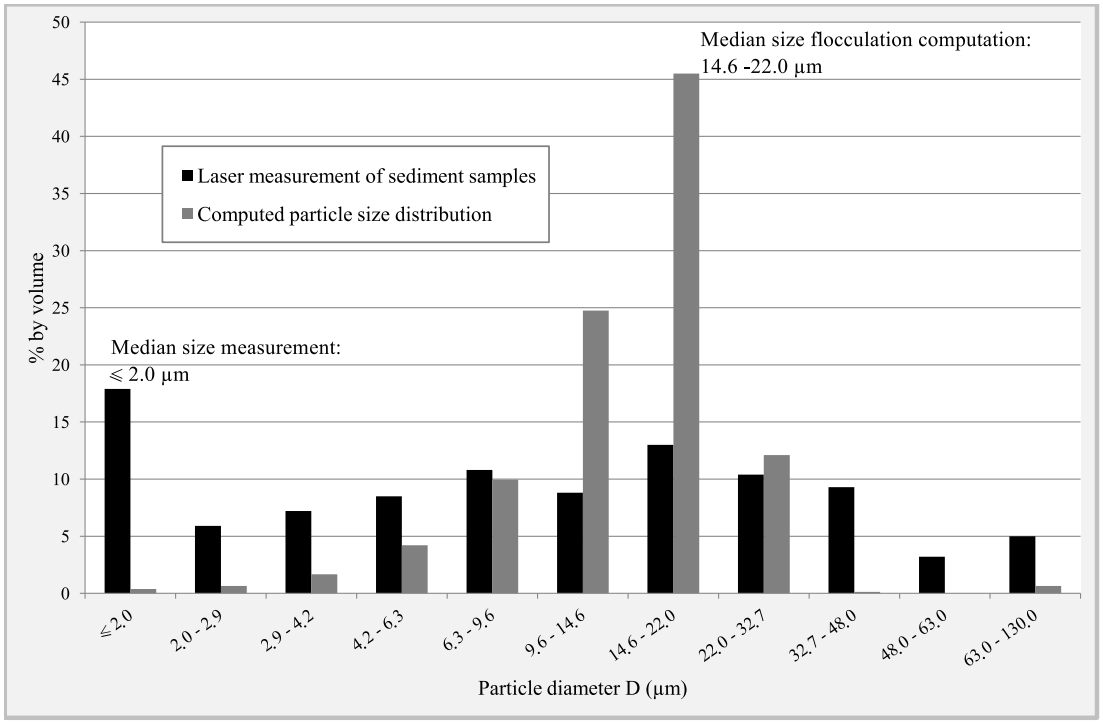

Figure 6.9: Comparison of measured and computed particle volume distribution in the Iffezheim reservoir at Rhine-km 330.0.

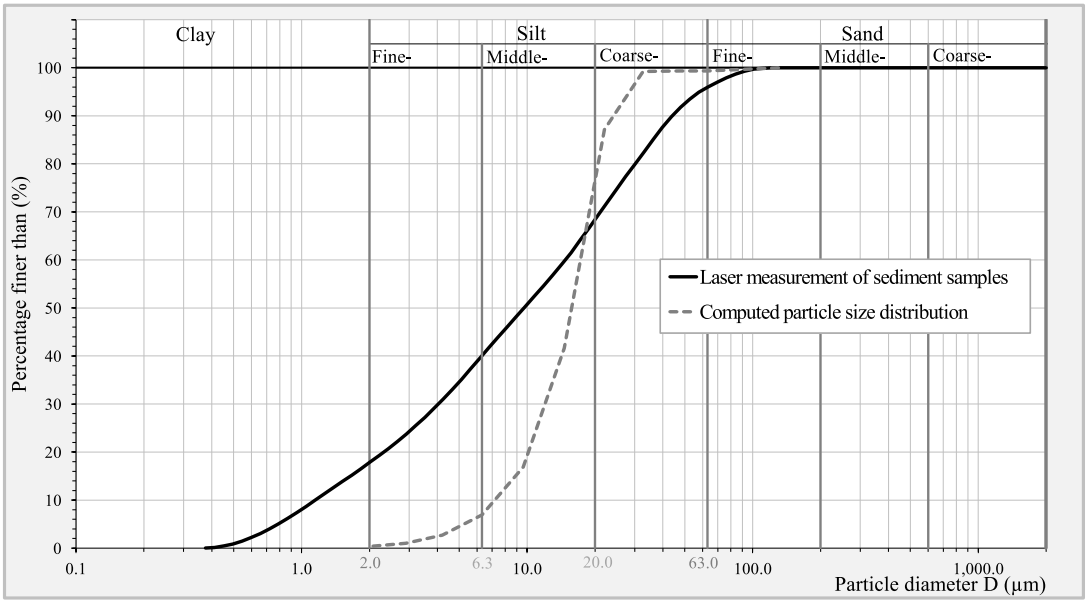

Figure 6.10: Laser particle size analyses from sediment samples in the Iffezheim reservoir at Rhine-km 330.0 and computed particle size distribution at Rhine-km 330.0 by application of the implemented flocculation algorithm.

are present, measured particle sizes on the coarse end of the size spectrum (here in size class range $32.7\,\mu\text{m} - 130.0\,\mu\text{m}$) do not reflect the real in situ floc sizes. Within the computation, the largest aggregates/flocs are computed in the size class range between $22.0\,\mu\text{m} - 32.7\,\mu\text{m}$. The very small computed proportion (0.64 %) of particles in the coarsest and non-cohesive size class refers to the percentage of suspended fine sand particles, which do not take part in the flocculation processes. In contrast, the measurements show a comparatively high proportion of particles/aggregates in this size class range (5.0 %). It is assumed that these measured particles are not discrete fine sand particles, but agglomerated flocs which were not disrupted by sample preparation or which were newly formed during the measurement and therefore are influenced by the respective boundary conditions in the laboratory.

Secondly, the definition of the primary particle sizes in the simulation plays a role. Within this simulation only the finest size class ($D_{11} = 2.0\,\mu\text{m}$) was assumed to be representative for the primary particles which are non-breakable by definition. However, the measured particle sizes indicate that both, smaller and larger primary particles than $2.0\,\mu\text{m}$ exist in the Iffezheim reservoir. If, for example, also larger primary particles (e. g. of size $63.0\,\mu\text{m}$) would be considered within the simulation, the computed floc sizes would be coarser predicted, since these larger primary particles would not be disrupted into smaller particles. In this case, the simulated floc sizes might exceed the measured particle sizes also on the coarser end of the cohesive size spectrum.

Thirdly, also the assumptions concerning the parameter values for modeling flocculation play a major role. For example, within this simulation the particle yield strength coefficient B_τ was set to the minimum value of $1.0\,\text{N/m}^2$. Additional simulations (not shown here) based on higher values than 1.0, e. g. $B_\tau = 10^4\,\text{N/m}^2$, led to higher particle yield strengths, so that particle disaggregation due to flow-induced or collision-induced shear stresses was totally prevented. In this case, only particle aggregation occurred and led to a sediment mass shifting into the size class ranges $32.7\,\mu\text{m} - 48.0\,\mu\text{m}$ and $48.0\,\mu\text{m} - 63.0\,\mu\text{m}$, whereas no sediment mass was shifted into size class ranges smaller than $9.6\,\mu\text{m} - 14.6\,\mu\text{m}$. The computed proportion of the coarsest and non-cohesive particles in the size class range $63.0\,\mu\text{m} - 130.0\,\mu\text{m}$ remained obviously the same, since these particles were excluded from flocculation.

A similar effect, i. e. a coarser computed particle size distribution curve, would be reached if, for example, the fractal dimensions n_f would be increased. Within this simulation the characteristic fractal dimension n_{fc} was set to 2.0 (see table 6.1). The definition of a higher characteristic fractal dimension n_{fc} would contribute to higher calculated fractal dimensions n_f. This would result in overall more compact and dense particles/flocs for the whole size spectrum, so that also the particle yield strengths would increase. In this case, it is assumed that the computed particle size distribution would also be coarser than shown in figure 6.9 and 6.10.

However, some considerations have to be made when defining other values for the parameters and coefficients in the flocculation algorithm, which will affect the coarser end of the computed size spectrum. For example, it should be taken into account that the class upper limit of the cohesive fractions has to be chosen coarse enough, so that also the largest possible floc sizes can be computed. In the presented simulation results for Rhine-km 330.0, taking into account the parameter definitions from table 6.1, the class upper limit of the cohesive size fractions ($= 63.0\,\mu\text{m}$) was chosen sufficiently coarse enough, since the largest flocs were computed in the size class range between $22.0\,\mu\text{m}$ and $32.7\,\mu\text{m}$.

The presented results and considerations clarify that measurement size techniques, which may disrupt or create additional sediment flocs, are not appropriate for providing representative values of the in situ

particle size distribution. As a consequence, these measured particle sizes are inadequate input data for both, cohesive sediment transport models which aim to approximate the in situ floc sizes by such data, and models which use these data for the validation of the computed floc sizes. The implemented algorithm, in general, is able to reproduce the observed phenomenon that the in situ sediment particles in the Iffezheim reservoir are flocculated and hence are transported as agglomerations of particles (flocs) of various sizes rather than as individual single particles.

From these studies it can be concluded that the simulated floc sizes in the Iffezheim reservoir seem physically plausible in comparison with measured mainly primary particle sizes. However, the degree of flocculation of the in-situ particles can not be determined in this study. This is largely attributed to the uncertainties in terms of the choice of unknown parameter values for the application of the implemented flocculation algorithm (e. g. for the particle yield strength coefficient B_τ and the fractal dimension n_f). Furthermore, uncertainties exist in terms of the definition of the primary particle size spectrum pointing out the difficulty of a physically precise and accurate flocculation modeling in a natural system like the Iffezheim reservoir. This becomes even more obvious when taking into account that assumptions were also done concerning the inflow particle sizes at the upstream model boundary. The impact of the boundary size distribution on the modeled floc sizes is analyzed and discussed in the next chapter. In this context, the influence of spatially varying turbulences on the modeling results is investigated as well.

6.3.3 Modeled Floc Sizes as a Function of the Boundary Size Condition and Spatially Varying Turbulences

Within the sensitivity analyses in the annular flume (see chapter 5.3.2.3) it was shown that the lack of knowledge of the initial floc size is insensitive towards the final modeled floc sizes, if the flocs have enough time to reach an equilibrium stage between floc growth and floc break-up. This implies that the water depth has to be sufficient, so that flocculation processes can fully develop to a steady-state situation, which is independent of the initially assumed particle size distribution. In this chapter, this finding is verified for the application of the flocculation algorithm on the Iffezheim reservoir, where the particles are supposed to be primarily transported by advection with the mean flow velocity. During the transportation of the sediment particles by the water flow, the particles have time for undergoing flocculation processes. In the following studies, it is investigated which flow path distance from the upstream model boundary is required to ensure that flocculation processes have enough time to fully develop to an equilibrium stage, which is not affected by the assumed inflow particle sizes at the upstream model boundary. This means, it was studied how the computed floc sizes develop in flow direction when different inflow particle sizes are assumed at the model boundary.

When analyzing modeled floc sizes in flow direction, also the spatial variability of the floc sizes due to varying turbulence-induced shear stresses in flow direction has to be taken into account. In chapter 6.2.2, it was shown that within the model domain fluid velocities and turbulences vary in the main flow path direction (see figures 6.3 and 6.5). Hence, along the flow path, modeled floc sizes are functions of the turbulence intensities and might simultaneously be influenced by the boundary condition of the inflow particle size distribution.

In the following, these two overlapping factors are described separately in order to clarify their influences. In the first part, the spatial variability of modeled floc sizes due to varying turbulence-induced shear stresses is exemplarily described for the first simulation run based on an inflow cohesive particle size of

$D_6 = 14.6\,\mu$m. In the second part, the sensitivity of the modeled floc sizes towards the assumption of the boundary condition is investigated by comparing the results of three different chosen inflow particle sizes.

Spatial Variability of Modeled Floc Sizes due to Varying Turbulences

In chapter 6.2.2, it was shown that the highest flow velocities and turbulences were computed near the upstream model boundary (Rhine-km 312.6), whereas the lowest values were simulated at the downstream model boundary in the weir channel (Rhine-km 333.9). As described in chapter 2.3.5, the turbulent structure of a fluid flow plays a major role in terms of the flocculation behavior of fine sediments. On the one hand, an increase in turbulence increases the number of collisions between suspended particles and thereby increases the probability of floc growth and floc size. At the same time, too high turbulent shear stresses may decrease the floc size by breaking up the fragile flocs. For the real case study in the Iffezheim reservoir, the question arises how spatially varying turbulence-induced shear stresses in the model domain affect the computed floc sizes.

In the implemented flocculation algorithm, turbulence characteristics are captured by the turbulent energy dissipation rate ϵ (see chapter 4.2). This parameter is used to compute the turbulence-induced shear stresses and the collision-induced shear stresses as well as the collision efficiency, i. e. the number of collisions between two particles per volume and time step (see diagram 4.5). Smaller ϵ-values in the main flow direction of the Iffezheim reservoir contribute to lower flow-induced and collision-induced shear stresses and to a temporal delay of the flocculation processes. Therefore, it is expected that particle disaggregation is reduced towards the downstream reaches of the model domain and as a consequence, modeled particle sizes increase from the upstream to the downstream model boundary. In this context, it has to be investigated also, whether the class upper limit of the cohesive size fractions ($= 63.0\,\mu$m) is chosen sufficiently coarse enough when downstream of Rhine-km 330.0 possibly even larger floc sizes can be created than shown above in figure 6.9 and 6.10.

In order to analyze how spatially varying turbulence-induced shear stresses in the model domain affect the computed floc sizes, the results of the flocculation computations based on an inflow cohesive particle size of $D_6 = 14.6\,\mu$m were evaluated and compared at 7 representative points within the Iffezheim reservoir (at km 313.6, km 318.5, km 323.1, km 326.1, km 330.0, km 332.5 and km 333.5). The locations of these points are shown in figure 6.11. They are characterized by a decreasing turbulent energy dissipation rate in the downstream direction.

In figure 6.12, the computed depth-averaged suspended sediment concentrations are illustrated in each size class and at each chosen location in the model domain. At first, it can be seen that the suspended sediment concentration of the non-cohesive size class $D_1 = 130.0\,\mu$m (fine sand particles) decreases continuously in the downstream direction. Whereas the constant inflow concentration of these particles at the upstream model boundary amounts to $2.5\,\mathrm{mg/l}$, this value has already decreased to $1.66\,\mathrm{mg/l}$ at Rhine-km 313.6, i. e. 1 km downstream of the upper model boundary at Rhine-km 312.6. At Rhine-km 330.0, only $0.3\,\mathrm{mg/l}$ of the fine sand particles are kept in suspension, whereas in the weir channel at Rhine-km 333.5 zero suspended sediment concentration of this size class is computed. As noted above in the previous chapter, this decrease in suspended sediment concentration is caused by the lower flow velocities and turbulence intensities towards the downstream reaches of the reservoir. As a consequence, along the flow path less fine sand particles can be kept in suspension which causes the particles to deposit.

Within the cohesive size classes D_2 to D_{11}, it can be seen that the suspended sediment concentration of the inflow particle sizes class $D_6 = 14.6\,\mu$m is steadily decreasing in the downstream flow direction.

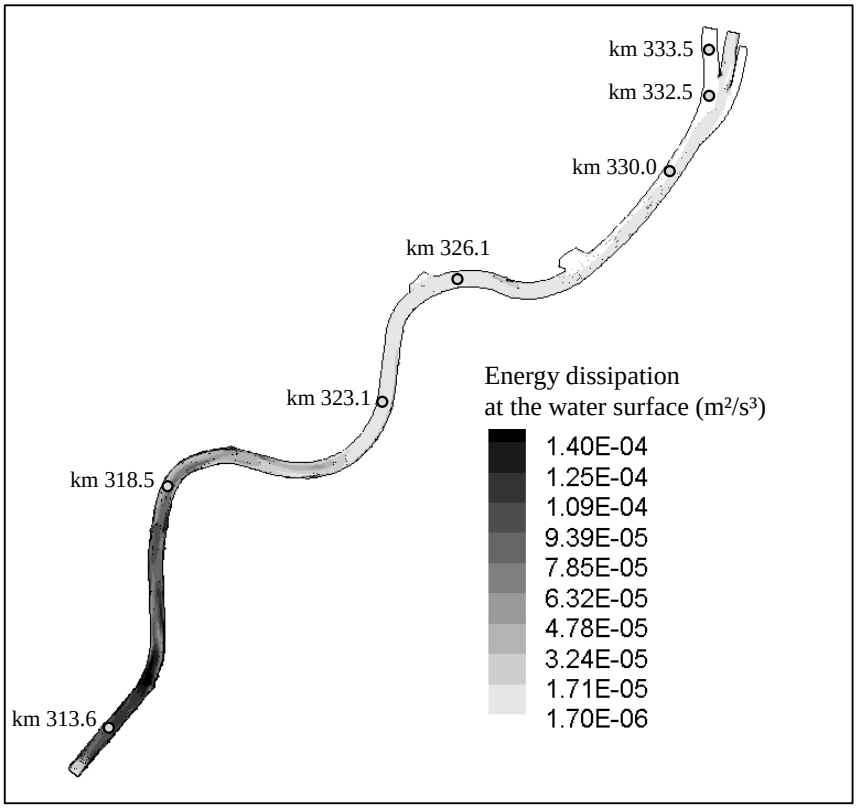

Figure 6.11: Chosen locations in the Iffezheim reservoir, at which the results of the flocculation modeling were compared with each other.

The concentration of these particles is shifted into coarser size classes (D_3 to D_5) due to aggregation, as well as into the finer size fractions (D_7 to D_{11}) due to flow-induced and collision-induced disaggregation processes. From Rhine-km 318.5 to Rhine-km 333.5 a distinct tendency in the computed concentrations is identifiable: whereas the sediment concentrations of the smaller particles in size classes D_6 to D_{11} are continuously decreasing, the concentrations in the coarser size fractions D_3 to D_5 in general are increasing. The maximum concentration of particles in size class $D_5 = 22.0\,\mu$m is reached at Rhine-km 330.0. For Rhine-km 332.5 and 333.5 a decrease in this particle concentration is computed. This decrease in sediment concentration is compensated by a comparatively high increase in sediment concentration in the coarser size class $D_4 = 32.7\,\mu$m. At Rhine-km 332.5 and 333.5 a small amount of particles is shifted also into the even coarser size class $D_3 = 48.0\,\mu$m. Within the whole model domain, no sediment mass is computed in the coarsest cohesive size class $D_2 = 63.0\,\mu$m indicating that the coarsest cohesive class D_2 was chosen coarse enough for the respective parameter definitions and assumptions made for this computation. These include, for example, the definitions of $B_\tau = 1.0\,\mathrm{N/m^2}$ and $n_{fc} = 2.0$, as well as the assumptions in terms of the primary particle and the inflow particle sizes. Other parameter definitions and assumptions, which lead to a coarser computed particle size distribution, may require the definition of a larger maximum particle diameter for the cohesive size fraction.

From figure 6.12 it can be seen that from Rhine-km 318.5 to Rhine-km 333.5, the computed spatial development of the suspended sediment concentrations in the respective size classes confirms the assumption made at the beginning of these analyses. Since the turbulences decrease in the downstream direction, also collision-induced as well as turbulence-induced shear stresses acting on the particles decrease. This

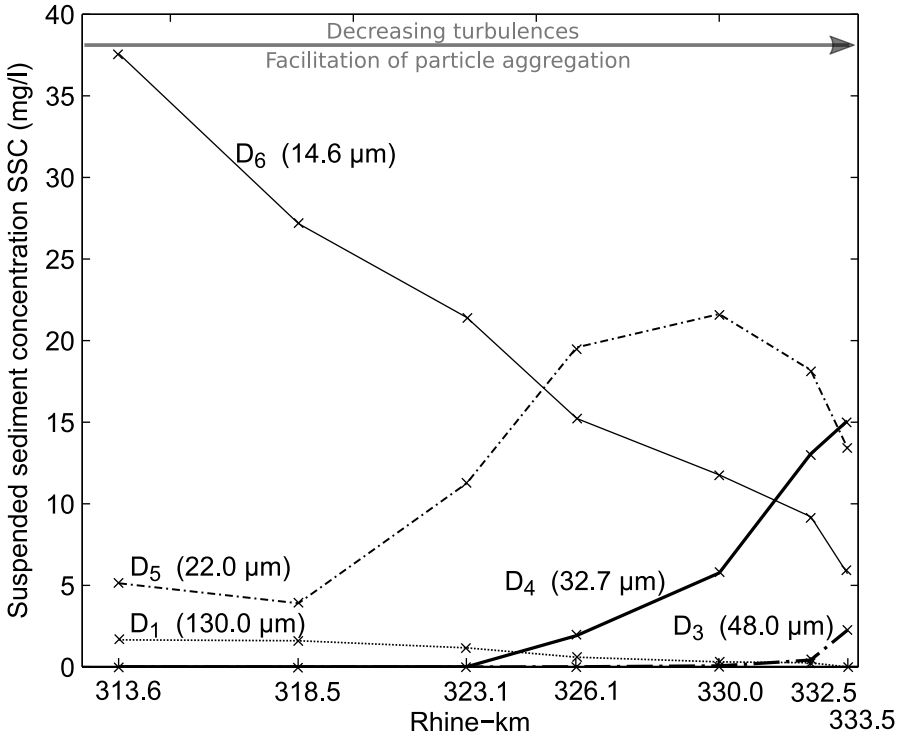

(a) Size classes D_1 to D_6. It has to be noted that the non-cohesive size class D_1 was excluded from the flocculation processes. No sediment mass was shifted into the coarsest cohesive size class $D_2 = 63.0\,\mu$m.

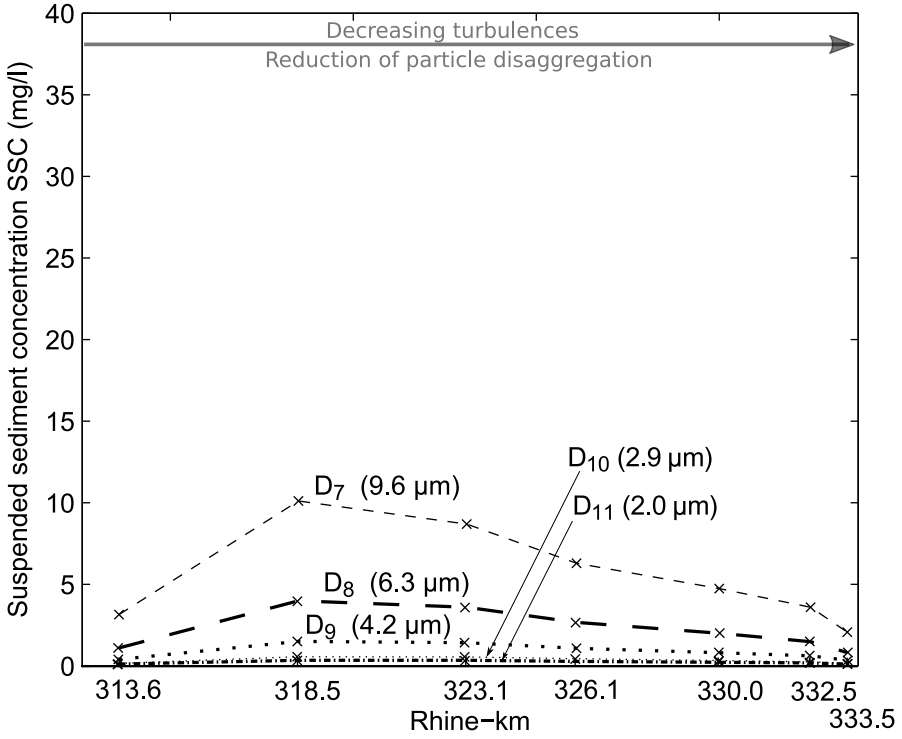

(b) Size classes D_7 to D_{11}.

Figure 6.12: Computed depth-averaged suspended sediment concentrations in each size class as a function of the Rhine-km for an inflow particle size of $D_6 = 14.6\,\mu$m (model boundaries: Rhine-km 312.6 to Rhine-km 333.9).

leads to a reduction of particle disaggregation, i. e. to a decrease in sediment concentration in the smaller size classes, and to a facilitation of particle aggregation, i. e. an increase in sediment concentration in the coarser size fractions, in the downstream direction. However, the figure also shows that this trend is not reproduced at the most upstream evaluated location at Rhine-km 313.6, i. e. 1 km downstream of the upstream model boundary. The opposite tendencies at this point suggest that the assumption of the inflow particle size affects the modeled floc size, at least until Rhine-km 313.6. This aspect is analyzed in the second part of this chapter.

Impact of the Inflow Particle Size

The investigations on the influence of any arbitrarily chosen boundary size distribution on the modeled floc sizes were conducted by three comparative numerical studies, for which different boundary size conditions were applied. Besides the above presented boundary condition which was used for the first simulation run (i. e. 5 % of the inflow concentration of $C = 50.0\,\mathrm{mg/l}$ consist of fine sand particles in the non-cohesive size class $D_1 = 130.0\,\mu\mathrm{m}$, while 95 % represent the cohesive fraction of size class $D_6 = 14.6\,\mu\mathrm{m}$), two additional simulations were carried out, for which extreme boundary conditions were assumed for the cohesive fraction. On the one hand, 95 % of the suspended sediment concentration were allotted only to the coarsest cohesive size class $D_2 = 63.0\,\mu\mathrm{m}$. On the other hand, it was assumed that the cohesive inflow particles consist solely of the finest size class $D_{11} = 2.0\,\mu\mathrm{m}$. For all three computations, these inflow particle sizes were kept constant during the whole simulation time and corresponded to the initial sediment concentrations in the size classes at time $t = 0$ in the whole model domain. Considering only the cohesive fractions, the inflow particle sizes are summarized as follows: $D_2 = 63.0\,\mu\mathrm{m}$, $D_6 = 14.6\,\mu\mathrm{m}$ and $D_{11} = 2.0\,\mu\mathrm{m}$.

In figure 6.13, the computed depth-averaged, arithmetic mean diameters D_m are shown as a function of the Rhine-km depending on the inflow particle size. In order to clarify the influence of the sediment mass fluxes between the size classes on the model results, the mean floc sizes were evaluated based on the simulated sediment concentrations of the flocculated, cohesive size size fractions D_2 to D_{11}. The non-cohesive size class D_1 was not taken into account in the evaluation in figure 6.13.[3]

At first, figure 6.13 shows that in general, the trend of larger floc sizes in the downstream direction is reproduced also by the two other computations ($D_2 = 63.0\,\mu\mathrm{m}$ and $D_{11} = 2.0\,\mu\mathrm{m}$) and can physically be attributed to the decreasing turbulence-induced shear stresses in flow direction. However, it can also be seen that the inflow particle size has a major impact on the modeled floc sizes. In the following, first the impact of the inflow particle size is described exemplarily for the first simulation run, i. e. for an inflow particle size of $D_6 = 14.6\,\mu\mathrm{m}$. Afterwards the sensitivity of any arbitrarily chosen boundary particle size on the modeled results is discussed by a comparison of the three computations.

Figure 6.13 depicts that for an inflow particle size of $D_6 = 14.6\,\mu\mathrm{m}$, the mean diameter increases from $D_m = 12.9\,\mu\mathrm{m}$ at Rhine-km 318.5 to $D_m = 25.3\,\mu\mathrm{m}$ at Rhine-km 333.5. This corresponds to an approximate doubling of the simulated mean floc size within a reach of 15 km. The opposite trend in computed floc sizes at Rhine-km 313.6, i. e. 1 km downstream of the model boundary, seems physically not plausible. Due to higher turbulence intensities in the upstream flow direction, one would expect a smaller modeled floc size at Rhine-km 313.6 than at Rhine-km 318.5, since higher turbulences promote disaggregation towards smaller particle sizes rather than aggregation towards larger flocs. The opposite

[3] A consideration of the coarsest size class D_1 in terms of the calculation of the mean floc size D_m would lead to a slight increase in D_m, in particular for the model reach between the upstream model boundary and Rhine-km 330.0.

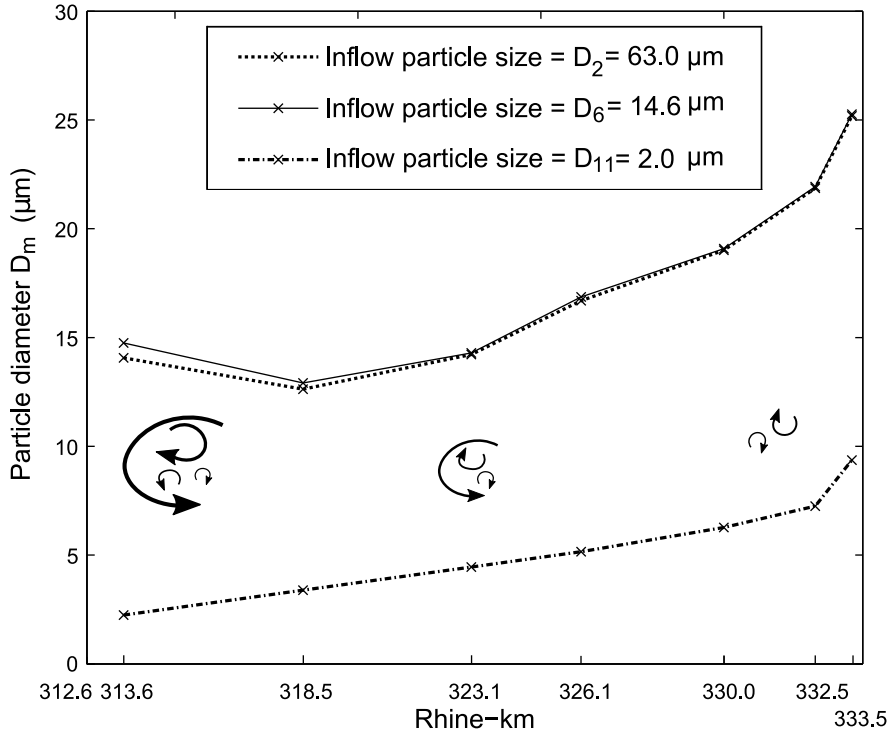

Figure 6.13: Computed depth-averaged mean particle diameter D_m as a function of the Rhine-km depending on the inflow particle size (model boundaries: Rhine-km 312.6 to Rhine-km 333.9).

trend at Rhine-km 313.6 indicates that the flow length of 1 km and therefore the available time for undergoing flocculation processes is not sufficient to reach an independence of the inflow particle size on the modeled floc sizes.

The maximum time for undergoing flocculation processes, i. e. the time that is available to grow to steady-state floc sizes, corresponds to the time the particles need to be transported from the upstream model boundary to Rhine-km 313.6. Once the inflow particles have reached this point, a steady-state situation in modeled floc sizes is computed and the particle sizes do not further change over time, since the inflow particle sizes are defined as a constant boundary condition during the whole simulation time. The computed mean floc size at Rhine-km 313.6 suggests that the particles have reached this location before the flocculation processes have fully been developed to an equilibrium stage. The sediment mass fluxes between the cohesive size classes take too long, so that after a flow path of 1 km a situation in computed floc sizes is reached, which is still affected by the defined inflow particle size. In the case that floc growth and floc break-up would have developed to an equilibrium stage before the particles reach Rhine-km 313.6, it is assumed that a smaller mean floc size at Rhine-km 313.6 would be computed than at Rhine-km 318.5. This means that a sensitivity of the modeled floc sizes towards the inflow particle size is found until at least Rhine-km 313.6. Hence, the flow length of 1 km is too short to achieve an independence of the particle size boundary condition on the flocculation modeling results. However, this does not necessarily imply that for locations downstream of Rhine-km 313.6 the assumption of any arbitrarily chosen initial floc size is insensitive towards the modeled floc sizes. Here, the comparison with the other two simulations is needed and is presented below.

From figure 6.13, it can be seen that for a coarse inflow particle size of $D_2 = 63.0\,\mu$m at Rhine-km 313.6 a smaller mean floc size is computed than for an inflow particle size of $D_6 = 14.6\,\mu$m ($D_m = 14.1\,\mu$m vs. $D_m = 14.7\,\mu$m). However, from Rhine-km 318.5, i. e. after a flow length of 5.9 km, the differences in modeled mean particle diameters are small ($D_m = 12.6\,\mu$m vs. $D_m = 12.9\,\mu$m) and are negligible further downstream. Based on these two comparative calculations, it might be concluded that the inflow particle size affects the computed floc sizes only in the reach between the model boundary and Rhine-km 318.5 to 323.1. However, the computation results for an inflow particle size of $D_{11} = 2.0\,\mu$m show that the modeled floc sizes depend on the inflow particle size along the whole flow path in the model domain. Even in the downstream reaches of the model domain at Rhine-km 333.5, i. e. after a flow length of 20.9 km, not the same floc size distribution is computed as for the other two calculations. At this point, for the very fine inflow particle size, the mean floc size is modeled approximately 2.5 times smaller than for the other two coarser inflow particle sizes ($D_m = 9.4\,\mu$m vs. $D_m = 25.3\,\mu$m). The results for the inflow particle size of $D_{11} = 2.0\,\mu$m indicate that the time for undergoing flocculation processes until the flocs have grown to an equilibrium stage was not sufficient for any flow distance from the upstream model boundary at Rhine-km 312.6.

The different temporal developments of the flocculation processes are shown exemplarily for Rhine-km 330.0 in figure 6.14. It can be seen that final, steady-state modeled floc sizes, i. e. when the inflow particles have reached Rhine-km 330.0, are almost identical for an inflow particle size of $D_2 = 63.0\,\mu$m and $D_6 = 14.6\,\mu$m. For both cases, at steady-state, sediment mass was shifted in the same proportions mainly into size classes D_5, D_6, D_4, D_7, D_8 and D_9 due to aggregation and disaggregation processes. As a consequence, at Rhine-km 330.0 the same mean particle diameter is computed, as shown in figure 6.13. The differences in these two simulations are present in terms of the development of the flocculation processes before the equilibrium stage is reached. Particles of size class $D_2 = 63.0\,\mu$m imply the lowest particle yield strength (see table 6.2). Hence, for the initial stages of flocculation, the probability for being disrupted by fluid shear stresses and collision-induced shear stresses is facilitated compared to the more compact particles of size class $D_6 = 14.6\,\mu$m. In figure 6.14, this is illustrated by the rapid decrease in the concentrations of the two coarser size classes D_2 and D_3 and the shifting towards the smaller size fractions.

For the inflow particle size of $D_{11} = 2.0\,\mu$m a different steady-state particle size distribution is computed than for the other two cases. Since the particles of size class $D_{11} = 2.0\,\mu$m are treated as solid primary particles, which can not be disrupted, in the initial stages of flocculation , the aggregation process towards larger floc sizes is dominant. The sediment mass is shifted successively from the finest size class D_{11} towards the coarser size classes D_{10}, D_9, D_8, D_7 and D_6. However, at steady-state no sediment mass is shifted into the even coarser size classes D_5 and D_4, as it was computed for the other two cases.[4]

For the inflow particle size of $D_{11} = 2.0\,\mu$m, the sediment mass fluxes between the size classes take too much time, so that a finer size distribution is reached than for the other two cases. After approximately 6.1 hours, the modeled size distribution stays constant, indicating that the particles of the upstream boundary have reached Rhine-km 330. However, at this stage the aggregation processes have not yet developed to an equilibrium stage, since no particle mass has been shifted into the coarser size classes D_5 and D_4, as it was calculated for the other two cases. The time of approximately 6.1 hours for the particle transport from the model boundary at Rhine-km 312.6 to Rhine-km 330 can be justified by taking a look

[4]The temporal development of the suspended sediment concentration in the non-cohesive size class D_1 is the same for all cases, since this class is excluded from the flocculation computations.

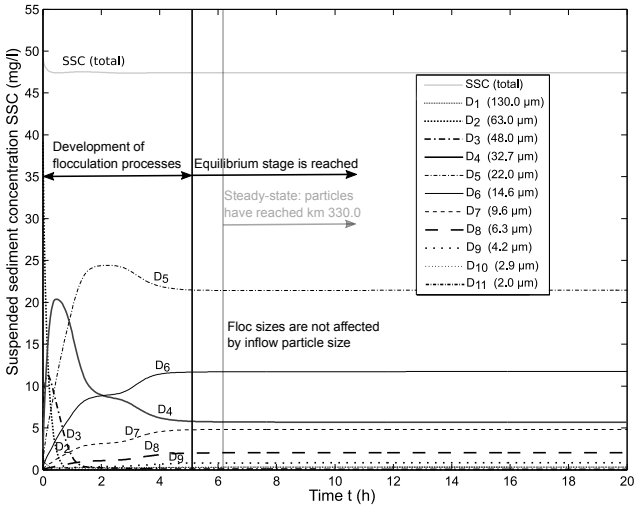

(a) Inflow particle size $D_2 = 63.0\,\mu$m

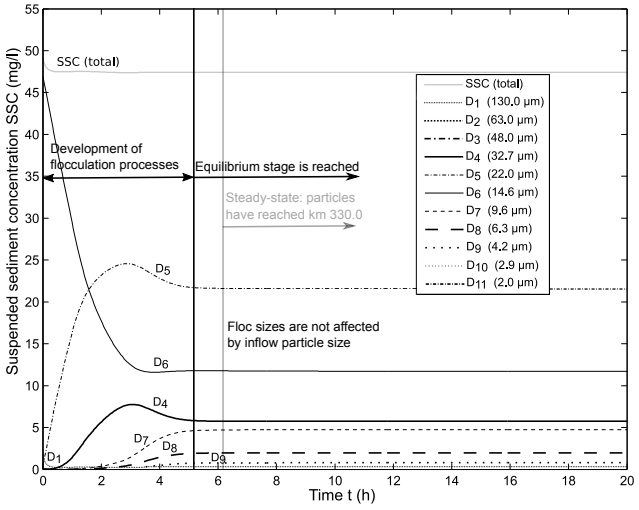

(b) Inflow particle size $D_6 = 14.6\,\mu$m

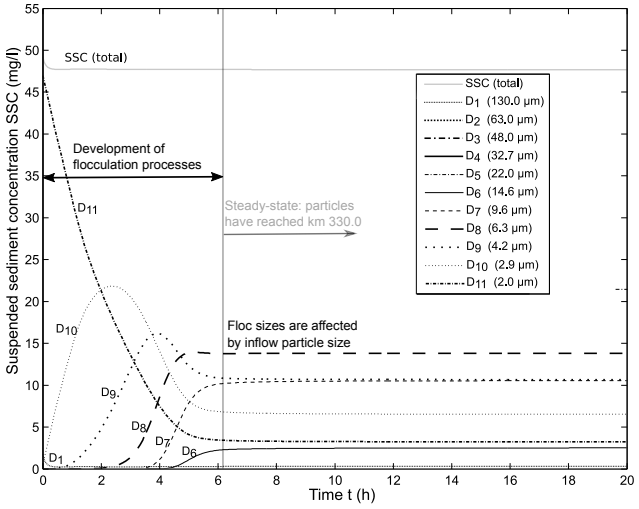

(c) Inflow particle size $D_{11} = 2.0\,\mu$m

Figure 6.14: Calculated temporal development of the depth-averaged concentrations in each particle size class at Rhine-km 330.0 depending on the inflow particle size.

at the calculated flow velocities. Assuming that the particles are primarily transported by advection with the mean flow velocity, the averaged flow velocity along this flow path is expected to be around 0.8 $^{m}/_{s}$. This is confirmed by the computed depth-averaged velocities in figure 6.3. For the inflow particle sizes of $D_2 = 63.0\,\mu$m and $D_6 = 14.6\,\mu$m, the flocculation processes have been fully developed at Rhine-km 330, since the time to reach an equilibrium stage (about 5.1 hours, black vertical line) is smaller than the time the particles need to be transported to this location (6.1 hours, grey vertical line).

One conclusion of the presented analyses above is that the assumption of any arbitrarily chosen inflow particle size affects the type of flocculation processes until an equilibrium stage is reached, i. e. it determines whether aggregation or disaggregation processes dominate. The type of the flocculation mechanism in turn influences the time to reach an equilibrium situation in floc size. As it was already shown before in chapter 5.3.2.3, the aggregation as well as the disaggregation process due to collision-induced shear stresses are modeled as time-dependent processes. In the first time step, aggregation or disaggregation processes lead to particle mass shifting from one size class into the other size classes. In the next time step, further mass shifting of the newly formed particle masses into the other size classes occur and so on. This case applies for an inflow particle size of $D_{11} = 2.0\,\mu$m. In contrast, disaggregation by turbulent shear stresses is modeled as a time-independent mechanism. As shown for an inflow particle size of $D_2 = 63.0\,\mu$m, it occurs much faster than the aggregation mechanism.

Due to the differences in the temporal development of the flocculation processes, the main conclusion of these studies is that the modeled floc sizes are sensitive towards the assumption of any arbitrarily chosen inflow particle size. For example, for an extreme fine boundary particle size of $D_{11} = 2.0\,\mu$m, the modeled final floc sizes are affected by this input size distribution even at the most downstream point of the model. The aggregation processes take too much time, so that no equilibrium between floc growth and floc break-up can be reached and computation results are representative only for this extreme (very fine) chosen inflow particle size. In order to ensure that the flocs have enough time to reach an equilibrium stage between floc growth and floc break-up, one might suppose to define a very coarse and weak inflow particle size. In the case that the turbulent stresses are strong enough, these particles would be disaggregated in the initial stages of flocculation within a very short time and the particle mass shifting between the size classes would occur very fast. As a consequence, the opportunity that the flocs have enough time to reach an equilibrium stage would be greater. Nevertheless, if the turbulent stresses in the study area are not strong enough to break up these particles, no particle mass shifting due to turbulence-induced disaggregation would occur. Then, flocculation processes because of aggregation and/or collision-induced disaggregation are dominant in the initial stages, which occur much slower, so that the processes might also not fully develop to an equilibrium situation. A very coarse chosen boundary size distribution at the model boundary in the Iffezheim model could be implausible also from a physical point of view. Since it is assumed that upstream of the Iffezheim model boundary turbulences are even higher due to the hydropower plant outlet of the upstream barrage Gambsheim, floc sizes are expected to be rather fine than coarse.

Hence, for future applications of this Iffezheim model, a plausible and appropriate inflow particle size has to be chosen in order to ensure that flocs have enough time to reach an equilibrium stage. Within these studies, under the respective parameter definitions listed in table 6.1, an inflow particle size of $D_2 = 63.0\,\mu$m or $D_6 = 14.6\,\mu$m is chosen adequately, so that steady-state modeled floc sizes are not affected by the boundary size distribution, at least downstream of Rhine-km 323.1. This is an important finding, when using this model for future numerical computations, which focus on cohesive sediment

related issues in the downstream reaches of the Iffezheim reservoir, e. g. the long-term prediction of sedimentation rates upstream of the weir.

The application of the implemented flocculation algorithm on a real case study like the Iffezheim reservoir in Germany has shown that the numerical modeling of flocculation processes in a natural system represents a major challenge. Based on the parameter definitions and assumptions made within these studies, it could be shown that the flocculation computations give physically plausible and reasonable results in terms of modeled floc sizes demonstrating that for future numerical studies in the Iffezheim reservoir the model extension represents a key simulation tool. However, the studies have also shown that the degree of flocculation of the in situ particles in the Iffezheim reservoir can not be determined within this work, since firstly too many assumptions for unknown parameter values in the implemented flocculation algorithm have to be made. In this context, as it was also pointed out within the sensitivity studies in the annular flume in chapter 5, the particle yield strength coefficient B_τ and the fractal dimension n_f were identified as two essential factors which have a major impact on the modeled floc sizes. Secondly, uncertainties exist also with respect to the definition of the primary particle size spectrum and the inflow particle size distribution at the model boundary. The choice of inappropriate assumptions may lead to physically modified or incorrect modeled floc sizes compared to observed in situ floc size distributions. Therefore, for future flocculation computations in the Iffezheim reservoir, those mentioned impact factors have to be taken into account, while simultaneously emphasizing that reliable measurement data of the characteristics of the in situ flocs are essential.

7 Conclusion and Outlook

Cohesive sediment dynamics in natural river systems is a major issue in sediment research and morphodynamics engineering. Especially the key micro-scale flocculation processes of cohesive sediments, i. e. the aggregation towards larger aggregates/flocs and the break-up (disaggregation) of the fragile flocs into smaller particles, are of great importance. Flocculation processes are not completely understood yet, since they are affected by a high number of influencing factors and due to the complex processes interactions (see chapter 2). For studying and making predictions of the complex fine-grained sediment dynamics, computational fluid dynamics (CFD) sediment transport models are increasingly used as simulation and research tools.

The major aim of this work was to gain insight into the flocculation mechanisms and its process complexity and to improve the understanding of the different involving mechanisms by using the three-dimensional CFD model SSIIM. For this purpose, the SSIIM software was extended by an implementation of a flocculation algorithm which is physically as accurate as possible for the description of particle aggregation and floc break-up.

SSIIM Extension by Implementation of a Flocculation Algorithm (see chapter 3 and 4)
A review on numerical modeling of flocculation from literature has shown that modeling cohesive sediment processes in general, and flocculation processes in particular, is still a crucial challenge in sediment engineering (see chapter 3). Due to the complex process interactions, inadequate or non-existent measurement data and the lack in current understanding of fine sediment flocculation processes, various approaches for the numerical modeling of flocculation processes were developed. The algorithms can be differentiated according to the number of parameters and sub-processes taken into account, and thus exhibit different degrees of complexity. Especially, the simulation of the disaggregation mechanisms represents a difficult issue in flocculation modeling, since the relation between floc strength and their mode of break-up mechanisms is influenced by many factors. Additionally, computing power capacity and running times induce conceptual improvements and/or simplifications of complex flocculation algorithms.

Based on the study and comparison of different flocculation models, one flocculation algorithm was chosen which allows the simulation of aggregation and disaggregation mechanisms and is also suitable for the implementation in SSIIM. In this work, a size-class based flocculation model derived by McAnally (2000) was implemented in SSIIM (see chapter 4). The flocculation model is a combination of a statistical and a deterministic, physics-based representation of aggregation and disaggregation processes. The algorithm allows aggregation of flocs due to collisions caused by Brownian motion, differential settling and turbulence. Flow-induced stresses due to turbulence as well as collision-induced shear stresses may lead to disaggregation of flocs, if these stresses exceed the floc yield strength. In order to reduce CPU time and model complexity, within this work collisions of only two particles were modeled. More-body collisions were assumed to play a minor role. The fractal structure of flocs was considered by the parameter

fractal dimension and was used to calculate the floc density and the particle settling velocity according to Winterwerp (1998).

In this work, the implemented flocculation model in SSIIM was applied on two case studies. Firstly, flocculation processes and deposition of cohesive sediments were analyzed and modeled in a physical model in the open annular flume (see chapter 5). Secondly, the implemented flocculation model was used in a real case study for modeling flocculation in the Iffezheim hydropower reservoir in Germany (see chapter 6).

Case Study Open Annular Flume (see chapter 5)
The flocculation model was applied for simulating measured floc sizes and suspended sediment concentrations of kaolinite over a time period of the first 5 hours of the experiment. The objective of this application at first was the testing and validation of the implemented flocculation algorithm. Secondly, it was investigated how accurate the measured laboratory data in the annular flume can be simulated by the algorithm and which impact uncertainties have relating to unknown empirical parameters and boundary/initial conditions on the modeling results.

As a first step towards a successful simulation of cohesive sediment transport in the annular flume, the hydraulics in the annular flume were analyzed by means of measurements and the numerical simulation. Good agreement between measurement and simulation was found for the longitudinal flow velocities and the secondary currents. Discrepancies were most significant in the determination of the magnitude of the turbulent kinetic energy and the turbulent dissipation rate, but general characteristics of the distribution were similar. Both simulation and measurements indicated a complex three-dimensional flow field in the annular flume.

The impact of unknown physico-chemical calibration parameter values and initial/boundary conditions on the flocculation modeling results was investigated by conducting sensitivity analyses towards: the time step Δt, the initial floc size, the aggregation coefficient α_a, the particle yield strength coefficient B_τ, the fractal dimension n_f and the impact of potential simultaneous erosion processes. The numerical studies showed a successful realization of the model implementation in SSIIM. The flocculation algorithm is able to compute aggregation and disaggregation mechanisms of cohesive sediments in a physically plausible way. From the sensitivity analyses it was found that the computed particle size distribution in the annular flume is sensitive towards all tested factors. However, the fractal dimension n_f was identified and evaluated as the strongest assumption which is made in the flocculation algorithm, as it exerts significant influence on both the floc size distribution and the settling velocity of the particles. A high sensitivity was also found towards the particle yield strength coefficient B_τ, since it affects the particle size distribution by the determination of the floc yield strength. Another main conclusion of the sensitivity analyses was that the temporal development of the flocculation processes strongly depends on the turbulence-induced floc break-up process as a consequence of different time scales for aggregation (time-dependent) and flow-induced disaggregation (time-independent). This is an essential finding for future applications of the flocculation algorithm, for example in terms of unsteady cohesive sediment calculations or when simulating flocculation for short flow paths.

Long-term simulations over the whole duration of the experiment (70 hours) have shown that despite various changes in parameter definitions and initial/boundary conditions still some deviations between measurements and simulation existed. It is assumed that the deviations are generated by a superposition of several factors, e. g.: uncertainties related to other physico-chemical parameters in the implemented flocculation algorithm which have not yet been tested towards their sensitivity, discrepancies in modeled

and measured turbulence characteristics, limitations of the floc size measurement device and the still existing knowledge gaps in cohesive sediment dynamics. The computation results in the annular flume emphasize that modeling flocculation and deposition processes constitutes a major challenge, even for a closed and simplified system in the laboratory, where boundary conditions are well known and constant.

To investigate the issue to which degree the observed processes in the laboratory can be simulated physically correctly by excluding the implemented flocculation algorithm from the computation, two simplified methods were applied. On the one hand, the well known settling velocity formula according to Stokes (1850) was used, which treats particles as solid, Euclidean spheres. On the other hand, flocculation was considered only indirectly by the application of the fractal dimension to calculate the settling velocity defined by Winterwerp (1998) instead of Stokes. From the comparative studies it was found that excluding the flocculation algorithm from the simulations and using instead simplified methods gives poor and unrealistic results. The implemented flocculation model provided physically more reasonable results in terms of the floc size evolution and a much better correspondence with measured aggregate sizes than the simplified models which exclude flocculation processes.

Case Study Iffezheim Reservoir (see chapter 6)
The model objective of the Iffezheim reservoir application was firstly the validation of the implemented algorithm with respect to the reproduction of flocculation processes for a natural water-sediment system. Secondly, it was analyzed which influencing factors and parameters need to be adressed when using the flocculation model for future practical applications in cohesive sediment modeling.

For modeling flocculation processes in the Iffezheim reservoir, a three-dimensional sediment transport model was established in SSIIM, which was coupled with the implemented flocculation model. The simulations were conducted under steady-state conditions with respect to the hydraulics using a constant discharge. Unsteady conditions were present in terms of modeling the temporal floc size evolution, while all boundary conditions and input data were kept constant during the whole simulation time. The simulated flow field was calibrated by using ADCP measurement data of water velocities. It was shown, that the numerical model gives plausible and appropriate results in terms of both, the flow velocities and turbulence characteristics. It could therefore serve as a basis for the application of the implemented flocculation algorithm.

The flocculation modeling results have shown that modeled floc sizes in the Iffezheim reservoir are in a physically plausible value range, since the sizes of the computed aggregated flocs were larger than the measured sizes of the primary particles. The modeled floc sizes were reasonable predicted also in terms of their spatially variability because of varying turbulence-induced shear stresses in the reservoir. Since turbulences decrease in the main flow direction of the reservoir, particle disaggregation due to flow-induced shear stresses was reduced, whereas particle aggregation was enhanced in the downstream direction. As anticipated, this led to an increase in simulated particle sizes from the upstream model boundary towards the downstream reaches of the reservoir.

Nevertheless, the degree of flocculation of the in situ particles in the Iffezheim reservoir could not be verified within this work. The reasons for that were largely attributed to the uncertainties in terms of the choice of unknown parameter values and boundary conditions for the application of the implemented flocculation algorithm. It is expected that in particularly uncertainties about the particle yield strength coefficient B_τ and the fractal dimension n_f will have a major impact on the modeled floc sizes, as it was already pointed out within the simulations in the annular flume. Additionally, assumptions were required

in terms of the definition of the primary particle size spectrum and the inflow particle sizes at the model boundary. The numerical investigations demonstrated that the choice of unrealistic assumptions for the inflow particle sizes may lead to physically imprecise or incorrect modeled floc sizes, especially in the upper reaches of the model domain. The definition of the primary particle size spectrum will affect the model results as well.

From both case studies it can be concluded that the implemented flocculation algorithm in SSIIM is able to reproduce aggregation and disaggregation mechanisms of cohesive fine sediments in a physically plausible way pointing out that the model extension can be used as a key simulation tool for numerical studies on cohesive sediments. It was also found to which degree assumptions for different unknown calibration parameter values affect the simulation results. The findings from these studies attribute to a better understanding of the modeled flocculation processes for future applications of the flocculation algorithm on cohesive sediment transport models.

However, both case studies also revealed the challenges in a physically precise and accurate flocculation modeling, even in a simplified system in laboratory. This is mainly attributed to the uncertainties in the specification of the numerous calibration parameters and the complex processes interactions of fine sediments. That in turn emphasizes that for future applications reliable measurement data of the characteristics of the flocs and/or the development of explicit theoretical formulations for calculating those parameters are necessary. Measurement data are the basis for the application of the flocculation algorithm on both, practical issues in order to make physically more precise predictions of the cohesive sediment processes and fundamental research in order to improve the knowledge of cohesive sediment processes in general, and flocculation processes in particular.

Recommendations for Further Work

The numerical studies in this work have shown that flocculation processes are still not completely understood and that the parameterization of the different influencing factors proves difficult due to missing measurement data or non-existent theoretical formulations. As a consequence, the use of the implemented flocculation algorithm on future cohesive sediment transport models is accompanied by limitations in terms of the precision and accuracy of the modeling results. Based on the findings in this work, further experimental and numerical investigations on flocculation are required to further improve the understanding in flocculation processes and to ensure reliable and quantitative simulation results for applications in cohesive sediment engineering. Future research on flocculation can include the following experimental and numerical investigations:

- **Collection of Measurement Data and/or Development of Theoretical Formulations:** This work emphasized that for future applications of the implemented flocculation algorithm, reliable measurement data are needed in order to avoid uncertainties in the estimation of the input empirical parameters. Two dominant influencing factors were identified from the sensitivity studies in the annular flume which imply a high impact on the model results: the fractal dimension n_f, which is used to describe the floc structure, and the particle yield strength coefficient B_τ, which also influences the particle yield strength. For future studies on cohesive sediment dynamics, it will be necessary to improve the understanding about processes that influence these parameters. Therefore, standardized measurements of the fractal dimension, e. g. by the use of image analysis, are recommended. Additionally, the development of explicit theoretical expressions for the calculation of the particle yield strength coefficient are proposed.

In this context, it has to be noted that measurement size techniques which may disrupt or create additional sediment flocs do not reflect the real observed floc sizes and thus are not appropriate for providing representative values of the in situ particle size distribution. Hence, in situ measurements of the floc characteristics that do not alter the floc properties are highly important for both, fundamental investigations in the laboratory and practical applications in cohesive sediment engineering.

- **Optimization of the Implemented Flocculation Algorithm and Further Numerical Studies:** In chapter 5.3.2.2 it was shown that a short time step for modeling flocculation is required from a physical point of view and in order to avoid mass conservation errors or to keep them as small as possible. However, short time steps affect the CPU time. For future flocculation modeling in SSIIM, possible methods (e. g. application of a sub-time step or a dynamically-adaptable varying time step) for reducing the CPU time and simultaneously ensuring mass conservation need to be tested. Especially, for long-term modeling of cohesive sediment this will be an important aspect.

  In this work, several sensitivity studies were conducted. In this respect, the impact of the hydraulics and in particular of the turbulence on the flocculation modeling results was an essential issue of the analyses. Furthermore, the influence of several sediment specific characteristics was studied (fractal dimension n_f, particle yield strength coefficient B_τ, aggregation coefficient α_a). The sensitivity of the modeling results towards further other parameters describing the physico-chemical properties of the sediment-fluid-flow system has not been analyzed yet within this work. In the implemented flocculation algorithm these parameters include: the empirical sediment- and flow-dependent density function B_ρ and the non-dimensional term Π_c which takes into account the ionic composition of the water and particle related characteristics. Since no information about these parameters were available, the factors/functions were either simplified or set to values recommended from McAnally and Mehta (2000). In future, the influence of these simplifications and assumptions need to be investigated in order to ensure physically precise flocculation modeling results.

- **Further Development of the Implemented Flocculation Algorithm:** The implemented algorithm can be extended by additional model approaches for a simultaneous calculation of particulate contaminants. Such an extension would allow to model flocculation while simultaneously taking into account adsorption or desorption processes of contaminants and would therefore provide the possibility to analyze and quantify the impact of particle-bound contaminants as well. Particularly for the Iffezheim reservoir, where deposition of contaminated fine sediments represents a major environmental and economic issue, the consideration of particle-bound contaminants in the numerical model is of crucial importance. First steps towards modeling particulate contaminants in combination with flocculation have been elaborated and can be found in Hillebrand and Klassen (2011). The implemented approach represents the simplest case considering contaminants as conservative tracer and can be used as a basis for further developments in terms of modeling adsorption and desorption processes.

Bibliography

Amos, C. L., Sutherland, T. F., and Zevenhuizen, J. (1996). The stability of sublittoral, fine-grained sediments in a subarctic estuary. *Sedimentology*, 43(1):1–19.

Andersen, T. J., Jensen, K. T., Lund-Hansen, L., Mouritsen, K. N., and Pejrup, M. (2002). Enhanced erodibility of fine-grained marine sediments by Hydrobia ulvae. *Journal of Sea Research*, 48(1):51–58.

Argaman, Y. and Kaufmann, W. J. (1970). Turbulence and Flocculation. *Journal of the Sanitary Engineering Division*, 96(2):223–241.

Ariathurai, R. and Arulanandan, K. (1978). Erosion Rates of Cohesive Soils. *Journal of the Hydraulics Division*, 104(2):279–283.

Baugh, J. V. and Manning, A. J. (2007). An assessment of a new settling velocity parameterisation for cohesive sediment transpot modeling. *Continental Shelf Research*, 27(13):1835–1855.

Böhm, L., Pohlert, T., and Düring, R. A. (2011). BMVBS research program KLIWAS - Impact of climate change on waterways and shipping - Development of adaptation options, subproject SORPTION - Identification of adsorbents for HCB and determination of sorption parameters in river sediments of the federal waterways (in German). Technical report, Justus-Liebig-Universität Giessen.

Billiones, R. G., Tackx, M. L., and Daro, M. H. (1999). The Geometric Features, Shape Factors and Fractal Dimensions of Suspended Particulate Matter in the Scheldt Estuary (Belgium). *Estuarine, Coastal and Shelf Science*, 48(3):293–305.

Breitung, V. (2009). Statement on dredging at the barrage Iffezheim (spillway channel) (Rhine-km 332,800-333,900) (in German). Technical report, Bundesanstalt für Gewässerkunde (BfG).

Bundesministerium für Verkehr, Bau- und Wohnungswesen (2004). Wet dredging strategies in Germany. Economical and environmentally compatible (in German). Technical report.

Burban, P.-Y., Lick, W., and Lick, J. (1989). The flocculation of fine-grained sediments in estuarine waters. *Journal of Geophysical Research: Oceans*, 94(C6):8323–8330.

Burt, T. N. (1986). *Estuarine Cohesive Sediment Dynamics: Proceedings of a Workshop on Cohesive Sediment Dynamics with Special Reference to Physical Processes in Estuaries, Tampa, Florida, November 12–14, 1984*, volume 14 of *Lecture Notes on Coastal and Estuarine Studies*, chapter Field Settling Velocities of Estuary Muds, pages 126–150. Springer New York.

Camp, T. R. and Stein, P. (1943). Velocity Gradients and Internal Work in Fluid Motion. *Journal of the Boston Society of Civil Engineers*, 30(4):219–237.

Carling, P. A. and McCahon, C. P. (1987). Natural siltation of brown trout (Salmo trutta L.) spawning gravels during low-flow conditions. In *J. F. Craig and J. B. Kemper (eds.), Regulated streams: Advances in ecology.*, pages 229–244. New York.

Chakraborti, R. K., Gardner, K. H., Atkinson, J. F., and van Benschoten, J. E. (2003). Changes in fractal dimension during aggregation. *Water Research*, 37(4):873–883.

Cheng, N.-S. (1997). Simplified Settling Velocity Formula for Sediment Particle. *Journal of Hydraulic Engineering*, 123(2):149–152.

Coufort, C., Dumas, C., Bouyer, D., and Liné, A. (2008). Analysis of floc size distributions in a mixing tank. *Chemical Engineering and Processing: Process Intensification*, 47(3):287–294.

Davies-Colley, R. J., Hickey, C. W., Quinn, J. M., and Ryan, P. A. (1992). Effects of clay discharges on streams, 1. optical properties and epilithon. *Hydrobiologia*, 248:215–234.

Delichatsios, M. A. and Probstein, R. F. (1974). Coagulation in turbulent flow: Theory and experiment. *Journal of Colloid and Interface Science*, 51(3):394–405.

Dharmappa, H. B., Vigneswaran, S., Verink, J., and Fujiwara, O. (1994). Water-Treatment-System Design for Turbidity Removal. *Journal of Environmental Engineering*, 120:900–914.

Dingman, S. L. (1984). *Fluvial Hydrology.* W. H. Freeman and Company, New York.

Dunn, I. S., Anderson, L. F., and Kiefer, F. W. (1980). Fundamentals of Geotechnical Analysis. Wiley, New York.

Dyer, K. R. (1989). Sediment processes in estuaries: Future research requirements. *Journal of Geophysical Research: Oceans*, 94(C10):14,327–14,339.

Ferziger, J. H. and Peric, M. (2002). *Computational Methods for Fluid Dynamics.* Springer-Verlag, Berlin.

Fleig, M., Sacher, F., Lehmann, M., Stork, J., and Schönberger, H. (2006). Determination of HCB sources at the Upper Rhine river, final report on the research project, no. L75 24007 (in German). Technical report.

Friedlander, S. K. (1957). Mass and heat transfer to single spheres and cylinders at low Reynolds numbers. *Americal Institute of Chemical Engineers Journal*, 3(1):43–48.

Gregory, J. (1997). The density of particle aggregates. *Water Science and Technology*, 36(4):1–13.

Haralampides, K., McCorquodale, J. A., and Krishnappan, B. G. (2003). Deposition Properties of Fine Sediment. *Journal of Hydraulic Engineering*, 129(3):230–234.

Hill, P. S., Voulgaris, G., and Trowbridge, J. H. (2001). Controls on floc size in a continental shelf bottom boundary layer. *Journal of Geophysical Research*, 106(C5):9543–9549.

Hillebrand, G. (2008). *Transport behavior of cohesive sediments in turbulent flows – Investigations in the open annular flume (in German).* PhD thesis, Universität Fridericiana zu Karlsruhe (TH).

Hillebrand, G. and Klassen, I. (2011). Modeling cohesive sediment aggregation processes in conjunction with persistent pollutants (in German). In *Kolloquium Partikuläre Stoffströme in Flusseinzugsgebieten, 20./21. September 2011*, Koblenz. Bundesanstalt für Gewässerkunde (BfG).

Hillebrand, G., Klassen, I., and Olsen, N. R. B. (2016). 3D CFD modelling of velocities and sediment transport in the Iffezheim hydropower reservoir. *Hydrology Research*.

Hillebrand, G., Klassen, I., Olsen, N. R. B., and Vollmer, S. (2012a). Modelling fractionated sediment transport and deposition in the Iffezheim reservoir. In *10th International Conference on Hydroinformatics, Hamburg, Germany*.

Hillebrand, G. and Olsen, N. R. B. (2010). Hydraulic Characteristics of the Open Annular Flume - Experiment and Numerical Modeling. In *The 1st Europ. Congr. of the IAHR. 4th-6th May 2010, Edinburgh*.

Hillebrand, G., Otto, W., and Vollmer, S. (2012b). Findings from ADCP-measured flow velocities and suspended sediment concentrations at the Upper Rhine. In *2nd IAHR Europe Conference, Munich, Germany*.

Hillebrand, G., Pohlert, T., Klassen, I., Breitung, V., and Vollmer, S. (2010). Impact of projected climate change on transport of cohesive sediments and particle-bound contaminants in the impounded section of the Upper Rhine River. In *HydroPredict'2010 - International Interdisciplinary Conference on Predictions for Hydrology, Ecology and Water Resources Management, Changes and Hazards caused by Direct Human Interventions and Climate Change*, Prague.

Hirsch, C. (2007). *Numerical Computation of Internal and External Flows: The Fundamentals of Computational Fluid Dynamics*. John Wiley & Sons, Ltd.

International Commission for the Protection of the River Rhine (ICPR) (2009). Sediment Management Plan Rhine (in German). Technical Report 175, Koblenz.

Johnson, C. P., Li, X., and Logan, B. E. (1996). Settling Velocities of Fractal Aggregates. *Environmental Science & Technology*, 30(6):1911–1918.

Jones, M. N. and Perry, R. (1979). The kinetics of cellular aggregation induced by turbulent flow. *Journal of Theoretical Biology*, 81(1):75 – 89.

Joubert, P., Le Quéré, P., Béghein, C., Collignan, B., Couturier, S., Glockner, S., Groleau, D., Lubin, P., Musy, M., Sergent, A., and Vincent, S. (2005). A numerical exercise for turbulent natural convection and pollutant diffusion in a two-dimensional partially partitioned cavity. *International Journal of Thermal Sciences*, 44:311–322.

Khelifa, A. and Hill, P. S. (2006). Models for effective density and settling velocity of flocs. *Journal of Hydraulic Research*, 44(3):390–401.

Kühn, G. (2007). *Studies on fine sediment dynamics in turbulent flows (in German)*. PhD thesis, Universität Fridericiana zu Karlsruhe (TH).

Klassen, I. (2009). Deposition behavior of cohesive sediments in turbulent flows - Identification of scale effects in the open annular flume (in German). Dipl.thesis, University Karlsruhe, Germany.

Klassen, I., Hillebrand, G., Olsen, N. R. B., and Nestmann, F. (2015). Sensitivity analyses for the numerical modeling of flocculation processes of fine sediments. In *River, Coastal and Estuarine Morphodynamics (RCEM)*, Iquitos, Peru.

Klassen, I., Hillebrand, G., Olsen, N. R. B., Vollmer, S., Lehmann, B., and Nestmann, F. (2011). Modeling fine sediment aggregation processes considering varying fractal dimensions. In *River, Coastal and Estuarine Morphodynamics (RCEM)*, Beijing, China.

Klassen, I., Hillebrand, G., Olsen, N. R. B., Vollmer, S., Lehmann, B., and Nestmann, F. (2013). Flocculation processes and sedimentation of fine sediments in the open annular flume - Experiment and numerical modeling. In *River, Coastal and Estuarine Morphodynamics (RCEM)*, Santander, Spain.

Kranck, K. (1986). Particulate matter grain-size characteristics and flocculation in a partially mixed estuary. *Sedimentology*, 18:107–114.

Kranck, K. and Milligan, T. (1980). Macroflocs: Production of Marine Snow in the Laboratory. *Marine Ecology - Progress Series*, 3:19–24.

Kranenburg, C. (1994). The fractal structure of cohesive sediment aggregates. *Estuarine, Costal and Shelf Science*, 39(6):451–460.

Kranenburg, C. (1999). Effects of floc strength on viscosity and deposition of cohesive sediment suspensions. *Continental Shelf Research*, 19(13):1665–1680.

Krishnappan, B. G. (1990). Modelling of settling and flocculation of fine sediments in still water. *Canadian Journal of Civil Engineering*, 17:763–770.

Krishnappan, B. G. (2006). Cohesive sediment transport studies using a rotating circular flume. In *The 7th International Conference on Hydroscience and Engineering*, Philadelphia, USA.

Krishnappan, B. G. (2007). Recent advances in basic and applied research in cohesive sediment transport in aquatic systems. *Canadian Journal of Chemical Engineering*, 34:731–743.

Krishnappan, B. G. and Marsalek, J. (2002). Modelling of flocculation and transport of cohesive sediment from an on-stream stormwater detention pond. *Water Research*, 36(15):3849–3859.

Krone, R. B. (1962). Flume studies of the transport of sediment in estuarial shoaling processes. Technical report, Hydraulic Engineering Laboratory and Sanitary Engineering Research Laboratory, University of California, Berkeley, USA.

Krone, R. B. (1963). A study of rheologic properties of estuarial sediments. Technical Report 7, Hydraulic Engineering Laboratory and Sanitary Engineering Research Laboratory, University of California, Berkeley, USA.

Krone, R. B. (1993). *Nearshore and Estuarine Cohesive Sediment Transport*, chapter Sedimentation Revisited, pages 108–125. American Geophysical Union.

Kumar, R. G., Strom, K. B., and Keyvani, A. (2010). Floc properties and settling velocity of San Jacinto estuary mud under variable shear and salinity conditions. *Continental Shelf Research*, 30(20):2067–2081.

Lagaly, G., Schulz, O., and Zimehl, R. (1997). *Dispersions and emulsions: Introduction to the colloid finely divided materials, including clay minerals (in German).* Steinkopff Darmstadt.

Lau, Y. (1994). Temperature effect on settling velocity and deposition of cohesive sediments. *Journal of Hydraulic Research*, 32(1):41–51.

Lick, W. (2009). *Sediment and Contaminant Transport in Surface Waters.* CRC Press, Boca Raton, FL.

Lick, W., Huang, H., and Jepsen, R. (1993). Flocculation of fine-grained sediments due to differential settling. *Journal of Geophysical Research: Oceans*, 98(C6):10279–10288.

Lick, W. and Lick, J. (1988). Aggregation and Disaggregation of Fine-Grained Lake Sediments. *Journal of Great Lakes Research*, 14(4):514–523.

Lick, W., Lick, J., and Ziegler, C. K. (1992). *Sediment/Water Interactions: Proceedings of the Fifth International Symposium*, volume 75, chapter Flocculation and its effect on the vertical transport of fine-grained sediments, pages 1–16. Springer Netherlands.

LUBW Landesanstalt für Umwelt, Messungen und Naturschutz Baden-Württemberg (ed.) (2011). German hydrological yearbook, Rhine area, Part 1 - High and Upper Rhine (in German). Technical report.

Luettich, R. A., Wells, J. T., and Kim, S.-Y. (1993). *Nearshore and Estuarine Cohesive Sediment Transport*, chapter In Situ Variability of Large Aggregates: Preliminary Results on the Effects of Shear, pages 447–466. American Geophysical Union.

Maerz, J., Verney, R., Wirtz, K., and Feudel, U. (2011). Modeling floccualtion processes: Intercomparison of a size class-based model and a distribution-based model. *Continental Shelf Research*, 31(10):84–93.

Maggi, F. (2005). *Flocculation Dynamics of cohesive sediment*. PhD thesis, Delft, University of Technology.

Maggi, F. (2007). Variable fractal dimension: A major control for floc structure and flocculation kinematics of suspended cohesive sediment. *Journal of Geophysical Research: Oceans*, 112(C7).

Maggi, F., Mietta, F., and Winterwerp, J. C. (2007). Effect of variable fractal dimension on the floc size distribution of suspended cohesive sediment. *Journal of Hydrology*, 343(1-2):43–55.

Mahmood, K. (1987). Reservoir Sedimentation: Impact, Extent and Mitigation. World Bank Technical Paper 71, Washington, DC, USA.

Malcherek, A. (1994). Numerical modeling of cohesive settling velocities. *International Journal of Sediment Research*, 9(97):97–106.

Malcherek, A. (1995). *Mathematical modeling of flow and mass transfer processes in estuaries (in German)*. PhD thesis, Institut für Strömungsmechanik und Elektronisch Rechnen im Bauwesen der Universität Hannover.

Mandelbrot, B. B. (1982). *The Fractal Geometry of Nature*. W.H.Freeman and Company, New York.

Manning, A. J. (2008a). Chapter 14 The development of algorithms to parameterise the mass settling flux of flocculated estuarine sediments. In *Sediment and Ecohydraulics - INTERCOH 2005*, volume 9 of *Proceedings in Marine Science*, pages 193–210. Elsevier.

Manning, A. J. (2008b). The development of algorithms to parameterise the mass settling flux of flocculated estuarine sediments. *Proceedings in Marine Science*, 9:193–210.

McAnally, W. H. (2000). Aggregation and Deposition of Estuarial Fine Sediment. Technical report, U.S Army Engineer Research and Development Center.

McAnally, W. H. and Mehta, A. J. (2000). Aggregation Rate of Fine Sediment. *Journal of Hydraulic Engineering*, 126(12):883–892.

McAnally, W. H. and Mehta, A. J. (2002). Significane of Aggregation of Fine Sediment Particles in Their Deposition. *Estuarine, Costal and Shelf Science*, 54(4):643–653.

McCave, I. N. (1984). Size spectra and aggregation of suspended particles in the deep ocean. *Deep Sea Research Part A: Oceanographic Research Papers*, 31(4):329–352.

McNown, J. S. and Malaika, J. (1950). Effects of particle shape on settling velocity at low Reynolds numbers. *Eos, Transactions American Geophysical Union*, 31(1):74–82.

Mehta, A. J. (1991). Characterization of cohesive coil bed surface erosion, with special reference to the relationship between erosion shear strength and bed density. UFL/COEL/MP-91/4 (not published), Gainesville: Coastal and Oceanographic Engineering Department, University of Florida.

Mehta, A. J. (2014). *An introduction to hydraulics of fine sediment transport*, volume 38 of *Advanced series on ocean engineering*. World Scientific Publishing Co. Pte. Ltd.

Mehta, A. J. and Lee, S.-C. (1994). Problems in linking the threshold condition for the transport of cohesionless and cohesive sediment grains. *Journal Coastal Research*, 10(1):170–177.

Mehta, A. J. and Partheniades, E. (1975). An Investigation Of The Depositional Properties Of Flocculated Fine Sediments. *Journal of Hydraulic Research*, 13(4):361–381.

Meyer-Peter, E. and Müller, R. (1949). A formula for calculating bed load transport (in German). *Schweizerische Bauzeitung*, 67(3).

Mühle, K. (1993). Floc Stability in Laminar and Turbulent Flow. In Dobias, B., editor, *Coagulation and Flocculation*, volume 47 of *surfactant science series*, pages 355–390. Marcel Dekker, New York.

Mitchener, H. and Torfs, H. (1996). Erosion of mud/sand mixtures. *Coastal Engineering*, 29(1-2):1–25.

Möller, G. (2001). *Geotechnics compact, soil mechanics (in German)*. Bauwerk Verlag, Berlin.

Moudgil, B. M. and Vasudevan, T. V. (1988). Characterization of flocs. In *Flocculation and dewatering*, pages 167–178. Engineering Foundation, New York.

Nestmann, F. (1992). Improvement of the Upper Rhine, Tail Water (TW) Iffezheim. In *Sediment Management*, pages 1130–1152. Proceedings of the 5th International Symposium on River Sedimentation, Karlsruhe.

Nestmann, F. (1996). Characteristics and uses of river systems (in German). *Wasserwirtschaft*, 86(7/8):378–383.

Nikuradse, J. (1933). *Flow laws in rough pipes (in German)*, volume 361. VDI-Verlag.

Olsen, N. R. B. (1991). *A three-dimensional numerical model for simulation of sediment movememts in water intakes*. PhD thesis, The Norwegian Institute of Technology, Trondheim.

Olsen, N. R. B. (2014). *A three-dimensional numerical model for Simulation of Sediment movements In water Intakes with Multiblock option. Version 1 and 2. User's manual*. Department of Hydraulic and Environment Engineering. The Norwegian University of Science and Technology, Trondheim. Norway.

Olsen, N. R. B. and Skoglund, M. (1994). Three-dimensional numerical modeling of water and sediment flow in a sand trap. *Journal of Hydraulic Research*, 32(6):833–844.

Parchure, T. M. and Mehta, A. J. (1985). Erosion of Soft Cohesive Sediment Deposits. *Journal of Hydraulic Engineering*, 111(10):1308–1326.

Parker, D. S., Kaufman, W. J., and Jenkins, D. (1972). Floc breakup in turbulent flocculation processes. *Journal of the Sanitary Engineering Division*, 98(1):79–99.

Partheniades, E. (1965). Erosion and Deposition of Cohesive Soils. *Journal of the Hydraulics Division*, 91(1):105–139.

Partheniades, E., Cross, R. H., and Ayora, A. (1968). Further results on the deposition of cohesive sediments. *Coastal Engineering Proceedings*, 1(11):723–742.

Patankar, S. V. (1980). *Numerical heat transfer and fluid flow*. Hemisphere Publishing Corp., Washington DC.

Pohlert, T., Hillebrand, G., and Breitung, V. (2011). Trends of persistent organic pollutants in the suspended matter of the river rhine. *Hydrological Processes*, 25:3803–3817.

Pope, S. B. (2000). *Turbulent flows*. Cambridge University Press.

Pruppacher, H. R. and Klett, J. D. (1978). *The microphysics of clouds and precipitation*. Riedel, Dordrecht.

Rasmussen, M. R. and Larsen, T. (1996). A method for measuring sludge settling characteristics in turbulent flows. *Water Research*, 30(10):2363–2370.

Raudkivi, A. J. (1998). *Loose Boundary Hydraulics*. A. A. Balkema, Rotterdam.

Reuter, C., Wedershoven, C., and Köngeter, J. (2003). Physical and Numerical Experiments on Turbulence Affected Sedimentation. In *XXX IAHR Congress, August 2003, AUTh, Thessaloniki, Greece; Proceedings. Theme C: Inland Waters: Research, Engineering and Management*, pages 157–162.

Riesterer, J. (2007). Numerical modeling of circular flows (in German). Dipl.thesis, Universität Fridericiana zu Karlsruhe (TH).

Roberson, J. A. and Crowe, C. T. (1993). *Engineering Fluid Mechanics*. Houghton Mifflin.

Russel, W., Saville, D., and Schowalter, W. (1989). *Colloidal Dispersions*. Cambridge University Press, New York.

Saffman, P. G. and Turner, J. S. (1956). On the collision of drops in turbulent clouds. *Journal of Fluid Mechanics*, 1(1):16–30.

Sanford, L. P. and Halka, J. P. (1993). Assessing the paradigm of mutually exclusive erosion and deposition of mud, with examples from upper Chesapeake Bay. *Marine Geology*, 114(1-2):37–57.

Sanford, L. P. and Maa, J. P. Y. (2001). A unified erosion formulation for fine sediments. *Marine Geology*, 179(1-2):9–23.

Schiller, L. and Naumann, A. (1933). Basic calculations for gravity processing (in German). *Zeitschrift der VDI*, 77:318–320.

Schlichting, H. (1979). *Boundary-layer theory*. McGraw-Hill Book Company, New York.

Schmidt, H.-H. (2006). *Fundamentals of Geotechnics (in German)*. Teubner Verlag.

Schroth, B. K. and Sposito, G. (1997). Surface charge properties of kaolinite. *Clays and Clay Minerals*, 45(1):85–91.

Schweim, C. (2005). *Modeling and prediction of erosion of fine sediments (in German).* PhD thesis, RWTH Aachen.

Shields, A. (1936). *Use of dimensional analysis and turbulence research for sediment transport.* 26. Preussen Research Laboratory for Water and Marine Constructions, Berlin, Germany.

Sigg, L. and Stumm, W. (2011). *Aquatic chemistry: Introduction to the chemistry of natural waters (in German).* vdf Hochschulverlag AG an der ETH Zürich.

Sills, G. C. and Elder, D. M. (1986). *Estuarine Cohesive Sediment Dynamics: Proceedings of a Workshop on Cohesive Sediment Dynamics with Special Reference to Physical Processes in Estuaries, Tampa, Florida, November 12–14, 1984*, volume 14 of *Lecture Notes on Coastal and Estuarine Studies*, chapter The Transition from Sediment Suspension to Settling Bed, pages 192–205. Springer New York.

Smoluchowski, M. (1916). Three lectures on diffusion, Brownian molecular motion and coagulation of colloid particles (in German). *Zeitschrift für Physik*, 17:557–585.

Son, M. and Hsu, T.-J. (2008). Flocculation model of cohesive sediment using variable fractal dimension. *Environmental Fluid Mechanics*, 8:55–71.

Spearman, J. R. and Roberts, W. (2002). Comparison of flocculation models for applied sediment transport modelling. In Winterwerp, J. C.and Kranenburg, C., editor, *Proceedings in Marine Science*, volume 5, pages 277–293.

Spicer, P. T. and Pratsinis, S. E. (1996). Shear-induced flocculation: the evolution of floc structure and the shape of the size distribution at steady state. *Water Research*, 30(5):1049–1056.

Spork, V. (1997). *Erosion behavior of fine sediments and their biogenic stabilization (in German).* PhD thesis, RWTH Aachen.

Stevens, R. L. (1991). Grain-size distribution of quartz and feldspar extracts and implications for flocculation processes. *Geo-Marine Letters*, 11(3):162–165.

Stokes, G. G. (1850). *On the effect of the internal friction of fluids on the motion of pendulums*, volume 9. Pitt Press.

Stolzenbach, K. D. and Elimelich, M. (1994). The effect of density on collisions between sinking particles: implications for particle aggregation in the ocean. *Deep Sea Research Part I: Oceanographic Research Papers*, 41(3):469–483.

Stone, M. and Krishnappan, B. (2003). Floc morphology and size distributions of cohesive sediment in steady-state flow. *Water Research*, 37(11):2739–2747.

Strom, K. and Keyvani, A. (2011). An explicit full-range settling velocity equation for mud flocs. *Journal of Sedimentary Research*, 81(12):921–934.

Stumm, W. (1992). *Chemistry of the Solid-Water Interface: Processes at the Mineral-Water and Particle-Water Interface in Natural Systems.* John Wiley & Sons, Inc.

Tambo, N. and Hozumi, H. (1979). Physical characteristics of flocs-II. Strength of floc. *Water Research*, 13:421–427.

Teisson, C. (1991). Cohesive suspended sediment transport: feasibility and limitations of numerical modeling. *Journal of Hydraulic Research*, 29(6):755–769.

Tennekes, H. and Lumley, J. L. (1972). *A First Course in Turbulence*. MIT Press, Cambridge.

Ternat, F., Boyer, P., Anselmet, F., and Amielh, M. (2008). Erosion threshold of saturated natural cohesive sediments: Modeling and experiments. *Water Resources Research*, 44(11):1–18.

Thomas, D. N., Judd, S. J., and Fawcett, N. (1999). Flocculation modelling: A review. *Water Research*, 33(7):1579–1592.

Thouy, R. and Jullien, R. (1996). Structure Factors for Fractal Aggregates Built Off-Lattice with Tunable Fractal Dimension. *Journal de Physique I, EDP Sciences*, 6(10):1365–1376.

Tian, Z. F., Tu, J. Y., and Yeoh, G. H. (2005). Numerical Simulation and Validation of Dilute Gas-Particle Flow Over a Backward-Facing Step. *Aerosol Science and Technology*, 39(4):319–332.

Tolhurst, T. J., Defew, E. C., de Brower, J. C. F., Wolfstein, K., Stal, L. J., and Paterson, D. M. (2006). Small-scale temporal and spatial variability in the erosion threshold and properties of cohesive intertidal sediments. *Continental Shelf Research*, 26:351–362.

Tsai, C. H., Iacobellis, S., and Lick, W. (1987). Flocculation of Fine-Grained Lake Sediments Due to Uniform Shear Stress. *Journal of Great Lakes Research*, 13(2):135–146.

Unalan, I. U., Cerri, G., Marcuzzo, E., Cozzolino, C. A., and Farris, S. (2014). Nanocomposite films and coatings using inorganic nanobuilding blocks (NBB): current applications and future opportunities in the food packaging sector. *RSC Advances (The Royal Society of Chemistry)*, 4:29393–29428.

van Leussen, W. (1994). *Estuarine macroflocs*. PhD thesis, University of Utrecht.

van Leussen, W. (1997). The Kolmogorov microscale as a limiting value for the floc sizes of suspended fine-grained sediments in estuaries. In *Cohesive Sediments*, pages 45–62.

van Rijn, L. C. (1984a). Sediment Transport, Part I: Bed Load Transport. *Journal of Hydraulic Engineering*, 110(10):1431–1456.

van Rijn, L. C. (1984b). Sediment Transport, Part II: Suspended Load Transport. *Journal of Hydraulic Engineering*, 110(11):1613–1641.

Verney, R., Lafite, R., Brun-Cottan, J. C., and Hir, P. L. (2011). Behaviour of a floc population during a tidal cycle: Laboratory experiments and numerical modeling. *Continental Shelf Research*, 31(10):64–83.

Vicsek, T. (1992). *Fractal Growth Phenomena*. World Scientific Publishing Co. Pte. Ltd., Singapore.

Walling, D. E. and Fang, D. (2003). Recent trends in the suspended sediment loads of the world's rivers. *Global and Planetary Change*, 39:111–126.

Wasserstraßen- und Schifffahrtsverwaltung des Bundes (WSA Freiburg) (2011). Technical report - Upstream spillway channel barrage Iffezheim 2011 (in German). Technical report.

Weilbeer, H. (2005). Modeling the transport of cohesive sediments (in German). In *Darmstädter Wasserbauliches Kolloquium / DWA-Seminar Feststofftransportmodelle*. Instiut für Wasserbau und Wasserwirtschaft, TU Darmstadt. Heft 139.

Widdows, J., Brinsley, M. D., Pope, N. D., Staff, F. J., Bolam, S. G., and Somerfield, P. J. (2006). Changes in biota and sediment erodability following the palcement of fine dredged material on upper intertidal shores of estuaries. *Marine Ecology Progress Series*, 319:27–41.

Wiesner, M. R. (1992). Kinetics of aggregate formation in rapid mix. *Water Research*, 26(3):379–387.

Winterwerp, J. C. (1998). A simple model for turbulence induced flocculation of cohesive sediment. *Journal of Hydraulic Research*, 36(3):309–326.

Winterwerp, J. C. (1999). *On the dynamics of high-concentrated mud suspensions*. PhD thesis, Delft University of Technology.

Winterwerp, J. C. (2002). On the flocculation and settling velocity of estuarine mud. *Continental Shelf Research*, 22(9):1339–1360.

Winterwerp, J. C. and van Kesteren, W. G. M. (2004). *Introduction to the physics of cohesive sediment in the marine environment*, volume 56. Developments in Sedimetology. Elsevier.

Wood, P. J. and Armitage, P. D. (1997). Biological Effects of Fine Sediment in the Lotic Environment. *Environmental Management*, 21(2).

Wu, J. (1969). Wind stress and surface roughness at air-sea interface. *Journal of Geophysical Research*, 74(2):444–455.

Wu, W., Rodi, W., and Wenka, T. (2000). 3D Numerical Modeling of Flow and Sediment Transport in Open Channels. *Journal of Hydraulic Engineering*, 126(1):4–15.

Xu, F., Wang, D.-P., and Riemer, N. (2008). Modeling flocculation processes of fine-grained particles using a size-resolved method: Comparison with published laboratory experiments. *Continental Shelf Research*, 28(19):2668–2677.

Yeung, A. K. C. and Pelton, R. (1996). Micromechanics: A New Approach to Studying the Strength and Breakup of Flocs. *Journal of Colloid and Interface Science*, 184(2):579–585.

Zanke, U. (1977). *Calculation of sediment settling velocities (in German)*. Number 46. Mitteilungen des Franzius-Instituts für Wasserbau und Küsteningenieurwesen der TU Hannover.

Zanke, U. (1982). *Basics of sediment movement (in German)*. Springer-Verlag, Berlin Heidelberg New York.

Zhang, Q., Hillebrand, G., Klassen, I., Vollmer, S., Olsen, N. R. B., Moser, H., and Hinkelmann, R. (2013). Sensitivity analysis of flow field simulation in the Iffezheim reservoir in Germany with the 3D SSIIM model. In *Proceedings of 35th IAHR World Congress, 8.-13. Sept. 2013, Chengdu, China.*

Zhang, Q., Speckter, T., Hinkelmann, R., Hillebrand, G., Hoffmann, T., and Moser, H. (2016). Sensitivity of deposition and erosion to bed composition in the iffezheim reservoir, germany. In *13th International Symposium on River Sedimentation, ISRS 2016*, Stuttgart, Germany.

Zhu, Z. (2014). Theory on Orthokinetic Flocculation of Cohesive Sediment: A Review. *Journal of Geoscience and Environment Protection*, 2(5):13–23.